Imperial College London

Time-lapse Seismic Monitoring of CO_2 Storage in Saline Aquifers: a Model-based Sensitivity Study

by

Grace Cairns

A dissertation submitted to the Department of Earth Science and Engineering of Imperial College London in partial fulfilment of the requirements for the degree of Doctor of Philosophy

Declaration

I declare that this thesis

Time-lapse Seismic Monitoring of CO_2 Storage in Saline Aquifers: a Model-based Sensitivity Study

is entirely my own research under the supervision of Prof. Ann Muggeridge, Dr Lidia Lonergan and Prof. Helmut Jakubowicz. The research was carried out in the Department of Earth Science and Engineering at Imperial College London. All published and unpublished material used in this thesis has been given full acknowledgement. None of this work has been previously submitted to this or any other academic institution for a degree or diploma, or any other qualification.

Grace Cairns

PhD student

Department of Earth Science and Engineering

Imperial College London

Abstract

The injection of Carbon Dioxide (CO_2) into saline aquifers could help to reduce anthropogenic CO_2 emissions, but due to the potential dangers posed by leakage, extensive monitoring will be required. Ideally this monitoring will be able to determine: CO_2 movement, the amount of CO_2 stored, the CO_2 phase (gaseous, supercritical or dissolved in brine), the trapping mechanism (structural or residual) and the occurrence of pore-pressure changes. The literature review highlighted five uncertainties which could impact on the ability of time-lapse seismic surveys to fulfil the monitoring requirements: the dependence on reservoir properties, the fizz gas effect, the CO_2 phase, uncertainty regarding the appropriate fluid distribution model and the effect of pressure build-up.

An integrated geological, rock physics, seismic and fluid-flow modelling approach was developed to predict the seismic response to CO_2 injection. Two approaches were taken, the first excluded fluid-flow simulation and predicted the sensitivity of the seismic response to reservoir changes, the second included outputs from fluid-flow simulation to predict the time-lapse response. The majority of the modelling was performed for a synthetic clastic saline aquifer at 1500m depth. The sensitivity study was applied to all the uncertainties, whereas fluid-flow simulation was only included to examine fluid distribution and pressure build-up. Through examination of these issues, the ability of the time-lapse seismic surveys to achieve the monitoring aims was established.

The zero-offset reflectivity was sensitive enough to detect the migration of both structurally and residually-trapped CO_2 irrespective of the fluid-distribution and reservoir depth (up to 2500 m). Unfortunately there was no success with establishing a seismic monitoring approach which could determine the CO_2 saturation when a homogeneous fluid distribution was assumed. With regards to detecting the CO_2 phase and trapping mechanism there were mixed results. The seismic response was not sensitive enough to distinguish brine from brine saturated with CO_2, however the gaseous and supercritical CO_2 could be differentiated by AVO cross plotting. The potential for a reflection of the interface between residually and structurally trapped CO_2 was identified; this reflection could help constrain how much CO_2 was retained via these different mechanisms. Overpressure could be identified by anomalously large amplitude changes and pushdown both within the plume and away from the plume on the zero-offset reflectivity. Pressure and saturation changes could be distinguished from each other using the AVO response. This research suggested a link between the trapping mechanism and fluid distribution model, which could mean that the appropriate fluid distribution model for seismic interpretation may vary over the life-time of a sequestration project.

These results were used to guide the development of a monitoring framework for sequestration sites, which could be tailored base upon the specific requirements of the site. Overall conducting this modelling study highlighted the advantages of incorporating fluid-flow simulation results into a seismic sensitivity study and underlined the importance of conducting a monitoring sensitivity study prior to site selection.

Acknowledgements

I would like to thank all my PhD supervisors, as without their combined knowledge and interests this project would not have been designed and successfully implemented. I would like to acknowledge the input provided by Professor Helmut Jakubowicz into this project and thank him for his feedback. I would like to thank Professor Ann Muggeridge for her unwavering support over the last three years. The discussions with her developed my understanding and the feedback she has provided throughout this process has been invaluable. I would also like to thank Dr Lidia Lonergan for the infectious enthusiasm she uses to approach technical challenges and for her efficiency which kept the process progressing when it felt like it was faltering.

I extend my gratitude to Professor Martin Blunt and Professor Colin Macbeth for agreeing to examine my PhD and apologise for all of the rather tedious work which will ensue. My gratitude is also extended to the EPSRC for the funding of this project.

I have been given great support by a large number of PhD students, postdocs and academics throughout my PhD, which has been really important and it has made the time I have spent here really enjoyable. More specifically I would like to thank Bilal Rashid, Aaron Goater, Lorena Lazaro and Lorraine Sobers for their technical help and their general support; our shared learning helped to guide this research and made the research process much easier.

Lastly I would like to thank my parents Jackie and David Cairns who have been very encouraging throughout this rather stressful process. Also I thank my wonderful partner Sam Bott who has been supportive and tolerant over the past three years and has even provided coding tips at times. Without the encouragement of all my friends and family, this process would not have progressed so smoothly.

List of Publications

Cairns, G.C., Muggeridge, A.J., Lonergan, L. and Jakubowicz, H. Using time-lapse seismic monitoring to identify trapping mechanisms during CO_2 sequestration. *International Journal of Greenhouse Gas Control* (in press).

Contents

Nomenclature 20

1. Introduction 21

2. Background and Literature Review 27

2.1 Introduction 27

2.2 Carbon Capture and Storage 29

2.2.1 Sequestration Sites 29

2.2.1.1 Unminable Coal Beds 31

2.2.1.2 Depleted Hydrocarbon Fields 31

2.2.1.2.1 EOR in Depleted Oil Fields: Weyburn 32

2.2.1.2.2 Producing Gas Field: In Salah 33

2.2.1.3 Saline Aquifers: Sleipner 34

2.2.2 Potential for Sequestration in the UK 35

2.3 CO_2 Storage 37

2.3.1 CO_2 Properties 37

2.3.2 Capillary Pressure and Relative Permeability 40

2.3.3 Physical Processes and Trapping Mechanisms 42

2.3.4 Pore Pressure 46

2.4 Monitoring CCS 47

2.4.1 Alternative Monitoring Techniques 48

2.4.2 Time-lapse Seismic Monitoring 51

2.4.2.1 Elastic Moduli 51

2.4.2.2 Understanding and Recording the Elastic Moduli 52

2.4.2.2.1 Pore-Pressure Changes 55

2.4.2.2.2 Fluid Substitution 56

2.4.2.3 Seismic Parameters 60

2.4.2.4 Time-lapse Seismic Monitoring Results 61

2.5 Current Limitations of the Time-lapse Seismic Approach 64

2.5.1 Importance of Reservoir Properties 65

2.5.2 Fizz-gas Effect....65
2.5.3 CO_2 Phase....66
2.5.4 Pressure Changes....67
2.5.5 Uncertainty Regarding the Fluid Distribution....68
2.6 Summary....71
3. Methodology and Theory: Predicting the Time-lapse Seismic Response....73
3.1 Introduction....73
3.2 Predicting the Seismic Response....76
3.2.1 Seismic Velocities....76
3.2.2 Reflectivity....76
3.2.3 Attenuation....79
3.2.4 Seismic Reflection Modelling....80
3.3 Rock Physics Modelling....81
3.3.1 Grain Modulus....81
3.3.2 Grain Framework Moduli....82
3.3.3 Fluid Substitution....84
3.3.3.1 Homogeneous distribution....84
3.3.3.2 Patchy Saturation....84
3.3.3.2.1 Hill and Voigt Models....85
3.3.3.2.2 White Modelling....87
3.4 Acoustic Properties of Reservoir Fluids....89
3.4.1 Brine Properties....89
3.4.2 CO_2 Properties....91
3.4.3 Brine Saturated with CO_2....94
3.5 Idealised Saline Aquifer....97
3.6 Typical Reservoir Properties....99
3.7 Fluid-Flow Simulation....101
3.8 Integrated Approach....103
3.8.1 Integrated Approach Workflow....103

3.8.2 Advantages and Disadvantages of the Combined Approach....104
3.8.2.1 Predicting Saturation. 104
3.8.2.2. Grid Block size....106
3.8.2.3 Differences in Scale....107
3.8 Summary 108
4. Sensitivity Study....110
4.1 Introduction 111
4.2 Model Verification and Extension....112
4.2.1 Verification....112
4.2.2 Improved Numerical Model 112
4.3 Importance of Reservoir Properties....114
4.3.1 Reservoir Depth....114
4.3.1.1 Fluid and Reservoir Properties 115
4.3.1.2 Seismic Response 117
4.3.2 Reservoir Thickness 122
4.4 Fizz-gas Effect....123
4.4.1 Zero-offset Seismic Response 124
4.4.2 AVO and Converted Waves. 125
4.4.3 Attenuation 127
4.5 CO_2 Trapping and Phase Changes....128
4.5.1 CO_2 Phase....128
4.5.2 Solubility Trapping....130
4.6 Conclusions 132
5. Dynamic Reservoir Properties and the Time-lapse Seismic Response 135
5.1 Introduction 136
5.2 Modelling Approach....137
5.2.1 Geological Properties 137
5.2.2 Reservoir Model 138
5.2.3 Rock Physics Modelling....139
5.3 Saturation and Pressure over Time....140

5.4 Sensitivity of the Seismic Response to Pressure and Saturation Changes. 143
5.4.1 Sensitivity to Fluid Content 143
5.4.2 Sensitivity to Pressure 144
5.5 Time-lapse Seismic Response 147
5.5.1 Seismic Velocities 147
5.5.2 Zero-offset Reflectivity 149
5.5.3 AVO Response 151
5.6 Summary 155
6. Fluid Distribution and the Seismic Response 157
6.1 Introduction 159
6.2 Reservoir Properties 160
6.3 Sensitivity Study: End-member Fluid Distribution Models 161
6.3.1 Seismic Velocities and P-wave Impedance 161
6.3.2 Zero-offset Reflectivity 163
6.3.3 AVO Response 164
6.4 Time-lapse Response 166
6.4.1 CO_2 Injection 166
6.4.1.1 Injection Parameters 166
6.4.1.2 Dynamic Reservoir Properties 167
6.4.2 Time-lapse Seismic Response 168
6.4.2.1 Proposed New Modelling Approach 168
6.4.2.2 End-member Models: Seismic Response 169
6.4.2.3 Proposed Model: Seismic Response 171
6.4.3 Determining the Trapping Phase 171
6.5 Predicting the Fluid Distribution 174
6.5.1 Modelling Approach 174
6.5.2 Predictions 175
6.6 Discussions 177
6.7 Conclusions 181
7. Conclusions and Future Work 183

7.1 Summary 183
7.1.1 Literature Review and Modelling Approach 183
7.1.2 Key Findings 184
7.2 Monitoring Approach 188
7.2.1 Site Selection 189
7.2.2 Monitoring Strategy 189
7.3 Modelling Challenges and Future Work 193
7.3.1 Simplified Geological Modelling 193
7.3.2 Seismic Modelling and Monitoring Approach 194
7.3.3 Application to a Specific Aquifer 195
7.3.4 Integration Issues 195
7.3.5 Fluid Distribution 196
Appendix 198
References 201

List of Figures

Figure 2-1 Map showing the global distribution of sequestration sites: yellow are in planning, red are cancelled or dormant, blue are pilot sites, green are operational and black are completed. (http://www.sccs.org.uk/storage/globalsitesmap.html. Accessed: December 23rd 2011.).....29

Figure 2-2 Figure compiled from Global CCS Institute (2011).The colours refer to the position of the project in the asset lifecycle model: identify refers to considering high level options, evaluate is when projects are short-listed, define is when selected projects are examined in more detail, execute refers to the design and build phase and then operate is when the CCS plant is actually operational. 30

Figure 2-3 Injection of CO_2 for EOR with some retained CO_2. The CO_2 which is produced with the oil is separated and re-injected back into the formation (IPCC 2005).....32

Figure 2-4 Schematic of the In Salah Gas Project, Algeria (IPCC 2005). 33

Figure 2-5 Simplified diagram of the Sleipner CO_2 storage project (IPCC 2005). 34

Figure 2-6 Map showing the location of offshore hydrocarbon fields and major oil and gas bearing sedimentary basins in the UKCS (Holloway 2009).....36

Figure 2-7 The range of temperatures and pressures found in the Alberta Basin and worldwide basins superimposed on the phase behaviour of CO_2 (Han et al. 2010). 37

Figure 2-8 Variation in CO_2 density as a function of temperature and pressure, showing the range of densities which would be encountered in sedimentary basins around the world (Bachu 2003).....38

Figure 2-9 Variation in CO_2 viscosity as a function of temperature and pressure (Bachu 2003) 38

Figure 2-10 Micro CT scan of a sandstone, the non-wetting phase is in blue, the rock is green and the wetting phase is grey (Dong 2007) 39

Figure 2-11Generic relative permeability curves, annotated to demonstrate where the residual gas and connate water saturation can be read off.....41

Figure 2-12 Profiles taken from Ngheim et al, (2004), showing the impact of CO_2 dissolution on brine properties 200 years after injection of CO_2. This shows how slow convective mixing is to develop. .43

Figure 2-13 Different trapping mechanisms and the way in which their occurrence varies with time following injection (IPCC 2005). 44

Figure 2-14 Schematic demonstrating the spatial distribution of injected CO_2 formed by the interaction of gravitational, viscous and capillary forces with the rock fabric. Two plume regions are formed:,a region of mobile CO_2 and a region of "immobile" residually-trapped CO_2 that is left behind because of snap-off, as the plume migrates upwards (Juanes et al. 2006). 45

Figure 2-15 The monitoring technologies under consideration at the In Salah sequestration site (Mathieson et al. 2010).....47

Figure 2-16 Velocity difference tomograms from the Nagoaka site: a) velocity difference between the baseline survey and a survey following injection of 3200 t of CO_2, b) Velocity difference between the baseline surveys and a survey following injection of 6200 t of CO_2 (Saito et al. 2006). 49

Figure 2-17 Vertical displacement detected by DInSAR at the In Salah sequestration site a) From 31/7/2004 to 24/9/2005, b) From 24/9/2005 to 31/5/2008 (Onuma and Ohkawa 2009). 50

Figure 2-18 Calculated bulk and shear moduli logs for the Stuttgart sands using Hashin-Shtrikman bound averages. Thin lines indicate narrow lower and upper bounds. Taken from: (Kazemeini et al. 2010). 53

Figure 2-19 1D forward modelling using the pre-injection P-velocity (blue line), S-velocity (green line), and density (red line) logs from well 15/9-A-16. First panel of traces on the left represents identical modeled traces stacked over an offset range of 0–618 m. The second panel is field data extracted from the 1994 (pre-injection) Sleipner near-offset image cube in the vicinity of well. Image taken from (Meadows 2008). 54

Figure 2-20 The relationship between the effective pressure and the grain framework elastic moduli, predicted using the friable-sand model (Dvorkin and Nur 1996), a) K_{dry}, b) μ_{dry}.....55

Figure 2-21 Composite image taken from MacBeth and Stephen 2008. Saturation heterogeneity at the: (a) pore scale due to viscous-dominated (fast) water displacement of oil; (b) core-scale with residual oil bypassed in pores and groups of pores; (c) individual bed scale where trapping of residual oil in laminae is visible. A selection of possible sub-seismic saturation scenarios induced by production: (d) Layer-cake reservoir, with high lateral continuity and poor vertical sweep due to compartments separated by impermeable intercalations. This gives an uneven sweep and early water breakthrough); (e) interconnected sand bodies in which there are dead ends and gravity traps (f) effect of rate of capillary displacement of oil from tight sand lenses for different production rates – an inappropriate balance of production rate and capillary forces can create isolated zones of bypassed oil. (g) Unstable displacement of oil by a greater mobility water; (h) dissolved gas drive reservoir, gas collecting up-structure – free gas pulled into well at high oil producing rates; (i) viscous fingering in essentially homogeneous rocks with little detectable permeability variation – a high mobility (less viscous) fluid displacing a less mobile fluid. 59

Figure 2-22 Blocky interval models of velocities and density before injection (yellow lines), after 30% uniform CO_2 saturation (green line,) and after 30% patchy CO_2 saturation (red lines) are posted on "measured" velocity and density logs (black curves) (Kazemeini et al. 2009). 60

Figure 2-23 Plume development at Sleipner site, monitored using time-lapse seismic monitoring (Arts et al. 2008). 62

Figure 2-24 Time-lapse amplitude difference maps for the Midale Marly Horizon at Weyburm. The negative amplitude differences accentuate the CO_2 saturation effects wells (White 2009).....63

Figure 2-25 Time-lapse traveltime maps determined for a sub reservoir horizon, representing the traveltime anomalies associated with propagation through the reservoir (White 2009). *63*

Figure 2-26 Comparison between theoretical models and log data for different depth intervals (1 and 2) at the Nagoaka site. GW:Homogeneous, GH: Patchy (Caspari et al. 2011). *69*

Figure 3-1 Flow chart showing the ways which disciplines are combined in the thesis to examine the limitations in the ability of time-lapse seismic surveys to monitor sequestration. The words in blue are the variables which are altered. *75*

Figure 3-2 Angle dependent P-wave reflection coefficient (Rpp(θ)) plotted against angle (θ). Reflectivity generated using: solid line: Zoepprit, dashed line: "three-term" approximation, dotted line: "two-term" approximation. *78*

Figure 3-3 AVO intercept (A) versus gradient (B) showing four quadrants. Brine-saturated sandstones and shales tend to fall along the background trend, whilst top gas-sand reflectors tend to fall below this trend and base-sand reflectors fall above the line (Castagna et al. 1998). *78*

Figure 3-4 Creation of a synthetic seismogram from an acoustic impedance log recorded in depth (Kazemeini 2009). *80*

Figure 3-5 40Hz zero-phase Ricker wavelet. *80*

Figure 3-6 Relationship between the saturated bulk modulus and CO_2 saturation, calculated using models in 3.3.3, assuming a residual gas saturation (S_{rg}) of 5% and a connate water saturation (S_{cw}) of 20%. *86*

Figure 3-7 Brine properties within the temperature ranges 0-75°C and the pressure range 0-30 MPa: a) Bulk Modulus in GPa, b) Density in kg/m^3 and c) Velocity in m/s. *90*

Figure 3-8 CO_2 properties: a and d) Density, b and e) Bulk modulus and c and f) Velocity, predicted using: Span and Wagner equation of state (S&W), Batzle-Wang equations (B-W) and the Xu approximation to the Batzle-Wang equations (Xu).a-c) for a constant temperature of 57˚, d-e) for reservoir depths. *92*

Figure 3-9 CO_2 properties plotted between 0-75˚C and 0-30 MPa. a) Bulk Modulus (GPa), b) Density (kg/m^3), c) Velocity (m/s) (NIST 2011). *93*

Figure 3-10 Brine saturated with CO_2 properties, plotted between 0-75˚C and 0-30MPa. a) Bulk Modulus (GPa), b) Density (kg/m^3), c) Velocity (m/s). *96*

Figure 3-11 Pressure relationships with depth. *98*

Figure 3-12Velocities, density, and Poisson's ratio logs for uniform- and patchy-saturation models at 30% CO_2 saturation. Last track shows how the shear modulus and dry-rock bulk modulus overlap in the relatively cleaner sandstone interval. From Kazemeini et al, 2010. ..... *100*

Figure 3-13 a) Hysteretic relative permeability curves, for brine (red) and CO_2 (blue), κ^d_{rw}: drainage brine curve, κ^I_{rw}: imbibition brine curve, κ^d_{rg}: drainage CO_2 curve, κ^I_{rg}: imbibition CO_2 curve. b) Capillary pressure curve. *102*

Figure 3-14 Workflow for the "integrated approach". *103*

Figure 3-15 Cartoon showing the three most common saturation states within the aquifer. On the left, where they are likely to occur within the plume and on the right how they will appear on the pore scale. 105

Figure 3-16 Predicted CO_2 saturation from simulations using different size grid blocks, a&d) half the number of grid blocks, b&e) original number of grid blocks, c&f) double the number of grid blocks, resulting from injection of 0.7M t of CO_2 over 10 years, a-c) saturation maps, d-f)Percentage of gridblocks containing specified saturations (excluded 0). 106

Figure 3-17Cartoon demonstrating the typical scale of a fluid flow simulation gridblock and a typical seismic pixel. 107

Figure 4-1 Change in density (a-b) and V_p/V_s ratio (c-d) as CO_2 displaces brine. a&c) Taken from McKenna et al. (2003), b&d) Generated using the modelling approach/ code which was then modified and used in this thesis.....113

Figure 4-2 Effects of rock and fluid changes on the seismic velocities and the V_p/V_s ratio(from Kazemeini (2009) modified from Tatham and McCormack (1991)). 114

Figure 4-3 Brine and CO_2 density and bulk modulus plotted against reservoir depth. 116

Figure 4-4 Relationship between seismic attributes and CO_2 saturation for reservoirs at 500 m depth intervals between 500 m and 2500 m: a) V_p, b) V_s, c) Percentage change in V_p from brine filled, d) Percentage change in V_s from brine filled, e) Percentage change in P-wave acoustic impedance (AI) from brine filled, dashed black line represents 4% change in P-wave impedance, which should produce a detectable time-lapse response (Lumley et al. 1997). 118

Figure 4-5 Zero-offset reflectivity generated using CREWES software assuming a 40Hz Ricker wavelet, plotted for a 100 m thick sandstone reservoir, containing varying amounts of CO_2 from brine filled to 100% CO_2 in 4% CO_2 increments. Shale is found both above and below the reservoir. The black dashed line represents the location of the pre-injection base-reservoir reflection. Reservoir at different depths: a) 500 m, b) 1000 m, c) 1500 m, d) 2000 m, e) 2500 m. 119

Figure 4-6Angle-dependent reflection coefficient ($R_{pp}(\Phi)$) plotted against angle (Φ) out to 30° incidence angle, plotted for brine-filled, and containing different saturations of CO_2: 2%, 60% and 100%. These plots are for five reservoir depths: a) 500 m, b) 1000 m, c) 1500 m, d) 2000 m, and e) 2500 m. 120

Figure 4-7 Cross-plot of AVO attributes A and B for five reservoir depths, at increments of 2% CO_2 saturation from brine-filled to 100% CO_2. 121

Figure 4-8 Reflectivity off a top and base-reservoir reflector for a reservoir of varying thickness. The wavelet is a 40Hz Ricker wavelet and the velocity in the reservoir is 2500 m/s 122

Figure 4-9 Zero-offset reflectivity for a 100 m thick clastic saline aquifer found at 1500 m depth for different saturation states, a) brine-filled, b) Residually trapped 30% CO_2, c) Structurally trapped 60% CO_2. 124

Figure 4-10 V_p/V_s ratio against CO_2 saturation. 125

Figure 4-11 Angle-dependent reflectivity plotted against incidence angle for CO_2 saturations from brine-filled (blue), and every 10% up to 80% CO_2 saturation.....126

Figure 4-12 AVO attributes plotted against CO_2 saturation, a) AVO intercept A, b) AVO curvature C, c) subtraction of C from A, to provide the density parameter.....126

Figure 4-13 Attenuation resulting from mesoscopic loss, plotted for gaseous and supercritical CO_2, with different size saturation heterogeneities. Predicted using the White model for patchy saturation (frequency:40 H)z.....127

Figure 4-14 Relationship between CO_2 saturation and seismic velocities for gaseous CO_2 (red) and supercritical CO_2 (blue) a) V_p, b) V_s, c) V_p/V_s ratio. 128

Figure 4-15 AVO behaviours as a function of saturation for gaseous (red) and supercritical CO_2 (blue) a) AVO intercept A, b) AVO gradient B, c) Angle dependent top reservoir reflectivity plotted against incidence angle out to 50°, for a brine-filled reservoir (black) and a reservoir containing varying amounts of CO_2, d) A cross-plotted with B, for different CO_2 saturations from 0% CO_2 to 100% CO_2 in 4% increments. 129

Figure 4-16 Percentage difference in fluid properties between brine and brine saturated with CO_2,for the temperature range 0-80°C and the pressure range 0-30 MPa: a) velocity, b) density, c) bulk modulus. Marked on is the temperature and pressure conditions for a reservoir at 1500 m depth..130

Figure 4-17 Percentage change in P-wave impedance from brine-filled to containing brine saturated with CO_2, for a range of temperatures and pressures,.....131

Figure 5-1 Simulation layout. 138

Figure 5-2 Injection well properties, for 10 years of injection and 10 years post-injection, a) well pressure, b) total injected CO_2.....140

Figure 5-3 Change in pore pressure at the top of the reservoir from the injector. Pre-injection pressures are shown in blue, the pressure after a certain time of injection is in green (2 years), red (4 years), turquoise (6 years), purple (8 years) and brown (10years), the pressure 10 years after injection ceased is shown as a dashed black line.....141

Figure 5-4 CO_2 saturation maps over the central portion of the reservoir: a) after 2 years, b) after 4 years, c) after 6 years, d) after 8 years, e) after 10 years, f) 10 years post-injection. 142

Figure 5-5 Percentage change in seismic velocities from brine filled against CO_2 saturation: a) P-wave velocity (V_p), b) S-wave velocity (V_s).....143

Figure 5-6 Fluid properties for the temperature range 0-75˚C and pressure range 0-30 MPa. The reservoir temperature and pressure before injection are indicated by a white triangle and after 10 years injection by a white diamond. a) CO_2 bulk modulus (GPa,) b) brine bulk modulus (GPa), c) CO_2 density (kg/m^3), d) brine density (kg/m^3). 144

Figure 5-7 Effective pressure against the different attributes for a brine-filled reservoir: a) V_p (m/s), b) V_s (m/s), c) V_p/V_s ratio, d) percentage change in P-wave acoustic impedance from pre-injection conditions. 145

Figure 5-8 %change in P-wave acoustic impedance, for a brine-filled (pre-injection) reservoir, caused by changes in CO_2 saturation and effective pressure. Colours indicate a detectable change (>4%). ..146

Figure 5-9 Relationship between CO_2 saturation and percentage change in V_p from pre-injection, i.e. brine-saturated pore-space, created using pre-injection pressures (blue) and post-injection pressures (red). 146

Figure 5-10 Diagrams illustrating how the seismic velocities in the reservoir change from pre-injection conditions after 10 years of injection, a,c,e,g,i) V_p, b,d,f,h,j) V_s. a,b) Pressure effects on fluid properties, c,d) pressure effects on the frame properties, e,f) total effect of pressure changes, g,h) effect of saturation, i,j) combined effect of pressure and saturation changes. 148

Figure 5-11 Zero-offset synthetic seismograms. a) After 10 years injection assuming constant pressure, b) after 10 years injection allowing pressure increase, c) change in the reflectivity (Figure 5-12a – baseline), from changes in saturation, d) change in reflectivity (Figure 5-12b-baseline), from changes in saturation and pressure..... 150

Figure 5-12 The base-reservoir pushdown assuming no change in pressure (blue) and allowing pressure to increase (red). Black dashed line represents the pre-injection base-reservoir reflection. 150

Figure 5-13 Percentage change in V_p, V_s, density (ρ) and V_p/V_s ratio from pre-injection conditions, resulting from saturation changes alone (55% CO_2) as well as a combination of saturation (55% CO_2) and pressure changes (8 MPa increase). 151

Figure 5-14 Synthetic seismograms produced taking into account changes in: a,d,g) saturation, b,e,h) both saturation and pressure, c,f,i) difference between pressure and saturation changes. Seismograms generated for different incidence angles to examine AVO: a,b,c) zero-incidence angle, c,d,e) 10° incidence angle, g,h,i) 20° incidence angle..... 152

Figure 5-15 P-wave reflection coefficient (R_{pp}) plotted against incidence angle (in degrees), for two different scenarios: saturation changes (red), combination of pressure and saturation (blue.).a) All the reflections within the reservoir interval, b) top-plume reflection (i.e. at injector), c) base-plume reflection (i.e. generated off interface between brine and CO_2), d) top-reservoir reflection, (away from plume), b) base-reservoir reflection. 153

Figure 6-1 Relationship between V_p and S_{CO2} calculated using a Gassmann- Reuss model appropriate for a homogeneous response (Blue line) and a Hill model appropriate for a patchy distribution (Red lines), with additional constraints of Scw:42% and S_{rg}:30%, appropriate for the saturation conditions in the reservoir..... 161

Figure 6-2 Variation in seismic properties with CO_2 saturation (S_{cw}=0.42) for two end-member fluid distribution models, Hill-drainage (red), Reuss (blue). a) V_p, b) V_s, which does not depend on fluid

distribution, c) V_p/V_s ratio, d) Percentage change in P-wave impedance from the brine-filled case. 162

Figure 6-3 Zero-offset reflectivity generated using the CREWES package assuming a 40Hz Ricker wavelet, plotted for a 100 m thick sandstone containing varying amounts of CO_2 from brine-filled to 58% CO_2 in 2% increments: a) Reuss model, b) Hill model. 163

Figure 6-4 Base-reservoir pushdown plotted against percentage change in P-wave impedance for different CO_2 saturations (0-58% every 2%), calculated using the Reuss (blue) and Hill-drainage (red) models. 164

Figure 6-5 Angle-dependent reflectivity: a) R_{pp}, b) R_{ps}., plotted for three different saturations, brine-filled (black, solid), 16% homogenous CO_2 (blue dotted) and 42% patchy CO_2 (red dashed). 165

Figure 6-6 AVO cross plots for a range of saturations from 0-58% CO_2 in 4% increments, predicted using the Reuss model (blue) and the Hill-drainage model (red) a) AVO intercept versus gradient, b) AVO intercept versus curvature. 165

Figure 6-7 Simulation layout 166

Figure 6-8 Amalgamation of results demonstrating the workflow from fluid-flow results to zero-offset seismic response. a) Graph showing the total amount of CO_2 injected against time. b-d) CO_2 saturation maps of a central portion of the reservoir over time. e-g) Saturation histogram showing frequency of saturations over time. h-j) V_p predicted using the Gassmann-Reuss (homogeneous) model. k-m) Zero-offset reflectivity generated using CREWES software with homogeneous velocities. n-p) V_p predicted using the Hill (patchy) model, k-m) Zero-offset reflectivity generated using CREWES with patchy velocities. Different time steps: b,e,h,k,n,q) after 20 years of injection, c,f,i,l,o,r) after 20 years injection and 20 years post injection, d,g,j,m,p,s) after 20 years of injection and 40 years post injection. 170

Figure 6-9 The seismic response after 20 years of injection and 20 years post-injection: a-c) V_p change from brine-filled, d-f) zero-offset reflectivity, g-i) reflectivity at 30° incidence angle. a,d,g) Homogeneous model. b,e,h) Proposed model model($S_{CO2}<S_{gr}$: Gassmann- Reuss, else:Hill. c,f,i) Modified Patchy model. 171

Figure 6-10 Top-reservoir reflectivity as a function of incidence angle to 30° for the two dominant saturations found in the reservoir 30% (residual) CO_2 assuming a homogeneous distribution and 60% (structural) CO_2 assuming a patchy distribution. 172

Figure 6-11 Plots of AVO attribute, A versus B after 20 years of injection and 20 years post injection. a) Reflections off the top of the reservoir, b) reflections within the reservoir interval, I: Edge of plume, II: interface between residual and structurally trapped CO_2, III: reflections within the residual CO_2 plume, IV: reflections within the structural CO_2 plume. 172

Figure 6-12 a) Schematic representation of CO_2 saturation within the reservoir, indicating where reflections are generated. b) V_p-saturation graph, showing the magnitude of the V_p changes expected across these interfaces.....173

Figure 6-13 Schematic diagram of the methodology (modified from Sengupta and Mavko, 2003). 174

Figure 6-14 Diagram showing temporal and spatial variations in saturation and velocity during sequestration. a-c) CO_2 saturation maps of the reservoir. d-f) Saturation histograms for the top 15 m of reservoir, g-i) Saturation histograms for the base 15m of plume. j-l) V_p-CO_2 saturation relationships for the coarse scale velocities generated using Hill averaging, separated into top and base plume and compared with the homogeneous, patchy-drainage and brie (e=4) models. Different columns show certain years, a,d,g,j) After one year injection, b,e,h,k) after one year injection, one year post injection, and c,f,i,l) after one year injection and neight years post-injection.....176

List of Tables

Table 1-1 List of someof the key terminology repeatedly used in this thesis.....25

Table 2-1 Summary of modelling approaches for fluid substitution and evidence for these approaches.....57

Table 2-2 Summary of the five key issues raised by this literature review and a brief mention of how they will be examined in this thesis.....72

Table 3-1 Velocities and densities used to predict the AVO response. 78

Table 3-2 The elastic moduli and densities of select minerals. K: Bulk modulus, μ: shear modulus and ρ: density. 82

Table 3-3 Coefficients used to calculate the density of brine saturated with CO_2.....94

Table 3-4 Mineralogies of different sandstones and mudstones. 97

Table 3-5Reservoir properties for clastic sequestration sites at various depths. Black data: predictions from synthetic modelling study, blue: data taken from well logs at existing/planned sequestration sites...99

Table 3-6 An example of the inputs into ECLIPSE. Number refers to number of gridblocks, dimensions gives the gridblock dimension, wells, X and,Y, give well location, Z1 and Z2 give the interval over which the well is open in the reservoir, I/P represented injector/producer, tstep gives the timesteps for the calculation, R/P gives information on the controls on the well, either rate or pressure, and finally O/C states whether the well is open or closed for that time period.....102

Table 4-1 Reservoir, mineral, frame and fluid properties for sandstone and shale at 500 m intervals from 500 m to 2500 m depth. 115

Table 4-2 Summary of the results from Chapter 4. Indicating the best seismic data to be collected to achieve certain monitoring aims. It is assumed that if non-zero offset reflectivity is collected so is the zero-

offset reflectivity. The colours indicate the confidence assigned to the approach.. Green: Should Succeed, orange: May succeed, red: Unlikely this approach will work. 134

Table 5-1 Pre-injection reservoir properties for an aquifer found at 1500 m depth. Average temperature and lithostatic pressure within the reservoir are included, while the porosity and permeability are assumed to be constant.....137

Table 5-2 Inputs into ECLIPSE. Number refers to number of gridblocks, dimensions gives the gridblock dimension, wells, X and,Y, give well location, Z1 and Z2 give the interval over which the well is open in the reservoir, I/P represented injector/producer, tstep gives the timesteps for the calculation, R/P gives information on the controls on the well, either rate or pressure, and finally O/C states whether the well is open or closed for that time period. 138

Table 5-3 Pre-Injection elastic properties and densities of the fluids, mineral and frame properties at 1500 m depth, calculated assuming a hydrostatic pressure gradient. 139

Table 5-4 Fluid and frame properties calculated using the pressure before and after 10 years of injection. 144

Table 5-5 Chapter 5 summary. Indicating the best data to be collected to achieve certain monitoring aims. Colours indicate the confidence with the approach.. Green: should succeed, orange: may succeed, red: unlikely to succeed.....156

Table 6-1 Reservoir, fluid, mineral and frame properties for a homogeneous saline aquifer found at 1500 m depth.....160

Table 6-2 Inputs into ECLIPSE. Number refers to number of gridblocks, dimensions gives the gridblock dimension, wells, X and,Y, give well location, Z1 and Z2 give the interval over which the well is open in the reservoir, I/P represented injector/producer, tstep gives the timesteps for the calculation, R/P gives information on the controls on the well, either rate or pressure, and finally O/C states whether the well is open or closed for that time period. 167

Table 6-3 Chapter 6 summary. Indicating the best data to be collected to achieve certain monitoring aims. Colours indicate the confidence with the approach.. Green: should succeed, orange: may succeed, red: unlikely to succeed.....182

Table 7-1 Indicating the best seismic data to be collected to achieve certain monitoring aims. It is assumed that if non-zero offset reflectivity is collected so is the zero-offset reflectivity. The colours indicate the confidence assigned to the approach.. Green: Should Succeed, orange: May succeed, red: Unlikely this approach will work……191

Nomenclature

CCS	Carbon capture and storage
CO_2	Carbon dioxide
K_{sat}	Saturated bulk modulus
μ_{sat}	Saturated shear modulus
K_{dry}	Grain framework bulk modulus
μ_{dry}	Grain framework shear modulus
K_{grain}	Grain bulk modulus
μ_{grain}	Grain shear modulus
K_{fluid}	Fluid bulk modulus
Φ	Porosity
V_p	P-wave seismic velocity
V_s	S-wave seismic velocity
ρ	Density
AI	P-wave acoustic impedance (V_p*ρ)
AVO	Amplitude variation with offset
A	AVO intercept/zero-offset reflectivity
B	AVO gradient
C	AVO curvature
S_{rg}	Residual gas saturation
S_{cw}	Connate water saturation
S_{CO2}	CO_2 Saturation
κ	Permeability

1. Introduction

Carbon Capture and Storage (CCS) is a way to reduce anthropogenic carbon dioxide (CO_2) emissions and therefore help mitigate global warming. Storage within geological formations is currently considered the most reliable method available, and there are a number of test sites in operation (Davis et al. 2003; Juhlin et al. 2007; Korbøl and Kaddour 1995; Onuma and Ohkawa 2009). More specifically saline aquifers have been identified as preferred storage locations due to their wide geographical spread and large storage capacities.

Injecting CO_2 into a saline aquifer will alter the subsurface in a variety of ways: changing the fluid content, altering the pore pressure and potentially affecting reservoir properties, such as porosity and mineralogy through chemical interactions between CO_2 and the host rock and brine. Any pore-pressure increases resulting from injection should be monitored, as they could cause failure of the reservoir rock or seal. After injection CO_2 can become trapped by four different mechanisms: structural trapping, residual trapping, dissolution and mineralisation (IPCC 2005; Kumar et al. 2005). The trapping security associated with each of these mechanisms is different, with structurally trapped CO_2 still being mobile and capable of escaping, while residually trapped CO_2 is immobile, CO_2 trapped via mineralisation is securely trapped, whereas brine containing dissolved CO_2 is mobile, and CO_2 could come out of solution if the pressure decreased. If trapping fails and the CO_2 leaks, either to the surface or into surrounding formations, this could result in plant death and acidification of the ground water (Kumar et al. 2008). Due to these environmental issues associated with leakage it is vital to verify that the injected CO_2 is retained within the reservoir. This verification will be achieved by monitoring.

At a sequestration site there are four main aims of monitoring: detecting the extent of the CO_2 plume and its migration, quantifying the amount of CO_2 within the reservoir (i.e. saturation), determining the mechanism by which the CO_2 is trapped and finally detecting and locating any build-up in pressure. A wide range of monitoring techniques are being tested and deployed at existing sequestration sites (Eiken et al. 2000; Eiken et al. 2011; Lumley 2010; Onuma and Ohkawa 2009). Time-lapse seismic surveys have been the most successful technique at detecting CO_2 migration on the field-scale (Arts et al. 2004a). They have also been successfully applied to detecting pressure changes during hydrocarbon production (Landrø et al. 1999; Watts et al. 1996), and at the Snohvit CO_2 injection site, in the Norwegian North sea (Eiken et al. 2011). Although time-lapse seismic surveys appear to be the best technology to safely monitoring CO_2 injection, there may be some reluctance to use them due to the cost. However modelling has suggested that if conducted every 5 years, the cost of repeat surveys is 0.3 US$ per tonne of CO_2 stored (Hendriks et al. 2004), in comparison to the European onshore costs of about 2.8 US$ per tonne of CO_2 stored (Myer et al. 2002). Therefore monitoring via time-lapse seismic surveys represents a small portion of the overall costs.

The goal of this thesis was to assess the ability of time-lapse seismic surveys to fully monitor CO_2 injection and storage in a generic clastic saline aquifer. This technology was judged by its ability to achieve the monitoring aims and the best seismic analysis approach use was found. There are a range of possible difficulties to achieving these aims, which were identified and examined. The assessment was performed using a modelling approach which integrated a variety of disciplines: geological, rock physics, seismic and fluid-flow models. Here a brief overview of the arrangement of this thesis is given.

A literature review is given in Chapter 2 which highlights some of the potential limitations and uncertainties with the use of time-lapse seismic surveys at sequestration sites. The review is divided into four main sections, which cover a range of topics associated with CO_2 sequestration from site selection (Section 2.2), to the behaviour of injected CO_2 (Section 2.3), monitoring technologies (Section 2.4) and the current limitations of the time-lapse seismic method at sequestration sites (Section 2.5). Section 2.2 discusses pilot sites and the types of geological formations which are used (Section 2.2.1), along with the potential for sequestration in the UK (Section 2.2.2). Injecting CO_2 can alter the subsurface in a number of ways which are discussed in Section 2.3. Predicting CO_2 behaviour using fluid-flow simulation requires knowledge of certain reservoir properties which are given in Section 2.3.1. The discussion then turns to the importance of capillary pressure and relative permeability (Section 2.3.2) and from that the physical processes which govern CO_2 behaviour and subsequent trapping (Section 2.3.3). In Section 2.3.4 the potential for pore-pressure increases due to injection are discussed. Ideally this subsurface behaviour would be detected using the monitoring approaches discussed in Section 2.4. These techniques fall into two categories: time-lapse seismic surveys (Section 2.4.1) and alternative geophysical techniques (Section 2.4.2). The discussion regarding time-lapse seismic monitoring also examined the elastic moduli and seismic properties and how they can either be taken from well information or derived from modelling. More specifically the impact of changes in fluid content and pressure on the elastic moduli. The research into the use of time-lapse seismic surveys at sequestration sites highlighted some uncertainties which may affect the ability of this approach to safely monitor sequestration. These include the impact of reservoir properties on the sensitivity of the seismic response to fluid content (Section 2.5.1), the fact that the "fizz-gas" effect (Han and Batzle 2002) makes it difficult to extract the CO_2 saturation (Section 2.5.2), the effect which CO_2 phase changes may have on the time-lapse seismic signature (Section 2.5.3), the impact of pore-pressure increase on the reservoir's elastic properties (Section 2.5.4) and ambiguity about which fluid distribution model should be used to interpret the data (Section 2.5.5). These five uncertainties guided the construction of the modelling approach in Chapter 3 and define the topics examined in Chapters 4-6.

An integrated-modelling approach to examine these limitations was developed and is given in Chapter 3. The numerical model incorporated equations to predict the seismic response (Section 3.2), rock physics (Sections 3.3 and 3.4) and geological models (Section 3.5). These predictions are compared to measured values at sequestration sites in Section 3.6. Fluid flow-flow simulation and its typical inputs are

discussed in Section 3.7. Different combinations of these disciplines were used for different purposes. If fluid-flow modelling was ignored, then the sensitivity of the seismic response to subsurface changes was determined this is described as a "sensitivity study", whereas the time-lapse seismic response was predicted using time variant properties provided by fluid-flow simulation, this is called the "combined approach". This combined approach is discussed in more detail in Section 3.8. The models and equations used throughout the thesis are given in Chapter 3. First, the equations to predict the seismic velocities (Section 3.2.1), reflectivity (Section 3.2.2) and attenuation (Section 3.2.3) are included in Section 3.2. To generate a synthetic reflectivity these seismic velocities were convolved with a wavelet using the seismic reflection software discussed in Section 3.2.4. Calculating the seismic velocities and reflectivity required the reservoir's elastic properties, which were predicted using rock physics modelling (Section 3.3). The elastic properties of a saturated porous rock were calculated by combining contributions from the mineral (Section 3.3.1), grain framework (Section 3.3.2) and fluid (Section 3.4). There are a variety of ways to combine these properties and calculate the overall saturated bulk moduli (Section 3.3.3) and the end-member models are given. The magnitude of any time-lapse seismic changes in the reservoir depended on the properties of the fluids (Section 3.4) and the three fluids phases which exist during injection into a saline aquifer are brine (Section 3.4.1), CO_2 (Section 3.4.2) and brine saturated with CO_2 (Section 3.4.3). Estimating the mineral, grain framework and fluid moduli required reservoir properties obtained from geological modelling (Section 3.5). These steps were combined into a rock physics sensitivity study. However predicting the time-lapse seismic response required knowledge of how properties vary in time and space, which was provided by fluid-flow simulation (Section 3.7). The combined approach is discussed in more detail (Section 3.8): the workflow is outlined (Section 3.8.1), then some of the advantages and disadvantages of using this approach are discussed in Section 3.8.2. With the exception of the fluid-flow simulation which use commercial codes (ECLIPSE) and seismic reflection modelling which use open source codes (CREWES), the rest of the modelling was done in Visual Studio using a C program built for this purpose.

In Chapter 4, three of the uncertainties highlighted in the literature review were examined in a rock physics-sensitivity study. First, the importance of reservoir properties was investigated (Section 4.3), then the fizz-gas effect (Section 4.4) and finally the phase of the CO_2 (Section 4.5). The numerical model was verified initially through comparison with published results and then extended to include a realistic overburden and "stiffer" sandstone (Section 4.2). This extended modelling approach was then applied to examine the impact of burial depth on reservoir properties and on the sensitivity of the seismic response to CO_2 injection (Section 4.3.1). Reservoir thickness also affects the ability to monitor injection, and was examined in Section 4.3.2. The fizz-gas effect makes it difficult to distinguish commercial (mobile) and residual gas accumulations using the zero-offset reflectivity. In the case of CO_2 sequestration, the interest is in differentiating structurally and residually trapped CO_2. A number of alternative techniques using different seismic properties and attributes were considered to distinguish CO_2 trapped by these different mechanisms (Section 4.4). These techniques were developed for natural hydrocarbon gases, but were applied to

supercritical CO_2. These techniques cover the AVO response including converted waves (Section 4.4.2) and the effects of attenuation (Section 4.4.3). Due to the differences between the properties of natural gas and supercritical CO_2 the zero-offset reflectivity was also examined in Section 4.4.1. Finally the issue of detecting the phase of the CO_2 was examined (Section 4.5) to assess whether time-lapse seismic surveys can differentiate between gaseous and supercritical CO_2 or detect the dissolution of CO_2 into brine.

The integration of time varying pressure and saturation values into the numerical model is discussed in Chapter 5. The modelling approach which combined geological (Section 5.2.1), fluid-flow (Section 5.2.2) and rock physics models (Section 5.2.3) is given in Section 5.2. The pressure and CO_2 saturation in the reservoir over time was predicted by fluid-flow simulation (Section 5.3) and the maximum pressure and saturation changes were used to examine the sensitivity of the seismic response to realistic changes in saturation (Section 5.4.1) and pressure (Section 5.4.2). The time dependent pressure and saturation values were then used to predict the time-lapse seismic response (Section 5.5). This was predicted for two cases: firstly where the pressure was kept constant while the saturation changes and secondly where both the pressure and saturation varied. These two scenarios were used to establish the ability of the seismic response to differentiate pressure and saturation changes.

Chapter 6 explores the issue of fluid distribution and the impact it may have on the ability to monitor sequestration. Three different modelling approaches were used: a rock physics sensitivity study (Section 6.3), the time-lapse seismic response was predicted (Section 6.4) and the idea of predicting the fluid distribution model was looked at (Section 6.5). These approaches were used to examine four issues about the distribution of the fluids in the pore space: (1) the sensitivity of the seismic response to fluid distribution, (2) whether the fluid distribution could affect monitoring ability, (3) which fluid distribution model is appropriate during the evolution of an injected CO_2 plume while it is stored in the reservoir and (4) can the fluid distribution be determined from the seismic response. Throughout the chapter the reservoir properties were kept constant, as given in Section 6.2. Initially the sensitivity study was conducted using end-member fluid distribution models. These end-member models predicted the range of seismic responses (Section 6.3) which could result from injection. Predicting the time-lapse seismic response required calculation of saturation within the reservoir over time. These were generated by fluid-flow simulation (Section 6.4). A new model was proposed in Section 6.4.2.1 which linked the fluid distribution model to the CO_2 trapping mechanism. The saturation results were then used to generate the time-lapse seismic response in Section 6.4.2. Because of the link suggested between the trapping mechanism and fluid distribution model, the ability to detect the trapping phase was discussed in Section 6.4.3. Predictions of the way in which the fluid distribution varies in time and space during injection are presented in Section 6.5. In Section 6.6 these results were amalgamated to try and answer the four questions posed above.

Chapter 7 concludes this thesis by clarifying some of the key findings (Section 7.1) and using these findings to generate an idealised monitoring approach (Section 7.2) and to highlight areas which may warrant further research and attention (Section 7.3). First, the workflow and literature review were summarised (Section 7.1.1) followed by a list of the key findings (Section 7.1.2), which were used to determine whether time-lapse seismic surveys can accurately monitor CO_2 injection. Then these results were used to formulate an idealised workflow which can be applied to the site selection phase (Section 7.2.1) and the development of a monitoring strategy (Section 7.2.2) at a CO_2 injection site. Conducting this research drew attention to possible interesting extensions to this modelling approach and areas of knowledge which could warrant further examination which are discussed in Section 7.3.

This work combines modelling and knowledge from different disciplines, therefore a list of key terminology used throughout this thesis is given in Table 1-1.

Table 1-1 List of someof the key terminology repeatedly used in this thesis.

Category	Term	Description
General	Geological Sequestration	Injection of CO_2 into permeable geological formations
	Enhanced Oil Recovery	Tertiary recovery process to extract bypassed oil.
CO_2 trapping	Residual Trapping	Trapped in the pore space by capillary forces
	Structural Trapping	Trapped by an impermeable barrier.
	Solubility Trapping	Trapped in solution within the brine
	Mineralisation	Trapped as a solid carbonate precipitate
	Mobile CO_2	CO_2 which is mobile in the pore space.
	Imm**o**bile CO_2	CO_2 which is trapped by capillary forces.
Fluid	Mobility	Ability of a fluid to move through interconnected pore space.
	Solubility	The amount of CO_2 in contact with brine which will dissolve.
	Viscosity	Resistance of a fluid to flow.
	Capillary pressure	Threshold pressure required to enter the rock pores.
	Relative permeability	Decrease in permeability resulting from the presence of a second fluid phase in the pore volume.
	Hysteresis	Dependence on the history of saturation changes.
	Wetting phase	Fluid phase which preferentially adheres to the grain.
	Drainage	Decrease in the wetting fluid phase.
	Imbibition	Increase in the wetting fluid phase.
	Residual gas saturation	Quantity of immobile gas trapped by capillary forces.
	Connate water saturation	Quantity of immobile water trapped by capillary forces.
Pressure	Lithostatic Pressure	Pressure exerted by the weight of the overlying material
	Hydrostatic Pressure	Pressure exerted by the weight of connected water column.
	Pore Pressure	Pressure of the fluid in the pore space.
	Overpressure	Difference between pore and hydrostatic pressure.
	Effective Pressure	Overburden stress supported by the rock frame.
	Fracture Pressure	Pressure at which fractures may reactivate.

Seismic	Attenuation	Reduction in magnitude of a seismic wave.
	AVO	Variation in reflection coefficient strength with angle.
	Zero-offset	Reflection at normal incidence, i.e. source and receiver in line.
	Converted Seismic waves	At non-normal incidence angles a P-wave will generate both a reflected P and converted S-wave.
	Pushdown	Reduction in velocity causes an increase in reservoir traveltime .
	Time-lapse	Repeat geophysical measurements.
	AVO Intercept	The amplitude of the reflection coefficient at normal incidence.
	AVO Gradient	How the amplitude varies at mid offsets.
Moduli	Shear Modulus	Resistance of an object to shear.
	Bulk Modulus	Resistance to compression.
	Mineral Moduli	Contribution of minerals to properties of the saturated rock
	Grain framework Moduli	Contribution of the frame to the overall strength of the rock.
	Fluid modulus	Compressibility of the fluid phases.
Fluid substitution	Fluid substitution	Rock physics problem of understanding how the seismic response depends on fluid content.
	Fluid distribution	How the fluids are distributed in the pore space, i.e. extent of connectivity of the individual fluid phases.
	Fluid distribution model	Models used to calculate the fluid bulk modulus for a rock saturated with multiple fluid phases. Appropriate model depends on fluid distribution (Table 2-1).
	Homogeneous distribution	Fluid phases are mixed below the critical length scale.
	Patchy distribution	Fluid phases present on length scales greater than the critical length scale
	Critical length scale	Maximum length scale over which pore-pressure gradients can relax and reach equilibrium during a seismic period.
	Saturation heterogeneity	A disconnected fluid phase within another fluid
	Fizz gas effect	Non linear relationship between gas saturation and P-wave seismic velocity.

2. Background and Literature Review

2.1 Introduction

Reducing the quantity of carbon dioxide (CO_2) emitted into the atmosphere is seen as essential to mitigate global warming. Carbon Capture and Storage (CCS) by which CO_2 is captured at point sources then stored, is an immediate way of reducing emissions. The use of geological formations as a depository for CO_2 is considered one of the most reliable methods available, and a number of test sites are currently in operation, e.g. the Sleipner field in the North Sea (Korbøl and Kaddour 1995), Weyburn in Canada (Davis et al. 2003), In Salah in Algeria (Onuma and Ohkawa 2009) and Ketzin in Germany (Juhlin et al. 2007). An important objective of CCS or sequestration as it is also known, is the safe and secure trapping of CO_2 for sufficient time to enable the surface carbon cycle to reduce atmospheric CO_2 levels (Haszeldine et al. 2005).

When CO_2 is injected into a reservoir its migration is controlled by gravity, viscous effects and capillary forces (Ide et al. 2007), as well as interactions with the host rock and formation fluids. Injected CO_2 can be trapped by a number of different mechanisms: structural trapping, residual trapping, dissolution and mineralisation (IPCC 2005; Kumar et al. 2005). These mechanisms vary in security and the rate at which they occur, with mineralisation being the slowest to develop, but the most secure, and structural trapping developing rapidly, but being the least secure. Leakage of CO_2 can lead to problems such as acidification of the ground water and plant death (Kumar et al. 2008). If CO_2 reaches the atmosphere then it is no longer sequestered and it adds to the excess CO_2 already there. Therefore the stored CO_2 must be monitored so any migration outside of the target formation can be identified and if possible stopped.

Monitoring approaches at existing sequestration sites have varied (Eiken et al. 2011; Lumley 2010), from satellite based methods (Onuma and Ohkawa 2009) to repeated field-scale seismic surveys (Davis et al. 2003; Eiken et al. 2000). These geophysical monitoring techniques all provide subsurface information, but their sensitivity to changes in the reservoir is variable. Time-lapse seismic surveys are able to track fluid movements in the subsurface (Watts et al. 1996) and have proved a great success at the Sleipner sequestration site (Chadwick et al. 2010).

Time-lapse seismic surveys have also successfully monitored CO_2 movement and plume extent at other sequestration sites (Arts et al. 2008; White 2009), but these results have highlighted some issues with the ability of this approach to fully monitor changes in the reservoir. CO_2 injection will alter more than just the fluid content. The pore pressure may increase, while the fluid properties, porosity, permeability and mineralogy of the reservoir rock may also change. The results of repeat seismic surveying include the changes to the reservoir fluid content along with all of these effects, therefore an understanding of the

timescales at which these processes act and their magnitude is required to fully understand the impact on the reservoir seismic properties.

This Chapter reviews the background literature regarding CO_2 sequestration. This review encompasses a variety of topics due to the diverse range of disciplines employed in this thesis. Section 2.2 covers general geological sequestration literature, such as potential sites and existing locations. Following this there is a discussion of topics more akin to reservoir engineering, i.e. physical processes which govern the interaction between the injected CO_2 and the reservoir (Section 2.3). After this the geophysical literature is reviewed in Section 2.4, discussing the different monitoring techniques which can be employed and then focussing specifically on time-lapse seismic surveys. Through this combined literature examination, five issues which may impact on the ability to monitor CO_2 injection using seismic monitoring are highlighted (Section 2.5).

2.2 Carbon Capture and Storage

CCS is a way of reducing anthropogenic CO_2 emissions, by capturing CO_2 at point source emitters, such as power stations, then purifying and transporting it via pipelines to storage sites. Storage mechanisms include geological storage, ocean storage (direct release into the ocean water column or onto the sea floor) and mineral carbonation (via the industrial fixation of CO_2 into inorganic carbonates) (IPCC 2005). There are already existing sites, where CO_2 is injected into geological formations (Kendall et al. 2003; Korbøl and Kaddour 1995), and the technology is well developed. Geological storage is regarded as the most viable option for immediate implementation and has the potential to cut global emissions by 20% by 2050 (Haszeldine 2009). It is the use of geological formations in the subsurface for sequestration of CO_2 that is considered in this thesis.

2.2.1 Sequestration Sites

There are a number of large-scale and pilot sequestration sites in various stages of planning around the world. Figure 2-1 shows the global distribution of these sites, including some cancelled projects, demonstrating the dominance of North America, Europe, Australia and East Asia in the technology. One global storage capacity estimate predicts potential storage of 2000Gt of CO_2 in depleted oil and gas reservoirs, with even greater storage potential being found in saline formations (IPCC 2005).



Figure 2-1 Map showing the global distribution of sequestration sites: yellow are in planning, red are cancelled or dormant, blue are pilot sites, green are operational and black are completed. (http://www.sccs.org.uk/storage/globalsitesmap.html. Accessed: December 23rd 2011.)

Four geological settings which can be used for sequestration are: unminable coalbeds, depleted oil reservoirs, depleted gas fields and saline aquifers. These formations are found in different global settings and provide varying levels of trapping security and storage capacity. To examine the different scale of projects being conducted and planned in these different geological environments Figure 2-2 was compiled using information from the 2011 Global CCS Institute report (Global CCS Institute 2011).

The largest projects are for Enhanced Oil Recovery (EOR) or within saline aquifers, whereas depleted oil and gas reservoirs have been chosen for smaller scale projects. The use of this technology in relation to EOR seems the most advanced with the more projects in operate and execute than the other field types, this may be due to the financial benefits from the additional oil recovery. Some of the projects which were cancelled or put "on hold" during 2011have been highlighted. The main reasons given for this were related to commercial issues, i.e. the weak economy and uncertainty regarding the national climate policy of the host country. In general the cancelled projects appear to be on the smaller end of the scale, possibly indicating a minimum size to make a project commercially viable.

The advantages and disadvantages of using these storage formations are outlined here, along with a more detailed discussion of some existing sites.

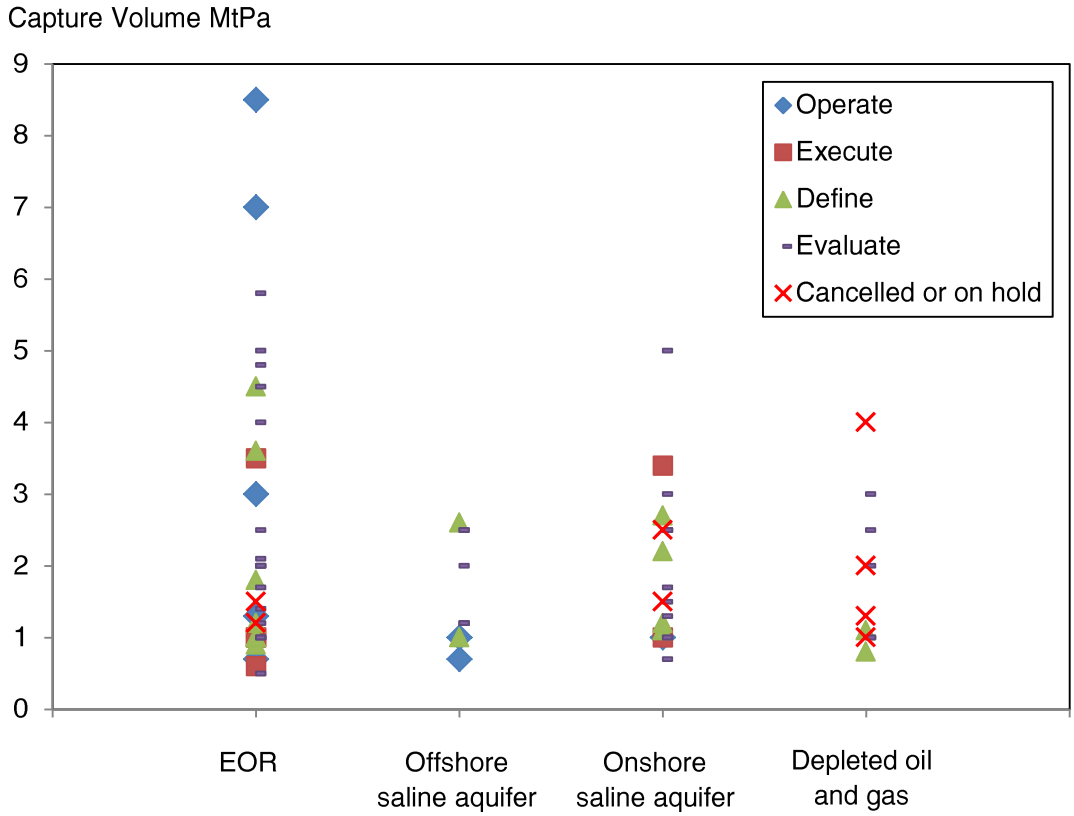


Figure 2-2 Figure compiled from Global CCS Institute (2011).The colours refer to the position of the project in the asset lifecycle model: identify refers to considering high level options, evaluate is when projects are short-listed, define is when selected projects are examined in more detail, execute refers to the design and build phase and then operate is when the CCS plant is actually operational.

2.2.1.1 Unminable Coal Beds

Storage of CO_2 in coal seams has been suggested as the injection of CO_2 will encourage methane (CH_4) production, a process called Enhanced Coal Bed Methane (ECBM). ECBM relies on the fact that coal absorbs gases, and has a greater affinity with CO_2 than methane, so CO_2 injection results in the release of methane. It is thought that ECBM can produce 90% of available CH_4 gas compared to 50% by reservoir-pressure depletion alone (Stevens et al. 1996).

Safe and successful injection of CO_2 into coal seams has occurred in the San Juan basin, USA as part of the Allison project, in the Alberta basin, Canada (Gunter et al. 2005) and at the REPCOL project in Poland (Van Bergen et al. 2002) .

2.2.1.2 Depleted Hydrocarbon Fields

Depleted oil and gas fields are prime candidates for CO_2 storage sites, due to:

- The presence of a proven seal, demonstrated by the accumulation of hydrocarbons.
- Previous extensive characterisation and studies conducted on the field, which would help predict CO_2 migration.
- Existing infrastructure, such as wells.
- The potential for enhanced recovery of oil and gas.
- The possibility that they may already be pressure depleted, therefore allowing for greater storage capacity.

Their history as hydrocarbon fields may also result in problems, such as leakage at abandoned wells and the presence of high permeability flow paths between wells, which may reduce the sweep and storage capacity. Also hydrocarbon fields are not distributed evenly worldwide, which obviously limits the global application of CCS.

2.2.1.2.1 EOR in Depleted Oil Fields: Weyburn

CO_2 injected into a depleted oil field can act as a tertiary recovery process, by displacing residual oil in the reservoir and by decreasing the oil viscosity making it easier for it to flow to the production wells. This is called Enhanced Oil Recovery (EOR). The arrangement for CO_2-EOR is shown in Figure 2-3. CO_2-EOR has been extensively used in the US, where oil production due to CO_2 enhancement accounted for 3.6% of the total oil production in 2004 (Bossie-Codréanu 2008). A current challenge for CO_2-EOR is to combine enhanced recovery with optimisation of CO_2 storage.

Weyburn is an enhanced oil recovery (EOR) project where a miscible CO_2 flood is injected into a thin (30 m) fractured carbonate reservoir, called Midale at 1450 m depth (Davis et al. 2003; White et al. 2004). The Midale reservoir is divided into two units: the upper more marly unit has a low permeability (10 mD) and a high porosity (26%), whereas the lower vuggy unit, has higher permeability (15 mD) and lower porosity (11%). The formation has an evaporite caprock. Field-scale CO_2 flooding was initiated in 2000, and by 2008 35 million tonnes of CO_2 had been stored, making this the largest land-based CO_2 storage project in the world (White 2009). To verify containment and trapping this project was monitored by a high-resolution, time-lapse, multicomponent seismic survey, which was used to determine the areal extent of the plume (White 2009). Passive seismic monitoring was also been deployed at the site.

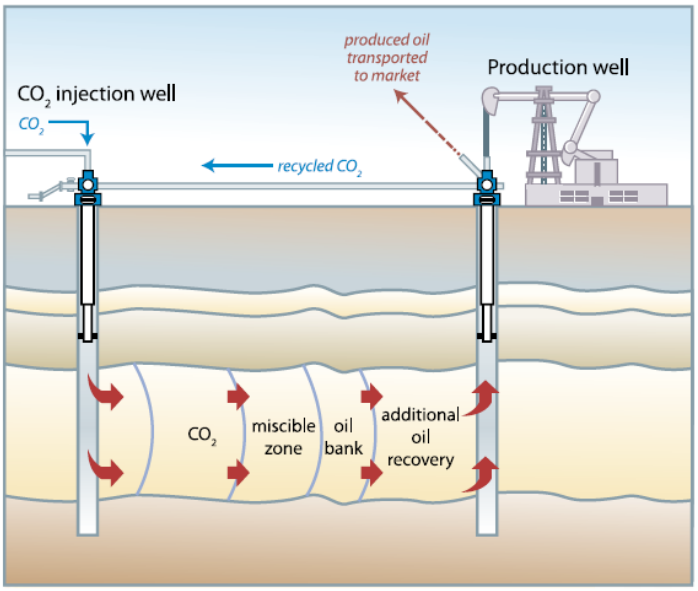


Figure 2-3 Injection of CO_2 for EOR with some retained CO_2. The CO_2 which is produced with the oil is separated and re-injected back into the formation (IPCC 2005).

2.2.1.2.2 Producing Gas Field: In Salah

CO_2 injection into a depleted gas field could be used for Enhanced Gas Recovery (EGR), pressure maintenance or storage. EGR is a tertiary recovery mechanism similar to EOR. A test CO_2-EGR site is been proposed in Austria at the Atzbach-Schwanenstadt gas field (Rossi et al. 2008).

CO_2 storage is currently taking place in the Krechba reservoir at In Salah in Algeria (Figure 2-4). Sequestration was required due to the high CO_2 content of the gas produced from the Krechba reservoir. As a result, CO_2 is separated from the hydrocarbon gas and re-injected into the reservoir for storage. Figure 2-4 shows the arrangement at the site, where there are three horizontal injectors down flank of the four producing wells. The formation is found between 1850 and 1950 m depth and is a 20 m thick fractured Carboniferous sandstone reservoir. The reservoir has porosities ranging from 13-20% and about 10 mD permeability (Mathieson et al. 2010). Injection began in 2004, and almost 4 million tonnes of CO_2 has since been sequestered (Eiken et al. 2011). A variety of monitoring strategies have been used to verify CO_2 containment (Mathieson et al. 2010)

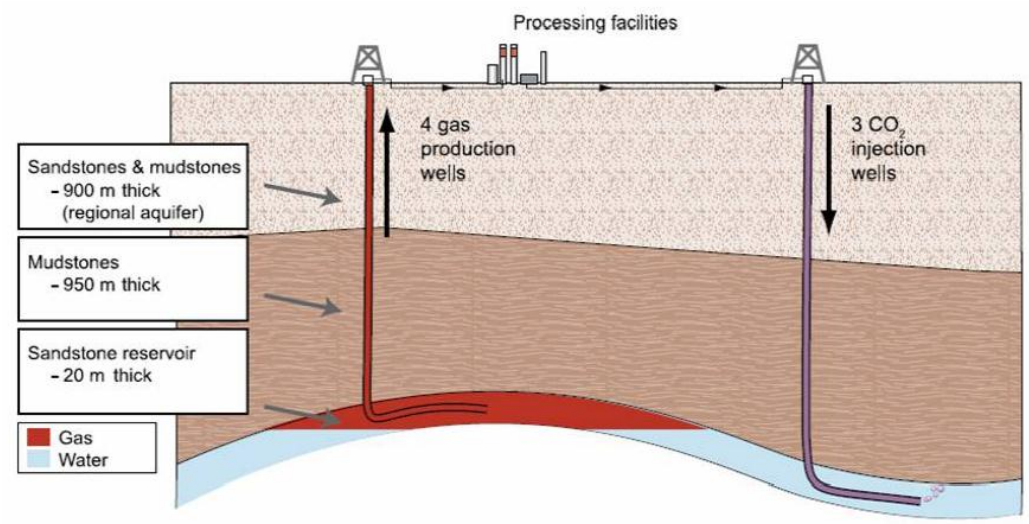


Figure 2-4 Schematic of the In Salah Gas Project, Algeria (IPCC 2005).

2.2.1.3 Saline Aquifers: Sleipner

Due to the vast size and common occurrence of saline aquifers, their storage capacity is up to 10 times greater than that in depleted oil and gas fields (IPCC 2005). However unlike depleted hydrocarbon fields, saline aquifers are often poorly characterised and extensive work is required to determine the integrity of the seal and predict CO_2 migration prior to their use for subsurface CO_2 storage. Post-injection monitoring is also required in saline aquifers, to verify their integrity for long-term storage of CO_2 (Lackner 2003).

The best known example of CO_2 sequestration in a saline aquifer occurs in the Sleipner field. CO_2 injection into the Utsira sand began in 1996 at a rate of 1Mt/year (Torp and Gale 2004). The Utsira sand is found at 1000 m depth, and has high porosity (30-40%) and permeability (1-3 D) (Chadwick et al. 2004b). Figure 2-5 shows the operations at the site. This project has been extensively monitored with a baseline 3D survey in 1994, and repeated seismic surveys in 1999, 2001, 2002, 2004, 2006 and 2008. Repeat gravity surveys have also been conducted. Through time-lapse seismic monitoring the CO_2 plume has been clearly imaged (Arts et al. 2008; Chadwick et al. 2004a) showing that the injected CO_2 has accumulated below inter-reservoir baffles and that there is no evidence of leakage from the site (Arts et al. 2004a). Other important saline pilot sites are at Ketzin, which west of Berlin (Juhlin et al. 2007) and Nagoaka, which is onshore Japan (Onishi et al. 2008).

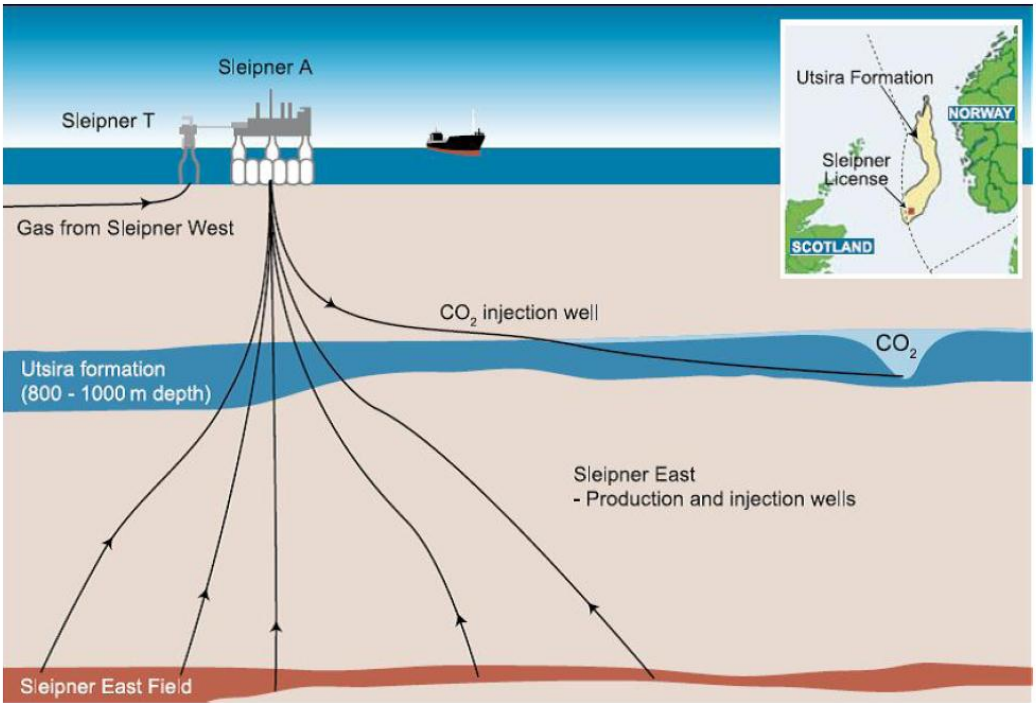


Figure 2-5 Simplified diagram of the Sleipner CO_2 storage project (IPCC 2005).

2.2.2 Potential for Sequestration in the UK

Currently there are no CO_2 sequestration sites operating in the UK, however significant potential has been recognised on the UK continental shelf (UKCS) (Holloway 2009). Figure 2-6 shows sedimentary basins and hydrocarbon fields both onshore and offshore in the UK with potential for sequestration. The storage capacity in depleted gas fields is up to 6.1 Gt of CO_2, and in depleted oil fields it is between 1.2 and 3.5 Gt of CO_2 (Holloway 2009). There is currently no published estimate for saline aquifers, but subsea saline aquifers in the UK are expected to offer far greater storage potential than depleted hydrocarbon fields (Gough 2008).

The majority of the UK storage potential is offshore in the North Sea, which has the advantage of being geologically well characterised and understood. It also has existing infrastructure and is close to fossil-fuel burning power stations onshore UK, which would decrease transportation costs. Leakage potential for subsea sites is lower than onshore as the sea would act as an additional barrier to CO_2 returning to the atmosphere. Wytch Farm in Dorset, is the only onshore hydrocarbon field currently considered for storage and has a maximum storage capacity of 5 million tonnes (Holloway 2009). Formations in the UK with sufficiently high porosity and permeability to sustain large-scale CO_2 injection and storage include the Greensand, Portland sandstone, Sherwood Sandstone and various Permian sandstones (Holloway 2009).

An important issue when planning CO_2 sequestration in the subsurface is the degree of fault-related compartmentalisation in the formation. Less compartmentalisation allows for greater pressure communication and requires fewer injection wells. Thus in the Southern North Sea storage would be preferable in the Triassic sandstones, rather than the Permian Rotliegand formation, which is highly compartmentalised (Holloway 2009). Other studies have suggested using other formations, e.g. Vandeweijer et al (2009) examined the Bunter sandstone in the Southern North Sea.

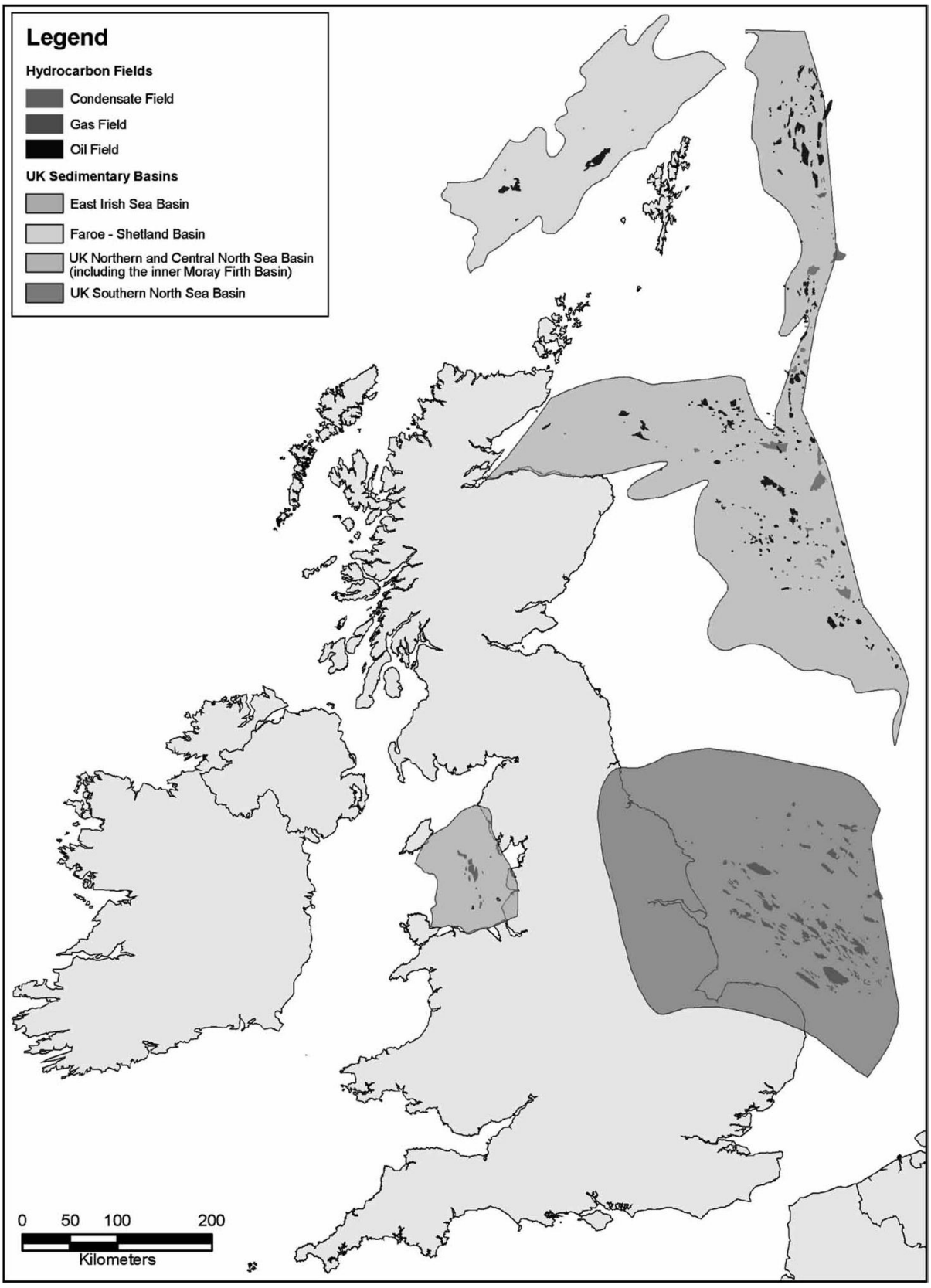


Figure 2-6 Map showing the location of offshore hydrocarbon fields and major oil and gas bearing sedimentary basins in the UKCS (Holloway 2009).

2.3 CO_2 Storage

Interpreting the time-lapse seismic response requires an understanding of how dynamic reservoir properties such as fluid content and pressure are affected by CO_2 injection. Behaviour of injected CO_2 is governed by the fluid properties and physics of fluid flow in the subsurface. At the pore scale the behaviour is controlled by the relative permeability and capillary pressure, which are unique to the fluids and rock in the reservoir; whereas on the field scale it is controlled by gravity and viscous effects. Interactions between these effects control CO_2 migration and trapping.

2.3.1 CO_2 Properties

Supercritical CO_2 is preferred to gaseous CO_2 for storage, due to its higher density which results in greater storage efficiency. The flow of CO_2 is influenced by its viscosity. It is therefore important to be able to describe how both viscosity and density change with temperature and pressure. Examining the interaction between two distinct fluid phases, in this case brine and CO_2 requires understanding of their mobility ratio, solubility and wettability.

CO_2 Properties: Density and Viscosity

Reservoir temperature and pressure control the CO_2 phase. This relationship is well constrained by experimental work (Han et al. 2010; Wang and Nur 1989) and can be predicted using an equation of state (Peng and Robinson 1976; Span and Wagner 1996). The CO_2 phase diagram, (Figure 2-7) shows the change from gaseous to supercritical CO_2 at 7.38 MPa and 31.1°C (Han et al. 2010), which is typically at about 800 m depth. This transition point depends on both the thermal and pressure gradients, so both these properties must be known to predict the CO_2 phase at a given depth.

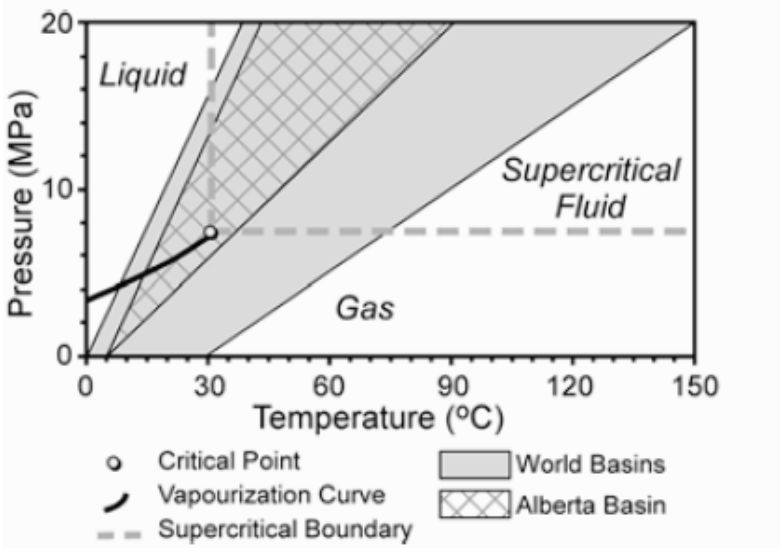


Figure 2-7 The range of temperatures and pressures found in the Alberta Basin and worldwide basins superimposed on the phase behaviour of CO_2 (Han et al. 2010).

At the critical point, the density of CO_2 increases significantly, from about 100-400 kg/m^3 for gaseous CO_2 to about 700-850 kg/m^3 for supercritical CO_2 (Figure 2-8). The density contrast between brine and CO_2 controls gravitational segregation in the reservoir, and will, along with its elastic properties, dictate the magnitude of the seismic response to injection. CO_2 viscosity describes the resistance to flow and is always lower than brine viscosity. The viscosity increases with pressure, but decreases with temperature, and supercritical CO_2 is significantly more viscous than gaseous CO_2 (Figure 2-9).

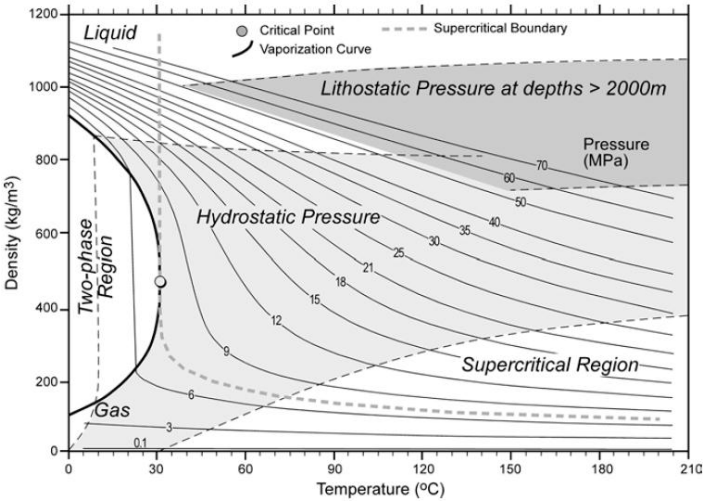


Figure 2-8 Variation in CO_2 density as a function of temperature and pressure, showing the range of densities which would be encountered in sedimentary basins around the world (Bachu 2003).

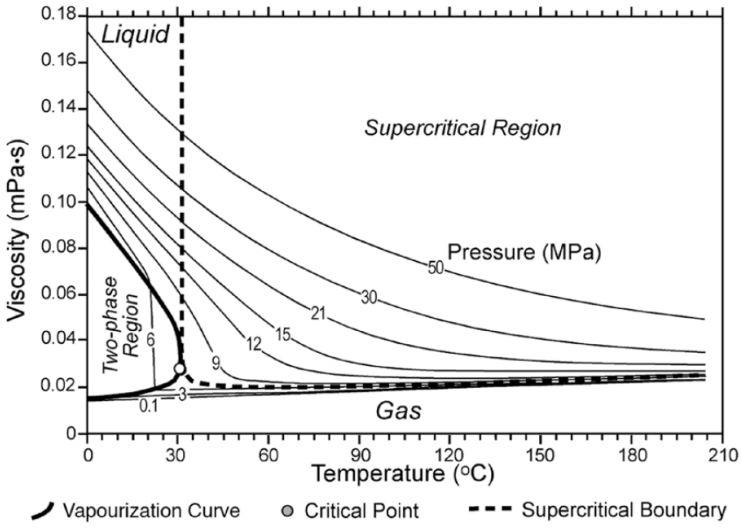


Figure 2-9 Variation in CO_2 viscosity as a function of temperature and pressure (Bachu 2003) .

Mobility

The mobility of a fluid is a measure of its ability to move through interconnected pore space, and is defined by the ratio of the effective phase permeability to the effective phase viscosity. The CO_2 mobility is typically an order of magnitude greater than that of brine (Juanes et al. 2009) because of CO_2's low viscosity. The ratio of the mobility of brine to CO_2 is a key parameter when assessing storage in saline aquifers (Juanes et al. 2009).

CO_2 Solubility

Quantifying the solubility of CO_2 in the formation brine is important, as dissolution is a permanent way to trap some CO_2. The solubility of supercritical CO_2 has been established in laboratory experiments (Carroll et al. 1991; Duan and Sun 2003; Spycher et al. 2003).

Wettability

In a porous medium containing two or more immiscible fluids; the wettability is defined as the tendency of one of the fluids to adhere to the surface of the solid. A water-wet rock will have a higher affinity to water than the other phase, such as CO_2. This wettability can be range from strongly water-wet to strongly CO_2-wet depending on the brine/CO_2 interaction with the rock surface. Wettability is measured in the laboratory through the contact angle. There is limited laboratory work regarding the wettability of the CO_2-brine systems in sandstones, however some results have indicated that supercritical CO_2 is the non-wetting phase in sandstones (Pentland et al. 2011). Figure 2-10 demonstrates how the non-wetting phase may be trapped by the wetting phase, with the wetting phase filling the pore throats and the non-wetting phase being confined to the centre of the pore.

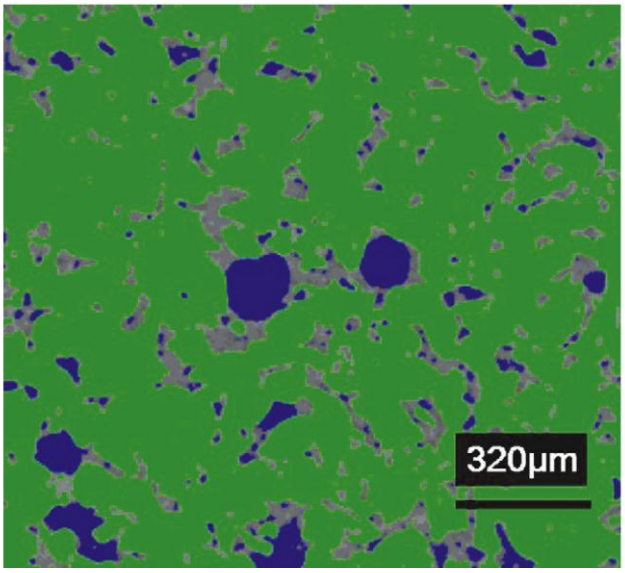


Figure 2-10 Micro CT scan of a sandstone, the non-wetting phase is in blue, the rock is green and the wetting phase is grey (Dong 2007) .

2.3.2 Capillary Pressure and Relative Permeability

At the pore scale, capillary effects govern the motion of a fluid phase as it moves into a porous medium previously occupied by another fluid. Capillary effects are described by two properties: relative permeability and capillary pressure.

Capillary Pressure

The capillary pressure determines the threshold pressure needed to enter the rock pores and it varies with the saturation state of the rock. It is defined as the pressure difference across the curved interface formed by two immiscible fluids in a small capillary tube:

$$P_c = P_{nw} - P_w \qquad 2\text{-}1$$

where P_c is capillary pressure, P_{nw} is the pressure in the non-wetting phase and P_w is the pressure in the wetting phase. The capillary pressure depends on: the pore-size distribution, permeability and porosity. Subsequently different rock samples yield a different relationship between fluid content and capillary pressure, which is described by the capillary pressure curve. As these curves are specific to both the fluid phases and the rock type, they are usually measured in laboratory experiments for each rock type (Bennion and Bachu 2008; Bennion and Bachu 2006; Pentland et al. 2011; Plug and Bruining 2007).

The example of the CO_2-brine system is used to explain how capillary pressure effects how injected CO_2 moves in the pore space:

1. When CO_2 is injected into a rock which is fully saturated with brine, it cannot enter the pore space unless it is pressurised above the capillary entry pressure for the largest pore throats. After invasion of the large pore throats, continually increasing the pressure will displace more brine, allowing CO_2 to enter successively small pore throats, until the **connate water saturation** is reached. As this is a reduction in the wetting phase it is described as a **drainage** process.

2. If the imposed pressure gradient which allowed CO_2 to fill the pore space dissipates when injection ceases then brine can re-enter the pore space. This occurs until the **residual gas saturation** is reached. This is an increase in the wetting phase and is described as an **imbibition** process.

Relative permeability is used to describe multiphase flow and the general definition is given as:

$$\kappa_r = \frac{\kappa_{eff}}{\kappa_{abs}} \qquad 2\text{-}2$$

where κ_r is relative permeability (between 0 and 1), κ_{eff} is effective permeability and κ_{abs} is absolute permeability. Relative permeability describes the decrease in permeability resulting from the presence of a second fluid phase in some of the pore volume.

Wettability conditions of the core can significantly impact on relative permeability, therefore it is important that it is measured under the same conditions as in the reservoir. In addition experiments to record relative permeability are designed to best represent the saturation path being modelled, i.e. drainage or imbibition. Different curves would be generated during drainage and imbibition experiments. This dependence on the history of saturation changes is called **hysteresis**.

Relative permeability hysteresis has been shown to significantly impact on both the movement and trapping of CO_2 during sequestration (Juanes et al., 2006) and there is some evidence that capillary pressure hysteresis may be important when simulating CO_2 storage (Doughty, 2007). These capillary pressure and relative permeability curves, are important controls on flow and trapping, and therefore are required as inputs into the fluid-flow model.

How the connate water and residual gas saturation can be derived from relative permeability curves is demonstrated in Figure 2-11. When relative permeability is zero then the fluid phase cannot flow and it is "trapped". For primary drainage, i.e. injection into a brine filled reservoir the residual gas saturation is 0, whereas for imbibition, i.e. brine re-invading the pore space the residual gas saturation is about 30%, and the connate water saturation is approximately 40%.

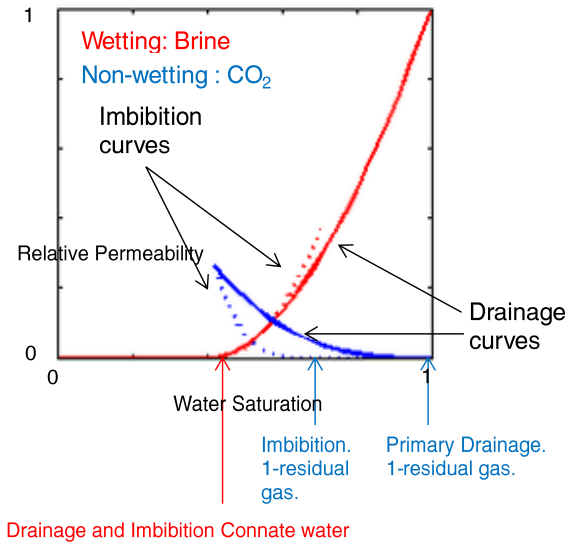


Figure 2-11Generic relative permeability curves, annotated to demonstrate where the residual gas and connate water saturation can be read off.

2.3.3 Physical Processes and Trapping Mechanisms

The migration and trapping of injected CO_2 within a reservoir is controlled by the interplay between gravitational, viscous and capillary forces (Ide et al. 2007). These processes are also influenced by geochemical reactions with the reservoir rock and fluids, and the permeability.

Injected CO_2 will migrate both laterally and upwards, due to viscous and gravitational forces. Once injection ceases and the pressure gradient which was driving lateral migration relaxes, gravity will dominate. In a saline formation CO_2 has a lower density than brine, so it will migrate to the top of the reservoir via gravitational segregation (Ennis-King and Lincoln 2002). It is then prevented from escaping an impermeable seal (Bachu et al. 1994) and is described as **structurally trapped**. Although it is effectively contained, it is still classified as "mobile" and could escape to the surface. This pooling of CO_2 under the caprock increases pore pressures at the interface, potentially resulting in overpressure developing and loss of integrity in the caprock (Rutqvist and Tsang 2002). As the caprock has non-zero permeability leakage may also occur if the caprock capillary entry pressure is exceeded. Coupled fluid flow and geomechanical analysis can be conducted to predict maximum safe injection pressures to prevent failure (Rutqvist et al. 2007).

Once injection has ceased, the buoyant CO_2 will continue to migrate upwards, with brine displacing CO_2 at the trailing edge of the plume in an imbibition-like process, until the residual gas saturation is reached. The remaining CO_2 exists as disconnected blobs and ganglia and can be considered immobile (Hunt et al. 1988). This disconnected CO_2 is generated via "snap-off" (Roof 1970), by which the pores are filled with CO_2, but the pore throats are filled with brine. This CO_2 is described as **residually trapped**, and will be distributed over a large area, which can enhance dissolution and mineral precipitation by increasing the contact between the CO_2 and the reservoir rock and brine. As it is immobilised before the reaching the top seal it may prevent the potentially dangerous build-up of pressure below the caprock (Ennis-King and Paterson 2005; Juanes et al. 2006; Kumar et al. 2005; Obi and Blunt 2006). Overall residual trapping enhances the trapping security in the reservoir (Obi and Blunt 2006; Qi et al. 2008).

Due to the solubility of CO_2 in brine, a portion of injected CO_2 in contact with brine will dissolve in the formation water as an equilibrium process; this is referred to as **solubility trapping**. The amount of CO_2 that goes into solution depends on the degree of contact between the two fluid phases, as well as the temperature, pressure and salinity in the reservoir. Dissolving CO_2 in brine produces carbonic acid, which may react with the host rock minerals and increase the porosity by up to 1%. (Johnson et al. 2004). Also brine containing dissolved CO_2 has a density approximately 1% greater than that of pure brine (Ennis-King and Paterson 2005; Lindeberg and Wessel-Berg 1997). When this CO_2-saturated water layer is sufficiently thick, then it becomes unstable due to its higher density than the underlying brine and plumes of CO_2-saturated water will migrate downwards. This is called convective mixing and can accelerate mixing in the

reservoir. Figure 2-12 shows convective mixing in a reservoir 200 years after injection ceased, with the higher density CO_2 saturated brine moving down through the reservoir. (Nghiem et al. 2004).

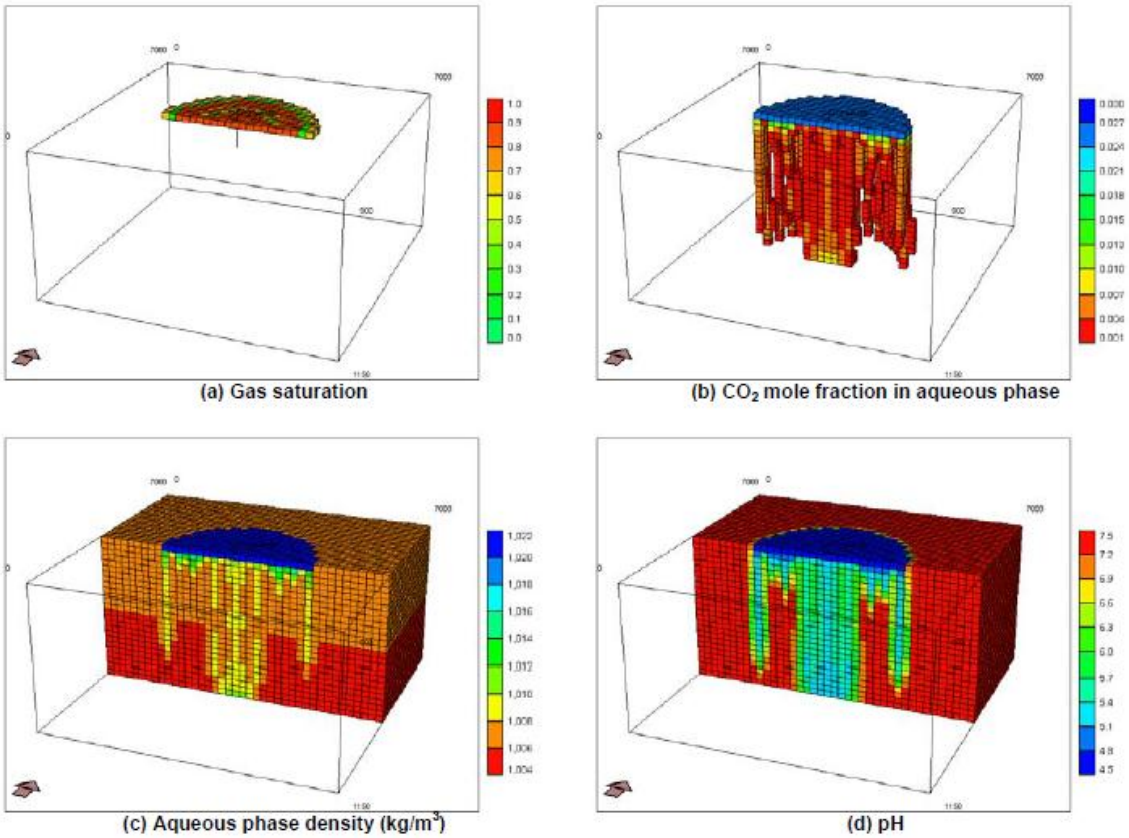


Figure 2-12 Profiles taken from Ngheim et al, (2004), showing the impact of CO_2 dissolution on brine properties 200 years after injection of CO_2. This shows how slow convective mixing is to develop.

Over more geologically significant periods of time **mineral trapping** may occur (Bachu et al. 1994). Mineral trapping is the most secure and permanent trapping mechanism, whereby chemical reactions result in CO_2 being stored as a solid. Mineral trapping could be a significant trapping mechanism (Johnson et al. 2004; Kumar et al. 2008). While it is assumed that dry CO_2 is chemically inert, carbonic acid is not, and it may react with the host rock minerals. Reaction with certain, non-carbonate, calcium-, iron-, or magnesium-rich minerals may result in trapping of CO_2 as a solid carbonate precipitate. The amount of CO_2 mineralisation depends on the mineralogy of the reservoir rock. Quartz, the major constituent of sandstone is chemically inert to CO_2, therefore any reaction within a sandstone aquifer would have to come from other minerals. The best minerals for trapping are olivine or minerals from the pyroxene, hornblende and amphibole groups (Pruess et al. 2003). CO_2 stored as stable carbonate precipitates will reduce the porosity and permeability.

Migration also depends on the properties of the reservoir itself, in particular the permeability. Important features may be baffles or preferential flow paths, either natural, (channels) or unnatural (resulting

from previous extraction of hydrocarbons). Permeability maps of the reservoir are used to take this behaviour into account during fluid-flow simulation.

The time scale for these trapping mechanisms are very different (Figure 2-13),with mineral trapping taking at least an order of magnitude greater time to develop than solubility trapping, which is yet another order of magnitude slower than residual and structural trapping. Studies have been performed to determine the quantity of CO_2 which could be trapped in the different phases (Kumar et al. 2005; Pruess et al. 2003). Under favourable conditions it is thought that the amount of CO_2 sequestered in a saline aquifer via mineralisation may be comparable to that dissolved in the brine (Pruess et al. 2003). Another study indicated that the amount of CO_2 stored as residual CO_2 could be greater than that stored by dissolution and mineralisation (Kumar et al. 2005).

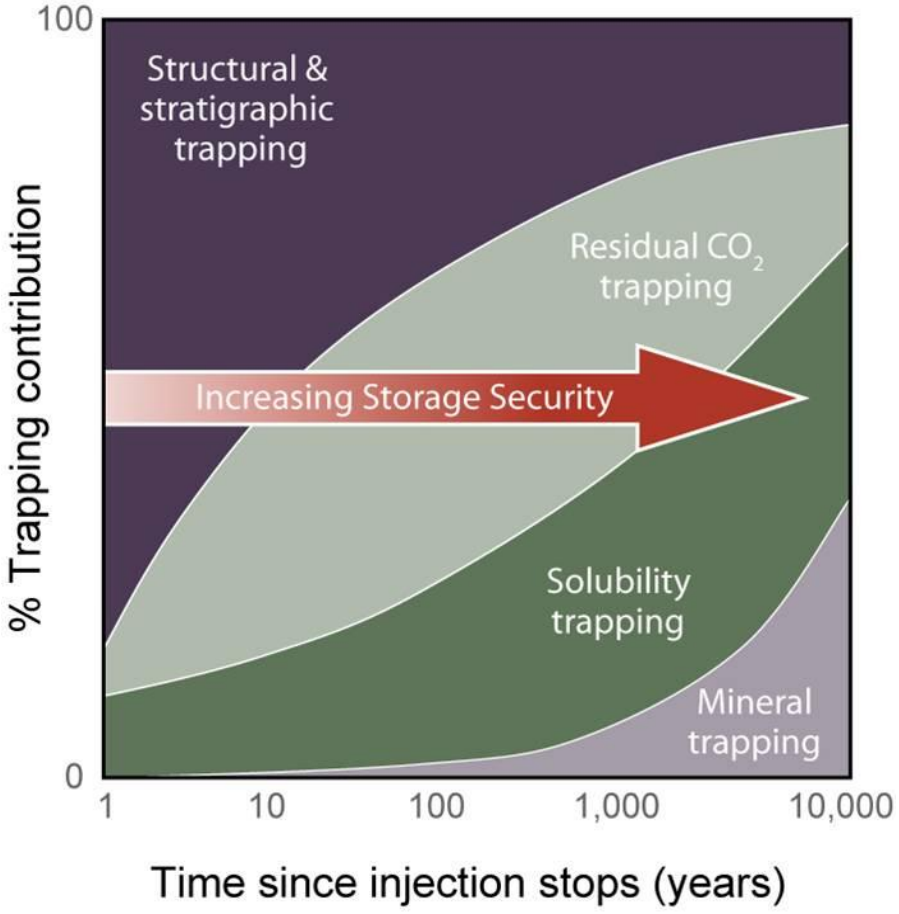


Figure 2-13 Different trapping mechanisms and the way in which their occurrence varies with time following injection (IPCC 2005).

Immediately following injection, structural and residual trapping will be the most important trapping mechanisms. Figure 2-14 shows where these trapping types should develop in the reservoir. Examination of the relative permeability curves (Figure 2-11) highlighted that these trapping mechanisms should be characterised by a specific CO_2 saturation. Subsequently these different regions are likely to have certain saturations.

1. Structural trapping.
    I. CO_2 invades brine filled reservoir. This is a drainage process and will continue until the connate water saturation is reached.
    II. Typical CO_2 saturation in structurally trapped plume should be: 1- connate water saturation.
2. Residual trapping.
    I. Brine re-invades the pore space previously filled with structurally trapped CO_2, it carries on until the residual gas saturation is reached.
    II. Typical CO_2 saturation in residually trapped plume should be: residual gas saturation.

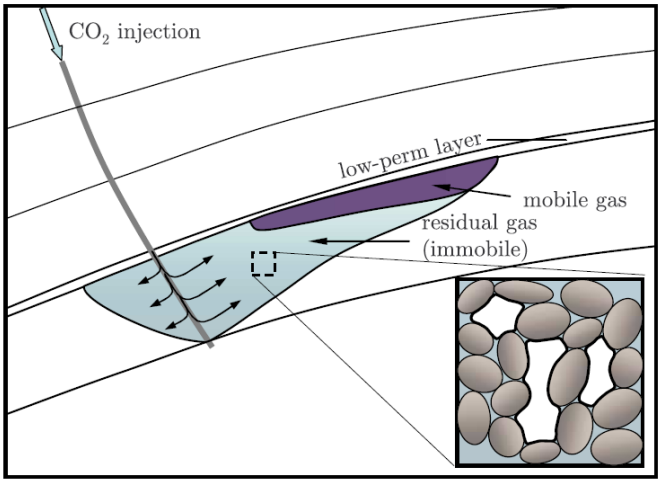


Figure 2-14 Schematic demonstrating the spatial distribution of injected CO_2 formed by the interaction of gravitational, viscous and capillary forces with the rock fabric. Two plume regions are formed:,a region of mobile CO_2 and a region of "immobile" residually-trapped CO_2 that is left behind because of snap-off, as the plume migrates upwards (Juanes et al. 2006).

2.3.4 Pore Pressure

Injection of CO_2 into a geological formation will alter the pore pressure in the subsurface. The magnitude of these changes depends on the type of site, the amount of CO_2 injected, the reservoir size and the level of pressure communication with surrounding formations. A substantial pore-pressure increase could result in failure of both the reservoir and caprock, and leakage to the surface. To mitigate any failure, the pressure must be kept below 90% of the fracture pressure (Bruce and Bowers 2002), at which fractures may reactivate. Also the pressure should be kept below the caprock capillary entry pressure, above which CO_2 can flow into the caprock.

The type of sequestration site is an important control on the magnitude of any changes in pore pressure resulting from injection. Old hydrocarbon fields may already be pressure depleted and old gas fields are likely to have even greater pressure depletion than oil fields, due to their higher primary recover rates. CO_2 injected into a depleted field is expected to fill the pore volume previously occupied by hydrocarbons. On the other hand, injecting CO_2 into a normally pressurised saline aquifer may induce problematic rises in pore pressure.

A reason for injecting into saline aquifers is their vast size, which allows pressure increases to be spread throughout the reservoir, potentially 10's of km away from the injection site (Vandeweijer et al. 2009). However any compartmentalisation will decrease the pressure communication, and result in pressure build-up. One rather controversial aspect of examining pressure increases is whether the aquifer is considered to be "open" or "closed". Storage capacity estimates based on a closed system are significantly below other published estimates (Ehlig-Economides and Economides 2010). However there are issues with the assumption of a closed system, as even shale has some permeability, and other pressure management strategies should be considered (Cavanagh et al. 2010).

Bergamo et al (2010) proposed a method to minimise pressure increases and optimise aquifer storage capacity by simultaneous CO_2 injection and brine production. This option is being considered at the Gorgon site, offshore Australia, as a way of minimising pressure on key faults (Flett et al. 2007). One limitation of this method is the requirement for a suitable repository for the produced brine nearby. If a pressure increase is detected, injection may have to stop. This occurred at Schnovit (a storage site in the Norwegian North Sea), where injection was stopped for four months (Eiken et al. 2011).

As there are potential dangers, such as fault reactivation and caprock leakage associated with pore-pressure increase, a full geomechanical study is a necessity for potential sequestration sites. These considerations are very site specific and could indicate the need for brine production in certain regions, or modification of the proposed injection scheme (Morris et al. 2011).

2.4 Monitoring CCS

Knowledge of the behaviour of CO_2 injected in the subsurface is necessary to verify containment and identify leaks. Prior to injection reservoir simulation studies will be conducted to predict CO_2 behaviour, this behaviour can then be confirmed by monitoring. Ideally monitoring will be able to determine:

- CO_2 location, i.e. plume extent.
- CO_2 saturation, to allow for calculation of the amount of CO_2 trapped.
- The trapping phase of the CO_2, to determine how securely it is trapped.
- Information on any pore-pressure changes in the reservoir.

Using this information a full assessment of the trapping security at a site can be conducted.

A range of monitoring techniques has been suggested for use at sequestration sites. Determining the appropriate monitoring technique depends on cost, monitoring requirements and site location. The cost varies with the environment; for example seismic surveys are more expensive onshore than offshore. Therefore at each site, a cost benefit analysis is required to determine which technologies are most appropriate. Figure 2-15 shows the analysis performed at In Salah, where onshore time-lapse seismic surveys are expensive, but have still been conducted due to their potentially high benefit. One of the greatest benefits of seismic surveys is their spatial coverage, as they can be used to monitor the entire field at a relatively fine resolution in comparison to other field-scale approaches.

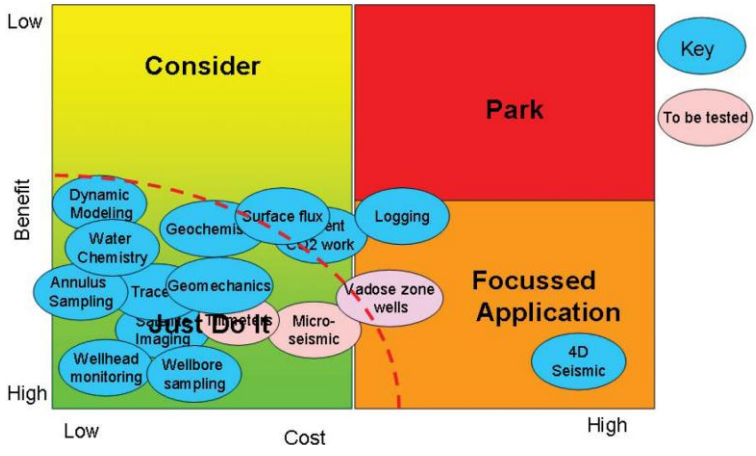


Figure 2-15 The monitoring technologies under consideration at the In Salah sequestration site (Mathieson et al. 2010).

Field-scale time-lapse seismic surveys are used in the hydrocarbon industry to monitor fluid movement in the subsurface, and they have been used at the majority of large sequestration sites (Arts et al. 2004b; Davis et al. 2003; Mathieson et al. 2010). Other geophysical techniques have also been applied (Nooner et al. 2007; Onuma and Ohkawa 2009; Saito et al. 2006). These alternative technologies are briefly described here, as they could be used in conjunction with time-lapse surveys. Through time, if CCS is proven safe, there may be a move away from time-lapse seismic to these cheaper alternative technologies.

2.4.1 Alternative Monitoring Techniques

Monitoring techniques applied at sequestration sites are usually based on comparing two data sets to determine differences over time. These changes may indicate alterations in the subsurface, such as CO_2 invasion or pressure build-up. The term "time-lapse" refers to repeat comparison surveys.

Passive Seismic Monitoring

Passive seismic monitoring detects small acoustic emissions or small earthquakes (microseismicity) associated with stress changes in and around the reservoir. Microseismic events related to movements on pre-existing faults or fractures, or the creation of new fractures, capture deformation resulting from stresses and strains induced by changing pressure conditions. The passive seismic technique has been used at Weyburn, as it is a low cost method to provide information about pressure changes in the reservoir (Verdon et al. 2010). This monitoring approach only provides information about geomechanical deformation and not the fluid content or phase.

Gravity Surveying

Time-lapse gravitational methods are sensitive to density changes in the subsurface, such as those that occur when brine is replaced by less dense CO_2. Repeat gravity surveys have been conducted at Sleipner in 2002, 2005 and 2009 (Eiken et al. 2011; Nooner et al. 2007). The surveys detected a signal which had a similar lateral extent to the plume mapped by seismic surveys. Additionally gravity measurements were used to help estimate the CO_2 density and constrain the reservoir temperature (Nooner et al. 2007). Modelling studies indicate that gravitational surveys can only provide the general location of density changes and not a detailed picture of the subsurface fluid movements, which can be obtained by time-lapse seismic monitoring (Gasperikova and Hoversten 2006). Therefore gravity surveys cost less, but provide lower resolution than repeat seismic surveys.

Well-based Monitoring

Well-based monitoring can provide high-resolution imagery of a small region either surrounding one well or between a few. It requires one or more wells in the reservoir interval, and cross-well studies requires wells relatively close to each other. Cross-well monitoring has been used at Ketzin, where the well spacing is 112m (Girard et al. 2011), but at In Salah the well spacing was deemed too large.

Cross-well seismic tomography produces a high-resolution velocity image, which can be used to infer the dynamic properties in the inter-well region. This has been applied at Nagoaka in Japan, where CO_2 is injected into an onshore aquifer (Onishi et al. 2008; Saito et al. 2006; Sato et al. 2011). Experimental work predicted a P-wave velocity decrease of about 10% after CO_2 injection, so the velocity decrease in the tomography results (Figure 2-16) was used to represent CO_2 movement. Time-lapse cross-well electrical or electromagnetic imaging have also been used to monitor fluid movement in the inter-well region, as electrical resistivity is sensitive to water saturation (Gasperikova and Hoversten 2006). At Ketzin, CO_2 injection has modified the current paths and increased electrical resistivity by 200% (Girard et al. 2011), indicating plume migration could be monitored by this method. Single well sonic logs can be used to better constrain the tomography results and indicate CO_2 breakthrough to the region around the well (Azuma et al. 2011). At Nagoaka time-lapse neutron porosity logs have been used to indicate CO_2 saturation, and when used in conjunction with the sonic logs, were used to infer the relationship between seismic velocities and CO_2 saturation (Azuma et al. 2011; Caspari et al. 2011).

These well-based approaches provide detailed information about CO_2 saturation and migration near the well; however they do not provide the field-scale information required at sequestration sites.

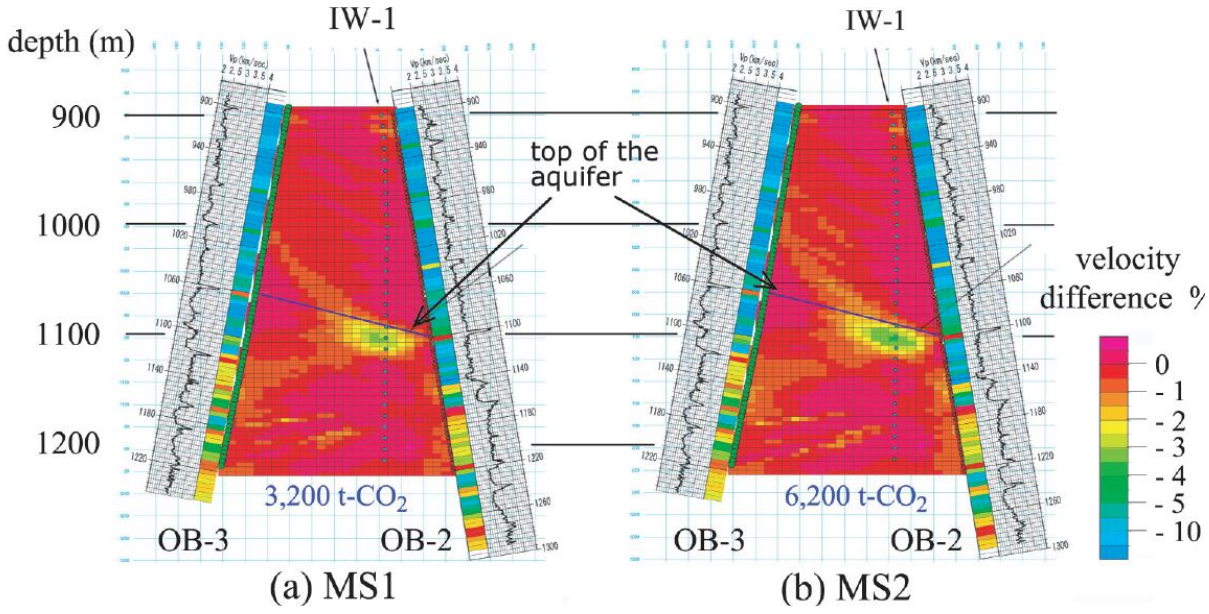


Figure 2-16 Velocity difference tomograms from the Nagoaka site: a) velocity difference between the baseline survey and a survey following injection of 3200 t of CO_2, b) Velocity difference between the baseline surveys and a survey following injection of 6200 t of CO_2 (Saito et al. 2006).

Satellite Monitoring

Differential Interferometric Synthetic Aperture Radar (DInSAR) monitors surface deformation over time, by repeatedly recording of the distance between the ground and the satellite. At In Salah in Algeria DInSAR has been used and a vertical displacement rate of approximately 7 mm/yr around the injection well was recorded (Figure 2-17**)** (Onuma and Ohkawa 2009). Preisig and Prevost (2011) used a fully-coupled two-phase thermo-poromechanical model to examine the uplift, and suggested that the ground deformation is a result of pressure increase near the well.. DInSAR is potentially a good low-cost tool for monitoring at onshore sites, but it fails to capture the detailed CO_2 migration in the reservoir.

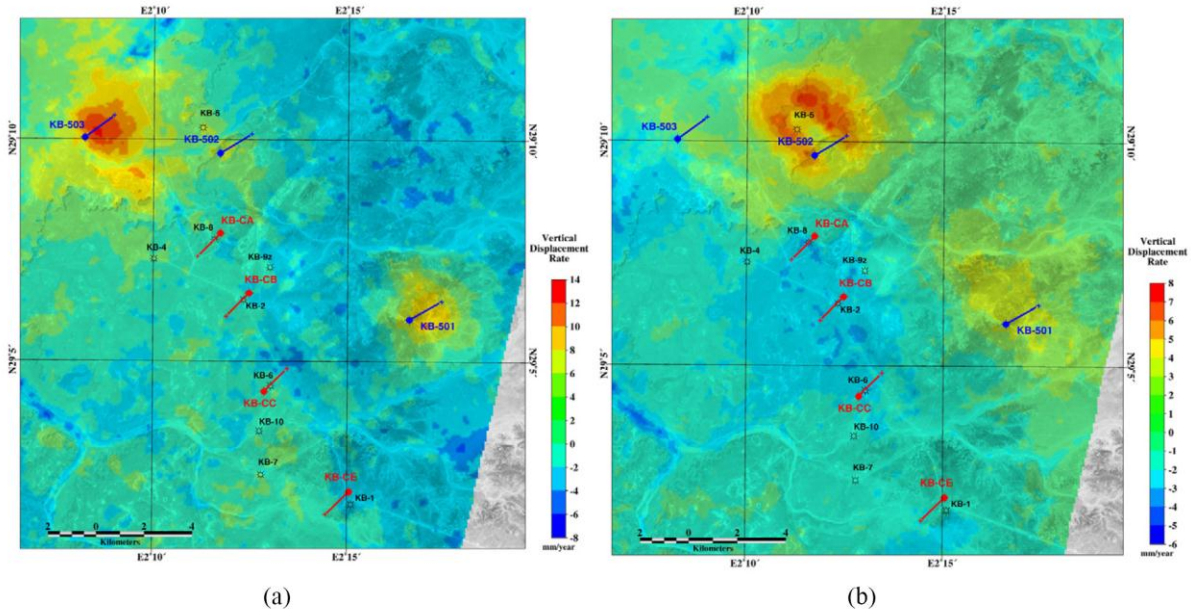


Figure 2-17 Vertical displacement detected by DInSAR at the In Salah sequestration site a) From 31/7/2004 to 24/9/2005, b) From 24/9/2005 to 31/5/2008 (Onuma and Ohkawa 2009).

2.4.2 Time-lapse Seismic Monitoring

Repeat seismic surveys have been used to monitor producing hydrocarbon fields (Watts et al. 1996) and to determine changes in pressure and saturation for almost two decades (Landro et al. 1999).Therefore they are naturally seen as an established technology which can be used to verify the integrity of CO_2 storage sites, and they have been used at the majority of existing projects (Arts et al. 2004b; Chadwick et al. 2004b; Davis et al. 2003; Juhlin et al. 2007; Mathieson et al. 2010)

This Section provides an overview of the time-lapse seismic method. First, the elastic moduli which control the propagation of the seismic wave are discussed (Section 2.4.2.1). How these elastic moduli are predicted and can be recorded using well data is explained in Section 2.4.2.2. This discussion is with particular reference to the relationship between these elastic moduli and pore-pressure changes (2.4.2.2.1) and alterations in the fluid content (Section 2.4.2.2.2). Some seismic properties commonly recorded during seismic surveys are introduced in Section 2.4.2.3, followed by a review of repeat seismic survey results from existing sequestration sites (Section 2.4.2.4).

2.4.2.1 Elastic Moduli

Seismic waves travel through the Earth as elastic waves that propagate through solid bodies by transferring forces as an elastic deformation of a body. This elastic deformation can be described in terms of stress and strain. If the strains are small, such as for a seismic wave (Sheriff and Geldhart 1995), then they can be related by Hooke's law, and the strain is directly proportional to the stress producing it. The elastic stiffness tensor relates the stress to the strain. In an isotropic linear elastic medium, only two components of the stiffness tensor are needed, and the relationship between stress (σ) and strain (ε) can be described as:

$$\sigma_{ij} = \lambda\delta_{ij}\varepsilon_{\alpha\alpha} + 2\mu\varepsilon_{ij}, i = j \qquad 2\text{-}3$$

where λ and μ are Lames coefficients, $\varepsilon_{\alpha\alpha}$ is the volumetric strain, $\sigma_{\alpha\alpha}$ is the mean stress times 3, i and j indicate the orientation of the stress and the strain. If $i \neq j$ then the properties are described as "shear" and $\delta_{ij}=0$, whereas if $i=j$ then the properties are "normal" and $\delta_{ij}=1$. The ratio of these stresses and strains define the elastic constants or moduli.

Young's modulus (*E*) is the constant of proportionality which relates the longitudinal strain to the corresponding stress component:

$$E = \frac{\sigma_{ij}}{\varepsilon_{ij}}, i = j \qquad 2\text{-}4$$

The **shear modulus (μ)** is constant of proportionality which relates the shear stress to shear strain:

$$\mu = \frac{\sigma_{ij}}{2\varepsilon_{ij}}, i \neq j \qquad 2\text{-}5$$

The **bulk modulus, or incompressibility** (***K***) is the dilation (Δ) experienced by a body under hydrostatic pressure (*P*), i.e. the shear components are zero:

$$K = -\frac{P}{\Delta} = \frac{\sigma_{\alpha\alpha}}{3\varepsilon_{\alpha\alpha}} \qquad 2\text{-}6$$

Poisson's ratio (*ν*), is defined as minus the ratio of the lateral strain to axial strain, assuming a uniaxial stress state:

$$\nu = -\frac{\varepsilon_{xx}}{\varepsilon_{zz}}, \sigma_{xx} = \sigma_{yy} = \sigma_{xy} = \sigma_{xz} = \sigma_{yz} = 0 \qquad 2\text{-}7$$

2.4.2.2 Understanding and Recording the Elastic Moduli

The elastic moduli given in Equations 2-4 through 2-7 vary with the rock composition, frame strength, porosity, pore pressure and fluid content. The two isotropic seismic velocities can be defined in terms of the bulk modulus and the shear modulus. These moduli depend on: mineralogy, frame properties and fluid content. Specific moduli are required for these three properties and the equations which can be used to predict the values are discussed in Chapter 3.3. Here is a brief description of the each elastic moduli.

Mineralogy: the contribution of the mineral grains to the elastic properties of the overall rock is represented by the grain bulk modulus and shear modulus. These moduli depend on both the composition of the minerals and their distribution, i.e. a more compressible mineral coating a less compressible mineral will result in a weaker rock than if the stiffer mineral was coating a weaker mineral. There are numerous relationships to predict the mineral moduli from the composition, and their use depends on the rock type.

Grain framework: the grain framework or dry moduli represent the contribution of the frame to the overall strength of the rock. This property is the largest uncertainty for Gassmann modelling (McKenna et al. 2003). Relationships have been developed to predict the grain framework moduli for specific lithologies, and the moduli depends on the mineral composition, porosity and the effective pressure.

Fluid: the bulk modulus of the overall rock depends on the compressibility of the fluid phases within the rock and how they are distributed. Fluid compressibility varies with reservoir temperature and pressure and can be predicted either by empirical relationships or using an equation of state.

These properties can be: derived from laboratory experiments on cores, taken from well logs, estimated using analogues, extracted from seismic or predicted using rock physics models. If a well is available then well logs can provide static "pre-operations" reservoir properties. Then following production or injection updated reservoir properties can be predicted from the static values using rock physics models.

Static Reservoir properties

Well data can be a vital source of information about reservoir properties. Key well information to help with geological and geophysical interpretation is:

- Resistivity → gives information on water saturation and porosity.
- Gamma Ray → used to infer lithology, i.e. shale content.
- Density → indicates lithology, porosity and overpressure detection.
- Sonic → provides information on porosity, mechanical/ elastic properties and overpressure.
- Cores → can provide direct measurements of lithology/mineralogy, porosity and permeability.

An example of using well data to estimate the elastic properties is shown in Figure 2-18, where mineralogical interpretation on the core is used with rock physics models to predict the grain bulk and shear modulus of the Stuttgart sand. Logging provides very fine scale information about the reservoir.

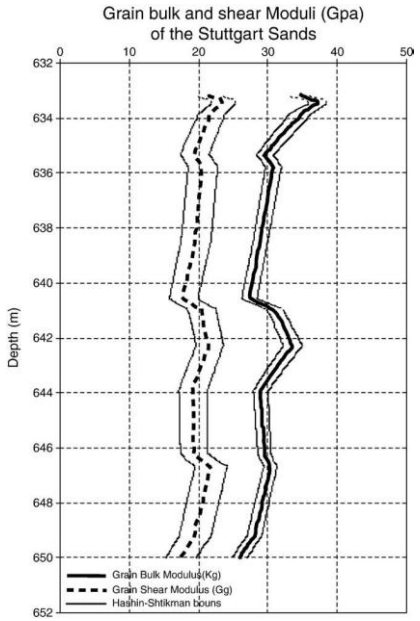


Figure 2-18 Calculated bulk and shear moduli logs for the Stuttgart sands using Hashin-Shtrikman bound averages. Thin lines indicate narrow lower and upper bounds. Taken from: (Kazemeini et al. 2010).

One of the key roles of well information is to offer a "ground truth" to seismic measurements. Well log data is used to "tie" the lithological interpretation at the well to the seismic data. This allows extrapolation of the detailed well information into the reservoir. This process is illustrated in Figure 2-19 for the pre-injection well tie at Sleipner. The well data is used to generate a synthetic seismic trace, which is then compared to the seismic. The significant change in lithology shown on the logs produces a large response on the modelled traces. This is matched to a similar response on the traces from the seismic survey. So this change in lithology can now be traced throughout the reservoir.

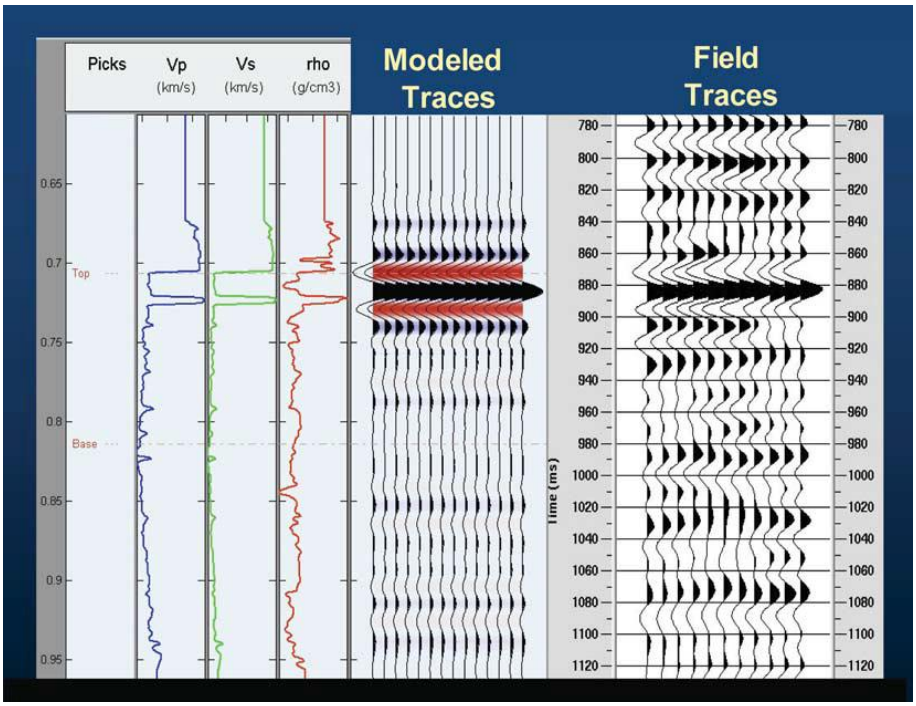


Figure 2-19 1D forward modelling using the pre-injection P-velocity (blue line), S-velocity (green line), and density (red line) logs from well 15/9-A-16. First panel of traces on the left represents identical modeled traces stacked over an offset range of 0–618 m. The second panel is field data extracted from the 1994 (pre-injection) Sleipner near-offset image cube in the vicinity of well. Image taken from (Meadows 2008).

Dynamic Reservoir Properties.

The previous brief explanation of the different elastic moduli illustrated how they depend on saturation, pressure and mineralogy. Rock physics modelling can be used to predict the relationships between these dynamic changes and the elastic moduli. Using these elastic moduli the synthetic seismic response can be predicted and then compared to the measured response, to try and interpret the specific specific subsurface change. Another rock physics analysis approach is to perform a seismic monitoring feasibility study and predict how successful time-lapse surveys would be at detecting subsurface changes at prospective sequestration sites (Kazemeini et al. 2010).

2.4.2.2.1 Pore-Pressure Changes

As highlighted in Section 2.3.4 pore-pressure build-up is a potential hazard during CO_2 injection, therefore a successful monitoring approach will detect this increase. This detection could be achieved via the impact of pressure changes on the grain framework moduli and fluid properties (Kirstetter et al. 2006). The effect of pressure changes on the fluid properties depends on the fluid type and is investigated in Chapter 5.

Increasing the pore pressure weakens the rock frame by reducing the stiffness at the grain contacts and opening microcracks in the pore space (Avseth et al. 2005). When examining a specific reservoir the relationship between pressure and the frame moduli can be calculated directly from core measurements (Vasquez et al. 2010). If these measurements are not available then grain contact models can be used and they were used in a rock physics sensitivity studies at a sequestration site (Trani et al. 2011). These models are only appropriate when the effects are reversible, i.e. when the pressure is below 30-40 MPa (Avseth et al. 2005). This approach assumes constant porosity, which is only true for small pressure changes, as these tend to produce minimal porosity changes in sandstone reservoirs (Landrø 2001). Figure 2-20 shows the relationship between effective pressure (the difference between lithostatic and pore pressure) and the grain framework moduli. An increase in pore pressure and subsequent decrease in effective pressure decreases both the grain framework moduli.

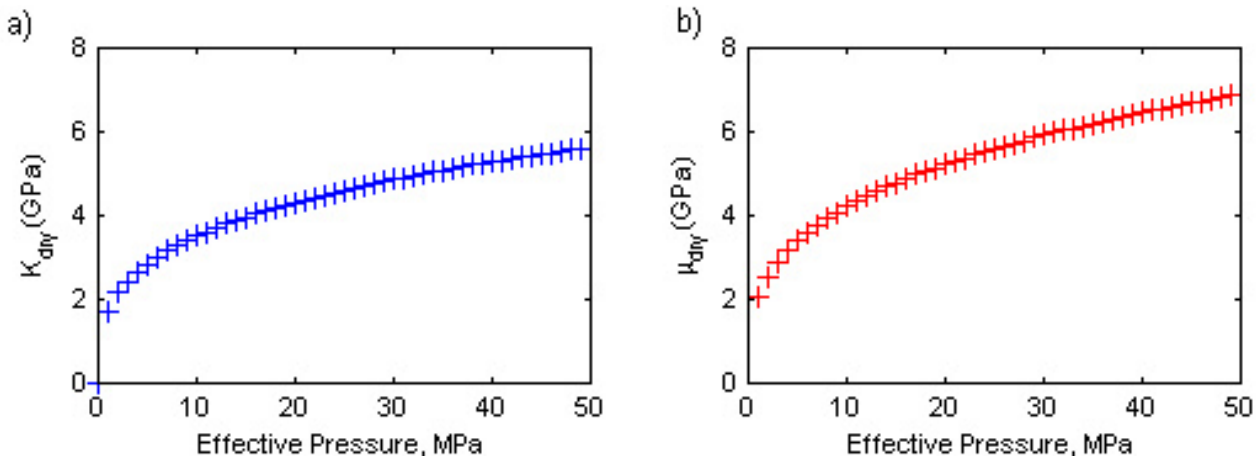


Figure 2-20 The relationship between the effective pressure and the grain framework elastic moduli, predicted using the friable-sand model (Dvorkin and Nur 1996), a) K_{dry}, b) μ_{dry}.

2.4.2.2.2 Fluid Substitution

A key rock physics analysis tool is the ability to predict the seismic response of a rock saturated with one fluid from the response of a rock saturated with a different fluid. Over time a number of theories and modelling approaches have been developed to perform this fluid substitution, as outlined in Table 2-1. These approaches have been divided into ones for media saturated with: liquid (fully saturated) and a mix of gas and liquid (partially saturated). Due to the properties of supercritical CO_2, i.e. density of a liquid, but a compressibility closer to a gas, its injection into a brine-filled aquifer could produce partial saturations

These partial saturations result in attenuation and velocity dispersion and the different mechanisms by which this may occur are outlined in Table 2-1. At frequencies below 1 kHz (typical seismic frequencies) the dominant mechanism is expected to be mesoscopic fluid flow (Müller and Gurevich 2005). This mechanism can be described by the interaction between the seismic wave and the pore fluids. When a seismic wave travels through a rock then the pores are more elastically compressed than the mineral grains (Mavko et al. 1998), this induces increments of pore pressure within the fluids which resist the compression. These pore-pressures can either result in flow (causing attenuation and dispersion) or no flow by which the increase in pore pressure "stiffens" the rock. Complex theoretical models have been developed to simulate the full range of this response (Table 2-1) however a simpler approach is the use of end-member models:

1. **Homogeneous or uniform**. Individual fluid phases exist on a scale which are sufficiently small that the induced pore-pressures equilibrate during the seismic period.
2. **Patchy.** Individual fluid phases are so large that they do not equilibrate during the seismic period.

The length scale which divides these two behaviours (L_c), which is the maximum length over which pore-pressure gradients can relax is calculated using the characteristic relaxation or diffusion time (τ). For heterogeneous pore pressures of the scale (L) τ is given by:

$$\tau = \frac{L^2}{4D} \qquad 2\text{-}8$$

where D is the diffusivity:

$$D = \frac{\kappa K_{fluid}}{\eta} \qquad 2\text{-}9$$

where κ is the permeability, K_{fuiid} is the bulk modulus and η is the viscosity. The critical length scale (L_c) is then given by (Sengupta and Mavko 2003):

$$L_c = \sqrt{\frac{4D}{f}} \qquad 2\text{-}10$$

where f is the frequency of the seismic wave.

Table 2-1 Summary of modelling approaches for fluid substitution and evidence for these approaches.

<table>
<tr><th></th><th>Approach</th><th>Description</th><th>Assumption</th><th>Approximations</th></tr>
<tr><td rowspan="8">Fully saturated porous media</td><td>Gassmann</td><td>Predicts elastic wave velocities in fluid saturated porous media at the low frequency limit.</td><td>• Homogeneous mineral modulus and statistical isotropy of the pore space.
• Rock is fully saturated.
• Valid at sufficiently low frequencies that pore pressures are equilibrated in the pore space.</td><td></td></tr>
<tr><td colspan="4">Theories/ Extensions
• Gassmann, 1951. A number of other variations on the equations exist (Mavko et al. 1998).
• For “partially” saturated rocks at low frequencies the Gassmann equation can be used. An fluid effective modulus is calculated using the Reuss average, which is an isostress average of the moduli of the liquid and gaseous phases. (Mavko et al. 1998).</td></tr>
<tr><td colspan="4">Evidence
Works well for low frequency in-situ seismic data (Mavko et al. 1998), i.e. frequencies <100 Hz.</td></tr>
<tr><td>Biot</td><td>• Predicts frequency-dependent velocity.
• Incorporates some mechanisms of viscous and inertial interaction between pore fluid and mineral matrix.
• “Biot” loss occurs when spatial gradients in pore fluid pressure develop over the λ of a P-wave, driving fluid flow relative to the rock, causing loss through viscous dissipation</td><td>• Isotropic rock.
• Minerals have same elastic moduli.
• Rock completely saturated.
• Pore fluid is Newtonian.
• Relative motion between solid and fluid governed by Darcy’s law.
• λ is substantially larger than the size of the largest grains or pores.</td><td>Low frequency approximation: Gassmann.</td></tr>
<tr><td colspan="4">Theories: Biot, (1956).</td></tr>
<tr><td colspan="4">Evidence
• Predicted slow P-wave has been observed in the laboratory (Mavko et al., 2009).
• For most crustal rocks Biot alone leads to poor predictions of high-frequency saturated velocities (Mavko et al., 2009), because the amount of “squirt” dispersion (discussed below) is of a comparable or greater magnitude.
• Not able to fully explain observed magnitude of attenuation and dispersion especially within the low frequency regime, measured by laboratory measurements (Gist 1994).
Partial fluid saturation of porous rock by multiple types of pore fluid, proposed as cause for mismatch.</td></tr>
<tr><td rowspan="2">Squirt Flow</td><td>• Fluctuating stresses in a rock caused by a seismic wave induce pore pressure gradients at virtually all scale of pore-space heterogeneity.
• Spatial gradients in fluid pressure cause flow from weak cracks to rounder pores.</td><td>• High seismic frequency, e.g. Lab.
• Rock is isotropic and mineralogy constant.
• Rock completely saturated.
Best for highly cracked rocks.</td><td>Low frequency: Gassmann.

Intermediate: frequency dependent velocity.

High: stiffening pore space.</td></tr>
<tr><td colspan="3">Theories:
There are a number of theories to represent this behaviour (Dvorkin et al. 1994; Dvorkin and Nur 1993; Mavko and Jizba 1991)</td></tr>
</table>

<table>
<tr><td rowspan="11">Partially fluid saturated Porous media</td><td rowspan="11">Mesoscopic fluid flow</td><td>Mesoscale (greater than the pore scale smaller then a wavelength) distribution of immiscible fluids.
Induced pressure gradients cause fluid to flow.
Responsible for significant attenuation in the frequency range: 10 to 1000 Hz (Toms et al. 2007).</td><td>Most appropriate when:
Wave velocities are low.
Porous rock saturated with relatively large (mesoscopic) fluid patches.
Patches results from: variations in porosity, permeability and grain types. Causes will be discussed later.</td><td>Follow Mavko and Mukerji, (1998).

- Low: effective fluid from Wood, then Gassmann, Uniform saturation.

-High: Gassmann on individual patches (Hill, 1963). Patchy saturation.

-Intermediate: frequency dependent velocity, found between bounds.</td></tr>
<tr><td colspan="3">Theories</td></tr>
<tr><td>Periodic distribution</td><td colspan="2">White, 1975
First to show theoretically that partial fluid saturation could cause significant attenuation and velocity dispersion. There are other approaches (Johnson 2001; Pride et al. 2004)</td></tr>
<tr><td>Random distribution</td><td colspan="2">More realistic models have a random distribution of heterogeneities (Ciz et al. 2005; Muller and Gurevich 2005).</td></tr>
<tr><td colspan="3">Evidence</td></tr>
<tr><td colspan="2">Laboratory experiments have shown that different velocities can be generated for the same saturation depending on the process of saturation (Cadoret et al. 1998; Domenico 1976; Knight and Nolen-Hoeksema 1990; Murphy III 1984).
It was found that, different fluid distributions and velocity-saturation relationships were formed by different saturation processes:
Imbibition: uniform distribution
Drainage: non uniform gas clusters.
Simultaneous measurements of P-wave velocities and rock sample X-ray computer tomography imaging have also been used and it found this same path dependence (Lebedev et al. 2009; Toms-Stewart et al. 2009).
Measurements for supercritical CO_2 agree (Lei and Xue 2009; Shi et al. 2007).</td><td>High/ lab frequencies.</td></tr>
<tr><td colspan="2">At the Nagoaka sequestration site sonic and neutron porosity logs have been used to infer the relationship between P-wave velocity and saturation.
Response was indicative of a “patchy” relationship.</td><td>Sonic frequencies.</td></tr>
<tr><td colspan="2">Computational modelling suggested that during drainage a patchy saturation will form, whereas during imbibition a homogeneous distribution should form (Sengupta and Mavko 2003).</td><td>Field scale seismic frequencies.</td></tr>
<tr><td colspan="3">NB, the evidence for mesocopic fluid distributions and a patchy seismic response in some cases is quite clear on the laboratory scale. However generalising the results to the field scale/ at low seismic frequencies is still a topic for debate.</td></tr>
</table>

These different behaviours are traditionally characterised by different saturation heterogeneity sizes, Squirt-flow is typical of high frequencies and pore-scale heterogeneities. Whereas mesoscopic saturation heterogeneities are larger than pore scale, but smaller than a seismic wavelength. Assuming a seismic frequency of 40 Hz and using the typical fluid properties for CO_2 and brine, the critical length scale which divides the uniform and patchy behaviour is about 50 cm. The value for the critical length scale (Equation 2-10) depends on frequency, and the value will be much lower for laboratory experiments, where a patchy response possibly could be produced by saturation heterogeneities within a core plug (a few cm).

The causes and scales of some of these saturation heterogeneities are illustrated in Figure 2-21. The scales scan the range from pore scale to core scale and then sub-seismic scale. These saturation heterogeneities can result from geological heterogeneities in the reservoir. Some are naturally occurring (Figure 2-21a-c), however some are related to reservoir production (Figure 2-21d-i). On the laboratory scale, variations in fluid distribution have been attributed to the wettability of the different fluid phases and the saturation process. In this way saturation heterogeneities can form without geological heterogeneities being present.

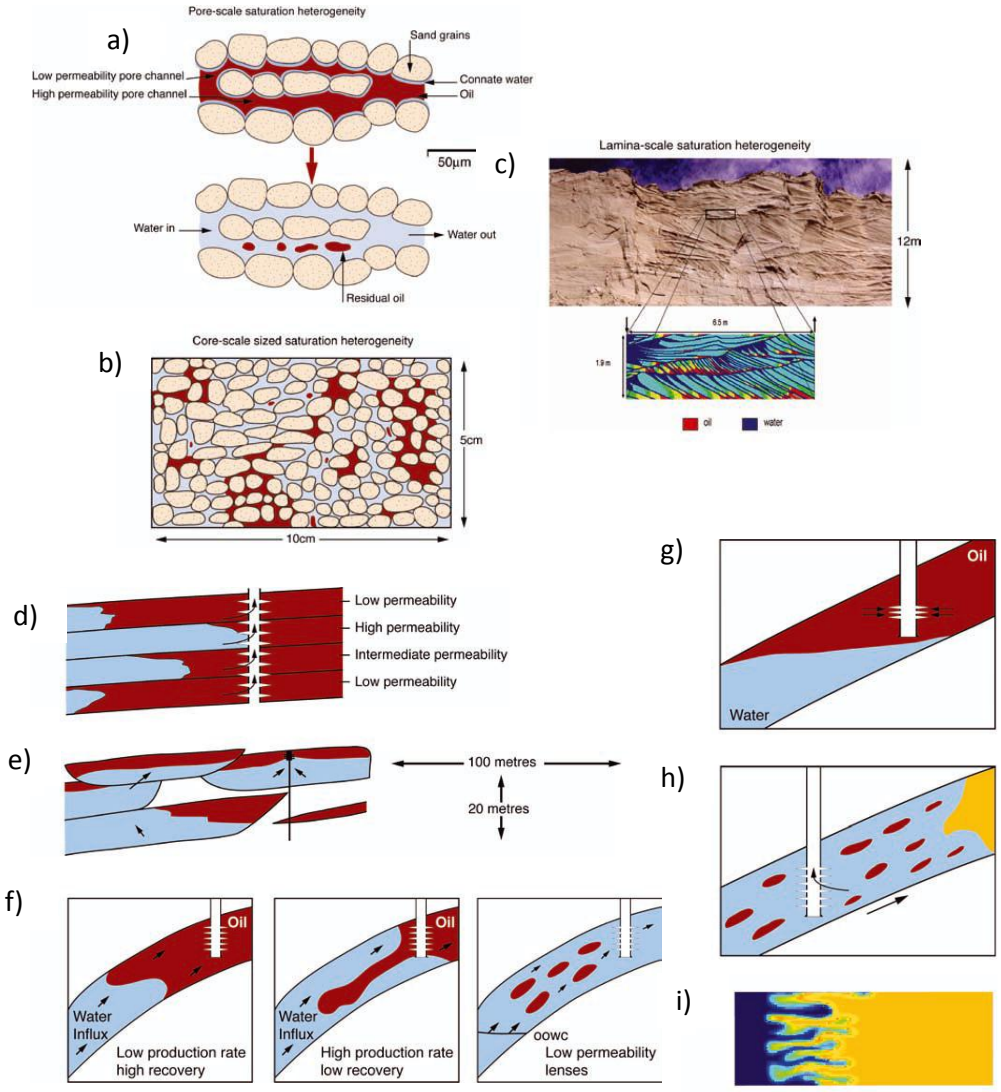


Figure 2-21 Composite image taken from MacBeth and Stephen 2008. Saturation heterogeneity at the: (a) pore scale due to viscous-dominated (fast) water displacement of oil; (b) core-scale with residual oil bypassed in pores and groups of pores; (c) individual bed scale where trapping of residual oil in laminae is visible. A selection of possible sub-seismic saturation scenarios induced by production: (d) Layer-cake reservoir, with high lateral continuity and poor vertical sweep due to compartments separated by impermeable intercalations. This gives an uneven sweep and early water breakthrough); (e) interconnected sand bodies in which there are dead ends and gravity traps (f) effect of rate of capillary displacement of oil from tight sand lenses for different production rates – an inappropriate balance of production rate and capillary forces can create isolated zones of bypassed oil. (g) Unstable displacement of oil by a greater mobility water; (h) dissolved gas drive reservoir, gas collecting up-structure – free gas pulled into well at high oil producing rates; (i) viscous fingering in essentially homogeneous rocks with little detectable permeability variation – a high mobility (less viscous) fluid displacing a less mobile fluid.

Fluid substitution can be performed on log data to predict how the seismic response will react to the introduction of CO_2 into the pore space. Figure 2-22 shows an example of this process at the Ketzin sequestration site in Germany. Fluid substitution was applied to the P-wave velocity, S-wave velocity and density. First, the detailed and spiky log data (black) was blocked (yellow) to allow for easier and meaningful interpretation, then the response following 30% CO_2 injection is calculated, using both the homogeneous (green) and patchy model (red). These bounds indicate the full range of responses. Injecting CO_2 decreased both the P-wave velocity and density.

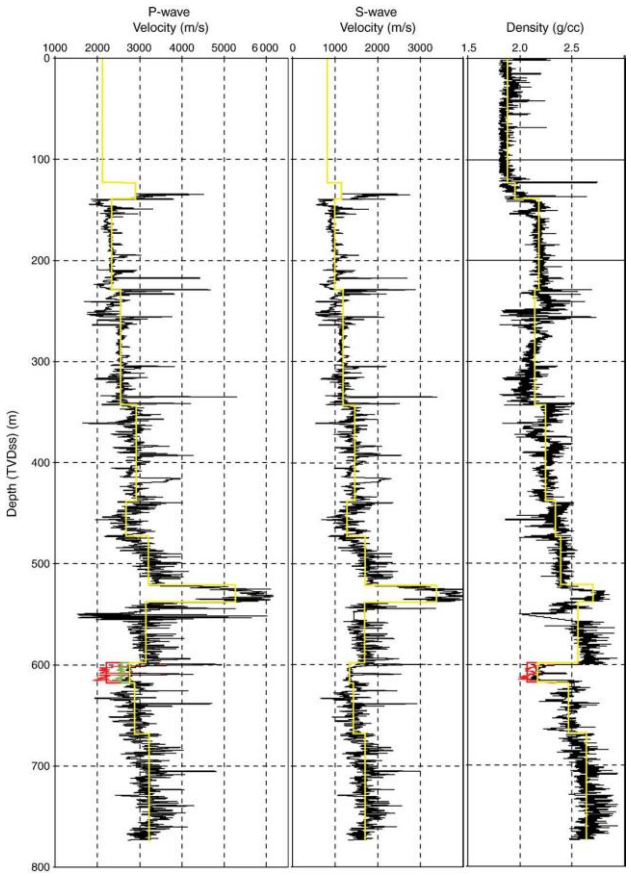


Figure 2-22 Blocky interval models of velocities and density before injection (yellow lines), after 30% uniform CO_2 saturation (green line,) and after 30% patchy CO_2 saturation (red lines) are posted on "measured" velocity and density logs (black curves) (Kazemeini et al. 2009).

2.4.2.3 Seismic Parameters

The isotropic seismic velocities can be predicted using the elastic constants discussed in the previous Section. The P-wave seismic velocity (V_p) depends on K, μ and density (ρ), whereas the S-wave velocity (V_s) depends on μ and ρ. So only V_p varies with fluid distribution which affects the bulk modulus. If a homogeneous fluid distribution is assumed then the relationship between V_p and CO_2 saturation (S_{CO2}) is very non-linear, this high sensitivity to small quantities of gas is called the fizz-gas effect (Domenico 1976; Han and Batzle 2002). Whereas if a patchy distribution is assumed then the relationship between V_p and S_{CO2} is more linear.

Seismic surveys provide information regarding the reflectivity and traveltime in the subsurface, which can be used to infer the seismic velocities and density. A reflection occurs when there is a change in the elastic properties across an interface, which may indicate a change in lithology or fluid content, so fluid movement could be shown by an alteration in reflectivity between surveys. A velocity change will alter the traveltime to the base-reservoir reflection, i.e. if the velocity decreases, the traveltime increases producing a pushdown of the reflection. The analysis of reflectivity can be divided into the zero-offset and far-offset reflectivity, which is often referred to as Amplitude Variation with Offset (AVO). The zero-offset response corresponds to when the source and receiver are at the same location, in reality this is not usually the case, but seismic surveys are processed to provide this. AVO refers to the fact that the reflection coefficient varies with the distance between the source and receiver (incidence angle). The variation is controlled by the contrast in V_p, V_s and ρ across an interface and is fully described using the Zoeppritz (1919) equations.

Both P- and S-waves can generate reflections and ideally data from both would be available. At Weyburn P- and S- wave sources and receivers were deployed (Davis et al. 2003), but this is not common and often only a P-wave source is used. At non-normal incidence angles, there are mode conversions and an incident P-wave will generate reflected and transmitted P and S-waves. The magnitude of the transmission and reflection coefficients depend on the angle and the properties of the two layers. A P-P reflection is a P-wave reflected as a P-wave, whereas a P-S wave is a P-wave reflected as an S-wave. Recording of shear waves is uncommon and requires multi-component geophones, such as those used at Weyburn. Using mode conversions is complex, but improvements have been made in the use of P-S stacks (Stewart et al. 2002).

Seismic attributes are quantities extracted or derived from seismic data that can be used to enhance the seismic information. Typical attributes are: amplitude, frequency, attenuation and coherency. For interpretation AVO is often modelled by the three-term approximation, and the response is characterised into seismic attributes: AVO intercept (*A*), AVO gradient (*B*) and AVO curvature (*C*) (Aki and Richards 1980; Shuey 1985). Attenuation which describes the reduction in magnitude of a seismic wave propagating through the subsurface is another attribute.

2.4.2.4 Time-lapse Seismic Monitoring Results

The most advanced and significant time-lapse monitoring studies for CCS have been conducted at Sleipner and Weyburn. Because these projects are very different (offshore vs onshore, sandstone aquifer vs fractured carbonate), they demonstrate a range of possible issues using time-lapse seismic surveys to monitor CO_2 injection. Results from In Salah are not discussed, as interpretation of any time-lapse signal was hampered by the poor quality of the overburden in the baseline survey (Eiken et al. 2011).

Sleipner

At Sleipner a baseline seismic survey was conducted in 1994 and repeat surveys were made in 1999, 2001, 2002, 2004, 2006 and 2008 (Figure 2-23). Due to the high porosity and weak rock frame of the Utsira sand, V_p is unusually sensitive to the pore-fluid type, so even moderate amounts of CO_2 were expected to reduce V_p by up to 30% (Arts et al. 2004b). This velocity decrease increased the reflection coefficients in the plume and produced pushdown on the base Utsira reflector (Figure 2-23). Figure 2-23 shows how easily the plume migration can be tracked. This clear seismic imaging has resulted in claims that there is no evidence of leakage from the aquifer (Arts et al. 2004a). Attempts to extract more quantitative information have included examinations of the reflectivity, pushdown, AVO analysis and spectral decomposition (Chadwick et al. 2010; Chadwick et al. 2005; Chadwick et al. 2004a).

Reviewing the literature about the survey results from Sleipner highlighted some key uncertainties with the method. There is uncertainty as to which fluid distribution model is appropriate at sequestration sites (Ghaderi & Landro 2009; Vanorio et al. 2010), and as this model dictates the relationship between S_{CO2} and and V_p (Mavko and Mukerji 1998) it could introduce errors during interpretation. When a homogeneous fluid distribution is assumed, then the fizz-gas effect makes quantifying the saturation almost impossible. The phase of the CO_2 also requires consideration, as it was found that the seismic response at Sleipner could either be accounted for using a lower reservoir temperature, assuming no dissolution or a higher temperature allowing for dissolution (Arts et al. 2008).

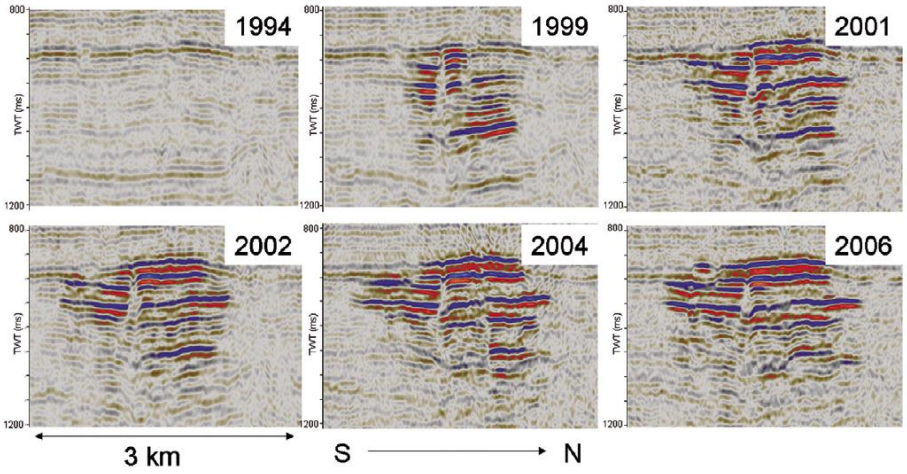


Figure 2-23 Plume development at Sleipner site, monitored using time-lapse seismic monitoring (Arts et al. 2008).

Weyburn

Time-lapse 3D, three component data was acquired over part of the Weyburn field to monitor the CO_2 flood. The baseline survey was conducted in 1999, then repeat surveys were conducted in 2001, 2002, 2004 and 2007 (White 2009). Far-offset information was collected for AVO analysis. The maximum decrease in V_p resulting from CO_2 injection was predicted to be 4-10% (White et al. 2004). This altered the seismic amplitude and traveltime (Figure 2-24 and Figure 2-25). As V_p was highly sensitive to even low levels of CO_2 saturation (5-10%), mapping the lateral extent of the CO_2 plume was relatively easy. White (2009) predicted that pressure build-up at Weyburn could potentially decrease the seismic velocity by <4%.

Again Weyburn highlights limitations with seismic monitoring. Some issues are similar to those encountered at Sleipner, such as the high sensitivity to small CO_2 saturations and uncertainties regarding the fluid distribution. The Weyburn results also show that the time-lapse response is a combination of pressure and saturation changes over time, which has to be considered during interpretation. The reservoir itself posed some challenges for monitoring, as its porosity and permeability are lower than at Sleipner, which produces smaller magnitude changes in the seismic response.

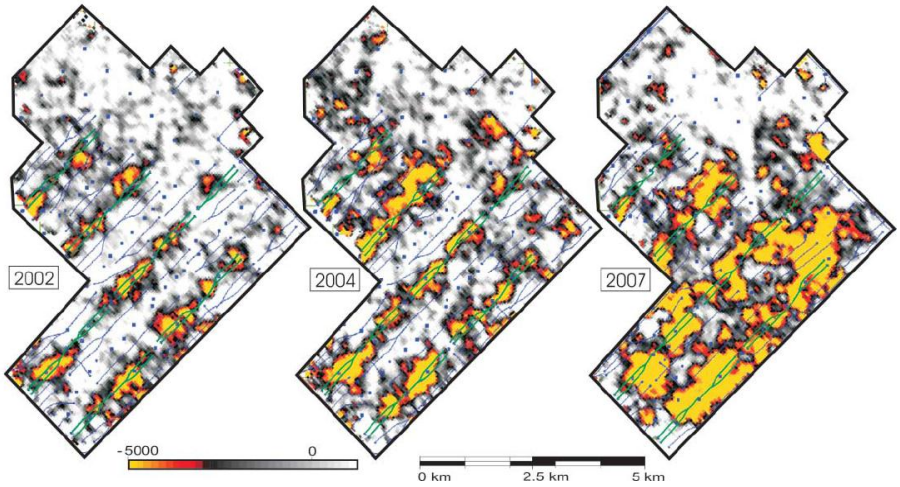


Figure 2-24 Time-lapse amplitude difference maps for the Midale Marly Horizon at Weyburn. The negative amplitude differences accentuate the CO_2 saturation effects wells (White 2009)

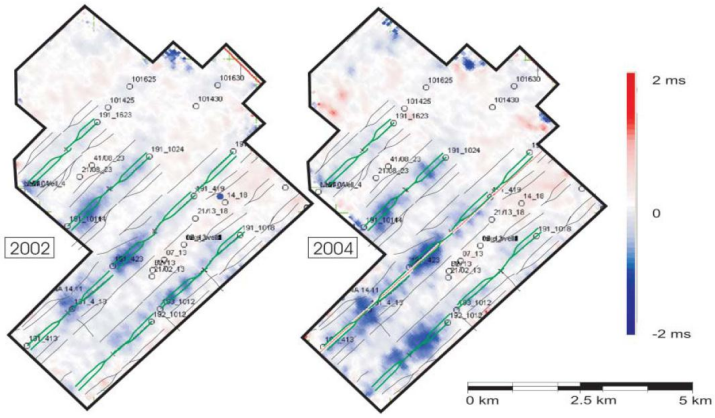


Figure 2-25 Time-lapse traveltime maps determined for a sub reservoir horizon, representing the traveltime anomalies associated with propagation through the reservoir (White 2009).

2.5 Current Limitations of the Time-lapse Seismic Approach

The results from Sleipner and Weyburn demonstrate that CO_2 injection can be monitored using time-lapse seismic surveys. However there are still some problems which must be resolved before it is established that time-lapse seismic monitoring can fully verify the containment of injected CO_2. In particular the difference in magnitude of the response at the two sites demonstrates the importance of reservoir properties. The shallow, high-porosity, uncemented sandstone aquifer at Sleipner represents an ideal monitoring scenario, whereas the deep, thin, low-porosity carbonate reservoir at Weyburn makes monitoring more challenging. Both sites also presented problems with extracting quantitative information about CO_2 saturation from the seismic response, due to the fizz-gas effect. Without being able to determine the saturation, it is not possible to verify that all the injected CO_2 is contained in the reservoir. The seismic response is an amalgamation of changes in fluid content and phase, with ambiguities regarding the CO_2 phase introducing potential errors into the seismic interpretation at Sleipner (Arts et al. 2008). Pressure changes within the reservoir also contribute to the time-lapse seismic response and at Weyburn pressure increases have been thought to have a notable effect (Ma and Morozov 2010; White 2009). Finally there is uncertainty as to the appropriate fluid distribution model to be applied at sequestration sites and different models have been used to interpret the Sleipner data (Chadwick et al. 2005). As the fluid distribution model dictates the P-wave seismic response (Mavko and Mukerji 1998), uncertainties about the appropriate model may introduce significant errors into interpretation.

Here the literature regarding these issues is reviewed. If these uncertainties are reduced, time-lapse seismic surveys may be able to fulfil all the sequestration monitoring requirements outlined in Section 2.4.

2.5.1 Importance of Reservoir Properties

The magnitude of the time-lapse responses at Sleipner and Weyburn, clearly illustrate that the seismic response is controlled by reservoir properties. The response is unique to a site, and can be assessed prior to injection using a rock physics feasibility study (Kazemeini et al. 2010; Rossi et al. 2008) either in conjunction with well information, or using analogues. Such a study would determine whether injection into a specific site could be monitored.

In addition to site specific studies, more general rules about monitoring ability have been developed. Certain reservoir characteristics produce seismic velocities which are very sensitive to the pore-fluid composition. The important properties are porosity, grain framework properties and mineralogy. High porosity, weak framework and weak mineralogy will produce a V_p which is very sensitive to fluid content. Therefore the most sensitive reservoir rocks are high porosity, unconsolidated, uncemented sandstones, similar to the Utsira sandstone. The properties of the reservoir fluids are also important, as the time-lapse response records the change in the fluid bulk modulus and density during injection. The difference in density between brine and gaseous CO_2 is large, but the density of supercritical CO_2 is much closer to that of brine. Therefore gaseous CO_2 will be easier to monitor.

All these individual properties are important, but also are all influenced reservoir depth. The porosity is expected to decrease with depth and the CO_2 will change phase from gaseous to supercritical CO_2 at about 800 m depth. Hence reservoir depth is an important factor in assessing whether monitoring will be successful at a site. McKenna et al (2003) identified optimal monitoring conditions as a shallow, high-porosity, unconsolidated sandstone, where CO_2 was in its gaseous phase. However for storage capacity and security reasons deeper reservoirs with greater overburden, where CO_2 is in its supercritical phase would be preferred. Ideally both these recommendations will be met.

2.5.2 Fizz-gas Effect

At Weyburn and Sleipner attempts have been made to quantify the volume of CO_2 trapped in the reservoir, by extracting the saturation from the P-wave reflectivity (Eiken et al. 2000). However due to the fizz-gas effect (i.e. assuming a homogeneous fluid distribution) no meaningful saturation information was found, this issue was discussed by Chadwick et al (2009). This problem has long plagued the hydrocarbon industry, as it results in commercial and residual gas saturations producing very similar zero-offset reflection coefficients and thus it is an area of active research (Chopra et al. 2004). Three main approaches have been suggested to distinguish residual and economic gas accumulations: using far-offset data (Gomez and Tatham 2007), using converted-wave data (Gonzalez et al. 2003) and attenuation (Chopra et al. 2004).

Although the V_p- S_{CO2} relationship is not ideal for extracting saturation information, ρ varies linearly with gas saturation and therefore represents the best seismic property for differentiating residual and

commercial gas (Avseth et al. 2005). Density can be derived from far-offset data, using three-term AVO analysis (Buland and Omre 2003; Kabir et al. 2000; Roberts 2000). This technology is immature and requires seismic data with high fold and large incidence angles, as well as knowledge of the porosity in the reservoir. AVO analysis was applied to examining CO_2 saturation, where it was found that all the AVO parameters were sensitive to changes in small CO_2 saturations (Ravazzoli and Gómez 2011).

It has been suggested that converted waves may be sensitive to saturations. Gomez and Tatham, (2007), suggested that P-SV or SH-SH AVO integrated with P-P AVO were the best attributes to use. P-to-S elastic impedance (PSEI) was also suggested as it was found to be sensitive to density, and could differentiate commercial and residual gas using well log data (Gonzalez et al. 2003).

Residual gas saturations produce greater attenuation than commercial gas saturations (Avseth et al. 2005). This behaviour has been shown in laboratory experiments, where when mixing gas and water, the peak attenuation is at 80% water saturation, i.e. residual gas saturation (Murphy III 1982). Theoretical models have been developed to predict this attenuation (Dutta and Ode 1979; White 1975). Laboratory work and modelling of attenuation was used for CO_2 (Lei and Xue 2009). It was found that the saturation at which maximum attenuation is generated depends on CO_2 phase, with peak attenuation being at 20% for gaseous CO_2 and 30% for supercritical CO_2. However estimating attenuation from seismic data is an immature technology and there are only a few published examples showing successful determination of gas saturation from attenuation effects (Chopra et al. 2004).

The approaches discussed above were developed for natural gas, which has a much lower density than supercritical CO_2. Therefore methodologies which rely on exploiting the density contrast between gas and brine may not be successful when applied to CO_2.

2.5.3 CO_2 Phase

The discussion in Section 2.3 about the dependence of the CO_2 phase on the geothermal and pressure gradients, and the potential for CO_2 to react with the reservoir rock and fluids and change phase, highlighted an issue with the interpretation of the time-lapse seismic response. This problem is that the phase of the CO_2, whether gaseous, supercritical, liquid, dissolved within the brine or precipitated as a solid carbonate, may change during sequestration. Uncertainty as to the CO_2 phase could complicate interpretation as was demonstrated at Sleipner where the recorded change in the seismic response could be explained either using a lower reservoir temperature without dissolution or a higher temperature with dissolution (Arts et al. 2008).

When the temperature and pressure conditions in the reservoir are close to the transition between gaseous and supercritical CO_2 (Figure 2-7), as is the case at Sleipner, it may be difficult to predict the phase. As the seismic response is very sensitive to CO_2 phase (Lumley et al. 2008) it important to know whether the

CO_2 is supercritical or gaseous. Ravazzoli and Gomez (2011) have suggested that the AVO coefficients could be used to distinguish the different phases.

CO_2 can be present as free CO_2, dissolved in brine or precipitated as a carbonate mineral. This trapping phase may affect the reservoir's elastic properties, by changing the fluid bulk modulus and altering the reservoir mineralogy and porosity. Rock physics modelling studies have been conducted to examine the relative contribution of these different trapping mechanisms to the seismic response. McKenna et al (2003) examined structural, solubility and mineral trapping in an Utsira-type sandstone. Trapping of CO_2 within its own phase significantly decreased V_p, but had a minimal effect on V_s. Mineralisation significantly increased both V_p and V_s. Solubility trapping stiffened the brine and increased V_p, but this increase was found to be so small it may not be detectable. However it was thought that the subsequent porosity increase resulting from the dissolution of susceptible minerals by brine saturated with CO_2 could be detectable. Vanorio et al (2010) conducted a study to quantify the impact of dissolution and porosity changes.

Recent experimental modelling results (Sun and Han 2009), could help update the approach used to examine dissolution. Previously it was assumed that dissolved CO_2 should increase the brine velocity (Liu 1998; McKenna et al. 2003; Wang 2001), however the experimental work from Sun and Han (2009) show this increase in velocity is only true below 60°C and above this temperature the relationship reverses.

Quantifying the amount of CO_2 trapped within each phase using the time-lapse seismic response would help determine the storage security in the reservoir.

2.5.4 Pressure Changes

Changes in pore pressure are expected when CO_2 is injected and an increase could result in failure of the reservoir or caprock (Section 2.3.4). This problem can be foreseen and mitigated by forward modelling to determine safe injection rates and strategy (Morris et al. 2011). However this approach requires knowledge of reservoir architecture and pressure communication which may not be available for saline aquifers, therefore any pressure increase must be detected.

At Snohvit there has been a clear trend of pressure increase caused by injection, which has been monitored via wells (Eiken et al. 2011). Attempts have been made to minimise these pressure increases by stopping injection. The longest stoppage was for four months, however this did not stabilise the pressure, and if injection continues at the current rates, it is thought the reservoir could reach the fracture pressure (Eiken et al. 2011). This pressure increase was reflected in the time-lapse seismic response, with the areal extent of the plume being too large to arise from saturation changes alone, and some of the amplitude changes were attributed to pressure increases (Eiken et al. 2011).

Time-lapse seismic surveys have been used to interpret pressure and saturation changes over producing hydrocarbon fields (Landrø et al. 1999; Ribeiro and MacBeth 2006; Watts et al. 1996), and synthetic studies have been conducted to determine the relative contribution of these properties to the response (Kirstetter et al. 2006; Landrø 2001; Landrø et al. 2003; Macbeth et al. 2006; Tura and Lumley 2000). In the case of hydrocarbon production, which resulted in pressure depletion, seismic velocities increased (Brown et al. 2002; Landro 2001). The opposite would be expected during injection.

A methodology which can differentiate saturation and pressure changes in the time-lapse seismic response would help assess the integrity of a storage site. The shear modulus is sensitive to pressure changes (Tura and Lumley 2000), whereas the bulk modulus is sensitive to saturation changes, so the V_p/V_s ratio is a good seismic property to tackle this problem. Tura and Lumley (2000) cross-plotted the P-wave and S-wave impedances and Rojas (2008) used the V_p/V_s ratio directly. AVO data can be used to discriminate between pressure and saturation changes, as the P-wave reflectivity is sensitive to the V_p/V_s ratio at mid to far offsets. A workflow based on AVO data was developed by Meadows (2001) and then extended by Trani et al. (2011), through the incorporation of traveltime information. This analysis requires near and far-offset data, from both the monitor and baseline surveys. Ribeiro and Macbeth (2006) also suggested a methodology by which pressure and saturation effects could be separated using the shear modulus and a saturation modulus. At Weyburn AVO attributes have been used to try and distinguish pressure and saturation signatures (Ma and Morozov 2010; White and Johnson 2009).

Other monitoring techniques can also be used to detect pressure changes and at In Salah pressure build-up is indicated by DInSAR and at Snovhit down-hole pressure recordings have been used (Eiken et al. 2011).

2.5.5 Uncertainty Regarding the Fluid Distribution

When interpreting the physical meaning of the time-lapse changes at the sequestration sites there is an uncertainty about which fluid distribution model to use (Ghaderi and Landro 2009; Vanorio et al. 2010). If a rock is saturated with multiple fluids of different compressibilities, such as brine and CO_2, then the seismic response is controlled by the fluid distribution in the pore space as discussed in Section 2.4.2.2.2 and Table 2-1. The impact of the fluid distribution in the pore space on the seismic response is incorporated via the fluid distribution model, which controls the relationship between the CO_2 saturation (S_{CO2}) and V_p. This relationship can vary between two end-member models, homogeneous and patchy. Some workers have used a mix of the models (Chadwick et al. 2005), although results from Sleipner indicated that the pushdown was best modelled using a homogeneous response (Chadwick et al. 2004a).

Laboratory experiments have demonstrated the importance of the distribution, as different velocities can be generated for the same rock sample with the same water content (Domenico 1976; Murphy III 1984).

The relationship between the velocity and S_{CO2} shows hysteresis. Samples undergoing imbibition during laboratory experiments form a homogeneous distribution on the pore scale, i.e. all the pores a mixture contain both fluid phases, whereas samples undergoing drainage form a heterogeneous saturation distribution at the pore and region scale (Cadoret et al. 1998; Domenico 1976; Knight and Nolen-Hoeksema 1990). A heterogeneous distribution was recorded during drainage experiments where CO_2 was injected into brine-filled sands (Lei and Xue 2009; Shi et al. 2007).

Some of the results collected at the Nagoaka site in Japan also indicate a patchy distribution (Azuma et al. 2011; Caspari et al. 2011). Using the sonic logs in combination with neutron porosity as a proxy for saturation, the V_p-S_{CO2} relationship was plotted and it is indicative of an intermediate-patchy response (Figure 2-26). It is important to note that this "patchy" response is likely to be due to geological heterogeneities (Figure 2-21), rather than heterogeneities related to saturation process/ The response depends on both the fluid distribution in the pore space and frequency, and as the frequency increases so does the patchiness of the response.

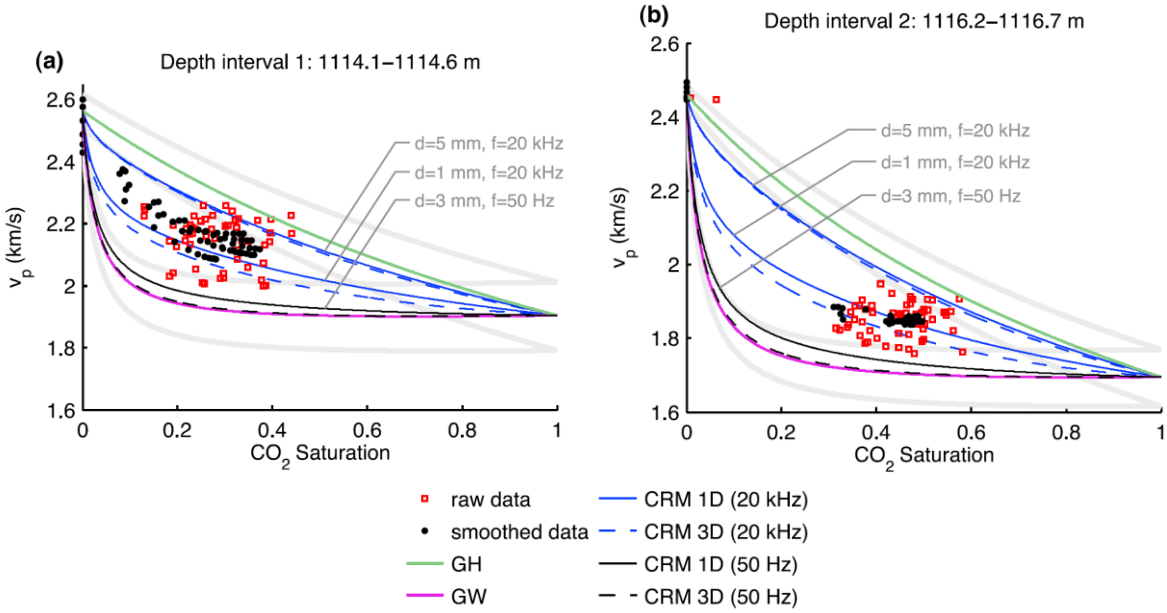


Figure 2-26 Comparison between theoretical models and log data for different depth intervals (1 and 2) at the Nagoaka site. GW:Homogeneous, GH: Patchy (Caspari et al. 2011).

Examining this at low frequencies on a field scale is difficult, as it requires large scale values for both the saturation and the seismic velocities. Sengupta and Mavko (2003) suggested that the fluid distribution in a reservoir can be predicted by combining fluid-flow and rock physics modelling. Using this methodology the impact of reservoir parameters, such as injecting fluid, mobility ratios, permeability distribution and pressure depletion were examined (Kirstetter et al. 2006; Sengupta and Mavko 2003). The simulation results found a similar V_p- S_{CO2} hysteresis to that suggested by the laboratory experiments. During waterflood of a water-wet reservoir (imbibition), a homogeneous saturation formed, whereas during gas

injection (drainage) a patchy distribution formed (Sengupta and Mavko 2003). However the underlying physical mechanisms are different. At the pore scale the distribution is governed by capillary pressure, whereas on the field scale the distribution is dictated by gravity and viscous effects. The reason for the patchy response resulting from gas injection is that gravity results in the formation of high saturation subseismic resolution gas caps (Sengupta and Mavko 2003). This move from homogeneous response at low gas saturations to a patchy response at high saturations has been predicted by laboratory and numerical studies (Lebedev et al. 2009). Therefore it is possible that these different fluid distribution responses could be found within different parts on the reservoir during sequestration. These responses could be linked to the trapping phase, with structurally-trapped (mobile) CO_2 producing a patchy response and residually-trapped (immobile) CO_2 producing a homogeneous response.

As the knowledge of the fluid distribution is essential for the interpretation of a time-lapse seismic signature, research has been conducted to examine its detection. These detection techniques are focussed upon the fact that the fluid distribution effects only V_p, not V_s or ρ, therefore an elastic property sensitive to the V_p and V_s ratio, such as the Poisson's ratio, could be used to detect the fluid distribution (Dvorkin and Nur 1998; Kazemeini et al. 2010). Kazemeini et al (2010) found that at Ketzin the different fluid distributions could be differentiated using a cross-plot of P-wave impedance versus Poisson's ratio. Shear-wave information was collected directly at Weyburn, but this additional acquisition is expensive. The V_p/V_s ratio is therefore often inferred from the AVO response, which is sensitive to the ratio at mid-far offsets (>25-30°) (Gomez and Tatham 2007). This suggests that mid-far offset data could be used to determine the appropriate fluid distribution model.

2.6 Summary

Literature on CCS shows that geological storage of CO_2 is viable, and that saline aquifers are likely to offer the greatest storage capacity. Evidence from existing sequestration sites indicates that time-lapse seismic surveys are likely to play an important role in monitoring storage, possibly in combination with other techniques. Changes in the seismic response at existing sites over time enabled mapping of the CO_2 plume and its migration. However the magnitude of this response depends on the reservoir properties, so there remains need for monitoring feasibility studies at proposed sequestration sites. Discussions regarding the behaviour of injected CO_2, its trapping and other dynamic effects in the reservoir highlighted some potential issues when interpreting the time-lapse response. CO_2 is expected to be trapped in different phases and distributions, which will vary with time, and injection may alter the reservoir pressure. To fully interpret the seismic response these dynamic changes must be considered, partially because they may mask saturation changes, but also because they may yield important information regarding trapping security and CO_2 containment.

More specifically this review of the literature highlighted five limitations to the use of time-lapse seismic surveys at sequestration sites. These key issues are summarised in Table 2-2 along with an indication of how they will be examined in this thesis.

Table 2-2 Summary of the five key issues raised by this literature review and a brief mention of how they will be examined in this thesis.

Issue	**Key literature themes and concerns**	**How examined?**
Dependence of the time-lapse seismic response on **reservoir properties**	Section 2.5.1 Differences between results from Sleipner and Weyburn Rock Physics modelling studies suggest reservoir depth is a key control on the seismic response. ➢ At some sites plume migration may not be detectable.	Section 4.3 Depth of reservoir is varied between 500-2500m, to examine how depth affects the ability to detect CO_2 plume migration.
Fizz-gas effect.	Section 2.5.2 Fizz gas effect made it difficult to extract CO_2 saturation from the seismic response at existing sites Saturation is a key parameter for: 1. Verifying CO_2 containment. 2. Helping differentiate residual and structural trapping and subsequently trapping security.	Section 4.4 The sensitivity of different seismic attributes to CO_2 saturation examined. Approach guided by suggestions in the literature to differentiate residual and commercial natural gas accumulations.
Uncertainty about **CO_2 phase.**	Section 2.5.3 CO_2 can be trapped in different phases over time. Interpreting the seismic response requires knowledge of the phase. ➢ Highlighted by Sleipner interpretation issue, i.e. lower temperature without dissolution or higher temperature with dissolution	Section 4.5 Seismic response is predicted for: gaseous and supercritical CO_2. Examine the use of AVO to differentiate the fluid phases. Elastic properties of brine saturated with CO_2 and brine compared.
Pressure build-up.	Section 2.5.4 Pressure changes from CO_2 injection have been: 1. Detected at sequestration sites. 2. Predicted from reservoir simulation. Increases in pore pressure could result leakage into the caprock, reactivation of fractures and may mask the seismic response to saturation changes.	Chapter 5 Examine the use of zero-offset and AVO information to differentiate pressure and saturation effects. Combined reservoir simulation and rock physics modelling allows use of realistic saturation and pressure values.
Uncertainty about which **fluid distribution** model to use.	Section 2.5.5 Fluid distribution model dictates the V_p-S_{CO2} relationship, evidence from: 1. Laboratory studies. 2. Theoretical models. 3. Limited field evidence. ➢ Some ambiguity about the relationship between lab and field scale observations. Potential relationship between CO_2 trapping phase and fluid distribution model.	Chapter 6. End-member fluid distribution models used to predict the range of seismic responses, and how it effects monitoring. Reservoir simulation and rock physics modelling combined to relate CO_2 trapping phase and fluid distribution model.

3. Methodology and Theory: Predicting the Time-lapse Seismic Response

3.1 Introduction

Time-lapse seismic surveys have been successfully applied to monitoring sequestration sites, mapping plume migration (Arts et al. 2008; White 2009) and detecting pressure build-up (Eiken et al. 2011). However interpreting these results is complicated by the fact that during injection there is the potential for phase changes, pressure build-up, geochemical reactions and changes in fluid content. Rock physics modelling provides the link between these changes within the reservoir and the change in the response between repeat seismic surveys.

In this Chapter the equations used throughout this these are given. First and foremost the equations used to predict the seismic response are discussed (Section 3.2), starting with the seismic velocities and densities (Section 3.2.1), which was used to calculate the reflectivity (Section 3.2.2) and attenuation (Section 3.2.3). Once the reflectivity was calculated it was convolved with a wavelet using seismic modelling software to generate a reflectivity series (Section 3.2.4). Calculating the seismic velocities and attenuation required the elastic properties of the reservoir and overburden, which were predicted using rock physics models (Section 3.3). The required elastic properties were the: mineral type (Section 3.3.1), grain framework (Section 3.3.2) and fluid (Section 3.4). For a saline aquifer the fluid properties were calculated for brine (Section 3.4.1), CO_2 (Section 3.4.2) and brine saturated with CO_2 (Section 3.4.3). There are different ways to combine rock and fluid properties to determine the elastic moduli of the saturated rock (Section 3.3.3). The methods discussed here are the Gassmann (1951) equation (Section 3.3.3.1), the Hill (1963) average (Section 3.3.3.2.1) and the White (1975) model (Section 3.3.3.2.2). The fluid, grain framework and solid elastic properties depend on certain reservoir properties, i.e. porosity, permeability, pressure, temperature and mineralogy. In Section 3.5 the equations used to predict these values are given. These calculated reservoir and elastic properties are compared to values from clastic sequestration sites at similar depths in Section 3.6. Predicting the seismic response over time requires an understanding of how saturation, pressure and CO_2 trapping phase change during sequestration, which was predicted using fluid-flow simulation. This is discussed in Section 3.7. Integrating the fluid-flow simulation results with rock physics modelling does pose some challenges which are discussed in Section 3.8. First, the workflow used to integrate the data is illustrated (Section 3.8.1), then some of the opportunities and issues which arise from using this combined approach are discussed in Section 3.8.2.

Two different workflows have been designed to examine the ability of time-lapse seismic surveys to monitor CO_2 injection into a generic clastic saline aquifer. The first workflow predicts the sensitivity of the seismic response to changes in the reservoir, whereas the second workflow predicts the time-lapse seismic response resulting from CO_2 injection. This second workflow differs from the first by the use of fluid flow simulation to predict realistic and spatially variable saturation and pressure changes in the reservoir.

The rough outline of these approaches is given in Figure 3-1, however modifications were required to fully examine the issues outlined in Table 2-2. The modifications to the models are discussed here:

- "Sensitivity Study". This combines geological, rock physics and seismic modeling. This approach used in:
  - Chapter 4: the variables examined are: reservoir depth, CO_2 saturation and CO_2 dissolution.
  - Chapter 5: pore pressure varied.
  - Chapter 6: multiple fluid distribution models were used (Section 2.4.2.2.2.)
- "Integrated Modeling". The modeling steps above are used in conjunction with fluid-flow simulation. This approach is used in:
  - Chapter 5: values of pressure and saturation are extracted from fluid-flow modeling results in the form of a 2 D slice through the reservoir and are used as inputs for rock physics modeling.
  - Chapter 6: values of saturation are extracted from fluid-flow modeling results in the form of a 2 D slice through the reservoir and are used as inputs for rock physics modeling. Using these inputs the fluid distribution model is varied to predict the potential range of seismic responses. Saturation outputs are used in conjunction with rock physics models to examine the use of multiple fluid distribution models within the same reservoir.

Aside from the fluid-flow and seismic reflectivity modelling which used commercial and open source codes respectively, the rest of the numerical modelling was conducted in Visual studio using a C program specially written for this purpose.

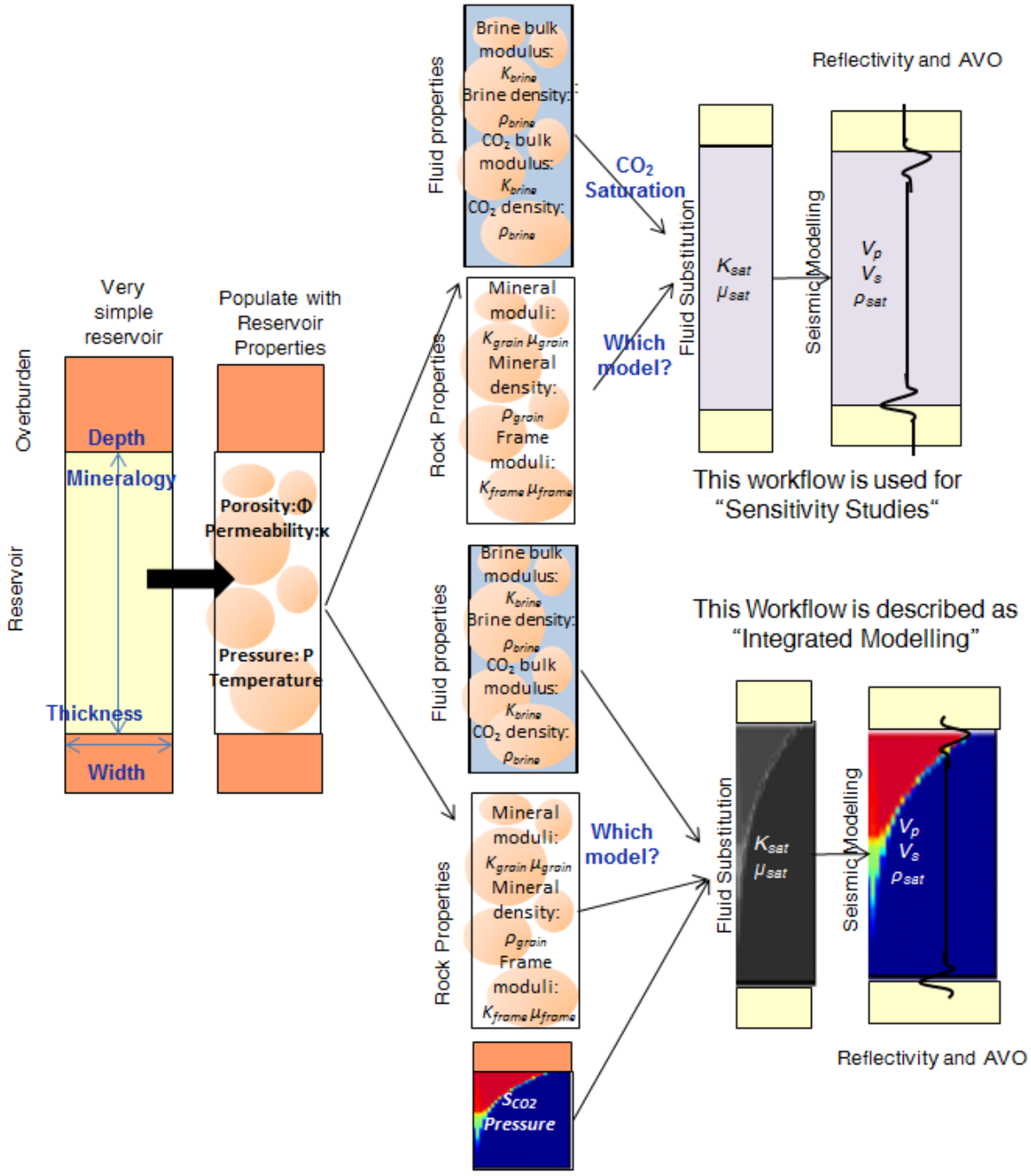


Figure 3-1 Flow chart showing the ways which disciplines are combined in the thesis to examine the limitations in the ability of time-lapse seismic surveys to monitor sequestration. The words in blue are the variables which are altered.

3.2 Predicting the Seismic Response

In the previous Chapter an overview was given of time-lapse seismic monitoring at sequestration sites, which highlighted key seismic properties for interpretation: seismic velocities, zero-offset reflectivity, mid to far-offset response and attenuation. Here the equations used to predict these properties are given.

3.2.1 Seismic Velocities

The seismic velocities: the compressional or P-wave velocity (V_p) and the shear or S-wave velocity (V_s) can be described in terms of the elastic moduli (Section 2.4.2.1). For the longitudinal or compressional wave, which travels through the medium as a series of dilations and compressions, the isotropic velocity is given by:

$$V_p = \sqrt{\frac{K + \frac{4}{3}\mu}{\rho}} \qquad 3\text{-}1$$

For the transverse or shear wave, the isotropic velocity is given by:

$$V_S = \sqrt{\frac{\mu}{\rho}} \qquad 3\text{-}2$$

where μ is the shear modulus and K is the bulk modulus. For subsequent discussions these elastic moduli will be referred to as K_{sat} and μ_{sat} indicating that they refer to a saturated porous medium.

The density (ρ_{sat}) is calculated using the arithmetic mean of its constituent parts:

$$\rho_{sat} = \Phi\rho_{fluid} + (1-\Phi)\rho_{grain} \qquad 3\text{-}3$$

where ρ_{fluid} is the average fluid density, ρ_{grain} is the density of the mineral grains and Φ is the porosity.

3.2.2 Reflectivity

At an interface between two thick, homogeneous, isotropic, elastic layers, the zero-offset P-P reflection coefficient (R_{pp}) and S-S reflection coefficient (R_{ss}) are given by:

$$R_{pp}(0) = \frac{V_{p2}\rho_2 - V_{p1}\rho_1}{V_{p2}\rho_2 + V_{p1}\rho_1} \qquad 3\text{-}4$$

$$R_{ss}(0) = \frac{V_{s2}\rho_2 - V_{s1}\rho_1}{V_{s2}\rho_2 + V_{s1}\rho_1} \qquad 3\text{-}5$$

where the subscripts denote the layer, i.e. 1 is the upper layer, and 2 is the lower layer..

At non-normal incidence angles the reflection coefficient for plane elastic waves as a function of incidence angle at a single interface is described by the Zoeppritz (1919) equations. The magnitude of the transmission and reflection coefficients depends on the incidence angle and the properties of the two layers. At non-normal incidence mode conversions occur with an incident P-wave generating both reflected and transmitted P and S-waves. In this thesis changes in incidence angles are explored rather than offset, but this analysis is usually called Amplitude Variation with Offset (AVO) rather than Amplitude Variation with Angle (AVA). For a full discussion of AVO theory and history see Castagna et al (1998).

The Zoeppritz equations are included in Appendix A with verification of the modelling, via comparison with results from the CREWES Zoeppritz Explorer (Margrave 2003). These equations are difficult to apply directly; therefore approximations are commonly used to aid interpretation and provide hysical insight. There are a number of approximations here the three-term approximation was used (Aki and Richards 1980; Shuey 1985). It describes the reflection coefficient (R_{pp}) as a function of incidence angle (θ):

$$R_{pp}(\theta) = A + B\sin^2\theta + C(\tan^2\theta - \sin^2\theta) \quad 3\text{-}6$$

where

$$A = \frac{1}{2}\left(\frac{\Delta V_p}{V_p} + \frac{\Delta\rho}{\rho}\right) \quad 3\text{-}7$$

$$B = \frac{1}{2}\frac{\Delta V_p}{V_p} - 2\frac{V_s^2}{V_p^2}\left(\frac{2\Delta V_s}{V_s} + \frac{\Delta\rho}{\rho}\right) \quad 3\text{-}8$$

$$C = \frac{1}{2}\frac{\Delta V_p}{V_p} \quad 3\text{-}9$$

where

$$\Delta\rho = \rho_2 - \rho_1 \qquad \rho = \frac{1}{2}(\rho_2 - \rho_1) \quad 3\text{-}10$$

$$\Delta V_p = V_{p_2} - V_{p_1} \qquad V_p = \frac{1}{2}(V_{p_2} - V_{p_1}) \quad 3\text{-}11$$

$$\Delta V_s = V_{s_2} - V_{s_1} \qquad V_s = \frac{1}{2}(V_{s_2} - V_{s_1}) \quad 3\text{-}12$$

where $\theta=(\theta_1+\theta_2)/2 \approx \theta_1$, θ_1 is the incidence angle and θ_2 is the transmission angle.

The approximation shown above is particularly useful as it can be interpreted in terms of different angular ranges: *A* is the zero-offset reflectivity or AVO intercept, *B* describes the AVO gradient and dictates the response at intermediate angles, and *C* is the curvature and dominates at large offsets close to the critical angle. The Zoeppritz equations predict the angle-dependent reflectivity for the full angular range, but the

three-term approximation is only valid for angles up to 30-40°. It can be further approximated by ignoring the third term and just fitting the data using the intercept and the gradient. This is typically valid for angles of less than 30˚. As AVO data is commonly only available for angles below 30-40˚ (Avseth et al. 2005), these approximations are normally adequate. To demonstrate the limitations of these approximations, they are compared to the exact angle-dependent reflectivity generated using the Zoeppritz equations in Figure 3-2 using the values in Table 3-1. The angle-dependent reflectivity can be approximated using the two-term approximation out to about 30°, and the three-term approximation fits the response out to 60°. This may not be true if there is a greater velocity contrast across the interface.

Table 3-1 Velocities and densities used to predict the AVO response.

V_{p1} (m/s)	V_{p2} (m/s)	ρ_1 (kg/m^3)	ρ_2 (kg/m^3)	V_{s1} (m/s)	V_{s2} (m/s)
2646.9	2627.66	2248.5	2110.7	1316.2	1421.7

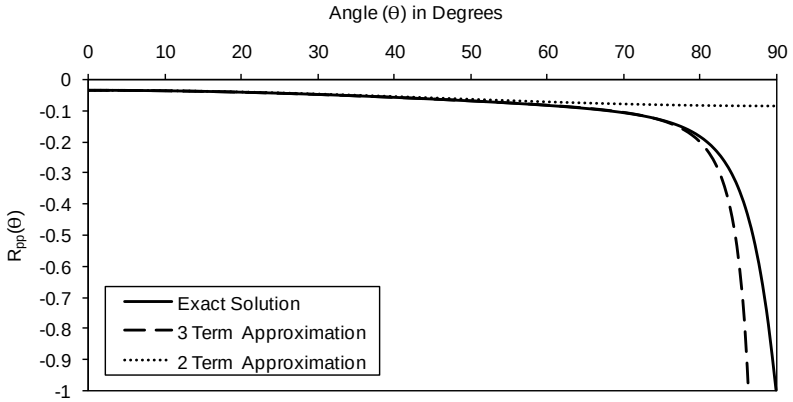


Figure 3-2 Angle dependent P-wave reflection coefficient (Rpp(θ)) plotted against angle (θ). Reflectivity generated using: solid line: Zoepprit, dashed line: "three-term" approximation, dotted line: "two-term" approximation.

Cross-plotting of the *A* and *B* terms is often used to help discriminate fluid content, lithology and other reservoir properties (Castagna et al. 1998). Reservoir sands can be classified by their intercept and gradient (Figure 3-3). If the sandstone or shale is brine filled then it tends to fall along the background trend, but deviations below this trend could be indicative of a top gas-sand reflection. The class of the gas-sand reflection depends on the P-wave impedance contrast across the interface which generated the reflection.

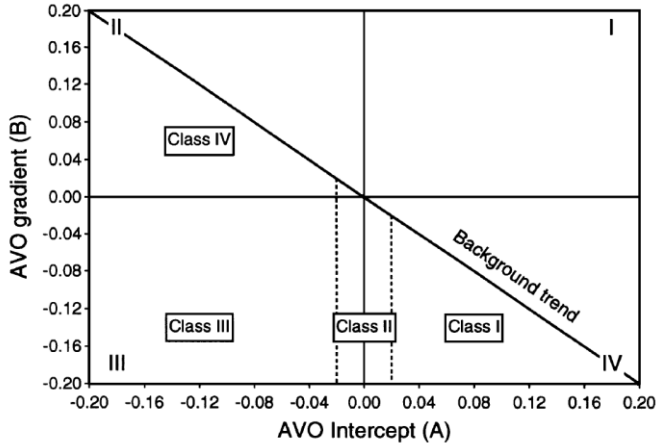


Figure 3-3 AVO intercept (A) versus gradient (B) showing four quadrants. Brine-saturated sandstones and shales tend to fall along the background trend, whilst top gas-sand reflectors tend to fall below this trend and base-sand reflectors fall above the line (Castagna et al. 1998).

The final product of seismic processing is a stack, such as one shown in Figure 2-23. Stacking combines the reflectivity at a range of offsets to increase the signal to noise ratio. This stacking may disguise some of information which can be gained from the AVO analysis above. To account for this different ranges of angular data can be combined into near, mid and far offset stacks. Here the focus is on pre-stack data. The zero-offset response is calculated rather than the near offset response, which also contains energy from non-normal incidence angles. This is an approximation, but in general the zero-offset and near-offset responses should be similar.

3.2.3 Attenuation

Sections 2.4.2.2.2 and 2.4.2.3 gave an overview of attenuation mechanisms. The amount of attenuation induced by a specific material is described by the quality factor (Q), with a low value of Q indicating high dissipation of energy and hence attenuation. $1/Q$ is a measure of the fractional loss of energy per cycle of oscillation (Mavko et al. 1998). One way of defining Q uses the P-wave modulus (M), which is the ratio of the stress and strain at a particular point. In viscoelastic materials the stress and strain may be out of phase with each other, which is then described by a complex P-wave modulus. This can be used to express Q, as the inverse of the ratio of the imaginary and complex parts of M:

$$\frac{1}{Q} = \frac{M_I}{M_R} \qquad 3\text{-}13$$

Patchy saturation is the most likely cause of attenuation at the seismic frequencies under examination here (Muller and Gurevich 2005). Attenuation has been recorded within the laboratory and on the well scale (Hauge 1981). Recording attenuation is challenging and requires good data quality. There are a variety of approaches for extracting attenuation information in the field (Quan and Harris 1997). Spectral decomposition, which decomposes a seismic trace into its constituent frequency components can be used (Partyka et al. 1999). However a major problem with the use of attenuation is that it is difficult to reliably estimate from seismic data (Chopra et al. 2004) and at these typical seismic frequencies the amount of attenuation is very small.

3.2.4 Seismic Reflection Modelling

Following the prediction of the seismic velocities and densities of the overburden and reservoir, synthetic seismograms are generated. The process used to generate a synthetic is shown in Figure 3-4, where a reflectivity logs is convolved with a wavelet to generate the synthetic. Here this process is performed using CREWES open source seismic modelling software (Margrave 2003), which is a series of numerical algorithms in MATLAB. There are a range of methods to generate a synthetic, here the seismic velocities and density are input as pseudo well log to generate a 1D synthetic seismogram. A number of 1D synthetic seismograms are then generated all along a 2D slice through the reservoir and when shown together they provide a 2D representation of the normal incidence seismic response. The model used was appropriate for a normal incidence reflection, with no multiple reflections generated. A further description of how the reservoir simulation results were incorporated is given in Section 3.8.1..A zero-phase 40Hz Ricker wavelet with a temporal sampling rate of 2.5ms was used unless otherwise indicated (Figure 3-5), and the SEG normal polarity was used.

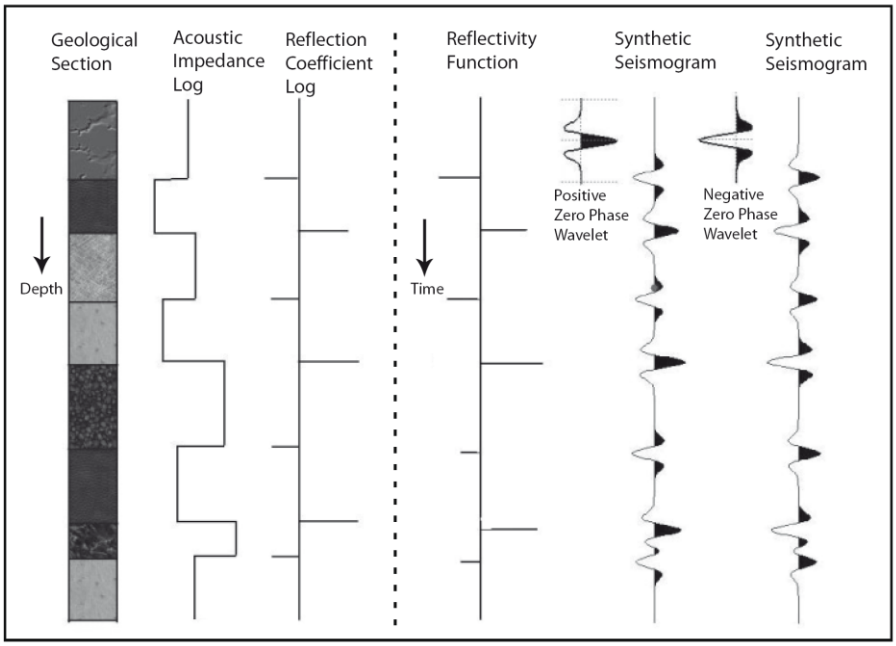


Figure 3-4 Creation of a synthetic seismogram from an acoustic impedance log recorded in depth (Kazemeini 2009).

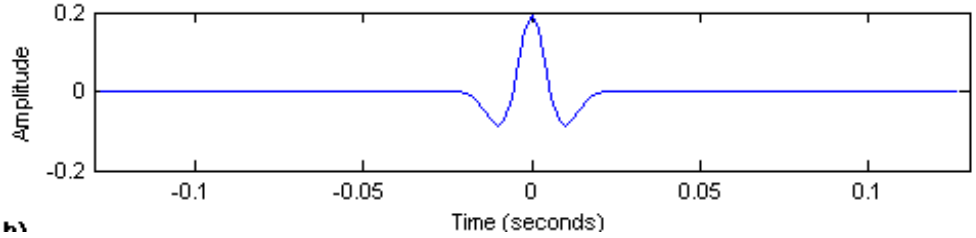


Figure 3-5 40Hz zero-phase Ricker wavelet.

3.3 Rock Physics Modelling

Rock physics modelling relates the dynamic changes in the reservoir to the time-lapse seismic response, as discussed in Section 2.4.2.2. In this Section the rock physics models used in this thesis are explained. First the equations used to calculate the properties of the solid portion of the reservoir, i.e. the mineral moduli (Section 3.3.1) and grain framework moduli (Section 3.3.2) are given. The fluid properties are discussed in Section 3.4. The elastic properties of a saturated porous medium depends on the properties of the fluid, grain and grain framework moduli. When the pore space is saturated with only one fluid phase then the elastic properties of the saturated porous medium can be predicted using the Gassmann (1951) equation. However when the pore space contains two or more fluid phases then there are different approaches to combine the fluid properties depending on the relationship between the critical length scale (Equation 2-10) and the size of the fluid patches (Section 3.3.3), as discussed in Sections 2.4.2.2.2 and 2.5.5. If the fluids are well mixed below the critical length scale, then the rock and fluid properties can be combined using the Gassmann (1951) equations (Section 3.3.3.1). However if fluids are unmixed on length scales above the critical length scale then the Hill (1963) average is used (Section 3.3.3.2.1). The attenuation and velocity dispersion resulting from this mesoscopic patchy saturation is predicted using the White (1975) equations (Section 3.3.3.2.2).

3.3.1 Grain Modulus

The grain bulk modulus (K_{grain}) and shear modulus (μ_{grain}) are calculated using the Hashin-Shtrikman bounds (Hashin and Shtrikman 1963). These bounds estimate the maximum and minimum elastic grain moduli for a specific mineral composition. They predict the narrowest possible range of elastic moduli for an isotropic mixture, without specifying anything about the geometries of the constituents (Mavko et al. 1998). Physically speaking the upper bound (K^{HS+}) is realised when the stiffer materials forms the shell and the lower bound (K^{HS-}) when it is in the core. The bounds are valid for two mineral phases, but a more general form has been developed (Berryman 1995):

$$K^{HS+} = \Lambda(\mu_{\max}), K^{HS+} = \Lambda(\mu_{\min}) \quad 3\text{-}14$$

$$\mu^{HS+} = \Gamma(\xi(K_{\max}, \mu_{\max})), \mu^{HS+} = \Gamma(\xi(K_{\min}, \mu_{\min})) \quad 3\text{-}15$$

where

$$\Lambda(z) = \left(\left\langle \frac{1}{K(r) + \frac{4z}{3}} \right\rangle \right)^{-1} - \frac{4}{3} z \quad 3\text{-}16$$

$$\Gamma(z) = \left\langle \frac{1}{\mu(r) + z} \right\rangle^{-1} - z \qquad 3\text{-}17$$

$$\xi(K, \mu) = \frac{\mu}{6}\left(\frac{9K + 8\mu}{K + 2\mu} \right) \qquad 3\text{-}18$$

Where K and μ refer to the bulk and shear moduli of the mineral constituents (Table 3-2), and the angular brackets represent a volume-fraction weighted average. As many effective-medium models, including Gassmann (1951) assumes a homogeneous mineral modulus, the mixed mineralogy is represented by an "average" mineral modulus (K_{grain} and μ_{grain}). Here there is no information regarding the geometry of the mineral constituents, so an average of the upper and lower bounds is used:

$$K_{grain} = \frac{K^{HS+} + K^{HS-}}{2} \qquad 3\text{-}19$$

$$\mu_{grain} = \frac{\mu^{HS+} + \mu^{HS-}}{2} \qquad 3\text{-}20$$

Table 3-2 The elastic moduli and densities of select minerals. K: Bulk modulus, μ: shear modulus and ρ: density.

Mineral	***K* (GPa)**	***μ* (GPa)**	***ρ* (kg/m^3)**
Quartz	37	44	2650
Average Feldspar	37.5	25.6	2620
Average Clay	25	9	2550
Muscovite	61.5	41.1	2790
Calcite	76.8	32	2650
Illite	39.5	11.7	2780
Pyrite	147.4	132.5	3550

3.3.2 Grain Framework Moduli

Two different models were used to predict the grain framework moduli. Firstly the Walton model (Walton 1987) was used for the Utsira sand, whose particularly weak frame resulted in a very high sensitivity to changes in fluid content. This replicated work performed by McKenna et al (2003). To test the sensitivity of a "stiffer" sandstone, the friable-sand model (Dvorkin and Nur 1996), which is appropriate for a sandstone was used for the generic reservoir. This model is stiffer than the Walton model, as small amounts of mineral cement have been added to the contacts of the spherical grains. The grain framework properties vary with pore pressure, and may be affected by pressure build-up.

The friable-sand model uses a "well-sorted" end-member, with a critical porosity (Φ_c :40%). The elastic properties of this end-member are calculated using Hertz-Mindlin theory (Mindlin, 1949) and are

then modified by the addition of grains in the pore space which deteriorates sorting and slightly increases the stiffness of the pore space (Avseth et al. 2005). The bulk (K_{HM}) and shear moduli (μ_{HM}) of the dry well-sorted end-member at the critical porosity is modelled as an elastic sphere pack subject to a effective pressure (P_{eff}), given by Hertz-Mindlin theory:

$$K_{HM} = \left[\frac{n^2 (1-\Phi_c)^2 \mu_{grain}^{\ 2}}{18\pi^2 (1-\nu_{grain})^2} P_{eff} \right]^{\frac{1}{3}} \quad 3\text{-}21$$

$$\mu_{HM} = \frac{5-4\nu_{grain}}{5(2-\nu_{grain})} \left[\frac{3n^2 (1-\Phi_c)\mu_{grain}^{\ 2}}{2\pi^2 (1-\nu_{grain}^{\ 2})^2} P_{eff} \right]^{\frac{1}{3}} \quad 3\text{-}22$$

where μ_{grain} and ν_{grain} are the shear and Poisson's ratio of the solid phase and n is the coordination number. The effective pressure is the difference between the lithostatic pressure and the pore pressure. Poisson's ratio is given in terms of the grain bulk modulus (K_{grain}) and shear modulus (μ_{grain}):

$$\nu_{grain} = \frac{3K_{grain} - 2\mu_{grain}}{2(3K_{grain} + \mu_{grain})} \quad 3\text{-}23$$

The coordination number represents the average number of contacts per grain and can be estimated from the porosity using the empirical relationship (Murphy 1982):

$$n = 20 - 34\Phi + 14\Phi^2 \quad 3\text{-}24$$

The high porosity end-member is then modified and the grain framework bulk modulus (K_{dry}) and grain framework shear modulus (μ_{dry}) are given by:

$$K_{dry} = \left[\frac{\Phi/\Phi_c}{K_{HM} + z} + \frac{1-\Phi/\Phi_c}{K + \frac{4}{3}\mu_{HM}} \right]^{-1} - \frac{4}{3}\mu_{HM} \quad 3\text{-}25$$

$$\mu_{dry} = \left[\frac{\Phi/\Phi_c}{\mu_{HM} + z} + \frac{1-\Phi/\Phi_c}{\mu + z} \right]^{-1} - z \quad 3\text{-}26$$

$$z = \frac{\mu_{HM}}{6} \left(\frac{9K_{HM} + 8\mu_{HM}}{K_{HM} + 2\mu_{HM}} \right) \quad 3\text{-}27$$

Shale properties are calculated using the constant clay model for sandy shales, this is similar to the friable-sand model, however the values for Φ_c are much higher for shale (65%), due to the "card-stack" arrangements of clay platelet.

Equations 3-21 and 3-22 demonstrate that the strength of the grain framework depends on the pressure in the reservoir.

3.3.3 Fluid Substitution

3.3.3.1 Homogeneous distribution

As discussed in Section 2.4.2.2.2, if multiple fluids are very finely mixed below L_c (Equation 2-10) then the Gassmann (1951) fluid substitution equation is used to describe the saturated bulk modulus (K_{sat}) and shear modulus (μ_{sat}) at low (<100 Hz) frequencies:

$$K_{sat} = K_{dry} + \frac{\left(1 - \frac{K_{dry}}{K_{grain}}\right)^2}{\frac{\Phi}{K_{fluid}} + \frac{1-\Phi}{K_{grain}} - \frac{K_{dry}}{K_{grain}^2}} \quad 3\text{-}28$$

$$\mu_{sat} = \mu_{dry} \quad 3\text{-}29$$

where K_{fluid} is the fluid bulk moduli. The shear modulus is mechanically independent of the presence of the fluid. An implicit assumption is that there is no chemical interaction between the porous rock. For an overview of the origins of the Gassmann equation see Berrymann (1999).

K_{fluid} is calculated using the Reuss average (Mavko et al. 1998):

$$\frac{1}{K_{fluid}} = \Sigma \frac{S_i}{K_i} \quad 3\text{-}30$$

where K_i denotes the bulk modulus of the individual gas and fluid phases and S_i represents their saturations.

3.3.3.2 Patchy Saturation

When the fluid ganglia dimensions are greater than L_c, they are described patchy. There are different approaches which can be used to predict the effect of patchy saturation on the seismic velocity, here the Hill average, Voigt average and White model are discussed. An empirical mixing equation is also mentioned as a way of fitting an intermediate response (Brie et al. 1995).

3.3.3.2.1 Hill and Voigt Models

If both fluid phases do not equilibrate during the seismic period then the bulk modulus is predicted using the Hill average (Hill 1963). This model is appropriate for regions with the same shear modulus (μ), but different a bulk modulus (K), i.e. for regions saturated with different fluids. The effective bulk modulus (K_{sat}) is given by (Mavko et al. 1998):

$$K_{sat} = \left\langle \frac{1}{K + \frac{4}{3}\mu} \right\rangle^{-1} - \frac{4}{3}\mu \qquad 3\text{-}31$$

This shows that the effective moduli of a composite with uniform shear modulus can be predicted exactly by only knowing the volume fractions of the constituents without knowledge of the constituent geometries. This approach predicts a quasi-linear relationship between V_p and saturation.

Equation 3-31 can be modified through the addition of limits to the range of possible saturations (Sengupta and Mavko 2003). In a saline aquifer the saturated bulk modulus (K_{sat}) is given by:

$$\frac{1}{K_{sat} + 4/3\mu_{sat}} = \frac{S^1_{CO2}}{K^1_{satCO2} + 4/3\mu_{satCO2}} + \frac{S^1_{brine}}{K^1{}_{satbrine} + 4/3\mu_{satbrine}} \qquad 3\text{-}32$$

Constraints on the range of potential saturations depend on the relative permeability and capillary pressure curves in the reservoir, and are the residual gas saturation (S_{gr}) and the connate water saturation (S_{cw}):

$$S^1{}_{CO2} = \frac{S_{CO2} - S_{rg}}{1 - S_{cw} - S_{rg}} \qquad 3\text{-}33$$

$$S^1{}_{brine} = \frac{S_{brine} - S_{cw}}{1 - S_{cw} - S_{rg}} \qquad 3\text{-}34$$

$$\frac{1}{K'_{satco2}} = \frac{S_{cw}}{K_{satbrine}} + \frac{1 - S_{cw}}{K_{satco2}} \qquad 3\text{-}35$$

$$\frac{1}{K'_{brine}} = \frac{1 - S_{rg}}{K_{satbrine}} + \frac{S_{rg}}{K_{satco2}} \qquad 3\text{-}36$$

where S_{brine} and S_{CO2} are the brine and CO_2 saturation and $K_{satbrine}$ and K_{satco2} refer to the bulk moduli of regions saturated with brine and CO_2 respectively calculated using the Gassmann equations.

An approximation to the patchy-saturation upper bound can be obtained using the Voigt isostrain average to predict the fluid modulus (Mavko et al. 1998):

$$K_{fluid} = \sum S_i K_i \qquad 3\text{-}37$$

Intermediate saturations can be fitted using the empirical Brie (1995) mixing equation:

$$K_{fluid} = (K_{liquid} - K_{gas})(1 - S_{gas})^e + K_{gas} \qquad 3\text{-}38$$

where K_{liquid} is the liquid bulk modulus, K_{gas} is the gas bulk modulus, S_{gas} is the gas saturation and e is an empirical coefficient. K_{fluid} predicted using the Voigt and Brie models are directly input into the Gassmann equation.

The Reuss average represents the weakest way that the fluids can mix and provides a lower bound, whereas the Voigt average represents the stiffest way fluids can be mixed and provides the upper bound. In contrast to the Reuss average which describes a number of real physical systems, real isotropic mixtures can never be as stiff as the Voigt bound (Mavko et al. 1998), and the Hill model is preferable for the upper bound.

The predicted saturated bulk modulus is plotted against CO_2 saturation for the models described here in Figure 3-6. The range of possible values lies between the Reuss lower bound and Hill upper bound. The saturation constrains on the Hill average significantly decrease the potential range of the saturated bulk modulus at a specific saturation.

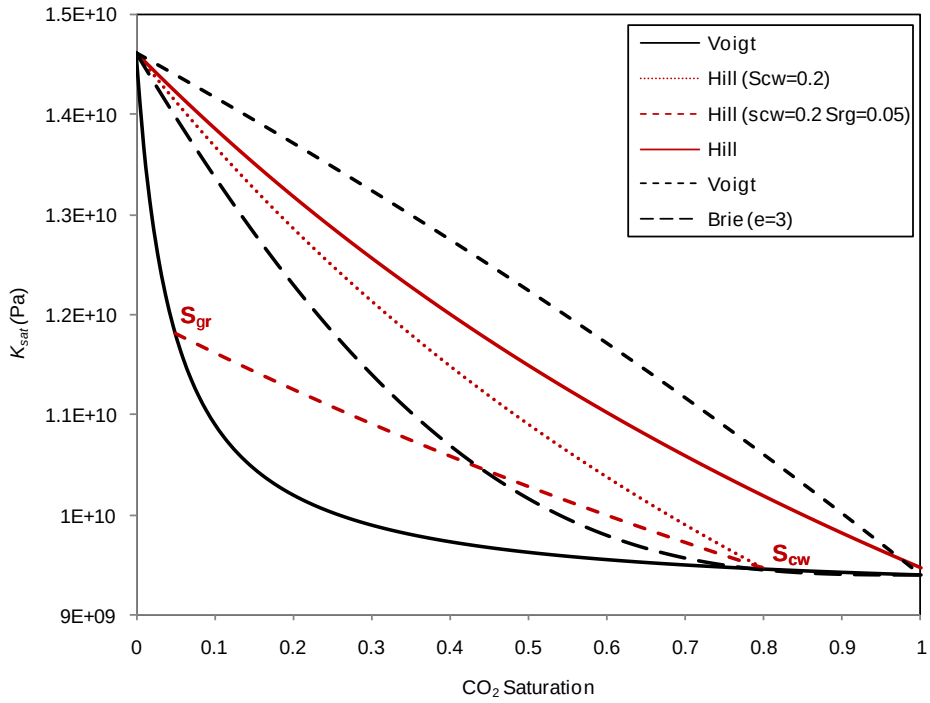


Figure 3-6 Relationship between the saturated bulk modulus and CO_2 saturation, calculated using models in 3.3.3, assuming a residual gas saturation (S_{rg}) of 5% and a connate water saturation (S_{cw}) of 20%.

3.3.3.2.2 White Modelling

White (1975) modelled the effects of mesoscopic patchy saturation by considering porous rocks saturated with brine, but containing spherical gas-filled regions. The idealised shape is a unit cell consisting of a gas-filled sphere of radius *a* within a brine filled sphere of outer radius *b*, (*b*>*a*), where the adjacent cells do not interact. The gas saturation (S_{gas}) is given by $S_{gas}=a^3/b^3$. The complex bulk modulus K* for porous rocks containing multiple fluid phases as a function of angular frequency ω is given by (Mavko et al. 1998):

$$K^* = \frac{K_\infty}{1 - K_\infty W} = K_r^* + iK_i^* \quad 3\text{-}39$$

$$W = \frac{3a(R_1 - R_2)(-Q_1 + Q_2)}{b^3 i\omega(\ Z_1 + Z_2)} \quad 3\text{-}40$$

$$R_1 = \frac{K_{sat1} - K_{dry}}{1 - K_{dry}/K_{grain}} \frac{3K_{sat2} + 4\mu}{K_2(3K_{sat1} + 4\mu(K_{sat1} - K_{sat2})S_{gas}} \quad 3\text{-}41$$

$$R_2 = \frac{K_2 - K_{dry}}{1 - K_{dry}/K_{grain}} \frac{3K_{sat1} + 4\mu}{K_2(3K_{sat1} + 4\mu) + 4\mu(K_{sat1} - K_{sat2})S_{gas}} \quad 3\text{-}42$$

$$Z_1 = \frac{\eta_1 a}{\kappa_1}\left[\frac{1 - e^{-2\gamma_1 a}}{(\gamma_1 a - 1) + (\gamma_1 a + 1)e^{-2\gamma_1 a}}\right] \quad 3\text{-}43$$

$$Z_2 = -\frac{\eta_2 a}{\kappa_2}\left[\frac{(\gamma_2 b + 1) + (\gamma_2 b - 1)e^{2\gamma_2(b-a)}}{(\gamma_2 b + 1)(\gamma_2 a - 1) - (\gamma_2 b - 1)(\gamma_2 a + 1)e^{2\gamma_2(b-a)}}\right] \quad 3\text{-}44$$

$$\gamma_j = \sqrt{\frac{i\omega\eta_j}{\kappa K_{EJ}}} \quad 3\text{-}45$$

$$K_{EJ} = \left[1 - \frac{K_{fluidJ}(1 - K_{satj}/K_{grain})(1 - K_{dry}/K_{grain})}{\phi K_{satJ}\left(1 - \frac{K_{fluidJ}}{K_{grain}}\right)}\right] K_{AJ} \quad 3\text{-}46$$

$$K_{AJ} = \left[\frac{\Phi}{K_{fluidJ}} + \frac{1 - \Phi}{K_{grain}} - \frac{K_{dry}}{K_{grain}^2}\right]^{-1} \quad 3\text{-}47$$

The subscripts *j*=1 or 2, denotes the different regions brine and CO_2 filled respectively; η and K_{fluid} are the fluid viscosity and bulk modulus; Φ is the porosity; κ is the permeability; K_{dry} and K_{grain} are the grain framework bulk modulus and grain bulk modulus respectively. The saturated bulk moduli K_{sat} and μ_{sat}, of the regions saturated with brine and CO_2 are obtained using the Gassmann (1951) equations (Equations 3-28 and 3-29).

At the high frequency limit when there is no fluid-flow across the interface between regions 1 and 2, the bulk modulus is given by:

$$K_{\infty}(no-flow) = \frac{K_2(3K_{sat1} + 4\mu) + 4\mu\ (K_{sat1} - K_{sat2})S_{gas}}{(3K_{sat1} + 4\mu) - 3(K_{sat1} - K_{sat2})S_{gas}} \quad 3\text{-}48$$

The complex P-wave velocity is predicted using the complex bulk modulus (K^*):

$$V_C = \sqrt{\frac{K^* + \frac{4}{3}\mu_{dry}}{\rho}} \quad 3\text{-}49$$

The quality factor (Q) is then be calculated (Carcione et al. 2003):

$$Q = \frac{(v_C)_R}{(v_C)_I} \quad 3\text{-}50$$

The subscripts denote the real and imaginary part of the complex P-wave velocity. The code implementing this model has been verified through comparison with published results (Carcione et al. 2003), see Appendix B.

3.4 Acoustic Properties of Reservoir Fluids

The Gassmann, Hill and White models demonstrate the dependence of the elastic moduli of the saturated porous media on the fluid's elastic properties. Fluid properties vary with temperature and pressure. At a saline sequestration site the possible pore fluids are brine, CO_2 and brine saturated with CO_2

3.4.1 Brine Properties

Brine properties are usually calculated using the Batzle-Wang equations (Batzle and Wang, 1992), whose relationships were produced using a combination of thermodynamic relationships, empirical trends and published data. The equations predict how brine properties vary with temperature (T in °C), pore pressure (P_P in MPa) and salinity (S in fractions of 1). The density of brine (ρ_B) in g/cm^{3}is given by:

$$\rho_B = \rho_w + S\{0.668 + 0.44S + 10^{-6}[300P_P - 2400P_PS + T(80 + 3T - 3300S - 13P_P + 47P_PS)]\} \quad 3\text{-}51$$

where the density of pure water (ρ_w) in g/cm^3 is

$$\rho_w = 1 + 10^{-6}(-80T - 3.3T^2 + 0.00175T^3 + 489P_P - 2TP_P + 0.016T^2P_P + 0.016T^2P_P \quad 3\text{-}52$$
$$-1.3\times10^{-5}T^3P_P - 0.333{P_P}^2 - 0.002T{P_P}^2)$$

The velocity of brine (V_B) in m/s is:

$$V_B = V_W + S(1170 - 9.6T + 0.055T^2 - 8.5\times10^{-5}T^3 + 2.6P_P - 0.0029TP_P \quad 3\text{-}53$$
$$-0.0476{P_P}^2) + S^{\frac{3}{2}}(780 - 10P_P + 0.16{P_P}^2) - 1820S^2$$

where the velocity of pure water (V_W) in m/s is:

$$V_W = \sum_{i=0}^{4}\sum_{j=0}^{3} W_{ij}T^i{P_P}^i \quad 3\text{-}54$$

The coefficients for W_{ij} are:

W_{00} =1402.85	W_{10}=4.871	W_{20}=-0.04783	W_{30}=1.487 x10^{-4}	W_{40}=-2.197 x 10^{-7}
W_{01}= 1.524	W_{11} = -0.0111	W_{21}= 2.747 x 10^{-4}	W_{31}=-6.503 x 10^{-7}	W_{41}=7.987 x 10^{-10}
W_{02} = 3.437 10^{-3}	W_{12} =1.739 x 10^{-4}	W_{22} = -2.135 x 10^{-6}	W_{32} = -1.455 x 10^{-8}	W_{42} =5.230 x 10^{-11}
W_{03} =-1.197 x 10	W_{13} =-1.628 x 10^{-6}	W_{23} = 1.237 x 10^{-8}	W_{33} = 1.327 x 10-^{10}	W_{43} = -4.614 x 10^{-13}

Using the velocity and the density the brine bulk modulus can be calculated:

$$K_B = \rho_B V_B^2 \quad 3\text{-}55$$

The viscosity (η) is given by:

$$\eta = 0.1 + 0.333S + (1.65 + 91.9S^3)\exp^{\{-[0.42(S^{0.8}-0.17)^2+0.045]T^{0.8}\}} \quad 3\text{-}56$$

For the range of temperatures and pressures likely to be encountered within a reservoir between 500 and 2500 m depth, the properties of brine (salinity 0.22) are predicted as per Figure 3-7.

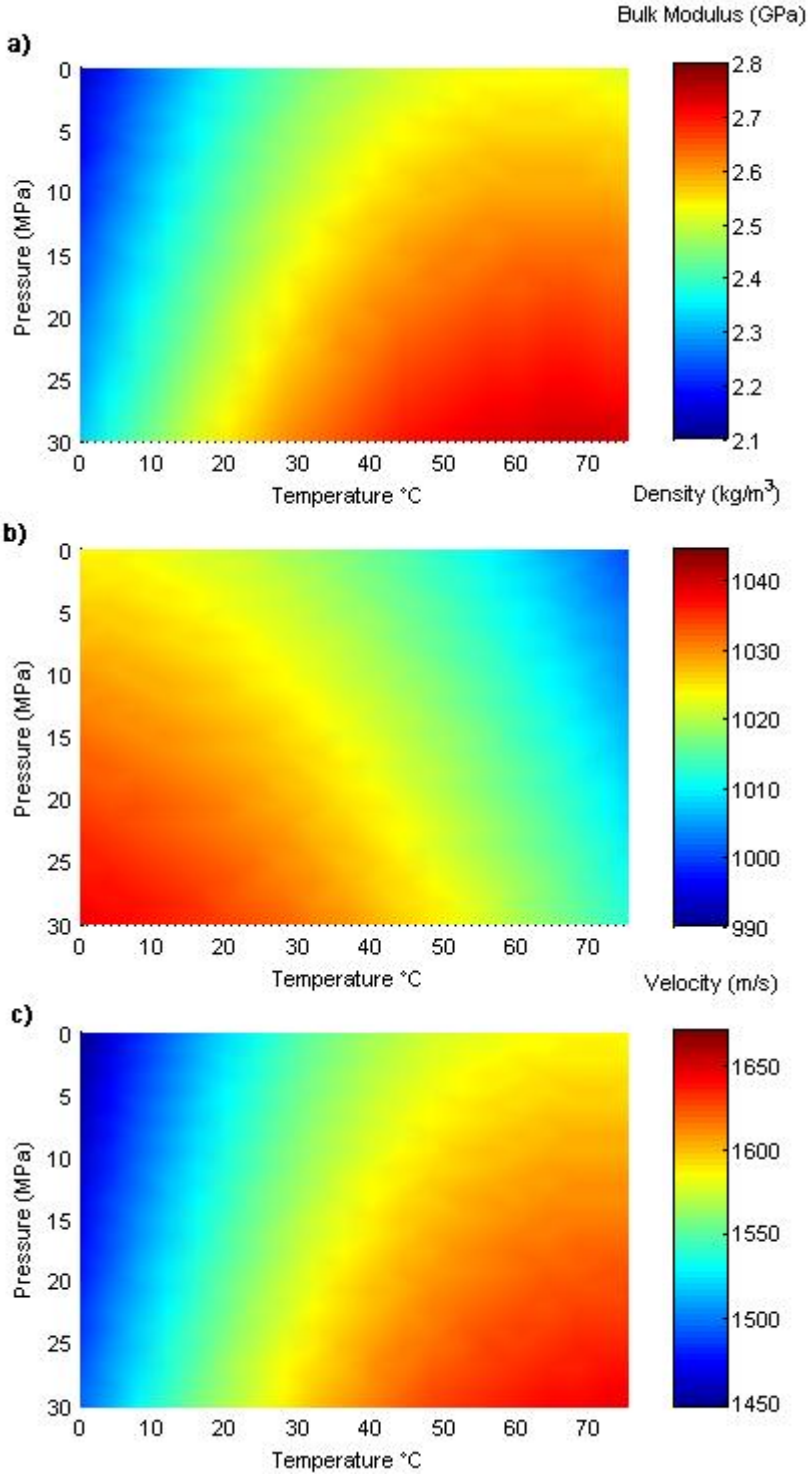


Figure 3-7 Brine properties within the temperature ranges 0-75°C and the pressure range 0-30 MPa: a) Bulk Modulus in GPa, b) Density in kg/m^3 and c) Velocity in m/s.

3.4.2 CO_2 Properties

Predicting the properties of CO_2 is complex, due to the phase behaviour (Section 2.3.1.1). Below the critical point (P_P:7.38MPa and T=31.1°C) CO_2 is thermodynamically a gas, but at higher temperatures and pressures CO_2 behaves as a supercritical fluid. A number of models have been formulated to predict the impact of this transition on the properties (Batzle and Wang 1992; Han et al. 2010; Peng and Robinson 1976; Span and Wagner 1996; Xu 2006). The numerical models are constrained by experimental data (Han et al. 2010; Wang and Nur 1989).

There is uncertainty as to which model is appropriate when examining monitoring. Look-up tables have been used (Brown et al. 2002; Kumar et al. 2008; Wang 2001; Yuh 2003), full equations of state (EOS) by others (Chadwick et al. 2005; Ghaderi and Landrø 2009; Meadows 2008) and either the Batzle-Wang equations (Sodagar and Lawton 2011) or modified Batzle-Wang equations (Xu 2006) by others (Ma and Morozov 2010). The difficulty in implementing these approaches varies significantly.

The Span and Wagner EOS (Span and Wagner 1996) has been shown to give a good fit to experimental data (Han et al. 2010). To determine whether a simpler approach using the Batzle-Wang equations or the modified Batzle-Wang equations could be used instead, their results were compared to those taken from the National Institute of Standards in Technology database (NIST 2011), which were calculated using the Span and Wagner EOS. The comparison at a constant temperature and varying pressure is shown in Figure 3-8 replicating a plot from Ma and Morozov (2010) and Xu (2006). The Xu approximation is better than Batzle-Wang at predicting CO_2 properties. Using realistic temperature and pressure gradients from the equations in Section 3.5, the difference between the models is shown in terms of reservoir depth (Figure 3-8d-f). The Batzle-Wang equations are poor at predicting any of the properties throughout the depth range. The Xu approximation is significantly better, however near the critical point (~800 m) its predictions diverge from the exact result.

From this analysis, the NIST data calculated using the Span and Wagner EOS is used throughout this these. Figure 3-9 shows the prediction of the CO_2 properties within the entire depth range (500-3000m).

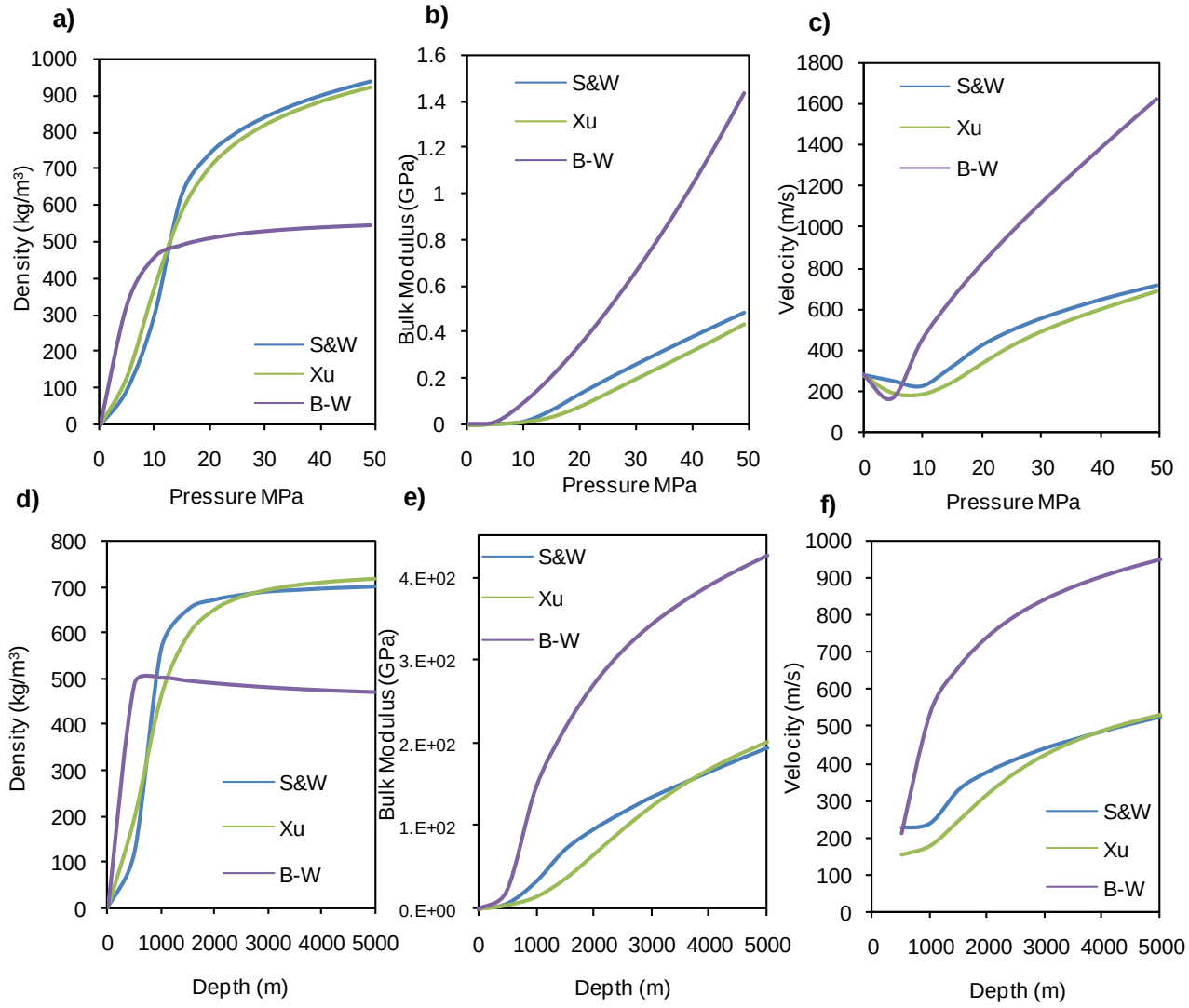


Figure 3-8 CO_2 properties: a and d) Density, b and e) Bulk modulus and c and f) Velocity, predicted using: Span and Wagner equation of state (S&W), Batzle-Wang equations (B-W) and the Xu approximation to the Batzle-Wang equations (Xu).a-c) for a constant temperature of 57˚, d-e) for reservoir depths.

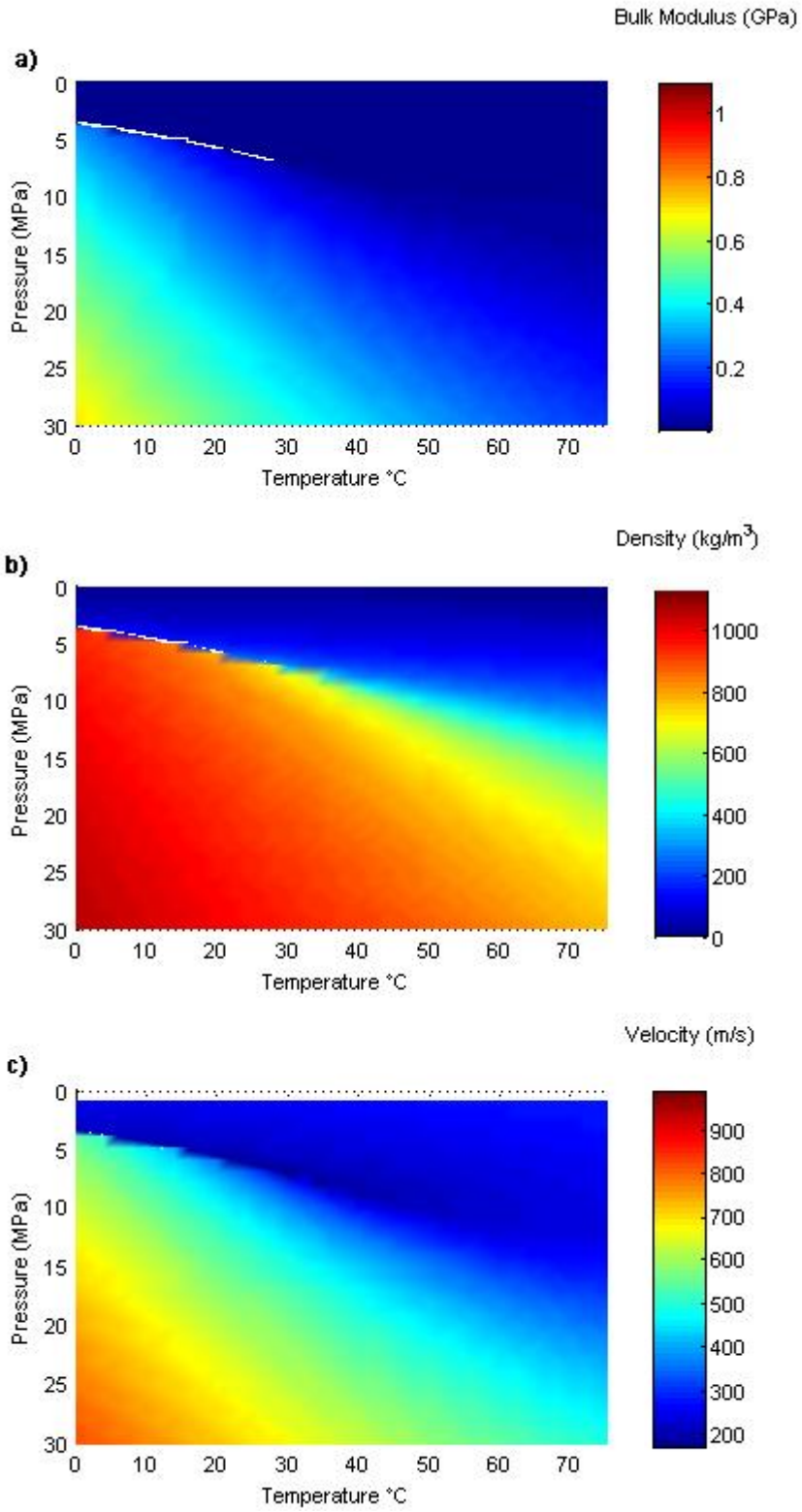


Figure 3-9 CO_2 properties plotted between 0-75˚C and 0-30 MPa. a) Bulk Modulus (GPa), b) Density (kg/m^3), c) Velocity (m/s) (NIST 2011).

3.4.3 Brine Saturated with CO_2

The dissolution of CO_2 into brine is an important trapping mechanism in saline aquifers as discussed in Section Physical Processes and Trapping Mechanisms2.3.3. Experimental work has determined the impact of CO_2 dissolution on the fluid properties (Hebach et al. 2004; Osif 1988; Sun and Han 2009; Vanorio et al. 2010). Modelling CO_2 dissolution is complex as it requires both the solubility at different temperatures and pressures and the elastic properties of brine with CO_2 in solution. Here the literature and experimental data on dissolution is discussed to determine the best method to use.

CO_2 Solubility

Extensive experimental work has been performed to establish CO_2 solubility at a range of temperatures and pressures. Duan and Sun (2003) developed a model which predicts CO_2 solubility in pure water and aqueous NaCl solutions and matches experimental data within or close to experimental uncertainty. Some previous seismic modelling approaches (Carcione et al. 2006) have also used models appropriate for methane, although the solubility of CO_2 in brine has been shown to be much greater than that of methane at certain temperatures and pressures (Sun and Han 2009).

Elastic Properties of Brine Saturated with CO_2

The impact of CO_2 dissolution on the compressibility and density of brine at different temperatures, pressures and compositions (P-T-X) has been quantified using experimental data (Hebach et al. 2004; Liu 1998; Osif 1988; Sun and Han 2009; Vanorio et al. 2010). Hebach et al (2004) compiled and fitted data on the density of brine saturated with CO_2. In its gaseous phase (CO_2 density less than 468 kg/m^3) the density of CO_2 saturated brine (ρ_{wc}) at certain temperatures (T in K) and pressures (P_P in Mpa) is given by:

$$\rho_{wc} = g_0 + g_1 P_P + g_2 T + g_3 {P_P}^2 + g_4 T^2 + g_5 P_P T + g_6 {P_P}^3 + g_7 T^2 P_P + g_8 T {P_P}^2 \qquad 3\text{-}57$$

whereas in its compressed vapour or liquid form (CO_2 density more than 468kg/m^3) ρ_{wc} is calculated using:

$$\rho_{wc} = I_0 + I_1 P_P + I_2 T + I_3 {P_P}^2 + I_4 T^2 \qquad 3\text{-}58$$

The coefficients are given in Table 3-3.

Table 3-3 Coefficients used to calculate the density of brine saturated with CO_2

I_0=949.7109	I_2=0.883148	I_4=-0.00228	g_1=44.12685	g_3=-1.45073	g_5=-0.19658	g_7=0.000209
I_1=0.559686	I_3=-0.00097	g_0=805.1653	g_2=1.573145	g_4=-0.00313	g_6=6.27x10^{-5}	g_8=0.004204

The bulk modulus of CO_2-saturated brine can be obtained either directly from compressibility measurements (Osif 1988) or indirectly from velocity measurements (Vanorio et al. 2010). Measurements at low temperatures and pressures indicate that CO_2 dissolution increases brine velocity by up to 3% (Liu 1998), with a similar relationship being found for temperatures and pressures in the supercritical range (Vanorio et al. 2010). Recent experimental work has measured the velocity of water saturated with CO_2 over a wide range of temperatures and pressures (Sun and Han 2009). It showed that the velocity of CO_2-saturated water has similar temperature and pressure trends to pure water, although at 60˚C there is a reversal in the relationship between the velocity of pure water and water saturated with CO_2. Below 60˚C CO_2 dissolution increases the velocity, whereas above 60˚C the CO_2-saturated water has a lower velocity than pure water. This odd relationship highlights a unique problem with modelling CO_2. To use this relationship, the data from Sun and Han (2009) was fitted. The velocity of pure water saturated with CO_2 (V_{wc}) is predicted using:

$$V_{wc} = 3.666^{-5} - 5 * T^3 - 0.026133 * T^2 + 3.718 * T + 1.7652 * P_P + 1404.2 \qquad 3\text{-}59$$

where P_P is pressure in MPa and T is temperature is °C. Here it is assumed that the water is fully saturated with CO_2.The velocity, bulk modulus and density are shown in Figure 3-10.

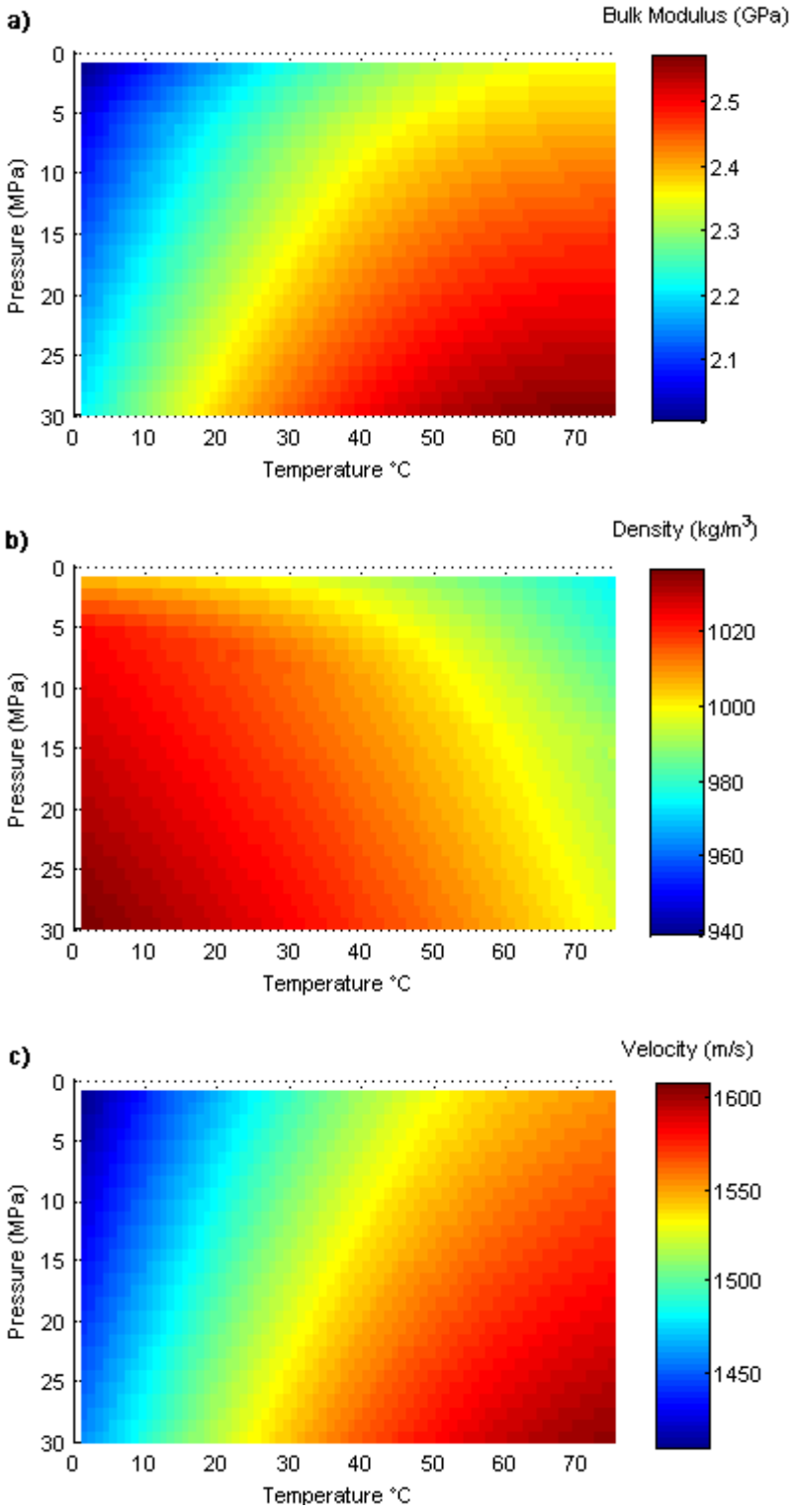


Figure 3-10 Brine saturated with CO_2 properties, plotted between 0-75˚C and 0-30MPa. a) Bulk Modulus (GPa), b) Density (kg/m^3), c) Velocity (m/s).

3.5 Idealised Saline Aquifer

Section 2.2.1 demonstrated that CO_2 can be sequestered in a variety of sedimentary environments. Reservoirs can be carbonate or clastic, saline or hydrocarbon, and shallow or deep. Here the focus is on clastic saline aquifers, as they provide the greatest storage capacity. The models used to predict the elastic properties of the reservoir rocks and fluids require the: porosity, permeability, temperature, pressure and mineralogy. To model the reflectivity values are required for the overburden, reservoir and caprock.

Mineralogy

The mineralogy of shale and sandstone can be very variable and different mineralogies are used in this thesis (Table 3-4). The Utsira formation was used when verifying results from McKenna et al. (2003) (Section 4.2). A generic sand reservoir and shale seal was then used for the modelling, to make the model as general as possible. Individual mineral constituents were then combined to give the effective mineral modulus (Section 3.3.1).

Table 3-4 Mineralogies of different sandstones and mudstones.

Rock Type	**Formation**	**Mineralogy**
Sandstone	Utsira	70% Quartz 10% Feldspar 5% Illite 5% Clay 5% Muscovite 5% Pyrite Modified: 70% Quartz 10% Feldspar 10% Clay 5% Muscovite 5% Pyrite
	Generic	100% Quartz
Shale	Generic	60% Illite 20% Quartz 10% Calcite 10% Feldspar

Porosity and Permeability

The porosity (Φ) was predicted using a porosity-depth relationship derived for normally pressurised North Sea sandstones (Sclater and Christie 1980):

$$\Phi = S_{\Phi} e^{pdc*h*0.001} \qquad 3\text{-}60$$

where S_{Φ} is the surface porosity (0.63 for shale, 0.49 for sandstone), *pdc* is the porosity depth coefficient (0.51 for shale, 0.27 for sandstone) and *h* is the depth in meters.

The horizontal permeability (κ in mD) was determined from the porosity using the Tixier equation (Schlumberger 1991):

$$\kappa = 62500\Phi^6 / S_{cw}^2 \qquad 3\text{-}61$$

where S_{cw} is the connate water saturation. The vertical permeability was taken to be one tenth of the horizontal permeability Here the permeability is calculated using the connate water saturation taken from the relative permeability curves, as discussed in Section 2.3.1. More commonly the connate water saturation would be calculated from laboratory permeability measurements, however as this is a synthetic modelling study without core data it is not possible to do so.

Temperature and Pressure

Several pressure values are required for modelling. These are plotted in Figure 3-11 and are:

- **Lithostatic Pressure**, exerted by the weight of the overlying material.
- **Hydrostatic Pressure,** exerted by the weight of the column of water above, assuming pressure communication.
- **Pore Pressure,** which is the pressure of the fluid in the pore space. This can be higher than hydrostatic if there is no pressure communication.
- **Overpressure,** due to the difference between the pore and hydrostatic pressure.
- **Effective Pressure,** from overburden stress supported by the rock frame. It is generally defined as the confining stress minus a fraction of *n* of the pore pressure, for soft sediments *n* is closed to 1 (Siggins and Dewhurst 2003).
- **Fracture Pressure,** representing the pressure at which fractures may reactivate. The fracture pressure gradient is given as 0.018096 MPa/m (Bruce and Bowers 2002).

The temperature (*T*) was determined assuming a geothermal gradient of 25 ˚C/km and a surface temperature of 11 ˚C:

$$T = 11 + 0.25 \times h \qquad 3\text{-}62$$

where *T* is the temperature and *h* is the depth in meters.

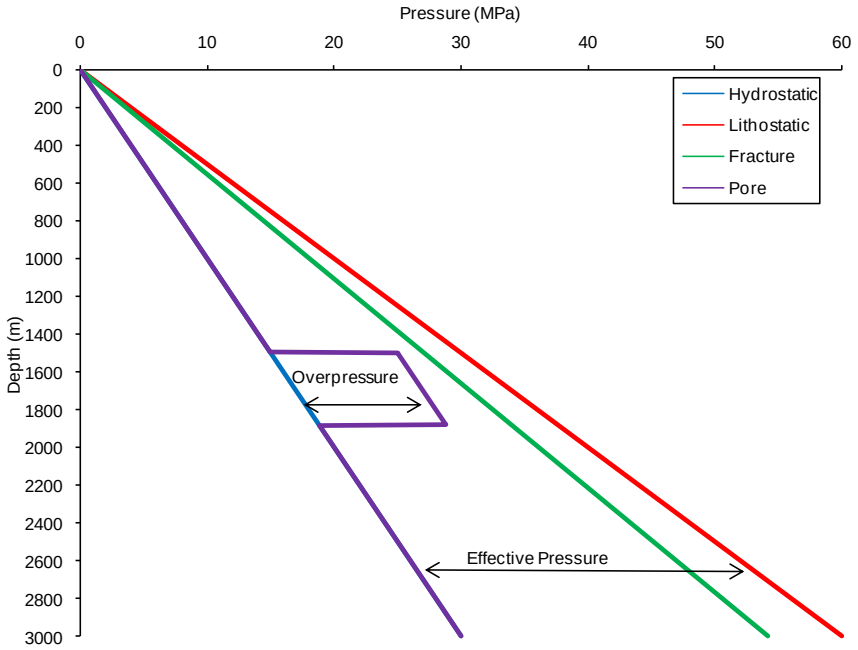


Figure 3-11 Pressure relationships with depth.

3.6 Typical Reservoir Properties

As this is a modelling study without any log or seismic data to constrain it, there is the potential to predict unrealistic reservoir properties. To mitigate this possibility, the predicted reservoir properties are compared to properties from clastic sequestration sites at similar reservoir depths (Table 3-5). The sites being compares are: Sleipner (Arts et al. 2004c), Ketzin (Kazemeini et al. 2010) and Atzbach-Schwanstadt (abbreviated to A-S) (Rossi et al. 2008).

Table 3-5Reservoir properties for clastic sequestration sites at various depths. Black data: predictions from synthetic modelling study, blue: data taken from well logs at existing/planned sequestration sites.

				Ketzin		Sleipner		A-S		
Depth (m)			**500**	**600-700**	**1000**	**~1000**	**1500**	**1588**	**2000**	**2500**
Temp		°C	23.5	34-37	36	36	48.5	54.7	61	73.5
Pressure		MPa	4.9	6.21-6.47	9.8	10	14.7	16.5	19.6	24.4
Porosity			0.43	0.2	0.37	0.37	0.33	0.17	0.28	0.25
Grain	Bulk Modulus	GPa	37	~30	37	36.7	37	24.3	37	37
	Shear Modulus		44	~20	44		44		44	44
	Density	kg/m^3	2650		2650	2650	2650	2625	2650	2650
Frame	Bulk Modulus	GPa	1.17	4.74	2.2		3.49	14.63	5.01	6.76
	Shear Modulus	GPa	1.64	3.9	2.85		4.23	7.9	5.96	7.86
CO_2	Bulk Modulus	GPa	0.0063	0.0082	0.065	0.0675	0.093	0.09	0.12	0.13
	Density	kg/m^3	131	174	687	650	705	776.75	710	712
V_p (S_w=1)		m/s	2036	2770	2355	2050	2650	3305	2910	3213
V_s (S_w=1)		m/s	906	1340	1170	643	1422	1849	1641	1866

There appears to be good correlation between the reservoir properties (temperature and pressure) at existing/planned sites and the synthetic modelling results. The predicted CO_2 properties also agree well. However there is some difference in other properties.

At Ketzin site, the porosity is much lower and the frame properties are much stiffer than predicted by this modelling study. The Stuttgart sands which are the main the reservoir at Ketzin are however weakly cemented (Figure 3-12). This cementation would explain the greater strength and lower porosity of this sandstone in comparison with the generic consolidated sandstone used here.

The Sleipner reservoir also shows some variation from what would be expected at that depth. The velocities are much lower than the predictions from modelling. However it should be remembered that the Utsira sandstone is actually unconsolidated, and therefore it would be expected to have a weaker frame and subsequently lower seismic velocities than a consolidated sandstone.

Comparison between the Atzbach-Schwanstadt reservoir and the modelling results highlights that the Austrian site has significantly lower porosity and higher frame strength than expected for a consolidated sandstone at that depth. These differences are due to the fact that the lithology is a shaley- sandstone, which would be more compacted than a sandstone, giving it a higher frame strength at this depth.

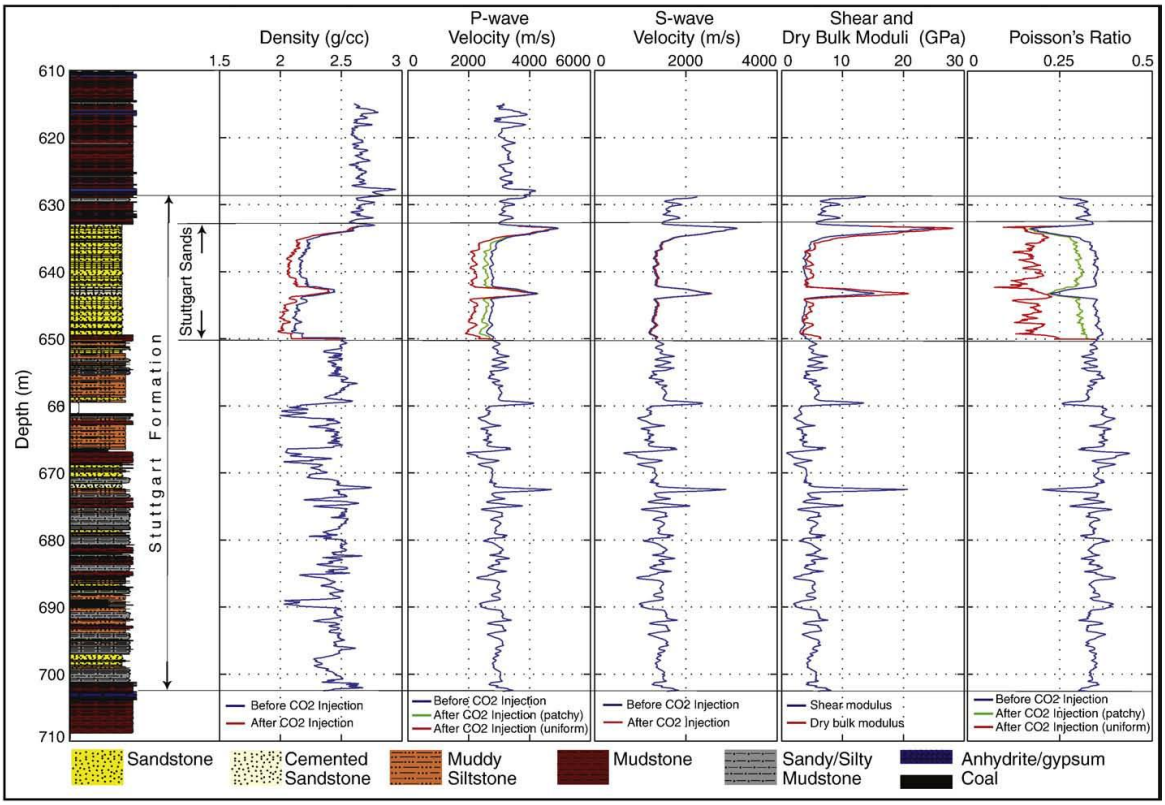


Figure 3-12Velocities, density, and Poisson's ratio logs for uniform- and patchy-saturation models at 30% CO_2 saturation. Last track shows how the shear modulus and dry-rock bulk modulus overlap in the relatively cleaner sandstone interval. From Kazemeini et al, 2010.

These variations demonstrate the difficulty in generalising results from one site to another. This emphasises the importance of keeping this synthetic sensitivity study as simple as possible, as the inclusion of lithological variations, such as cementation would complicate the analysis. Overall this comparison provides good confidence in the reservoir property prediction and shows some relative agreement in the elastic properties, even though there are significant lithological variations.

3.7 Fluid-Flow Simulation

Fluid-flow modelling predicts how fluids flow through the porous rock and interact with the host rock and fluids. This can provide saturation, pressure, solubility and mineralisation inputs for the rock physics model. Reservoir simulation software requires values generated using geological modelling and the capillary pressure and relative permeability. A number of the key reservoir simulation terms were discussed in Sections 2.3.1 and 2.3.2. Fluid-flow simulation can be performed using a variety of different software, which are based upon similar governing equations.

Here the ECLIPSE reservoir simulation software was used to predict the CO_2 and brine flow. ECLIPSE 300, is a finite difference grid-based simulator, which specialises in compositional modelling. It is a fully implicit compositional simulator and the CO2STORE option was used, which considers the mutual solubilities of CO_2 and H_2O (Schlumberger 2009). Previous simulation studies examining sequestration used other software as they each have disadvantages and advantages. ECLIPSE is a traditional grid-based method, which has been used to examine storage capacity estimates (Korbøl and Kaddour 1995; Pawar et al. 2006) and for issues such as the impact of relative permeability hysteresis (Juanes et al. 2006). When examining the interactions between the fluids and rock, GEM which is a fully-coupled geomechanical equation of state compositional simulator may be appropriate (Kumar et al. 2008; Nghiem et al. 2004). Streamline-based simulations have been used to predict flow and design storage(Obi and Blunt 2006; Qi et al. 2008).

The ECLIPSE fluid flow simulator requires a range of inputs. The following reservoir properties are required and were calculated using the approach outlined in Section 3.5: temperature, pressure, porosity and vertical and horizontal permeability. In addition to these values, relative permeability and capillary pressure functions are required. The values used here were derived from experimental work on a relatively clean and high porosity sandstone (Bennion and Bachu 2008; Bennion and Bachu 2006). Relative permeability hysteresis was included but only the drainage capillary pressure curve was available (Figure 3-13). The curves assume a zero residual gas saturation for primary drainage and a residual gas saturation of 30 % for imbibition, whilst during CO_2 injection the connate water saturation is about 40%.

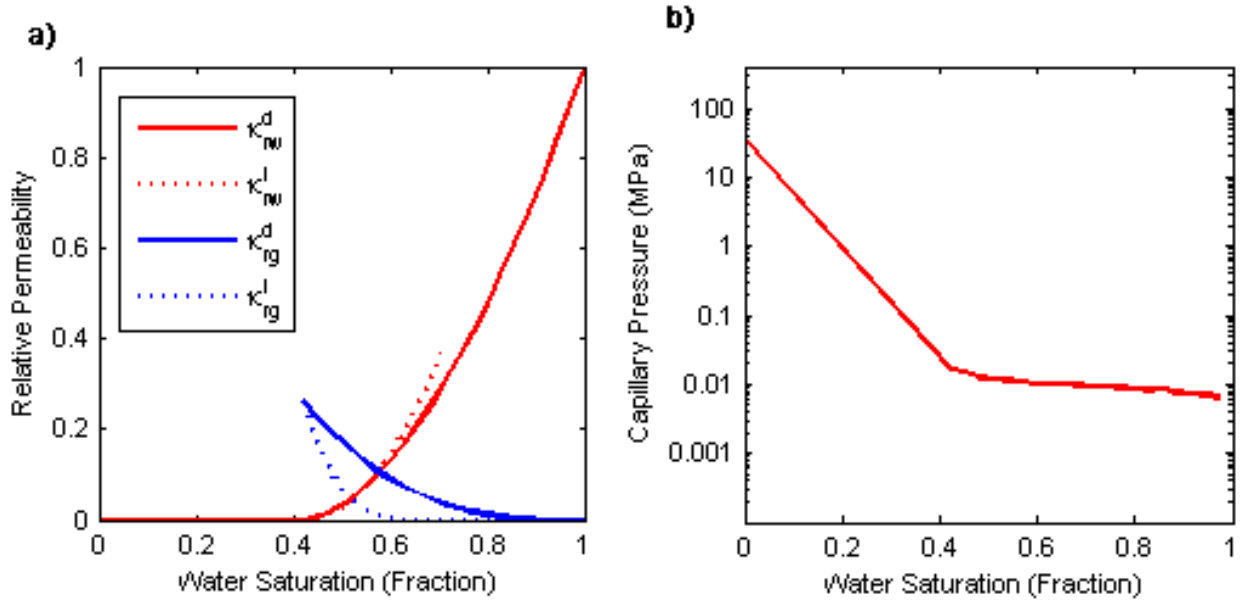


Figure 3-13 a) Hysteretic relative permeability curves, for brine (red) and CO_2 (blue), κ^d_{rw}: drainage brine curve, κ^I_{rw}: imbibition brine curve, κ^d_{rg}: drainage CO_2 curve, κ^I_{rg}: imbibition CO_2 curve. b) Capillary pressure curve.

In addition to reservoir properties ECLIPSE also requires inputs clarifying the reservoir size, layout, well information and timings. These values are varied in Chapter 5 and Chapter 6 and a table clearly stating these values will be given, Table 3-6 is an example of one. In the example below there was 100 x 100 x 50 gridblocks which were 100m x 100m x 2 m, i.e. the reservoir was 10 km x 10 km x 100m. There was one injection well placed in the centre of the reservoir and this well was open and injecting 4305 tonnes of CO_2/day (reservoir volumes) for 10 years. The simulation then continued for a further 10 years while the well was closed.

Table 3-6 An example of the inputs into ECLIPSE. Number refers to number of gridblocks, dimensions gives the gridblock dimension, wells, X and,Y, give well location, Z1 and Z2 give the interval over which the well is open in the reservoir, I/P represented injector/producer, tstep gives the timesteps for the calculation, R/P gives information on the controls on the well, either rate or pressure, and finally O/C states whether the well is open or closed for that time period.

Grid						**Wells**								
Number			Dimensions											
X	Y	Z	X	Y	Z	X	Y	Z1	Z2	I/P	TSTEP	R/P		O/C
100	100	50	100	100	2	50	50	1	50	INJ1	10*365	RESV	4305	OPEN
										INJ1	1*3650			CLOSED

3.8 Integrated Approach

This Section discusses more specifically the integrated approach used in Chapters 5 and 6. Section 3.8.1 discussed the workflow in more detail and clearly states how the outputs from fluid-flow simulation are incorporated into the seismic modelling. Use of this integrated modelling approach introduces some potential issues and opportunities which are discussed in Section 3.8.2.

3.8.1 Integrated Approach Workflow

The way in which pressure and saturation values are taken from ECLIPSE and input into the rock physics modelling is demonstrated in Figure 3-14. The steps are:

1. Fluid-flow simulation is run in 3D.
2. 2D slices of pressure and saturation values are extracted from the 3D cube.
3. Using rock physics modelling (Section 3.3) the elastic properties of the reservoir are calculated for each grid block. The elastic properties for the overburden and region below the reservoir are predicted assuming the shale is brine-filled and normally pressurised.
4. Seismic velocities and density calculated for each grid block, and the surrounding reservoir.
5. For each step in the X direction all of the grouped together and combined with the overburden properties and a 1D synthetic seismogram is generated.
6. These synthetics are treated as a seismic trace, with the trace being one gridblock in width and subsequently the seismic response across the reservoir can be generated.

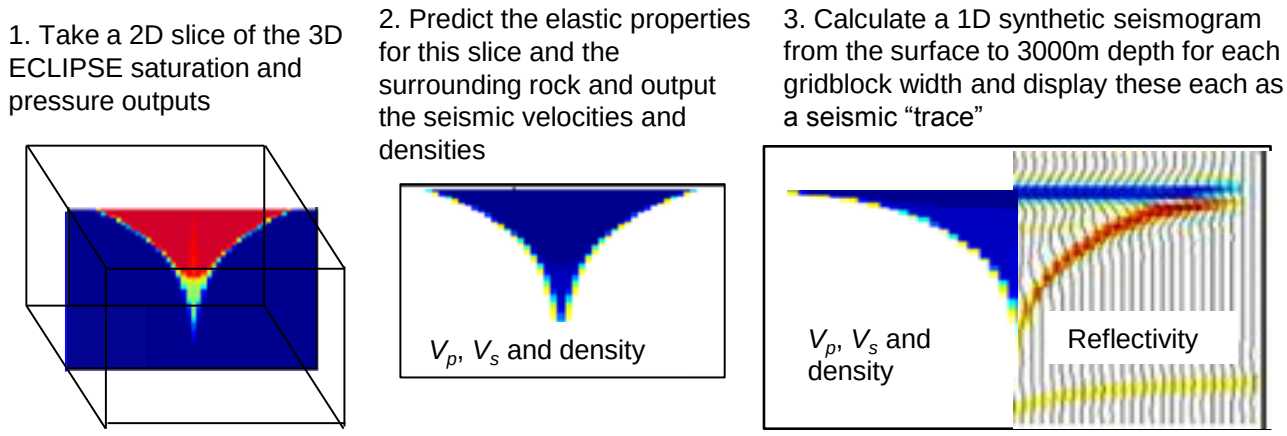


Figure 3-14 Workflow for the "integrated approach".

3.8.2 Advantages and Disadvantages of the Combined Approach

3.8.2.1 Predicting Saturation.

One of the advantages of using this combined approach is that the information from reservoir simulation can be used to help guide the rock physics modelling. Section 2.3.2 explained how the relative permeability and capillary pressure functions of a specific brine-CO_2-mineral system control the possible saturations in the reservoir. Using the curves used here (Figure 3-13) some generalisations can be made about the CO_2 saturations likely to be generated in this homogeneous synthetic saline aquifer. Subsequently four possible saturation "types" have been interpreted in the saline aquifer:

4. **Brine-filled.** Away from the CO_2 injection site the pores will be saturated with mobile brine: 100% brine

5. **CO_2 and residual brine**. Formed during drainage, the CO_2 within the plume is mobile, whilst the brine is immobile and trapped by capillary forces at the connate water saturation: 60% CO_2, 40% brine. As it is assumed that the rock is water-wet the water phase will remain within the smaller pores and a continuous film will coat the walls of the larger pores.

6. **Brine with residual CO_2.** During imbibition the CO_2 will get trapped as the brine re-invades the pore space, CO_2 will be trapped within the middle of the larger pores via snap-off. CO_2 will be present at the residual gas saturation: 30% CO_2, 70% brine.

7. **Both mobile CO_2 and brine present.** This describes the "transition" region between regions 2 and 1/3.

The majority of the aquifer can be described using these first three cases and a cartoon illustrating these three cases is shown in Figure 3-15. These typical CO_2 saturation values: 0%, 30% and 60% will be used as a guide for the following seismic modelling studies. However the full range of saturations will also be examined so that the small "transition zone" can also be described. .

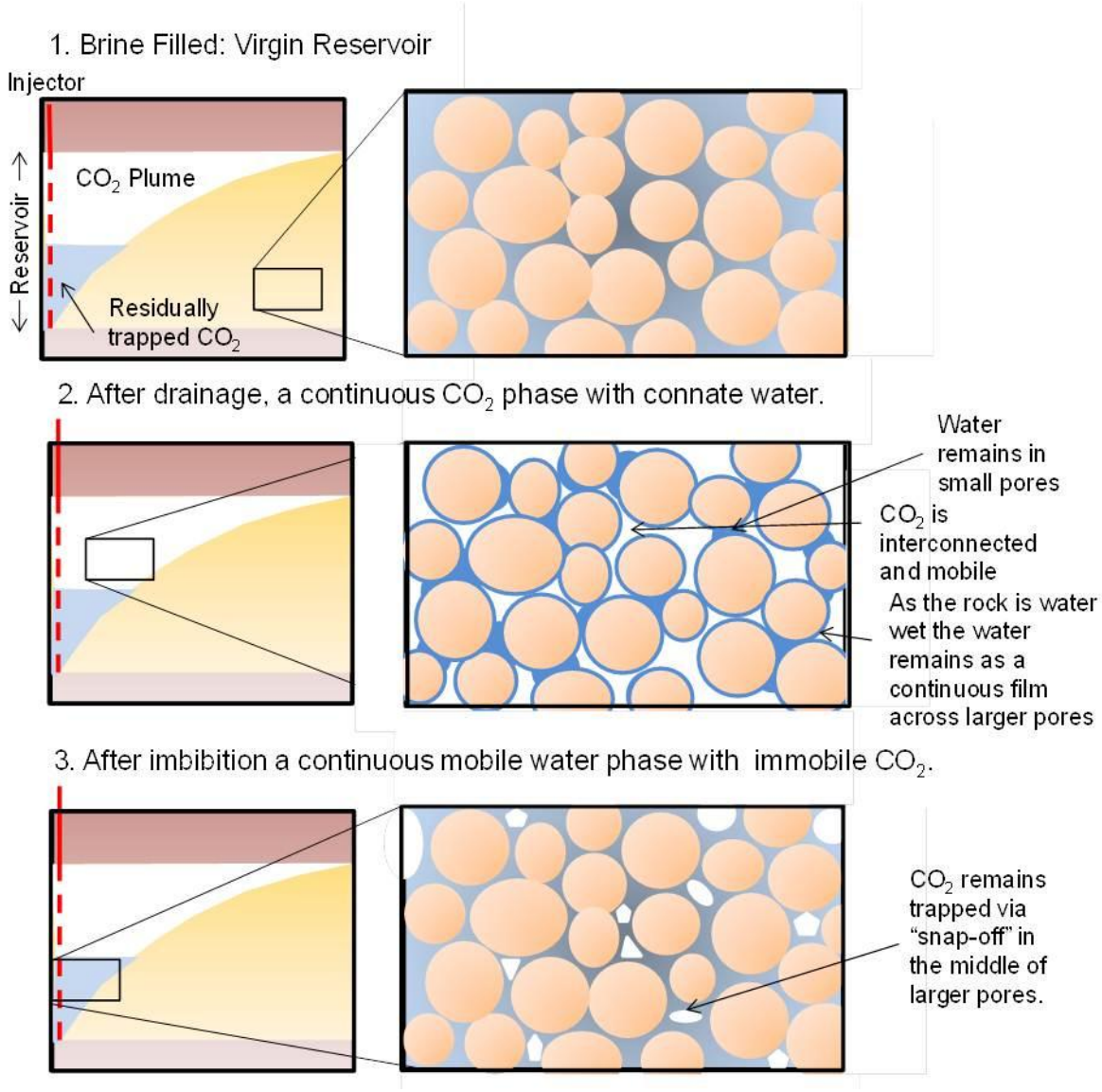


Figure 3-15 Cartoon showing the three most common saturation states within the aquifer. On the left, where they are likely to occur within the plume and on the right how they will appear on the pore scale.

3.8.2.2. Grid Block size

Integration of the fluid-flow simulation and rock physics modelling posed some problems. One issue of interest was that of numerical dispersion (Figure 3-16). Using smaller grid blocks resulted in a more realistic distribution and movement of fluids in the aquifer over time. In the case of CO_2 injection into brine this resulted in a greater segregation of fluids (Figure 3-16c), than for courser grid blocks. In simulations of flow in 3D heterogeneous aquifers it may not be possible to use this level of grid refinement which will produce a more gradual transition between high and low saturations (Figure 3-16a). This would not be an issue if there was a linear relationship between CO_2 saturation and V_p, however this is not true when a if a homogeneous fluid distribution is assumed. Also here the fine grid simulations predicted that a very rapid change in saturation and hence in elastic properties at this interface. This interface may cause reflections due to the sudden change in elastic properties, but this would not be seen if seismic properties were calculated from the coarse grid simulation results. The largest discrepancy due to grid-block size in the saturation prediction was towards the edge of the plume. In the case of a homogeneous reservoir, as was modelled here, this did not make up much of the reservoir. Therefore grid-block resolution effects were not very important in the reservoir modelled here, but they may be a more important problem in a heterogeneous reservoir.

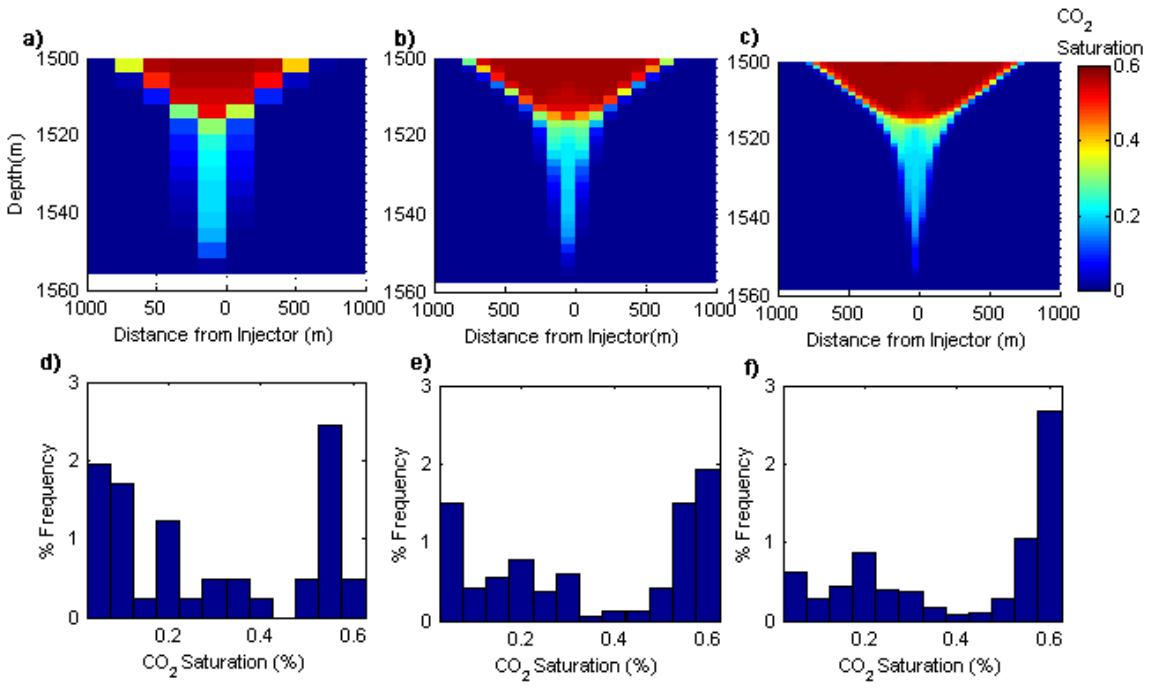


Figure 3-16 Predicted CO_2 saturation from simulations using different size grid blocks, a&d) half the number of grid blocks, b&e) original number of grid blocks, c&f) double the number of grid blocks, resulting from injection of 0.7M t of CO_2 over 10 years, a-c) saturation maps, d-f)Percentage of gridblocks containing specified saturations (excluded 0).

3.8.2.3 Differences in Scale

A further complication to attempting to combine data from fluid flow simulation, rock physics modelling and seismic surveying is the differences in the scale at which these different disciplines typically operate. Figure 3-17 illustrates these differences and shows how this may affect how a typical reservoir would be interpreted and modelled. A seismic pixel, is defined by the seismic resolution, i.e. in the vertical direction this is the tuning thickness, which is the thickness over which two reflectors can be distinguished (Section 4.3.2). Both reservoir simulation gridblocks and seismic pixels represent an averaging of reservoir properties as interpreted from core, well logs or outcrops. For example a 20 m thick reservoir may be represented by just two gridblocks and two seismic wiggles in the vertical direction.

Here rock physics modelling has been conducted on the reservoir simulation gridblock. Subsequently in the horizontal direction the seismic resolution has been underestimated (the typical gridblocks used in this thesis are 100m). However in the vertical direction care was taken to use very fine gridblocks (~2m). Then when the synthetic seismogram was generated these fine elastic/ seismic properties were averaged. The level of detail seen in the vertical direction depends on the frequency of the seismic wave.

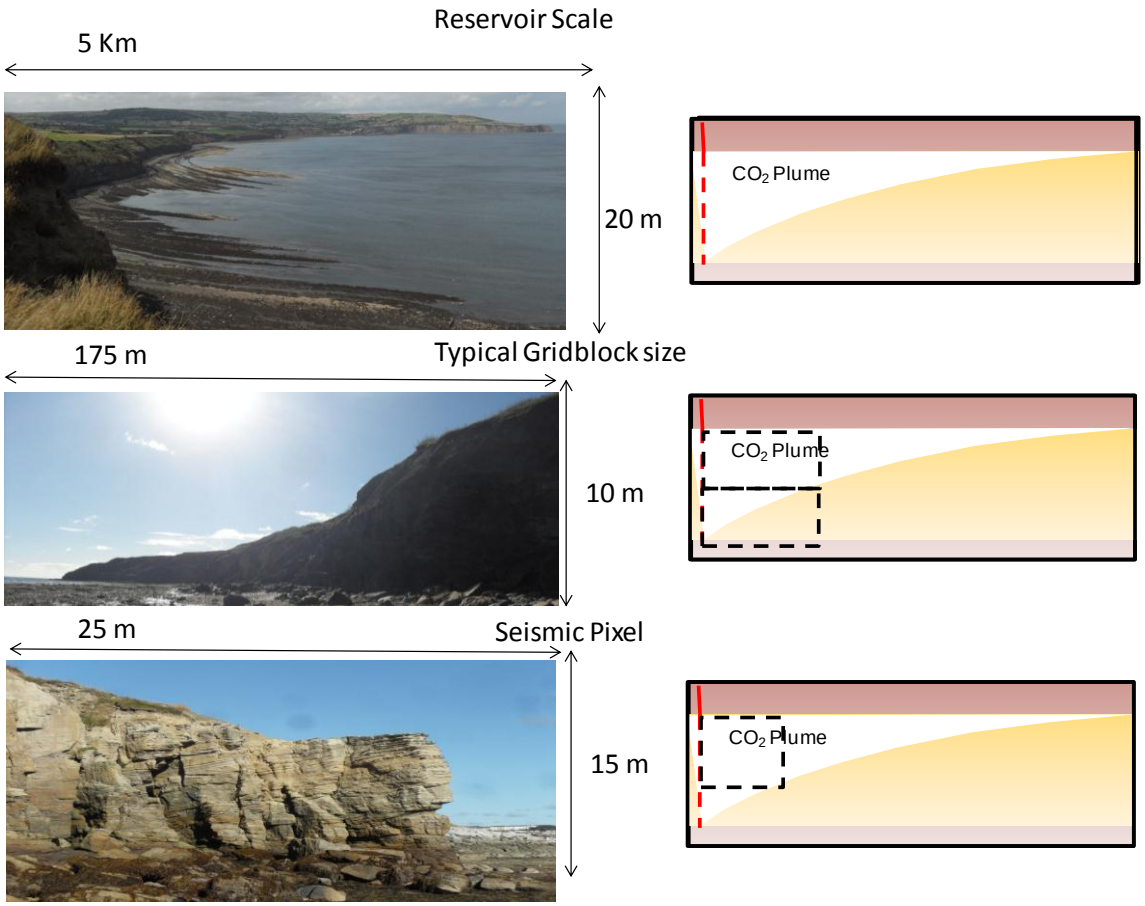


Figure 3-17Cartoon demonstrating the typical scale of a fluid flow simulation gridblock and a typical seismic pixel.

3.8 Summary

This Chapter outlined the theoretical approach used to predict the time-lapse seismic response to CO_2 injection in a clastic saline aquifer. Attempts have been made to make the reservoir as generic as possible, so that the results from this study can be applied elsewhere.

First, the seismic modelling approach was outlined, with emphasis on the elastic constants which control the propagation of the seismic wave through the subsurface. Equations for key seismic values were given: the isotropic seismic velocities, zero-offset reflectivity and AVO response. The three-term approximation to the full Zoeppritz equations was shown to be appropriate for the angular range under examination (0-30°). Displaying reflectivity requires seismic modelling software to convolve the reflectivity series with a 40 Hz Ricker wavelet here this was done using CREWES software.

The seismic velocities and attenuation depend on the elastic moduli of the porous medium which were estimated using rock physics models. Calculating the saturated porous medium elastic moduli required values for the grain/mineral, grain framework and fluid elastic moduli. The grain moduli were calculated using the Hashin-Shitrkman bounds (Hashin and Shtrikman 1963) which are the narrowest bounds available for an isotropic mixture without specifying anything about the geometries of the constituents. The grain framework moduli were calculated using the friable-sand model (Dvorkin and Nur 1996), which is appropriate for an uncemented sandstone. Grain framework moduli depend on the effective pressure, and can be used to examine the impact of pressure changes. The brine properties were predicted using the Batzle-Wang equations, the CO_2 properties came from NIST (NIST 2011) and the properties of brine saturated with CO_2 were predicted using a mixture of the Hebach equations and a relationship derived from experimental work by Sun and Han (2009). Once the elastic moduli were predicted they were combined, using an approach that depended on the level of fluid mixing in the reservoir and the frequency of the seismic wave. At low frequencies for a well-mixed reservoir the properties were combined using the Gassmann (1951) model and the fluid bulk modulus was predicted using the Reuss isostress average. For patchy saturations where the fluids are not well mixed the Hill (1963) average was used. The Hill and Reuss models are the end-member fluid distribution models. The White (1975) model was used to examine the effect of velocity dispersion and attenuation.

The parameters required to perform this rock physics modelling, are porosity, permeability, temperature, pressure and mineralogy. The porosity was calculated using a relationship appropriate for North Sea sandstones (Sclater and Christie 1980), and from this the permeability was estimated using the Tixier equation (Schlumberger 1991). The temperature and pressures were calculated using generic geothermal and pressure gradients. The mineralogy of a generic sandstone and shale were used. The time-dependent reservoir properties were estimated through fluid-flow modelling using ECLIPSE (Schlumberger 2009). This

simulation required relative permeability and capillary pressure values, which were taken from Bennion and Bachu (2006) and Bennion and Bachu (2008).

The approach to integrating these different disciplines is given in more detail in Section 3.8, where the workflow is stated. Combining the disciplines has provided some guidance regarding the saturations expected in the reservoir, i.e. 0%, 30% and 60% CO_2. These saturation values will be used in subsequent Chapters to help guide the sensitivity study. A brief study of gridblock size was also conducted, highlighting the importance of gridblock size and numerical dispersion. Then finally a discussion regarding the different scales at which disciplines operate was given. An approximation used here is that the rock physics and seismic modelling is conducted at a simulation gridblock scale, which may lead to an underestimation of horizontal seismic resolution.

4. Sensitivity Study

This Chapter reports the results of a rock physics sensitivity study on the use of time-lapse seismic surveys for monitoring CO_2 sequestration in clastic saline aquifers. The issues examined are, the importance of the reservoir properties, the fizz-gas effect and the impact which CO_2 phase and trapping phase have on the seismic response.

Reservoir properties dictate the magnitude of any change in the seismic response during injection and so require examination prior to selection of a sequestration site. Here reservoir depth which affects the porosity, fluid properties and rock-frame properties was examined, in order to determine the best depth for monitoring. At all the depths examined the P-wave seismic velocity (V_p) was substantially more sensitive to fluid content than the S-wave seismic velocity (V_s). Injection into shallow reservoirs, at 500 m depth for example, could result in large changes in both V_p (-35%) and V_s (12%), but the magnitude of these changes decreases with depth. At 2500 m V_p decreased by about 10% and V_s increased by only 1%. The zero-offset reflectivity was able to detect small amounts (3%) of CO_2, although it was less sensitive with increasing depth. In some lithologies, such as a low-porosity stiff caprock, the zero-offset reflectivity may not be sufficient and the AVO response could be used instead.

The fizz-gas effect makes extraction of saturation information difficult, so the ability of seismic properties to distinguish between structurally trapped (60%) and residually trapped (30%) CO_2 saturations, was examined instead. The zero-offset reflectivity alone was insufficient to distinguish the two saturations and the AVO gradient (*B*) was relatively insensitive to saturation. However, converted shear waves and AVO density parameters were more sensitive to CO_2 saturation, potentially helping to distinguish residual and structurally trapped CO_2. Unfortunately the low density contrast between brine and supercritical CO_2 makes it unlikely these effects would be detectable. The exception could be in shallow reservoirs where CO_2 is in a gaseous phase. Attenuation was a maximum at low CO_2 saturations, particularly for gaseous CO_2, therefore high attenuation could indicate low saturation regions. However at low seismic frequencies typical of "standard" 3D surveys the magnitude of the attenuation would be very low, and it is very difficult to reliably estimate attenuation from seismic data.

Gaseous and supercritical CO_2 phase could theoretically be distinguished using AVO attributes, as gaseous CO_2 produced larger changes in the intercept (*A*) than supercritical CO_2, but produced a change in the gradient (*B*) which was of a similar or slightly smaller magnitude than supercritical CO_2. Therefore an *A*-*B* crossplot could determine the CO_2 phase. The elastic properties of water containing CO_2 were found to be very similar to that of pure water at 1500 m depth, implying that it is unlikely that dissolution could be monitored or quantified.

4.1 Introduction

The literature review conducted in Chapter 2 highlighted some specific issues and limitations related to the ability of time-lapse seismic surveys to fully monitor sequestration. Within this Chapter three of these possible issues are examined using the sensitivity study approach (Figure 3-1). This work differs from that presented in Chapters 5 and 6, as it does not incorporate any fluid-flow simulation work. Under examination here are, the dependence of the seismic response on reservoir properties as discussed in Section 2.5.1, the fizz gas effect and the impact this has on the ability to quantify the amount of CO_2 retained within the aquifer which was explored in Section 2.5.2 and the fact that CO_2 phase may vary through time as mentioned in Section 2.5.3. These issues were examined with reference to the first three monitoring aims:

- Detecting the extent of the CO_2 plume and its migration
- Quantifying the amount of CO_2 within the reservoir (i.e. saturation).
- Determining the mechanism by which the CO_2 is trapped.

First, the numerical model was verified through comparison with results from McKenna et al (2003) (Section 4.2). The code was then adapted to allow modelling of a stiffer sandstone, and a realistic overburden which was necessary for reflectivity modelling (Section 4.2.2). Then this was used to examine the impact of reservoir properties on the magnitude of the time-lapse seismic response (Section 4.3). A variety of reservoir depths (Section 4.3.1) were modelled showing the impact depth has on reservoir and fluids properties (Section 4.3.1.1). The seismic response to CO_2 sequestration was then predicted for aquifers found between 500 and 2500 m depth (Section 4.3.1.2). Injection into thin reservoirs was then examined (Section 4.3.2). In Section 4.4 the fizz-gas effect was discussed, along with the different seismic properties used to try and differentiate high and low CO_2 saturations. The use of the different seismic properties to distinguish gaseous and supercritical CO_2 was examined in Section 4.5.1, Finally the impact of dissolution on the elastic properties was determined using newly published experimental data (Sun and Han 2009) (Section 4.5.2).

4.2 Model Verification and Extension

McKenna et al (2003) constructed a combined geological, rock physics and seismic model to predict the seismic response to CO_2 injection for a range of depths. In this Section the code used in this thesis was verified through comparison with results from McKenna et al (2003). The numerical model was then extended to be appropriate for a stiffer sandstone with a shale overburden. The original seismic model was limited to velocities, however the inclusion of an overburden here allowed for reflectivity modelling.

4.2.1 Verification

The McKenna model was developed for a saline aquifer consisting of an Utsira-type sandstone located at depths up to 3000 m. Generic temperature, pressure and porosity curves were used. The grain framework properties were predicted using the smooth-Walton model (Walton 1987), the mineral properties were predicted using the Hashin-Shtrikman bounds (Section 3.3.1), the brine properties were found using Batzle-Wang equations (Section 3.4.1) (salinity: 35,000ppm), and it was assumed that the CO_2 properties were also be predicted using the Batzle-Wang equations. The Gassmann-Reuss equations (Section 3.3.3.1) were used. The results were compared graphically with those from McKenna et al (2003) shown in Figure 4-1. The graph show good agreement and small mismatches were considered to be due to the use of differing mineral compositions, in particular clay mineral moduli are highly variable (Avseth et al. 2005) and the values used were not given in the paper. This comparison provided confidence in the numerical approach.

4.2.2 Improved Numerical Model

The McKenna et al (2003) work was designed for the Utsira sandstone which has a high sensitivity to fluid content, due to its weak frame, high porosity and unconsolidated nature (Table 3-5). In this thesis the friable-sand equation (Section 3.3.2) was used, as it predicts a slightly higher stiffness, which makes the results more general. Another limitation of the previous modelling approach was the lack of a realistic overburden, which prevented examination of reflectivity changes and pushdown due to CO_2 injection. Here an overburden was modelled. A generic sandstone lithology was assumed for the reservoir and generic shale lithology was used above and below the reservoir (Table 3-4). The Batzle-Wang equations were used by McKenna, but these have been shown to be a poor approximation (Figure 3-8), so in this work the values are taken in the NIST database.

The equations used to predict the reservoir properties, the elastic properties and subsequently the seismic response are included in Chapter 3.2-3.5. This improved modelling approach was used. For the majority of the Chapter it was assumed that the fluids were well mixed below the critical length scale and so the Gassmann- Reuss equations (Section 3.3.3.1) were employed, however in Section 4.4.3 the White model (Section 3.3.3.2.2) was used to examine the relationship between saturation and attenuation.

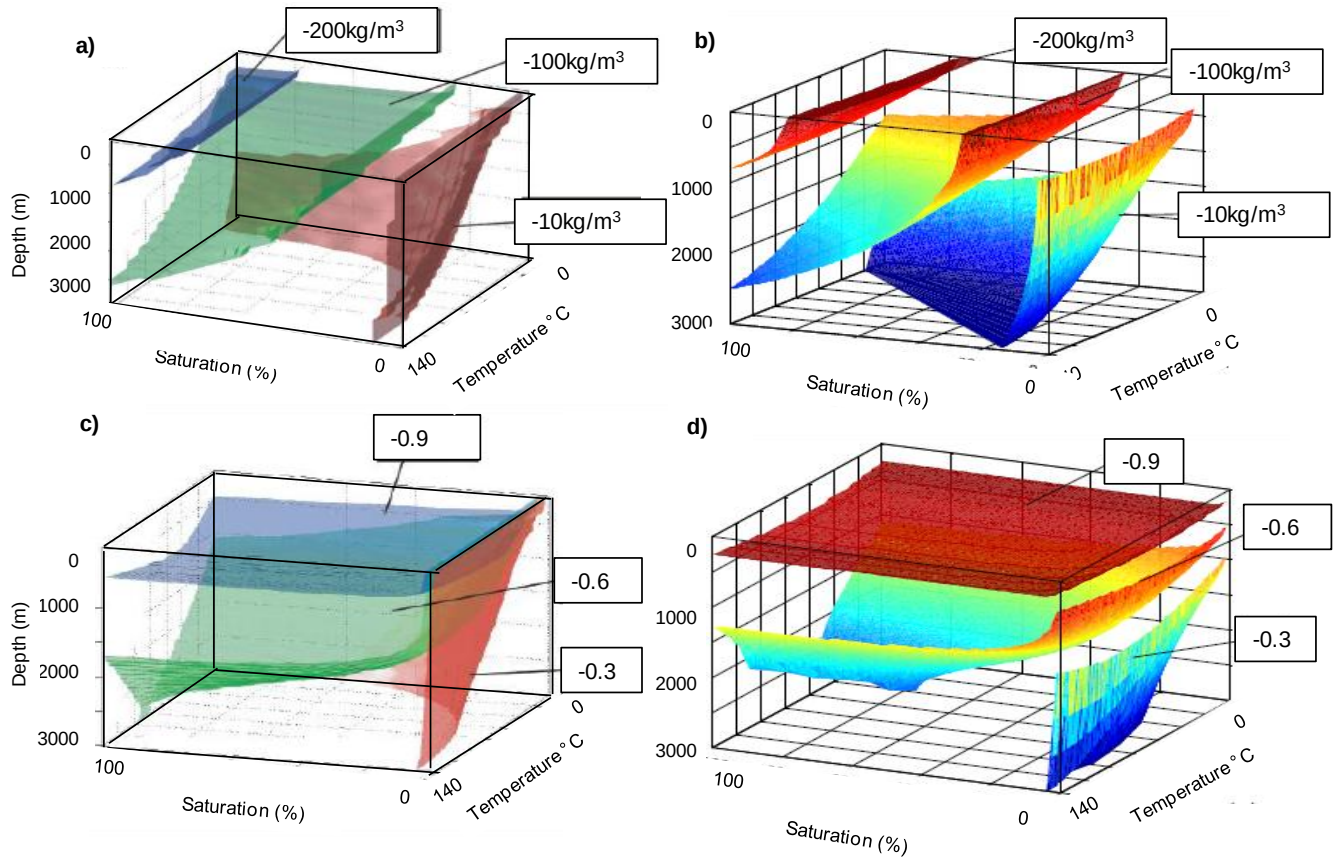


Figure 4-1 Change in density (a-b) and V_p/V_s ratio (c-d) as CO_2 displaces brine. a&c) Taken from McKenna et al. (2003), b&d) Generated using the modelling approach/ code which was then modified and used in this thesis.

4.3 Importance of Reservoir Properties

This Section examines the effect of changing the reservoir properties on the sensitivity of the seismic response to changing CO_2 saturations. The reservoir properties varied were the reservoir depth and the thickness of the reservoir. Figure 4-2 shows a similar analysis which examined the seismic response to changes in fluid content, porosity, temperature, pressure and lithology.

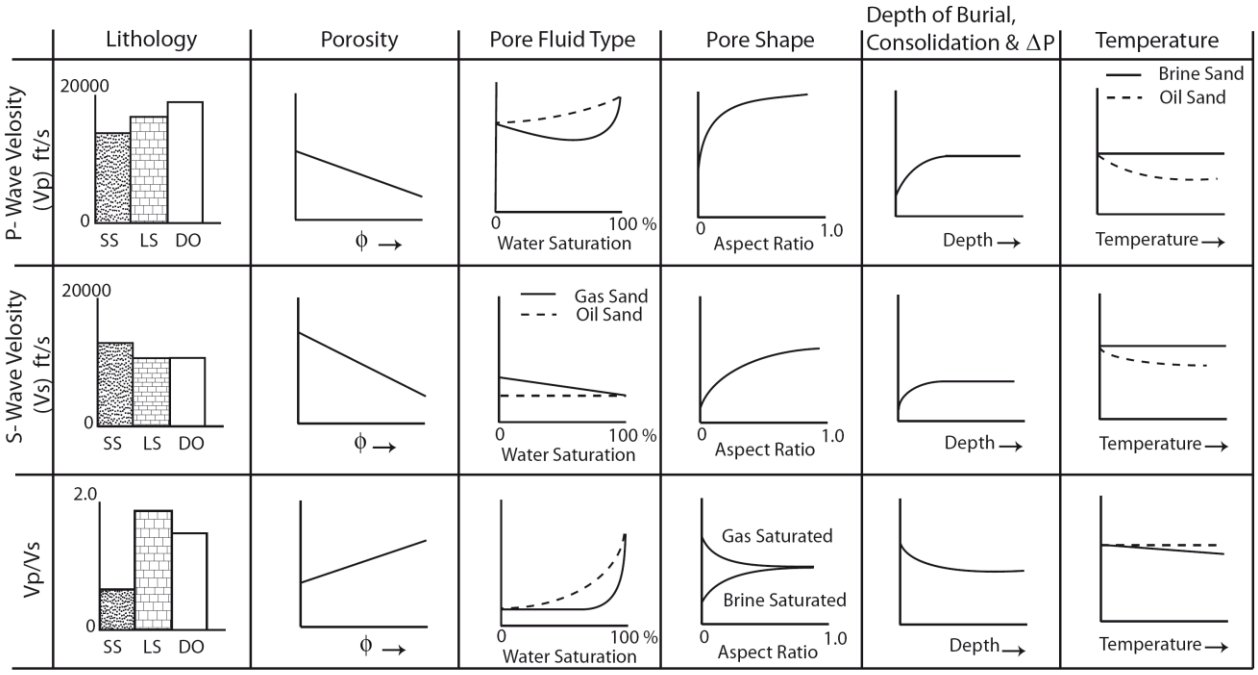


Figure 4-2 Effects of rock and fluid changes on the seismic velocities and the V_p/V_s ratio(from Kazemeini (2009) modified from Tatham and McCormack (1991)).

4.3.1 Reservoir Depth

First the sensitivity of seismic response to changing reservoir depth was examined. The seismic response was predicted for five cases of injection into a saline aquifer between 500 and 2500 m depth. McKenna et al (2003) identified a shallow, unconsolidated sandstone reservoir where CO_2 is in its gaseous phase, as ideal for monitoring. However it is unlikely that CO_2 will be injected as a gas, as to maximise the storage efficiency CO_2 should be sequestered in its supercritical phase. Here the idea of monitoring the injection of supercritical CO_2 was explored, to determine the best approach for this monitoring.

4.3.1.1 Fluid and Reservoir Properties

Interpreting variations in the seismic response at different reservoir depths requires an understanding of how the reservoir and fluid properties vary with depth. As described in Section 3.5 the temperature and pressure in this simple modelling scenario increased linearly with depth. Here the porosity of both the shale and sandstone decreased with depth, with the shale initially having a higher porosity than the sandstone, but this reversed at 1110 m depth. This agrees well with the explanation given for the disparity between the predictions from this study and the properties of the shaley-sandstone at the Atzbach-schwanstadt site (Table 3-5). The grain framework moduli of both the shale and sandstone were altered by the porosity decrease and an increase in effective pressure, which produced a much stiffer rock framework. The mineralogy was assumed to be constant. The reservoir and elastic properties are included in Table 4-1.

Table 4-1 Reservoir, mineral, frame and fluid properties for sandstone and shale at 500 m intervals from 500 m to 2500 m depth.

Depth (m)				**500**	**1000**	**1500**	**2000**	**2500**
Reservoir	Temperature		℃	23.5	36	48.5	61	73.5
	Pressure	Hydrostatic	MPa	4.9	9.8	14.7	19.6	24.4
		Lithostatic	MPa	9.3	19	29.2	39.7	50.5
	Porosity	Sandstone		0.43	0.37	0.33	0.28	0.25
		Shale		0.49	0.38	0.29	0.23	0.18
Grain	Sandstone	Bulk Modulus	GPa	37	37	37	37	37
		Shear Modulus	GPa	44	44	44	44	44
		Density	kg/m^3	2650	2650	2650	2650	2650
	Shale	Bulk Modulus	GPa	33.4	33.4	33.4	33.4	33.4
		Shear Modulus	GPa	22.5	22.5	22.5	22.5	22.5
		Density	kg/m^3	2741	2741	2741	2741	2741
Frame	Sandstone	Bulk Modulus	GPa	1.17	2.2	3.49	5.01	6.76
		Shear Modulus	GPa	1.64	2.85	4.23	5.96	7.86
	Shale	Bulk Modulus	GPa	0.87	2.11	3.94	6.32	9.14
		Shear Modulus	GPa	1.01	2.24	3.91	5.95	8.18
Fluids	CO_2	Bulk Modulus	GPa	0.0063	0.065	0.093	0.12	0.13
		Density	kg/m^3	131	687	705	710	712
	Brine	Bulk Modulus	GPa	2.35	2.46	2.54	2.61	2.63
		Density	kg/m^3	1013	1012	1009	1005	1002

As the fluid properties depend on reservoir temperature and pressure they change with depth (Figure 4-3). Brine properties were found to be relatively insensitive to depth, but CO_2 properties were very sensitive, particularly the CO_2 density. The transition from gaseous to supercritical CO_2 at 800 m resulted in an increase in density from 131 kg/m^3 at 500 m to 687 kg/m^3 at 1000 m. The CO_2 bulk modulus increased gradually with depth. The CO_2 phase change from gaseous to supercritical altered the seismic response, by decreasing the density contrast between brine and CO_2, while a large compressibility contrast remained.

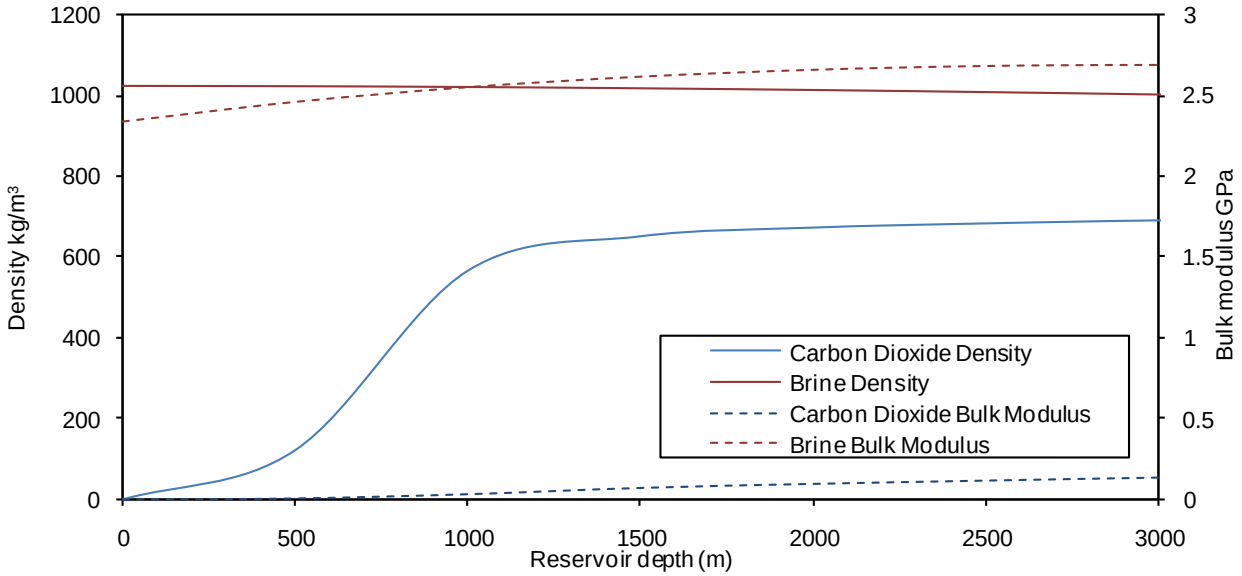


Figure 4-3 Brine and CO_2 density and bulk modulus plotted against reservoir depth.

4.3.1.2 Seismic Response

Seismic Velocities

The relationship between the seismic velocities and CO_2 saturation (S_{CO2}) is shown in Figure 4-4a&b. The seismic velocities increased with depth due to decreasing porosity and increasing grain framework strength. The sensitivity of the velocities to CO_2 was greatest at shallower depths where there was a large difference between the properties of brine and CO_2 (Figure 4-4c&d). The sensitivity was also higher at shallower depths due to the higher porosities and weaker rock frames. The different sensitivities of the two velocities to changes in fluid content was reflected by the relationships between velocity and S_{CO2}. Because V_s only depended on density changes, there was a quasi-linear relationship between V_s and S_{CO2}. In contrast V_p also depends on fluid compressibility and substituting relatively incompressible brine for very compressible CO_2 produced a non-linear response. Very small amounts of CO_2 decreased V_p significantly with further increases in saturation having little effect, in fact at 500 m depth after the initial large decrease V_p began to increase, due to the reduction in density. This highly non-linear relationship between V_p and S_{CO2} made determining the fluid content from the P-wave reflectivity challenging. On the other hand the linear relationship between V_s and S_{CO2} would allow for easy extraction of saturation information.

The magnitude of the change in the two seismic velocities caused by substituting brine for CO_2 in the pore space was different. At 500 m depth the maximum decrease in V_p was almost 35%, whereas the maximum increase in V_s was 12%. Between 500 m and 1000 m the CO_2 changed phase, which reduced the density contrast between brine and CO_2, and in turn reduced the increase in V_s to only a few percent. Supercritical CO_2 is much more compressible than brine, so there were still large changes in V_p produced by small amounts of CO_2 at all depths. Although V_p was highly sensitive to small CO_2 saturations at all depths the relationship became slightly more linear at greater depths due to the small increase in CO_2 bulk modulus. Overall V_p was found to be very sensitive to small amounts of CO_2, so the P-wave zero-offset reflectivity could be used to locate CO_2. However determining the volume of CO_2 trapped in the reservoir would require a velocity more sensitive to the entire saturation range, such as V_s.

The variation of P-wave impedance with saturation was plotted (Figure 4-4e), to examine whether these V_p changes could be detected. Assuming a 4% change in P-wave impedance is detectable between time-lapse seismic surveys (Lumley et al. 1997), the smallest detectable quantity of CO_2 at different reservoir depths was calculated. At 500 m 1% CO_2 in brine-filled rock was detectable, whereas at 2500 m 3% CO_2 saturation was required to produce a detectable change in reflectivity. Therefore as expected the sensitivity of seismic monitoring decreased with depth. However at all depths very small quantities (<3%) of CO_2 could still be detected. The P-wave impedance was more sensitive to a greater range of saturations than V_p due to the additional dependence on density, so it could be used to distinguish different saturations.

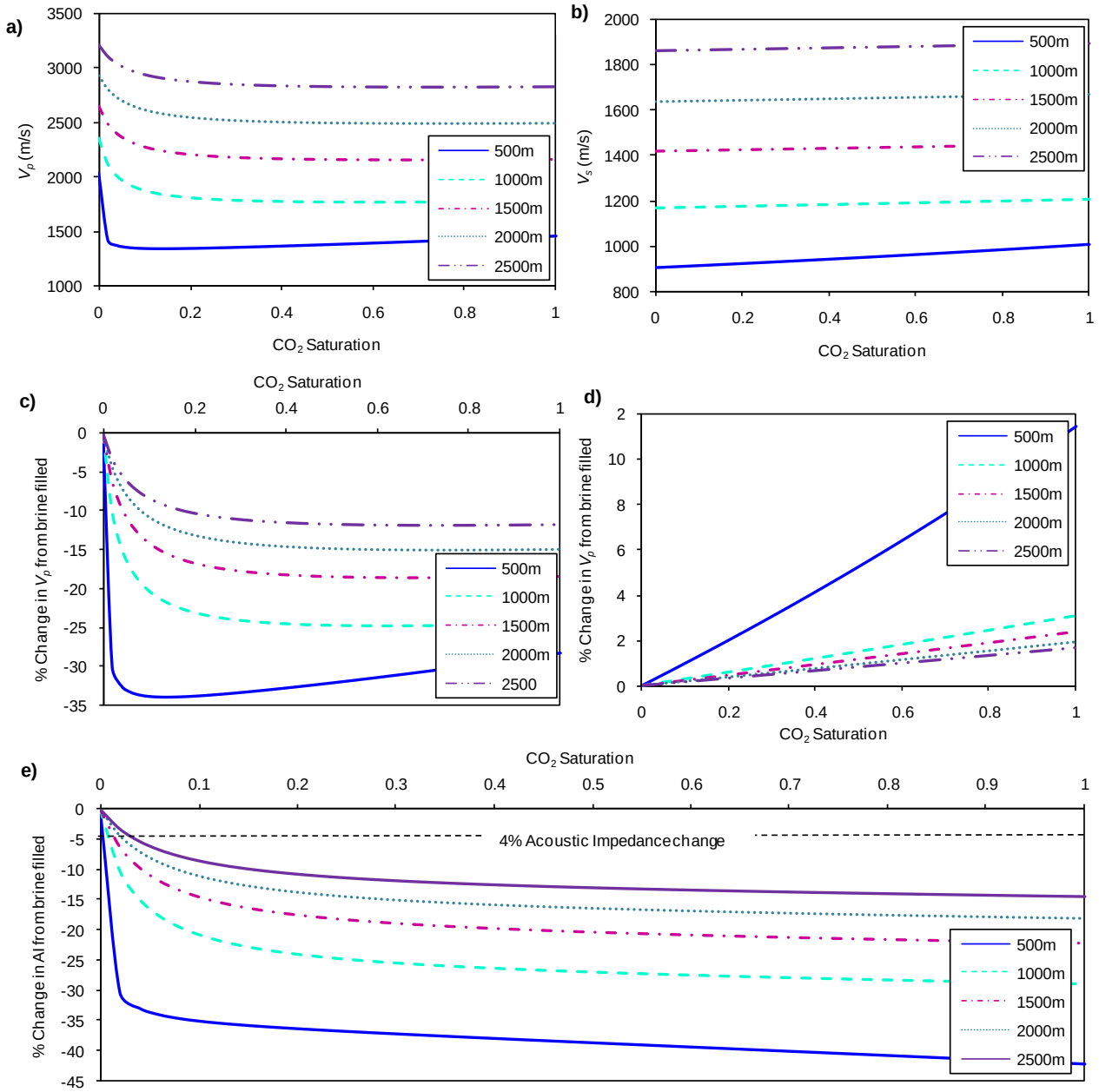


Figure 4-4 Relationship between seismic attributes and CO_2 saturation for reservoirs at 500 m depth intervals between 500 m and 2500 m: a) V_p, b) V_s, c) Percentage change in V_p from brine filled, d) Percentage change in V_s from brine filled, e) Percentage change in P-wave acoustic impedance (AI) from brine filled, dashed black line represents 4% change in P-wave impedance, which should produce a detectable time-lapse response (Lumley et al. 1997).

Zero-offset Reflectivity

The values of V_p and density from the surface to 3000 m depth were used to model the zero-offset reflectivity for a range of CO_2 saturations (Figure 4-5). It was assumed that the entire 100 m sandstone reservoir contained a specified saturation and that this saturation increased by 4% CO_2 for every trace. The largest change was at 500 m depth, where CO_2 injection changed the pre-injection top-reservoir reflectivity from a small positive reflection to a large negative reflection and produced 500 ms of pushdown on the base-reservoir reflection. In general the reflectivity echoed what was seen in the P-wave impedance (Figure 4-4e),

where the majority of the change was seen after the injection of the first few percent of CO_2, and the magnitude of any change decreased with depth. Overall the introduction of small quantities of CO_2 produced large changes in the amplitude of the top-reservoir and base-reservoir reflections and introduced significant base-reservoir pushdown at all depths. This amplitude change and pushdown could be used to map the location of CO_2 even at low saturations; however the magnitude of any changes reducing with increasing depth, potentially complicates detection. In addition the sensitivity of seismic data will decrease with depth, due to amplitude decay.

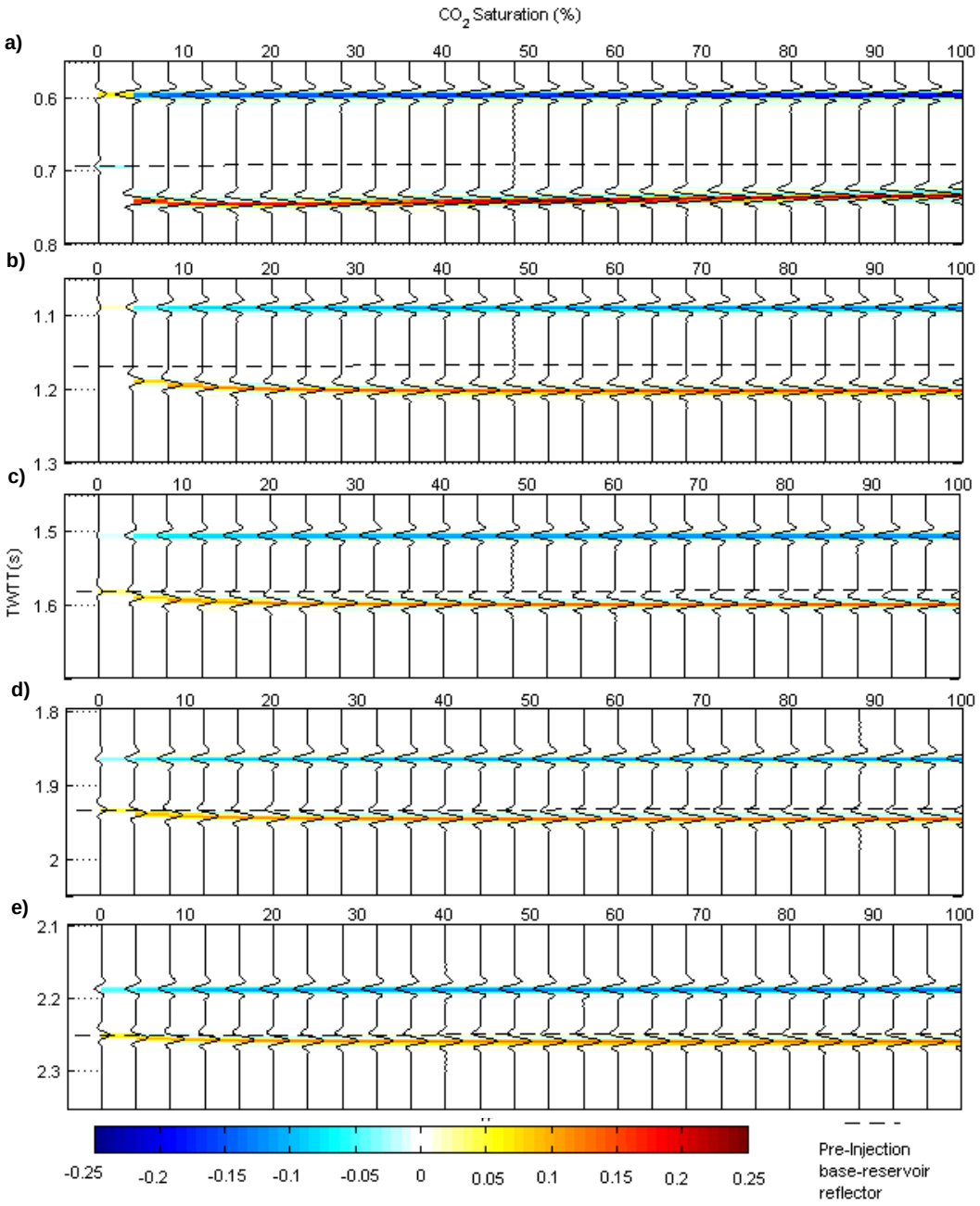


Figure 4-5 Zero-offset reflectivity generated using CREWES software assuming a 40Hz Ricker wavelet, plotted for a 100 m thick sandstone reservoir, containing varying amounts of CO_2 from brine filled to 100% CO_2 in 4% CO_2 increments. Shale is found both above and below the reservoir. The black dashed line represents the location of the pre-injection base-reservoir reflection. Reservoir at different depths: a) 500 m, b) 1000 m, c) 1500 m, d) 2000 m, e) 2500 m.

AVO Response

As the ability to detect the small amounts of CO_2 using the zero-offset response decreased with depth, it may not be possible to detect CO_2 migration for some reservoir conditions. Brown and Bussod (2007) suggested that within a carbonate aquifer the AVO response may be more sensitive to CO_2 saturation than the zero-offset response. Whether this is true for clastic saline aquifers was examined.

The angle dependent reflectivity was plotted for different saturation states in Figure 4-6. The fizz-gas effect (Section 2.5.2) dominated the response at all angles, and the reflectivity was very sensitive to saturation changes at small quantities of CO_2 and insensitive to changes at higher saturations. At all depths, there was a large difference in AVO from the pre-injection brine-filled pore-space, to a pore space containing CO_2. The pre-injection reflectivity was typical of a Class I sand (Figure 3-3) at both 500 m and 1000 m depth (increase in impedance across the interface). At 1500 m where the porosity of the shale caprock and sandstone reservoir were similar there was a Class II reflection (small change in P-wave impedance across the interface). At 2000 m where the sandstone had a higher porosity than the caprock, the reflections were typical of a Class III sand (decrease in impedance across interface), and at 2500 m there was a Class VI reflector. After CO_2 injection these top reservoir reflections became Class III sands producing a "bright spot", with an increase in reflectivity with offset. This increase in reflectivity with offset increases the contrast between the pre-injection and post-injection reflectivity, therefore if the zero-offset response is insufficient to detect CO_2 presence then the far-offset response could be of use.

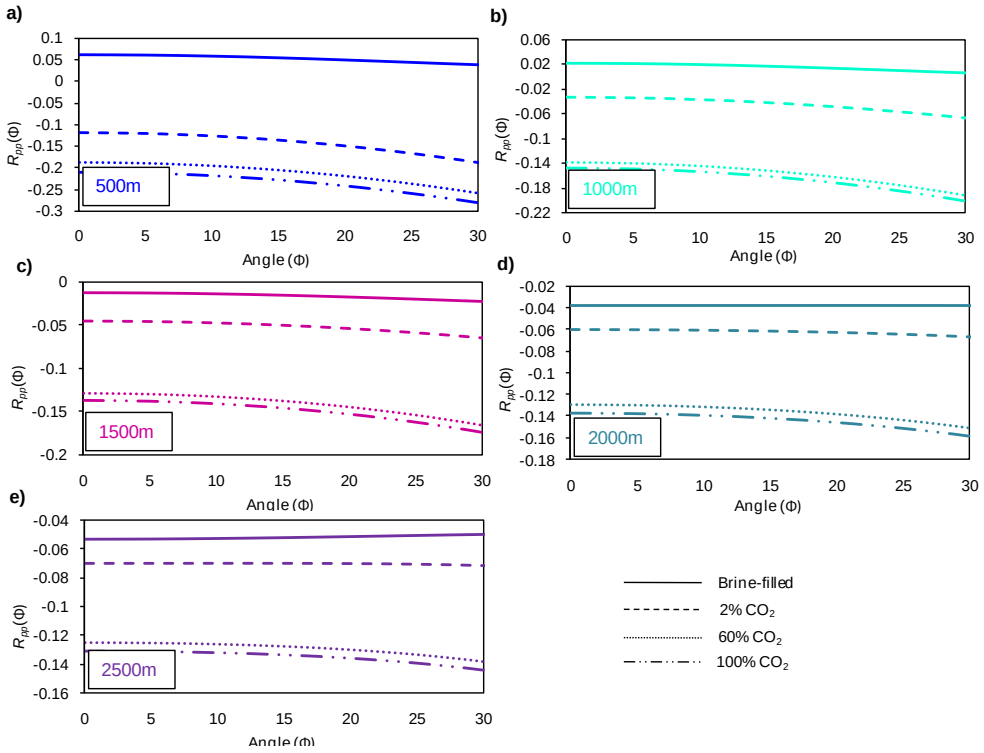


Figure 4-6Angle-dependent reflection coefficient ($R_{pp}(\Phi)$) plotted against angle (Φ) out to 30° incidence angle, plotted for brine-filled, and containing different saturations of CO_2: 2%, 60% and 100%. These plots are for five reservoir depths: a) 500 m, b) 1000 m, c) 1500 m, d) 2000 m, and e) 2500 m.

AVO interpretation for hydrocarbon detection is based on the fact that the V_p/V_s ratio of hydrocarbon-bearing sands deviates from the background trend, producing anomalous responses at mid to far offsets. This is done by cross-plotting of AVO attributes *A* and *B*. Whether this is true for CO_2-saturated sands is examined in Figure 4-7. Injecting CO_2 decreased both *A* and *B*, which is the same as a typical hydrocarbon response. However for gaseous CO_2 (500m depth) *B* began to increase with increasing saturation above a certain point, while *A* decreased. This agrees with Ravazolli et al (2011), who showed that above small saturations, *B* begins to increase for gaseous CO_2. No large increase was found for supercritical CO_2 (>800 m depth), indicating that the CO_2 phase (gaseous versus supercritical) could be determined from AVO response. Figure 4-7 illustrates that the zero-offset reflectivity (*A*) would be sufficient to differentiate brine-filled from gas-saturated cases, with the AVO gradient (*B*), being relatively insensitive to fluid content except at low saturations and shallow depths.

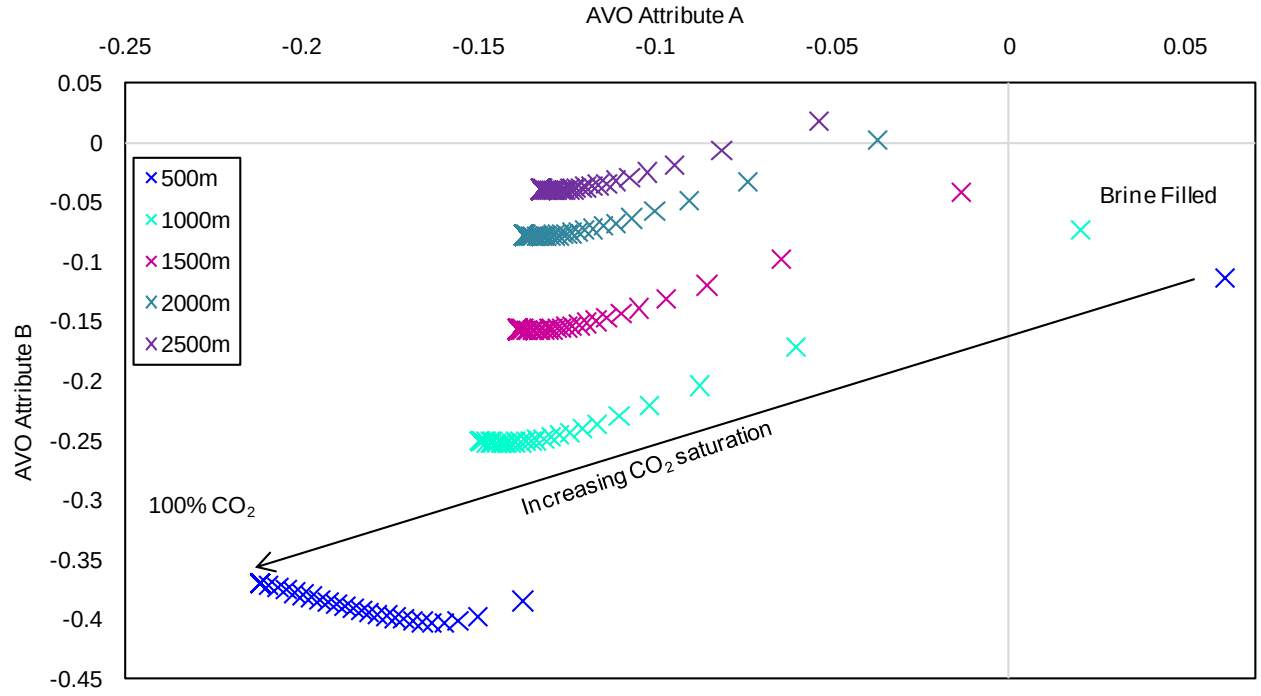


Figure 4-7 Cross-plot of AVO attributes A and B for five reservoir depths, at increments of 2% CO_2 saturation from brine-filled to 100% CO_2.

4.3.2 Reservoir Thickness

Information regarding the fluid content is commonly inferred from the reflection amplitude, however this link becomes ambiguous when there are multiple closely spaced reflectors. This is because reflections off multiple interfaces may interfere constructively or destructively, depending on both the time delay between the events and the wavelet. This is called the tuning effect. The "tuning" thickness is defined as the thinnest interval over which the distance between two closely spaced reflectors can be measured (Widess 1973). This thickness depends on the frequency and speed of the seismic wave and is a quarter of a wavelength. The tuning effect is shown in Figure 4-8 for a 40 Hz Ricker wavelet. At this frequency the tuning thickness is about 17 m. This may cause interpretation problems either for thin reservoirs or thin CO_2 accumulations (such as might be found in gravity tongues), but it can addressed using spectral decomposition.

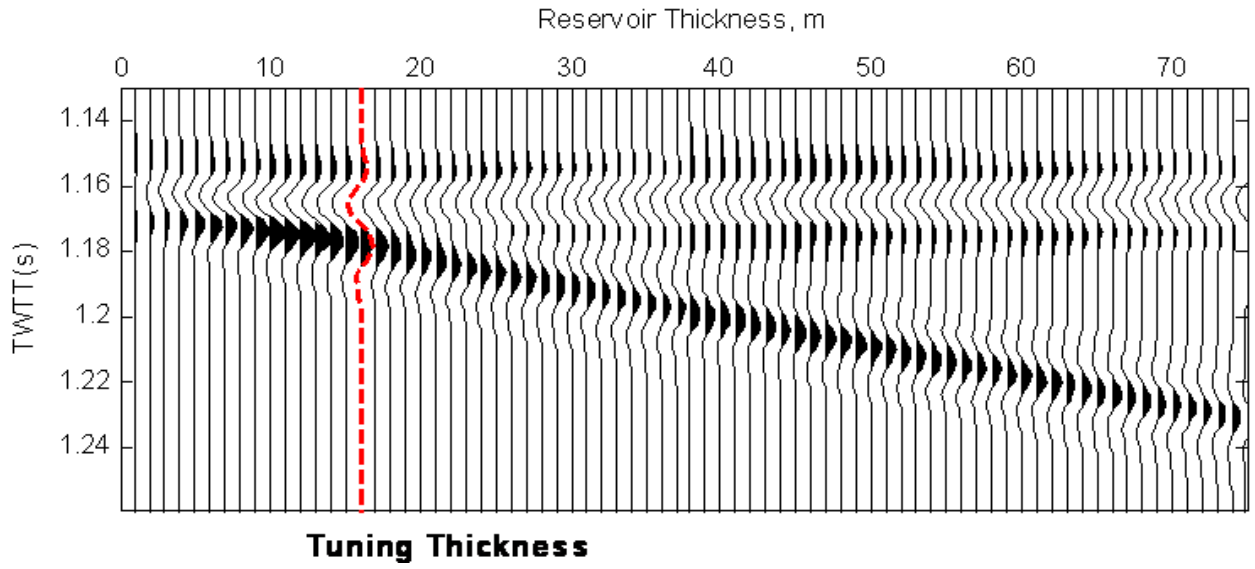


Figure 4-8 Reflectivity off a top and base-reservoir reflector for a reservoir of varying thickness. The wavelet is a 40Hz Ricker wavelet and the velocity in the reservoir is 2500 m/s

4.4 Fizz-gas Effect

The fizz-gas effect makes distinguishing commercial (mobile) and residual gas saturations from seismic data difficult. In the case of CO_2 sequestration it is differentiating residually (30%) and structurally (60%) trapped CO_2 which is of interest. In addition the fizz gas effect hinders attempts to determine the volume of CO_2 stored at sequestration sites from the zero-offset reflectivity. The high sensitivity to small amounts of gas is due to the very high compressibility of gas in comparison to brine. Methods have been developed in attempts to distinguish commercial and residual gas saturations for hydrocarbon exploration which were discussed in Section 2.5.2, such as the use of AVO data, converted waves and attenuation. One potential issue is that these methods rely on the large density decrease when gas is present, which increases V_s. However as shown in Figure 4-3 this large density is not present for supercritical CO_2.

The previous examination of reservoir depth indicated that the relationship between P-wave impedance and CO_2 saturation is more gradual for supercritical CO_2 than gaseous CO_2, indicating that the P-wave impedance may be of use when attempting to distinguish different saturations of supercritical CO_2. Here three methods are examined to see if they would be useful to determine the CO_2 saturation at a sequestration site: the zero-offset seismic reflectivity (Section 4.4.1), the far-offset response including the use of converted waves (Section 4.4.2) and attenuation (Section 4.4.3). The saline aquifer was assumed to be at 1500 m depth and its properties were previously given in Table 4-1. The reservoir was 100 m thick and fully saturated with the defined quantity of CO_2.

4.4.1 Zero-offset Seismic Response

The time-lapse zero-offset seismic response can be quantified by two pieces of information: the change in the reflection amplitude and the change in the traveltime in the reservoir, i.e. the pushdown. The zero-offset reflectivity was predicted for high and low saturations (Figure 4-9).

The pre-injection brine-filled top-reservoir reflection coefficient was -0.035 whereas following 30% CO_2 injection it was -0.13 and following 60% CO_2 injection it became -0.14. Therefore the change from brine-filled to containing residually trapped CO_2 was very large, but the move to saturations typical of structural trapping resulted in a minimal change in reflection coefficient. Increasing the CO_2 saturation from low to high only decreased the P-wave impedance by 2.4%, which probably cannot be detected.

The maximum base-reservoir pushdown was 16 ms produced by 60% CO_2, though the large majority of this pushdown was produced by the first 30% CO_2. The change from low to high saturations produced a pushdown of 5 ms on the base-reservoir reflection. Chadwick et al. (2005) found that the pushdown was sensitive to CO_2 saturation. This indicates that with a thick plume, pushdown could differentiate high and low saturations. However this model assumes a constant saturation throughout the reservoir which is unrealistic and variable saturations would complicate the analysis.

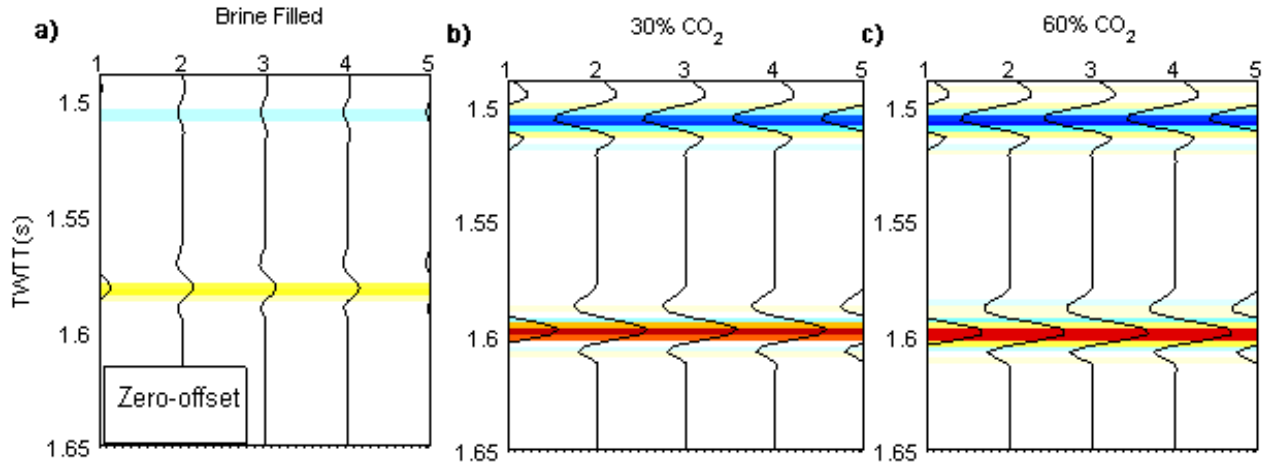


Figure 4-9 Zero-offset reflectivity for a 100 m thick clastic saline aquifer found at 1500 m depth for different saturation states, a) brine-filled, b) Residually trapped 30% CO_2, c) Structurally trapped 60% CO_2.

4.4.2 AVO and Converted Waves.

The far-offset response has been shown to have a higher sensitivity to an extended range of CO_2 saturations than the zero-offset seismic response (Brown et al. 2007). Plotting the V_p/V_s ratio against saturation should indicate the sensitivity at mid-offsets (Figure 4-10). The ratio had a similar sensitivity to saturation as P-wave impedance.

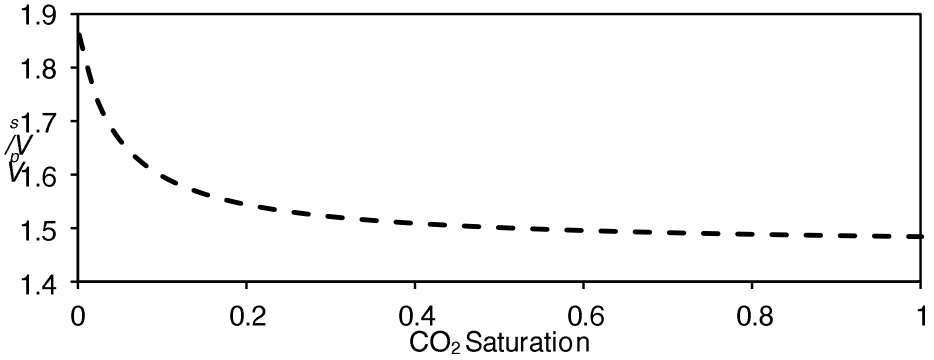


Figure 4-10 V_p/V_s ratio against CO_2 saturation.

To verify that the mid-offset P-wave reflectivity was not much more sensitive to the saturation than the zero-offset response, the AVO response was plotted for a range of saturations out to 30˚ offset angle (Figure 4-11a). The mid-offset response appeared just as insensitive to CO_2 saturations as the zero-offset response. At non-normal incidence wave conversions can occur, and converted waves have been used to distinguishing residual and commercial gas saturations (Gomez and Tatham 2007; González et al. 2003). The converted shear-wave reflectivity is plotted in Figure 4-11b. The shear wave reflectivity was much more sensitive to CO_2 saturation than the P-wave reflectivity, however its magnitude was small and undetectable. At shallower depths where V_s is more sensitive to CO_2 saturation there may be a stronger mode conversion.

Three-term AVO analysis, using the curvature (*C*) was suggested as a method to distinguish commercial (mobile) and residual gas saturations (Roberts 2000). This technique determines the density by subtracting *C* from the intercept *A* (Figure 4-12). *A*-*C* varied linearly with saturation, and could be used to quantify the volume of trapped CO_2. Unfortunately because of the relatively small density contrast between brine and supercritical CO_2 the variations in *A*-*C* were too small to be detectable. There are other issues with this approach, mainly that the large offsets required to determine C are not commonly recorded at sequestration sites and would in any case have a poor signal-to-noise ratio (Avseth et al. 2005).

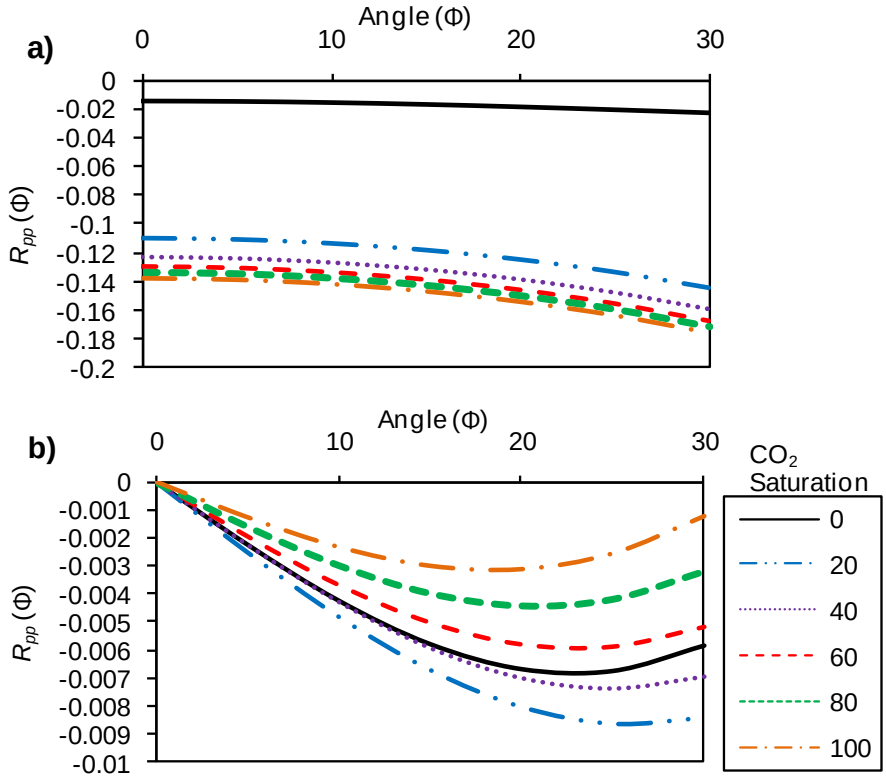


Figure 4-11 Angle-dependent reflectivity plotted against incidence angle for CO_2 saturations from brine-filled (blue), and every 10% up to 80% CO_2 saturation

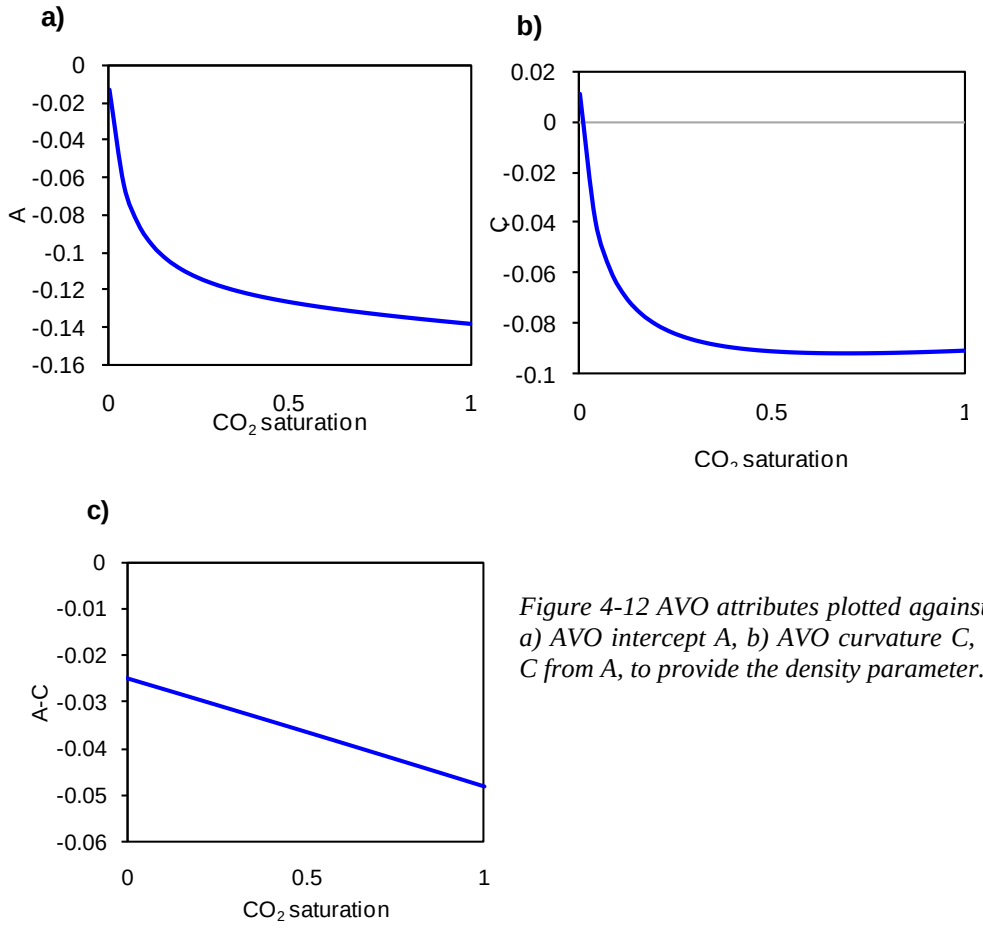


Figure 4-12 AVO attributes plotted against CO_2 saturation, a) AVO intercept A, b) AVO curvature C, c) subtraction of C from A, to provide the density parameter.

4.4.3 Attenuation

Laboratory measurements and modelling has suggested that residual gas saturations produce greater attenuation than mobile gas saturations (Avseth et al. 2005). To examine this, attenuation due to mesoscopic loss was predicted using the White (1975) model (Section 3.3.3.2.2.) for both gaseous and supercritical CO_2 and for a range of heterogeneity sizes (Figure 4-13). The greatest attenuation for gaseous CO_2 occurred at low saturations and large patch sizes. For supercritical CO_2 the peak attenuation was at about 10% saturation, which agreed well with the results from Carcione et al. (2006), while the peak attenuation for gaseous CO_2 was at 2% saturation.

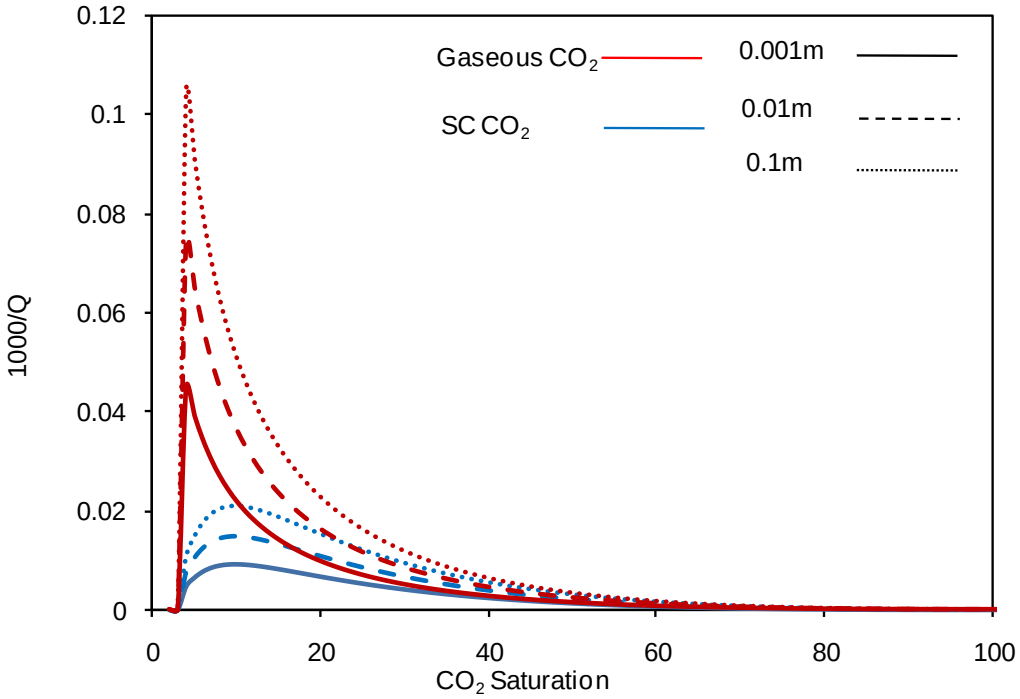


Figure 4-13 Attenuation resulting from mesoscopic loss, plotted for gaseous and supercritical CO_2, with different size saturation heterogeneities. Predicted using the White model for patchy saturation (frequency:40 H)z.

4.5 CO_2 Trapping and Phase Changes

In this Section the sensitivity of different seismic properties to CO_2 phase was examined, along with whether CO_2 dissolution will produce a detectable response. Mineralisation was not examined as the mineralogy of this saline aquifer makes mineralisation unlikely.

4.5.1 CO_2 Phase

CO_2 trapped in its own phase can be gaseous or supercritical. At about 800 m depth CO_2 undergoes a transition between these phases and around this point the CO_2 properties are very sensitive to changes in temperature and pressure. To examine the effect of CO_2 phase, an aquifer whose properties were appropriate for a reservoir depth of 1000 m (Table 4-1) was modelled using two different sets of CO_2 properties: gaseous CO_2 (500 m depth in Table 4-1) and supercritical CO_2 (1000 m depth in Table 4-1).

Figure 4-14 shows the effect of phase on the relationship between CO_2 saturation, the seismic velocities and V_p/V_s ratio. Gaseous CO_2 produced a much larger increase in V_s than supercritical CO_2. The V_p-S_{CO2} relationship was sensitive to phase. Small amounts of gaseous CO_2 greatly decreased V_p, then when more CO_2 was added V_p began to increase. On the other hand the addition of supercritical CO_2 only decreased V_p. The change in V_p indicated some potential issues with interpretation, as at saturations below 50%, gaseous CO_2 produced higher velocity changes than supercritical CO_2 while above 50% the relationship reversed. The V_p/V_s ratio was sensitive to CO_2 phase, with a lower ratio for gaseous CO_2 than supercritical CO_2, indicating that the AVO response at moderate angles may be useful in determining the phase (Ravazzoli and Gómez 2011).

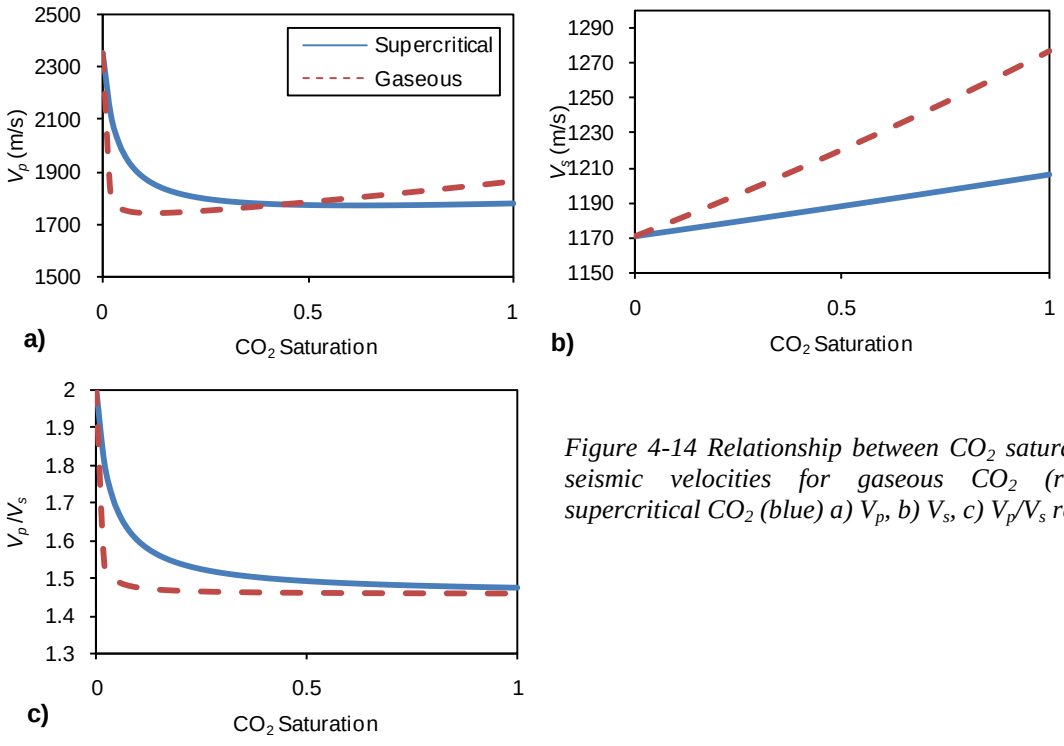


Figure 4-14 Relationship between CO_2 saturation and seismic velocities for gaseous CO_2 (red) and supercritical CO_2 (blue) a) V_p, b) V_s, c) V_p/V_s ratio.

The introduction of CO_2 into the pore space significantly altered the top-reservoir AVO response, producing large changes in both the intercept (*A*) and gradient (*B*), irrespective of the phase (Figure 4-15c). Figure 4-15a shows that for a defined quantity of CO_2, gaseous CO_2 always produced a higher zero-offset reflectivity that supercritical CO_2. It also demonstrates a non-uniqueness since the same *A* value were generated by combining the phase and saturation in different ways. The relationship between *B* and S_{CO2} for the different phases was more complicated. At low saturations (<50%) gaseous CO_2 predicted larger changes in *B* than supercritical CO_2, however at high saturations (>50%) supercritical CO_2 predicted larger changes in *B* than gaseous CO_2. As both these AVO attributes depend on phase, cross-plotting of *A* and *B* could produce a response unique to the phase (Figure 4-15d). Supercritical CO_2 produced smaller changes in *A* than gaseous CO_2 for nearly all saturations, but at high saturations (>40%) gaseous CO_2 had a smaller decrease in *B* than supercritical CO_2. Therefore a very large change in zero-offset reflectivity, accompanied by a smaller than expected change in the far-offset reflectivity could indicate gaseous CO_2 present at high saturations.

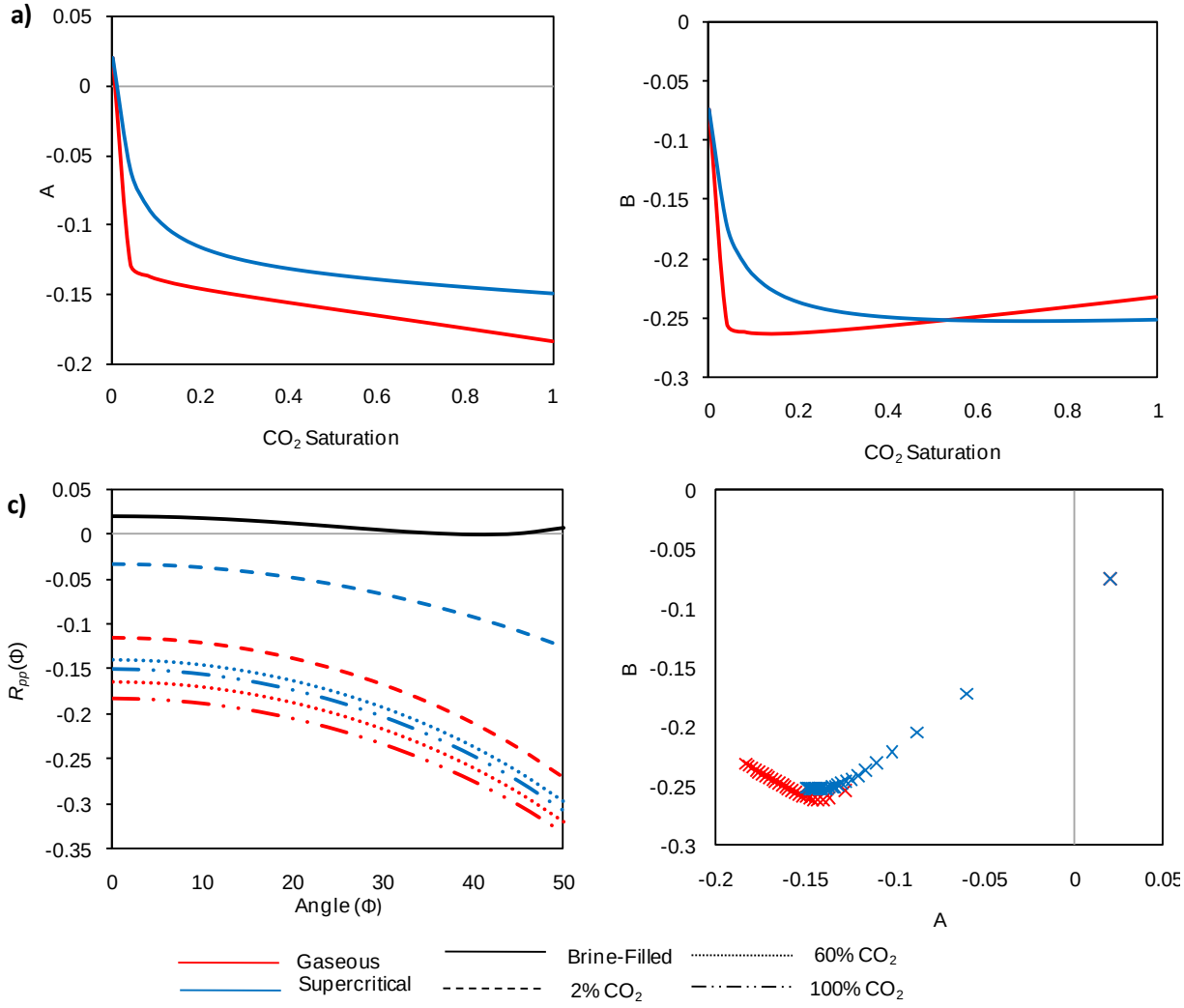


Figure 4-15 AVO behaviours as a function of saturation for gaseous (red) and supercritical CO_2 (blue) a) AVO intercept A, b) AVO gradient B, c) Angle dependent top reservoir reflectivity plotted against incidence angle out to 50°, for a brine-filled reservoir (black) and a reservoir containing varying amounts of CO_2, d) A cross-plotted with B, for different CO_2 saturations from 0% CO_2 to 100% CO_2 in 4% increments.

4.5.2 Solubility Trapping

In this preliminary examination of the impact of CO_2 dissolution on brine properties, recent experimental results (Sun and Han 2009), which are appropriate for pure water were used to predict the effect of CO_2 dissolution on brine properties. The impact of the subsequent reduction in CO_2 saturation and the dissolution of susceptible minerals were ignored. The elastic properties of pure water were predicted using the Batzle- Wang equations (Equations 3-50 to 3-55) and the properties of the CO_2 saturated water were found using the approach given in Section 3.4.3. The difference between the density, bulk modulus and velocity of the pure water and CO_2-saturated water is plotted in Figure 4-16. The velocity of CO_2-saturated water was higher than that of pure water below 60°C. The relationship then reversed above this temperature, where the density of water saturated with CO_2 was about 1-2% higher than that of pure water; this causes convective mixing in the reservoir. The dissolution of CO_2 into brine increased the bulk modulus.

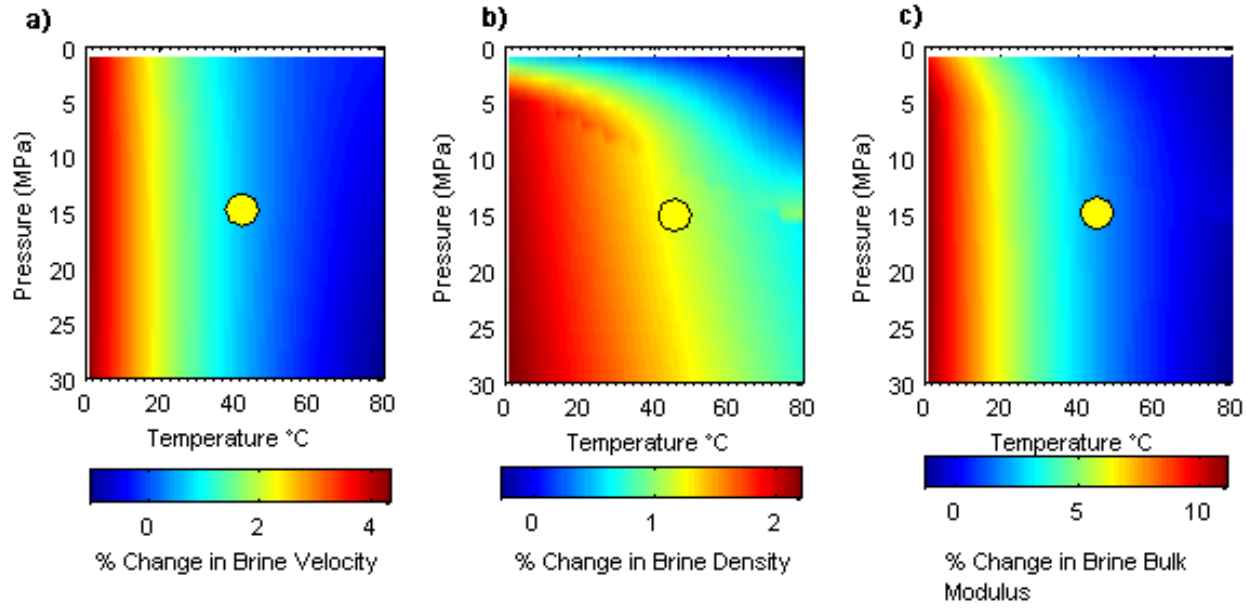


Figure 4-16 Percentage difference in fluid properties between brine and brine saturated with CO_2,for the temperature range 0-80°C and the pressure range 0-30 MPa: a) velocity, b) density, c) bulk modulus. Marked on is the temperature and pressure conditions for a reservoir at 1500 m depth.

The temperature and pressure conditions for the aquifer at 1500 m depth are marked on Figure 4-16. At this point the impact that changes in brine properties would have on the overall seismic response was calculated. The reservoir properties at a depth of 1500 m are shown in Table 4-1. The fluid properties used were bulk modulus of pure water (2.45 GPa), density of pure water (992 kg/m^3), bulk modulus of CO_2 saturated water (2.47 GPa) and the density of CO_2 saturated water (1002 kg/m^3). The approximate overall rock velocities were quickly estimated from these fluid properties using the Wyllie time average equation (Wyllie and Gregory 1956). This approximates the traveltime of a wave passing through a rock by calculating the volume-weighted average of the travel times through a layer of solid rock and a layer of pore fluid:

$$\frac{1}{V_p} = \frac{\Phi}{V_{pfluid}} + \frac{1-\Phi}{V_{pgrain}} \quad 4\text{-}1$$

where

$$V_{pfluid} = \left(\frac{K_{fluid}}{\rho_{fluid}} \right)^{1/2} \quad 4\text{-}2$$

and

$$V_{pgrain} = \left[\frac{3K_{grain} + 4\mu_{grain}}{3\rho_{grain}} \right]^{1/2} \quad 4\text{-}3$$

The Wyllie time average equation usually overestimates velocity (Jaeger et al. 2007), and here it predicted a velocity of 3204 m/s for pure-water and 3202 m/s for CO_2 saturated brine. This very small difference in velocity was also mirrored by a small change in density, indicating that both changes would be very difficult to detect at 1500 m. To examine the detectablity at other reservoir depths the P-wave impedance change was plotted for a range of temperature and pressures (Figure 4-17). The predicted changes in P-wave impedance were also small and were likely to be undetectable. Thse results are for pure-water, so the behaviour in brine may be different. Also a full examination of the effect of CO_2 dissolution should take into account any porosity and mineral composition changes resulting from the dissolution of susceptible minerals. However it is assumed that dissolution of CO_2 in brine would have minimal impact on the seismic response and is therefore ignored in subsequent studies.

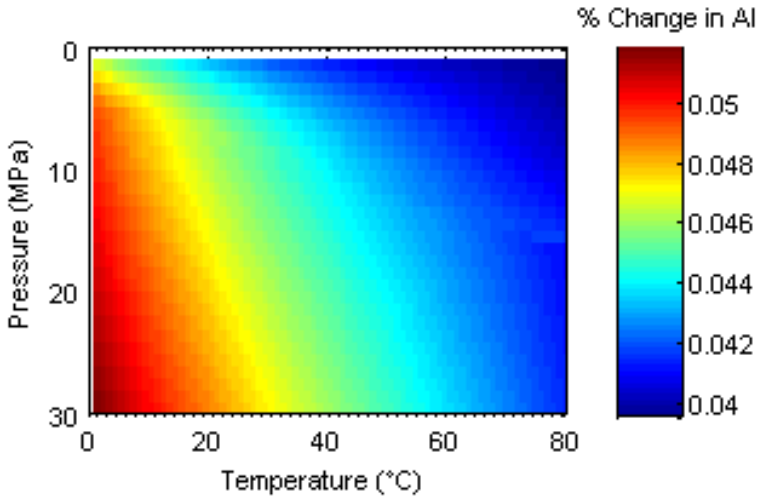


Figure 4-17 Percentage change in P-wave impedance from brine-filled to containing brine saturated with CO_2, for a range of temperatures and pressures,

4.6 Conclusions

A rock physics sensitivity study was conducted to examine the use of the time-lapse seismic method at clastic sequestration sites. Three issues were investigated: the importance of reservoir properties, the fizz-gas effect and CO_2 phase. The resulting effect on the seismic response was used to place limitations on monitoring ability and highlight the best seismic property to detect CO_2-related subsurface changes.

First, the modelling approach was compared to the results from a rock physics study of CO_2 injection into an unconsolidated Utsira-like sandstone (McKenna et al. 2003). The results appeared very similar, with any discrepancies likely to be the result of using slightly different mineralogies. This initial numerical model was then modified to consider a stiffer sandstone, improved prediction of CO properties and a shale overburden to allow for more realistic reflectivity modelling. For the majority of this Chapter a homogeneous fluid distribution was assumed, therefore these results may not be true if the fluids are "patchily" distributed, this is examined in Chapter 6.

A brief discussion highlighted lithology, porosity, pore-fluid type, level of consolidation and reservoir thickness as key reservoir controls on the seismic sensitivity to fluid content. Reservoir depth influenced most of these properties, so the seismic response to CO_2 injection was predicted for a range of depths (500 m to 2500 m). V_p was substantially more sensitive to fluid content than V_s at all depths. The negative relationship between V_p and S_{CO2} was governed by the fizz-gas effect making extraction of saturation information impossible, whereas V_s increased in a quasi-linear fashion with S_{CO2}. Injection into a shallow reservoir (500 m) produced large changes in both V_p (-35%) and V_s (12%). However the magnitude of these changes decreased with depth, and at 2500m V_p decreased by about 10% and V_s increased by about 1%. The ability to monitor small amounts of CO_2 using the zero-offset reflectivity also decreased with depth, although at 2500 m 3% CO_2 could still be detected. The base-reservoir pushdown was sensitive to CO_2 saturation. The zero-offset reflectivity demonstrated that monitoring becomes more challenging at greater depths, with decreases in the amplitude changes and amount of pushdown. AVO analysis indicated that the zero-offset reflectivity (A) should be sufficient to detect CO_2 presence, with the gradient (B) being relatively insensitive to fluid content except at low saturations and shallow depths. The reflection amplitude increase with offset magnified the contrast between the pre-injection and post-injection responses. So if the zero-offset reflectivity is insufficient the far-offset response could be used to monitor plume migration. The tuning thickness for this data was 17 m, so accumulations below this thickness would complicate interpretation.

The importance of being able to determine the saturation is two-fold. First, in an ideal world the saturation would be determined using the seismic response to calculate the volume of CO_2 trapped and verify containment. Second, as residual and structural trapping are characterised by different saturations, it could help infer the dominant trapping mechanism. The zero-offset reflectivity, AVO response, converted waves and attenuation were examined to see if they were sensitive to CO_2 saturation for an aquifer at 1500 m depth.

The zero-offset reflectivity was used to try and distinguish residually and structurally trapped CO_2, but the move from 30% to 60% CO_2 only altered the P-wave impedance by about 2.4% and would be undetectable. The pushdown on the base-reservoir reflection was sensitive to saturation, however the model used here was unrealistic as it is unlikely the saturation would be constant in the reservoir. *B* was also insensitive to CO_2 saturation, but the density parameter derived by subtracting *C* from *A* varied linearly with saturation. Converted shear-wave reflectivity was also sensitive to saturation. However due to the low density contrast between supercritical CO_2 and brine, the change in both the density parameter and converted reflectivity with increasing saturation was very small. Attenuation was much higher at low saturations, and for gaseous CO_2 the maximum loss due to mesoscopic patchy saturation was at 2% CO_2, whereas for supercritical CO_2 it was at about 10% CO_2. There are issues with using attenuation information related to the fact that at these (low) seismic frequencies the amount of attenuation is small and because it is very difficult to reliably estimate attenuation from seismic surveys.

The issue of the CO_2 phase and trapping phase was then examined. The impact of CO_2 phase on the seismic response was interesting, as gaseous CO_2 always yielded higher changes in *A* than supercritical CO_2 for a defined saturation. However the *B* showed a different relationship and at low saturations (<50%) gaseous CO_2 induced larger changes in *B* than supercritical CO_2, while at higher saturations the relationship was reversed. Cross-plotting *A* and *B* could help distinguish gaseous and supercritical CO_2, with a high *A*, but lower than expected *B* being indicative of large accumulations of gaseous CO_2. The issue of dissolution was examined for pure water using recent experimental results and it was found that it was not be possible to differentiate water saturated with CO_2 from pure water using the zero-offset response. However McKenna et al (2003) indicated that resultant physical changes, such as a porosity increase caused by the dissolution of susceptible minerals could be detectable.

In conclusion, the zero-offset reflectivity should be sufficient to achieve the first monitoring goal, i.e. it was very sensitive to small quantities of CO_2 at all depths and could be used to map plume location. As the response was still very sensitive at great depths gaseous CO_2 is not a requirement for safe monitoring. Unfortunately achieving the next monitoring goal of determining the saturation was more difficult. Most of the theoretical relationships tried were originally developed for accumulations of natural gas and were not appropriate for supercritical CO_2. The low density contrast between brine and supercritical CO_2 resulted in small changes in both the density parameter and converted shear wave reflectivity with increasing saturation. Although high attenuation could be indicative of low saturations, it is unlikely any losses will be detectable at the field-scale. Determination of the CO_2 phase, i.e. whether it is supercritical or gaseous was possible through cross-plotting *A* and *B*. Unfortunately as the dissolution of CO_2 into brine produced minimal changes in the zero-offset reflectivity quantifying the amount of CO_2 retained in this phase may not be possible. In summary it is possible to map the migration and determine the phase of the CO_2 using time-lapse seismic

surveys, however they may not be suitable for extracting more quantitative information regarding saturation and trapping mechanism. These results are summarised in Table 4-2

Table 4-2 Summary of the results from Chapter 4. Indicating the best seismic data to be collected to achieve certain monitoring aims. It is assumed that if non-zero offset reflectivity is collected so is the zero-offset reflectivity. The colours indicate the confidence assigned to the approach.. Green: Should Succeed, orange: May succeed, red: Unlikely this approach will work.

	Zero- offset Reflectivity		Mid-offset Reflectivity	Far-offset Reflectivity	Converted S-Waves	Attenuation
Monitoring Aim	Amplitude	Pushdown	Amplitude	Amplitude	Amplitude	Amplitude
Detecting CO_2 migration						
Distinguishing residual and structural trapping.						
Differentiating gaseous and supercritical CO_2						
Detecting CO_2 dissolution into brine						

5. Dynamic Reservoir Properties and the Time-lapse Seismic Response

The integrated modelling approach was used to examine the ability of time-lapse seismic surveys to detect and distinguish two dynamic changes in the reservoir during sequestration: fluid content and pressure. The pressure and saturation during CO_2 injection were predicted using commercial reservoir simulation software. Over 10 years 12.5 Mt of CO_2 was injected into a brine filled, 100m thick sandstone aquifer which extended 10 km by 10 km laterally. Injection induced pore-pressure increases of up to 8 MPa and high CO_2 saturations (~55%) within the structurally trapped portion of the plume. A rock physics study was used to predict the sensitivity of the seismic response to changes in pressure and saturation of this magnitude. This modelling approach allowed pressure increases to alter both the grain framework and fluid properties. Subsequently it also affected the relationship between the P-wave seismic velocity (V_p) and CO_2 saturation (S_{CO2}). Increasing the pressure magnified the changes attributed to CO_2 and therefore did not impact on the ability to detect plume migration.

V_p was much more sensitive to fluid content than the S-wave velocity (V_s). For example a substitution of 55% CO_2 for brine in the pore space resulted in a decrease of 16% in V_p, but a V_s increase of only 1%. By contrast V_s was slightly more sensitive to pressure changes than V_p, and a pore-pressure increase of 8MPa decreased V_p by 5-7%, and V_s by 6-10%. The time-lapse seismic response was predicted for two scenarios, one where the pressure was kept constant throughout sequestration and a second where the pressure was allowed to increase during injection (as predicted by reservoir simulation). Combined pressure and saturation changes produced a greater change in V_p, top-reservoir reflectivity and pushdown, than saturation changes alone. Also pressure increases altered the seismic response beyond the CO_2 plume, affecting both the top-reservoir and base-reservoir reflections. Anomalously large changes in reflectivity and pushdown, together with zero-offset changes away from the region saturated with CO_2 highlighted pressure build-up. As the two isotropic seismic velocities were sensitive to different dynamic changes in the reservoir (V_p was sensitive to saturation, V_s was sensitive to pore pressure), the AVO response at mid-offsets was examined to differentiate these effects from changes in the V_p/V_s ratio. Pressure build-up decreased the AVO intercept *A*, but increased the gradient *B*, while increasing CO_2 saturation decreased both and *A* and *B*. As a result cross-plotting *A* and *B* could be used to distinguish pressure and saturation changes and enable the detection of potentially dangerous pore-pressure build-up on a reservoir scale.

5.1 Introduction

CO_2 injection induces changes in and around the reservoir. These changes are not only in reservoir fluid content, but also potentially: geochemical interactions (Kumar et al. 2005) and pore-pressure build-up (Vandeweijer et al. 2009). Within this Chapter the time initially after injection was examined, with the focus on changes in fluid content and pore pressure within the reservoir interval and the impact on the time-lapse seismic response. At these early times mineralisation is unlikely to be important and was neglected. Similarly dissolution of CO_2 in the brine is ignored due to the results of the sensitivity study (Section 4.5).

The effect of changes in fluid content on the seismic response was examined in Section 4.2 using a rock physics sensitivity study and assuming a homogeneous fluid distribution. Here this examination was extended using saturation maps generated by fluid-flow simulation. Pore-pressure build-up was identified in Section 2.5.4 as a potential danger associated with sequestration (Vandeweijer et al. 2009), and a possible impediment to monitoring fluid migration (Wulff et al. 2008). In this Chapter a rock physics sensitivity study, similar to that in Section 4.2 is conducted for pore pressure. Then the dynamic properties predicted by reservoir simulation are incorporated to predict the time-lapse seismic response.

A geological model was used to predict the properties of a sandstone reservoir at 1500 m depth (Section 5.2.1). Using these properties a reservoir model was created for fluid-flow simulation (Section 5.2.2). The modelling approach is outlined in Section 5.2.3. Time-dependent saturation and pressure maps of the reservoir were generated by the fluid-flow simulation (Section 5.3). Using values for the typical pressure and saturation changes, the sensitivity of the seismic response to these dynamic properties was established in Section 5.4. The sensitivity of the seismic velocities to saturation changes was quantified (Section 5.4.1), then the effect of the pore-pressure increase on the frame and fluid properties was explored (Section 5.4.2). The time-lapse seismic response was predicted in Section 5.5. The seismic velocities were then decomposed into the saturation changes and pressure effects on both the fluid and grain framework (Section 5.5.1). Using the velocities and the densities the zero-offset reflectivity was predicted for two scenarios, first, one where the pressure was kept constant during injection and second where the pressure increased (Section 5.5.2). The AVO response was then predicted for both these scenarios, to determine whether it could be of use to differentiate saturation and pressure changes (Section 5.5.3).

5.2 Modelling Approach

5.2.1 Geological Properties

The reservoir was a 100m thick, homogeneous, clean sandstone saline aquifer, surrounded by shale and found at 1500m depth. A "generic" mineralogy for both the shale and sandstone were used (Table 3-4). The reservoir properties were calculated using relationships given in Section 3.5 and the pre-injection conditions are recorded in Table 5-1. A large aquifer (10km by 10km by 100m) was investigated to help ensure that pore-pressure build-up did not exceed the fracture pressure.

Table 5-1 Pre-injection reservoir properties for an aquifer found at 1500 m depth. Average temperature and lithostatic pressure within the reservoir are included, while the porosity and permeability are assumed to be constant.

Pre-Injection Properties			
Temperature		°C	50.5
Pressure	Lithostatic	MPa	31.7
	Pore	MPa	15
Porosity			0.31
Permeability	Horizontal Vertical	mD mD	570 57

5.2.2 Reservoir Model

The dynamic changes in this saline aquifer were predicted using ECLIPSE, with the aquifer being represented by 500,000 grid blocks, see Table 5-2. The finer resolution in the vertical direction was required to resolve the gravity override of the less-dense CO_2 over brine and the lateral extent of the plume (Fayers and Muggeridge 1990; Yamamoto and Doughty 2011). Injection was into the middle of the reservoir at a rate of 1.25Mt/year for 10 years, then the simulation continued for another 10 years to model the dispersal of the plume. If the well pressure exceeded 90% of the fracture pressure (24.5MPa), then injection would cease (Bruce and Bowers 2002). The arrangement of the simulation study is illustrated in Figure 5-1

Table 5-2 Inputs into ECLIPSE. Number refers to number of gridblocks, dimensions gives the gridblock dimension, wells, X and,Y, give well location, Z1 and Z2 give the interval over which the well is open in the reservoir, I/P represented injector/producer, tstep gives the timesteps for the calculation, R/P gives information on the controls on the well, either rate or pressure, and finally O/C states whether the well is open or closed for that time period.

Grid						**Wells**								
Number			Dimensions											
X	Y	Z	X	Y	Z	X	Y	Z1	Z2	I/P	TSTEP	R/P		O/C
100	100	50	100	100	2	50	50	1	50	INJ1	10*365	RESV	4305	OPEN
										INJ1	1*3650			CLOSED

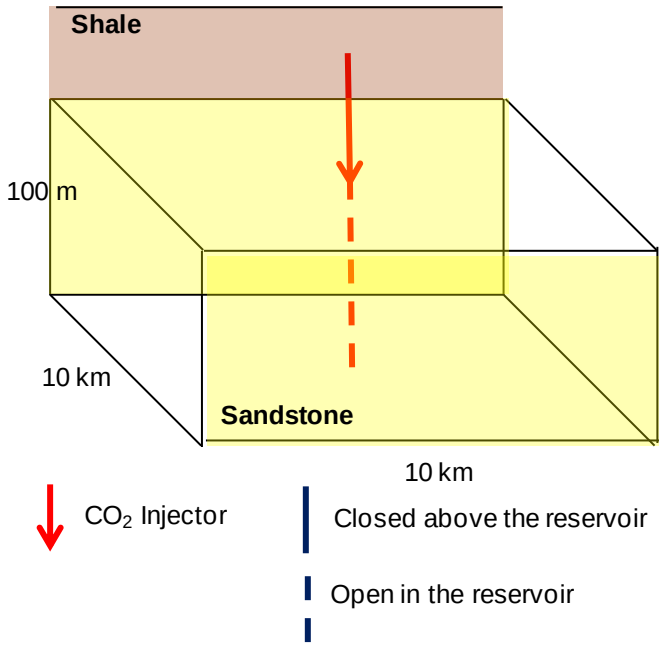


Figure 5-1 Simulation layout, it was assumed there was no flow across the boundaries.

5.2.3 Rock Physics Modelling

The modelling approach used to predict the elastic properties of the reservoir was given in Sections 3.3 and 3.4, and the "pre-injection" elastic properties are stated in Table 5-3. These elastic properties were combined using the Gassmann-Reuss approach (Section 3.3.3.1), thereby assuming a homogeneous fluid distribution.

Time-dependent pressure and saturation values obtained from fluid-flow modelling were used to predict the time-lapse seismic response. Temperature was assumed to be constant and CO_2 dissolution and mineralisation were ignored. Using the pressure and saturation values the elastic properties of each simulation grid block were predicted. Alterations in the fluid content changed the fluid bulk modulus whilst pore-pressure increases affected both the fluid bulk modulus and the grain framework moduli (Sections 3.3 and 3.4). Using these time-varying elastic properties the time-lapse seismic response was predicted for two different scenarios, one where pore pressure was kept constant during injection and a second when pore pressure was predicted by reservoir simulation.

Table 5-3 Pre-Injection elastic properties and densities of the fluids, mineral and frame properties at 1500 m depth, calculated assuming a hydrostatic pressure gradient.

Fluid Properties			
CO_2	Density	kg/m^3	705
	Bulk Modulus	GPa	0.0993
	Viscosity	Pa.s	5.80E-05
Brine	Density	kg/m^3	1009
	Bulk Modulus	GPa	2.55
	Viscosity	Pa.s	6.10E-04
Mineral Properties			
Sandstone	Bulk Modulus	GPa	36.9
	Shear Modulus	GPa	44
	Density	kg/m^3	2650
Shale	Bulk Modulus	GPa	33.4
	Shear Modulus	GPa	22.25
	Density	kg/m^3	2741
Frame Properties			
Sandstone	Bulk Modulus	GPa	3.5
	Shear Modulus	GPa	4.3
Shale	Bulk Modulus	GPa	3.9
	Shear Modulus	GPa	3.9

5.3 Saturation and Pressure over Time

Fluid-flow simulation provides information about the saturation and pressure changes in the reservoir at both the well and field scale. The predicted well pressure at the injection well as a function of time is shown in Figure 5-2a, and the amount of CO_2 injected is shown in Figure 5-2b. Fracture re-activation was an important consideration, but it can be seen that the simulation input controls are such that fracture pressure was not exceeded. Injection continued steadily for 10 years, and a total of 12.5 Mt of CO_2 was injected into the aquifer. Following this the simulation continued for another 10 years.

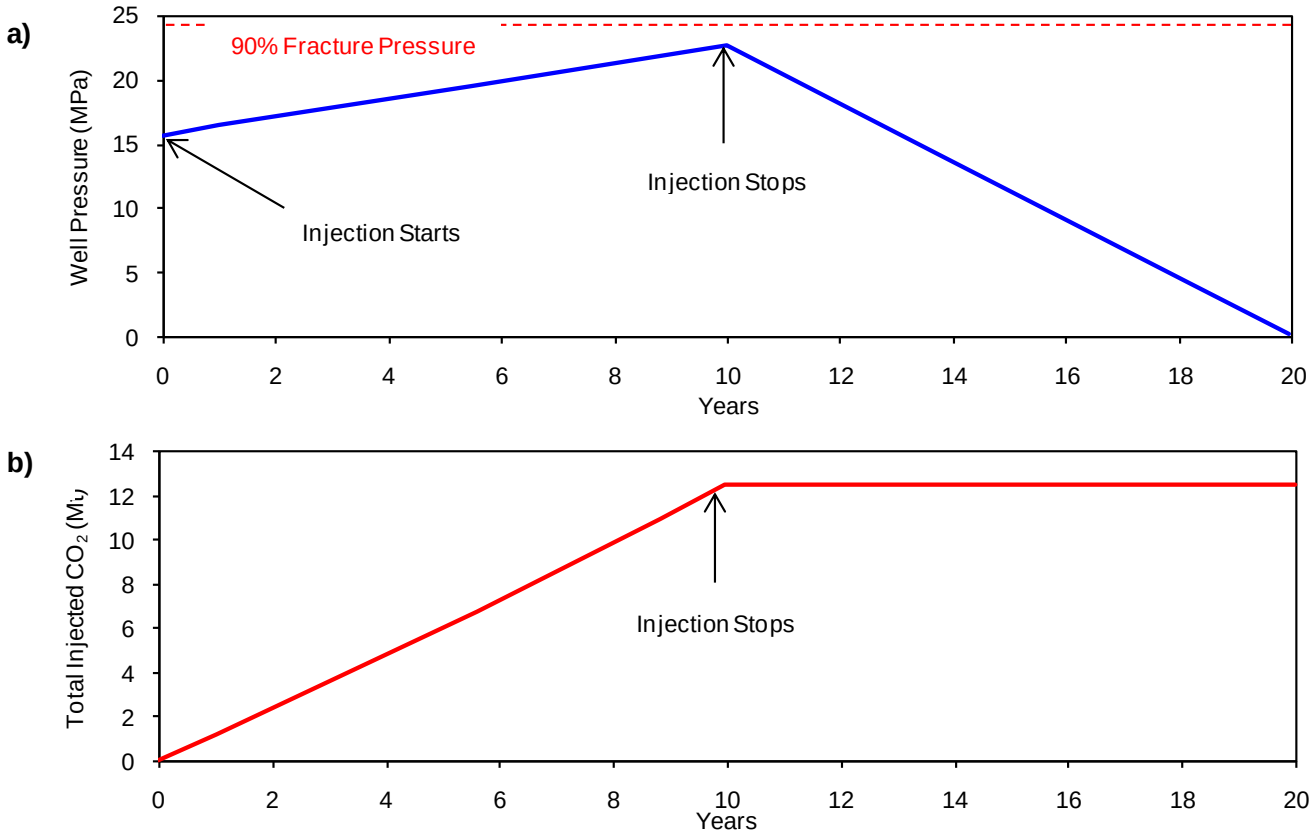


Figure 5-2 Injection well properties, for 10 years of injection and 10 years post-injection, a) well pressure, b) total injected CO_2.

The pressure increase from pre-injection conditions seen at the well was also present throughout the reservoir (Figure 5-3). Before injection the pressure was constant in the reservoir at about 15 MPa. Once CO_2 injection commenced, the pressure increased throughout the whole reservoir almost instantaneously due to the low water compressibility. There was a slightly larger pressure increase predicted near the injector. After injection stopped, the pressure increase spread uniformly throughout the reservoir. The aquifer modelled here was only 10km long and wide but in reality such aquifers may be more laterally extensive and in communication with other formations, in which case pressure build-up may dissipate over time. After 10 years of injection, the maximum pressure increase was about 8 MPa.

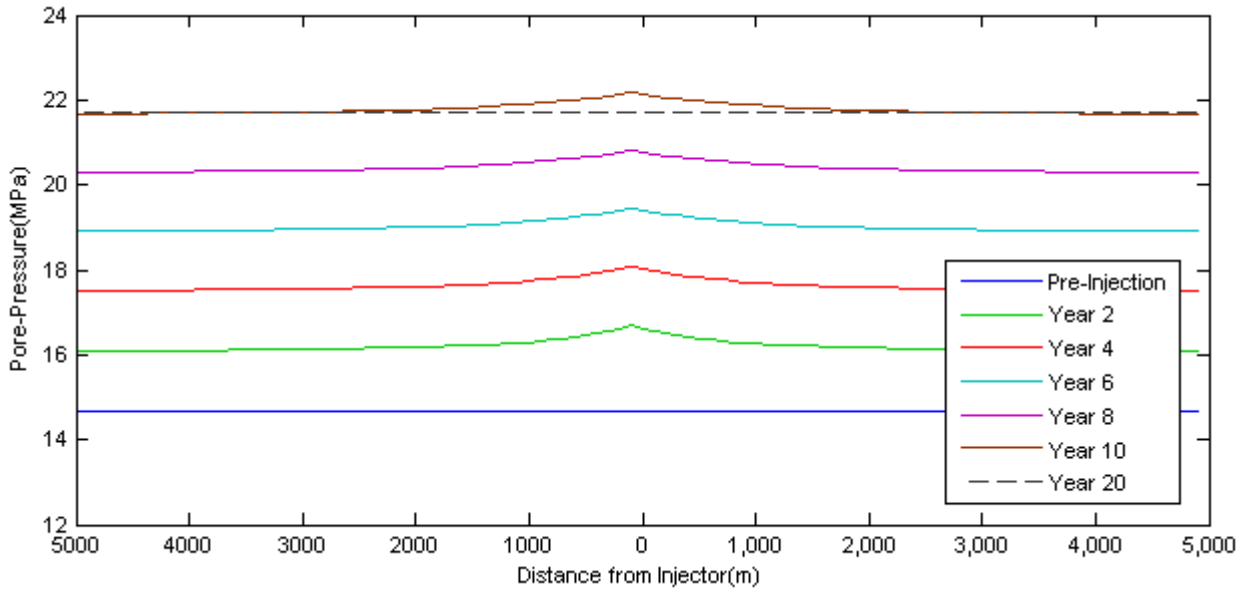


Figure 5-3 Change in pore pressure at the top of the reservoir from the injector. Pre-injection pressures are shown in blue, the pressure after a certain time of injection is in green (2 years), red (4 years), turquoise (6 years), purple (8 years) and brown (10years), the pressure 10 years after injection ceased is shown as a dashed black line.

Vertical sections taken through the 3D numerical results allowed the CO_2 saturation through the centre of the CO_2 plume to be examined (Figure 5-4). CO_2 was injected through a vertical injector in the middle of the reservoir. The CO_2 migrated laterally and rose via gravitational segregation to the top of the reservoir, pooling below the caprock and becoming structurally trapped. As more CO_2 was injected the plume grew, and the saturation in the structurally-trapped portion of the plume increased to almost 60%. Due to the presence of 40% connate water this saturation represented the maximum possible CO_2 saturation in the pore space. After injection CO_2 continued to rise to the top of the reservoir and became trapped via capillary forces at the trailing edge of the plume (Figure 5-4f). This residually-trapped portion of the plume had a low CO_2 saturation (~30%) compared to the structurally-trapped portion of the plume (~55%).

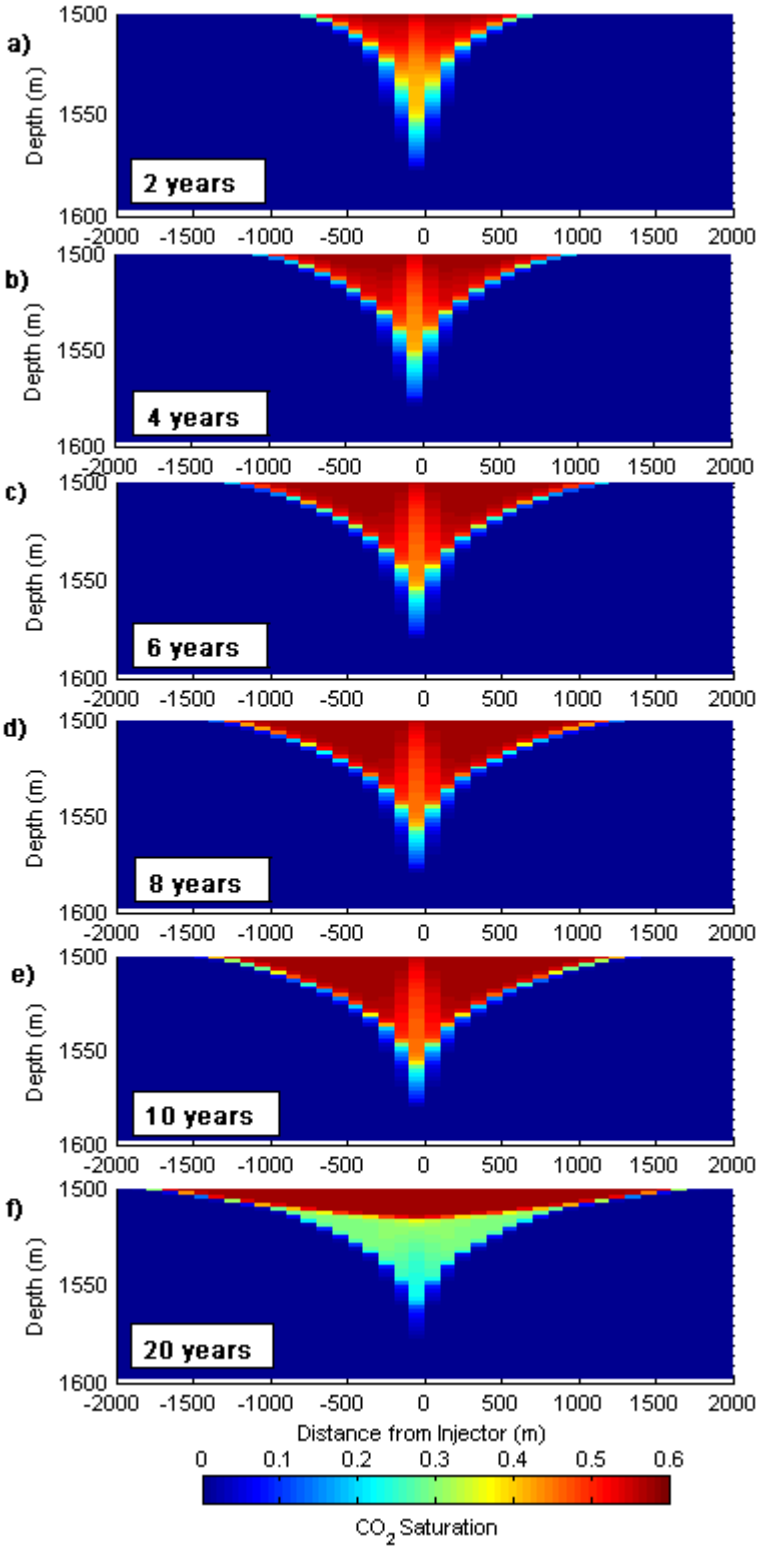


Figure 5-4 CO_2 saturation maps over the central portion of the reservoir: a) after 2 years, b) after 4 years, c) after 6 years, d) after 8 years, e) after 10 years, f) 10 years post-injection.

5.4 Sensitivity of the Seismic Response to Pressure and Saturation Changes.

The sensitivity of the seismic response to pressure and saturation changes due to CO_2 injection was assessed using the maximum pore-pressure increase of 8 MPa and maximum CO_2 saturation of 55% predicted by the fluid-flow simulation in the previous Section.

5.4.1 Sensitivity to Fluid Content

The change in the seismic velocities and V_p/V_s ratio which resulted from substituting brine for CO_2 in the pore space is shown in Figure 5-5. These results are similar to those in Section 4.4.1. V_p was very sensitive to small quantities of CO_2, and 30% CO_2 (typical of residual trapping) produced a decrease of about 18%, but subsequent additions of CO_2 had a minimal effect. By contrast V_s increased linearly with CO_2 saturation, with 100% CO_2 increasing V_s by about 2%. At the maximum CO_2 saturation of 55%, V_p decreased by about 19%, and V_s increased by only about 1%, showing that V_p was much more sensitive to CO_2 saturation than V_s. Increasing the CO_2 saturation decreased the V_p/V_s ratio.

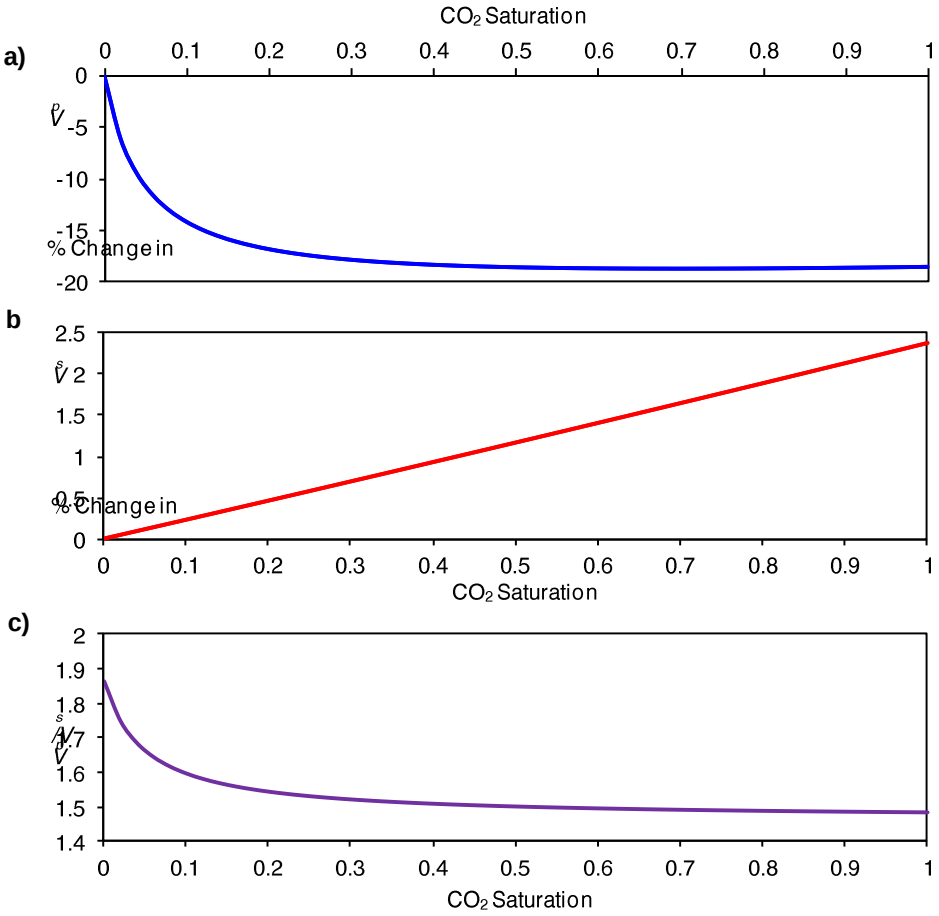


Figure 5-5 Percentage change in seismic velocities from brine filled against CO_2 saturation: a) P-wave velocity (V_p), b) S-wave velocity (V_s)

5.4.2 Sensitivity to Pressure

Pore-pressure increases have a two-fold impact on the seismic response, as both the pore fluid and frame properties vary with pressure. In Chapter 4 it was shown that the relationship between CO_2 saturation and V_p depended on the fluid phase (Figure 4-15a), so this relationship may evolve as the fluid properties change. To fully examine the effect of pressure changes, these three effects were considered.

Impact on fluid properties

The dependence of the fluid properties on the reservoir temperature and pressure is shown in Figure 5-6. Increasing the pressure increased the bulk modulus and density of the fluids. The fluid properties before and after injection are given in Table 5-4. CO_2 is more sensitive to pressure changes than brine.

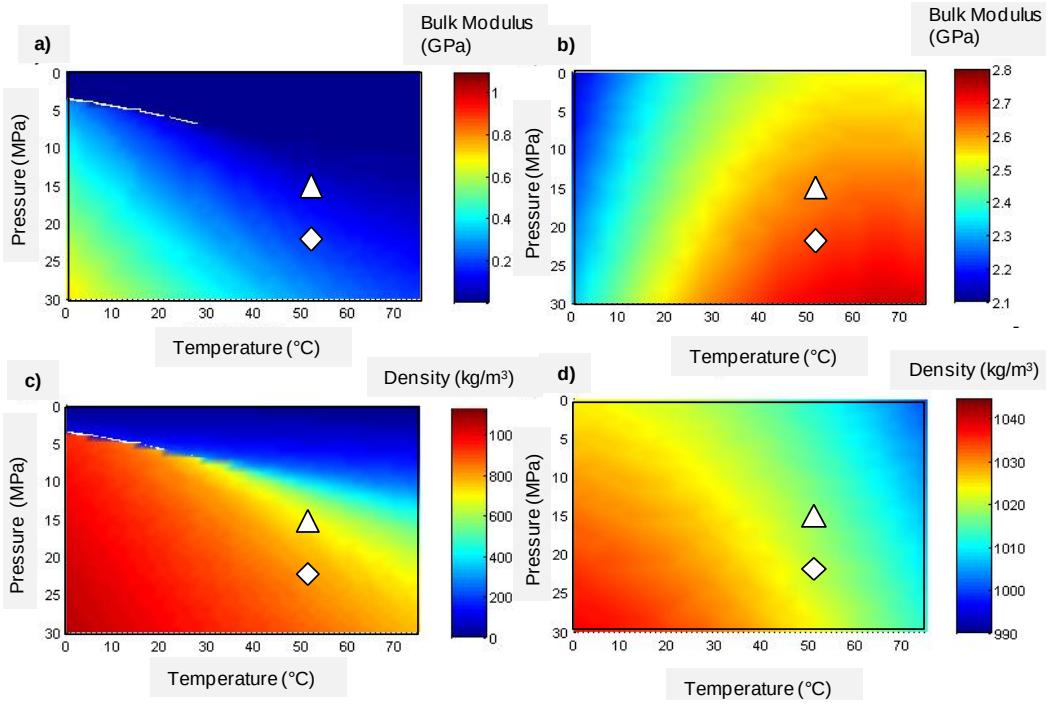


Figure 5-6 Fluid properties for the temperature range 0-75˚C and pressure range 0-30 MPa. The reservoir temperature and pressure before injection are indicated by a white triangle and after 10 years injection by a white diamond. a) CO_2 bulk modulus (GPa,) b) brine bulk modulus (GPa), c) CO_2 density (kg/m^3), d) brine density (kg/m^3).

Table 5-4 Fluid and frame properties calculated using the pressure before and after 10 years of injection.

			Pre-Injection	Post-Injection	% Change
CO_2	Density	kg/m^3	705	816	15.7
	Bulk Modulus	GPa	0.0993	0.20	117.1
Brine	Density	kg/m^3	1009	1013	0.3
	Bulk Modulus	GPa	2.55	2.59	1.9
Frame	Bulk Modulus	GPa	4.16 GPa	3.42GPa	17.8
	Shear Modulus	GPa	4.98 GPa	4.06GPa	28.5

Impact on grain framework properties

The effective stress is generally defined as the confining stress minus a fraction of *n* of the pore-pressure. However for shallowly buried rocks, such as those used here, *n (*effective stress coefficient*)* is close to 1 (Siggins and Dewhurst 2003), so this value is used for the modelling. The confining pressure was assumed to be lithostatic pressure (31.7 MPa) and was taken to be a constant during injection and identical in the horizontal and vertical directions. The average pre-injection pore pressure was 15.5 MPa, so the effective pressure was about 16 MPa. After 10 years of injection the pore-pressure was 22 MPa and the effective pressure was about 9 MPa.

The impact that decreasing the effective pressure from 16 Mpa to 9 MPa had on the seismic velocities is shown in Figure 5-7a-c. V_p was reduced by 150 m/s which was approximately a 5% decrease from pre-injection conditions. V_s also decreased by 150 m/s, which equated to a 6% decrease. Decreasing the effective pressure by 7 MPa increased V_p/V_s from 1.8 to 1.9. The percentage change in P-wave impedance caused by the pore-pressure was 5%, which was above the detectability limit, indicating that this pressure change between surveys could be identified.

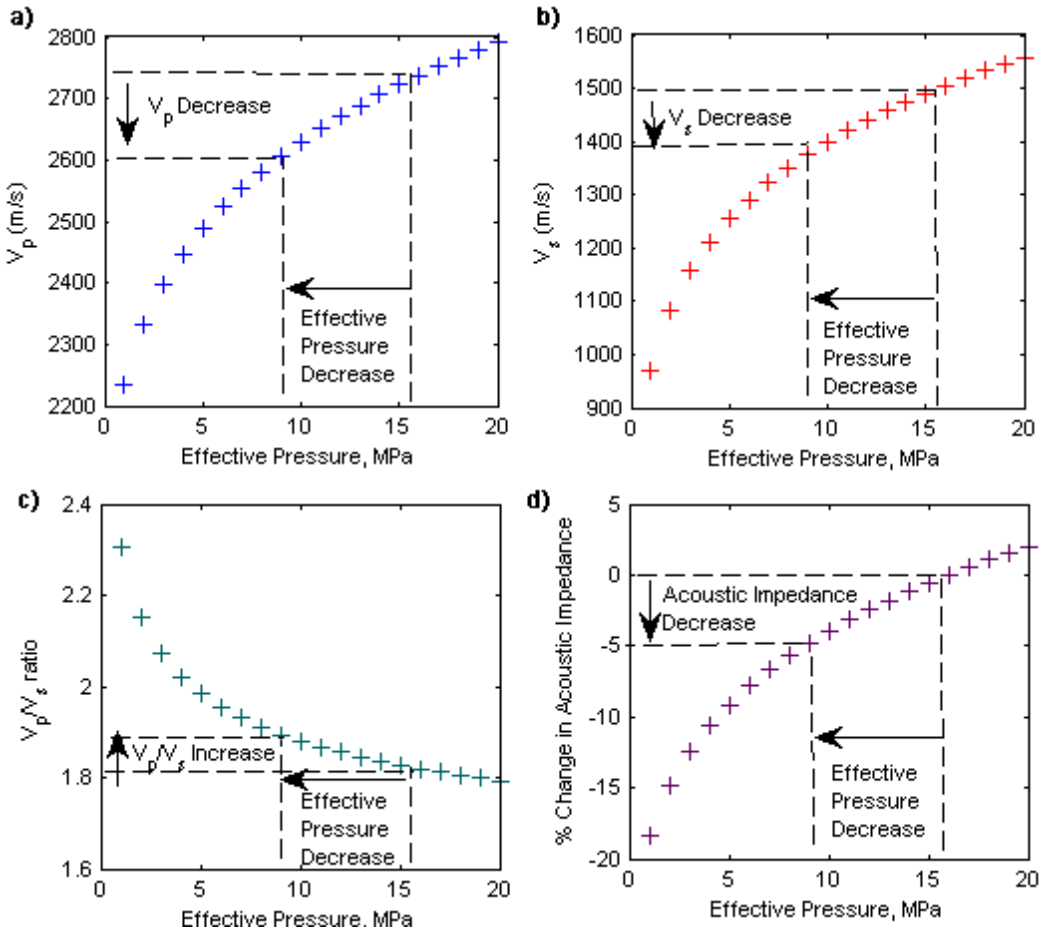


Figure 5-7 Effective pressure against the different attributes for a brine-filled reservoir: a) V_p (m/s), b) V_s (m/s), c) V_p/V_s ratio, d) percentage change in P-wave acoustic impedance from pre-injection conditions.

Interaction between pressure and saturation

Results from a feasibility study at the Enfield 4D monitoring project indicated that during hydrocarbon production the changes in saturation and pressure can interact to mask each other (Wulff et al. 2008). To study this, the change in P-wave impedance resulting from pressure changes on the grain framework and changes in CO_2 saturation were considered (Figure 5-8). During injection the effective pressure decreased, and all but very small saturation changes were detectable. However if the effective pressure increased then it could mask some small saturation changes. This sensitivity can be compared to other rock types (Alvarez and MacBeth 2012).

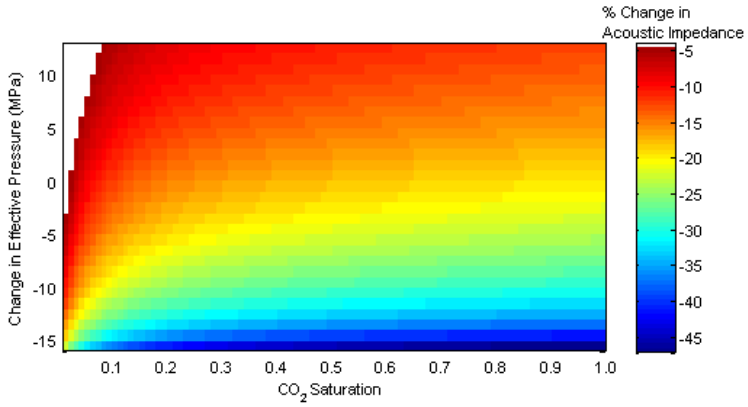


Figure 5-8 %change in P-wave acoustic impedance, for a brine-filled (pre-injection) reservoir, caused by changes in CO_2 saturation and effective pressure. Colours indicate a detectable change (>4%).

Impact on relationship between V_p and S_{CO2}.

The V_p- S_{CO2} relationship depends on the phase and properties of the CO_2. Pore-pressure increases had a minimal effect on brine properties, but substantially stiffened the CO_2 and increased its density (Table 5-4). This stiffening produced a more linear relationship between S_{CO2} and V_p, at higher pressures. The pore-pressure increase decreased the grain framework moduli, making the rock more sensitive to fluid content changes. Combining these two effects, i.e. the increasingly linear relationship and the greater sensitivity to pore fluids, produced a non-intuitive relationship between the percentage change in V_p and S_{CO2} (Figure 5-10). At low CO_2 saturations the increase in pressure produced smaller changes in V_p than before injection, but at high saturations the pressure increase introduced larger changes in V_p than at the original pressures.

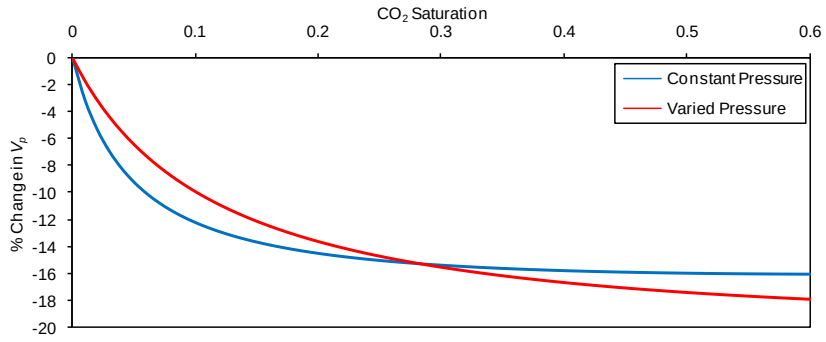


Figure 5-9 Relationship between CO_2 saturation and percentage change in V_p from pre-injection, i.e. brine-saturated pore-space, created using pre-injection pressures (blue) and post-injection pressures (red).

5.5 Time-lapse Seismic Response

The pressure and saturation values calculated during reservoir flow modelling were used to predict the seismic response after ten years of injection.

5.5.1 Seismic Velocities

The effect of pressure and saturation changes on the seismic velocities in and around the reservoir are illustrated in Figure 5-10 with the combined effect of both saturation and pressure changes being shown in Figure 5-10i-j. These changes were then decomposed into the effect of pressure changes on the fluids and the grain framework (Figure 5-10a-d), and the impact of changes in fluid content (Figure 5-10g-h).

The effect of pore-pressure increase on fluid properties appeared to be limited to the region saturated with CO_2 (Figure 5-10a-b), this was because CO_2 was more sensitive to pressure changes than brine (Table 5-4). The higher fluid density resulting from the increase in pore pressure produced a small decrease in V_s. The change in V_p was more complex due to the interesting relationship shown in Figure 5-9. Increasing pore pressure decreased V_p in the centre of the plume, where there are high CO_2 saturations, whereas at the edge of the plume, where the saturation were relatively low (<30%) V_p increased. Overall the velocity changes resulting from the changes in fluid properties were very small.

Reducing the effective pressure and its effect on the grain framework moduli, decreased both seismic velocities throughout the reservoir (Figure 5-10c-d). Due to the dependence of the V_p-S_{CO2} relationship on the pore pressure there was a slight concentration of the predicted velocity changes within the plume. The magnitude of the change in the velocities was substantial.

The net effect of pressure on both the fluid and frame properties is shown in Figure 5-10g-h. Pressure changes altered the velocities throughout the entire reservoir, with slightly greater changes being predicted within the plume. V_p decreased by 150-180 m/s (~5.5-7%) and V_s decreased by about 140-160 m/s (~10-11%). Saturation changes only effected the plume region, decreasing V_p by about 470 m/s (~18%) and 100 m/s (~4%) at the centre and edge of the plume respectively and increasing V_s by about 20 m/s (~1.5%) (Figure 5-10g-h).

The combined impact of saturation and pressure changes was to decrease V_p by up to 650 m/s (~25%) in the plume and by about 140 m/s (~5%) in the surrounding reservoir, whereas V_s decreased by about 140 m/s (~9.8%) within the plume and 160 m/s (~11.2%) in the surrounding reservoir.

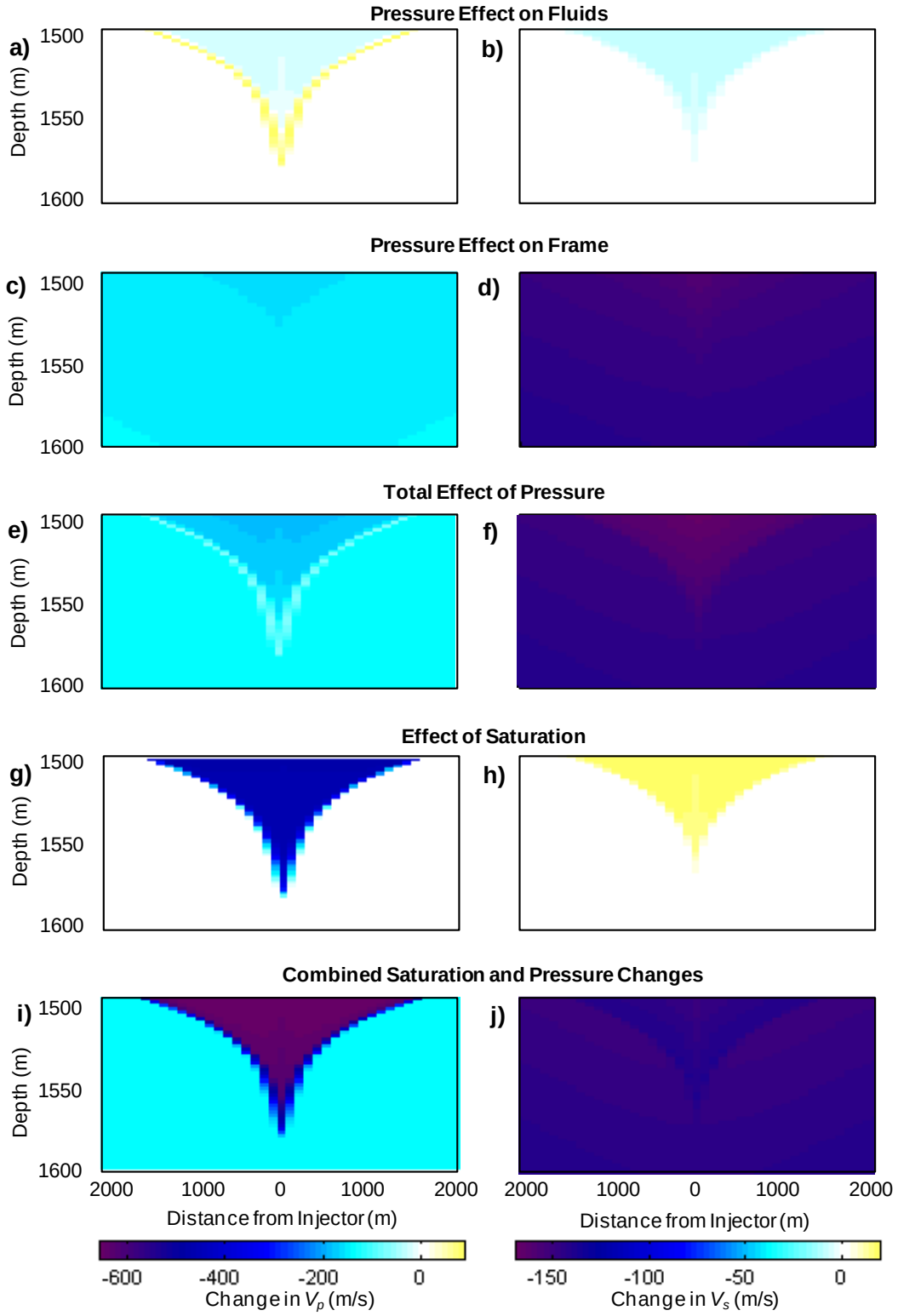


Figure 5-10 Diagrams illustrating how the seismic velocities in the reservoir change from pre-injection conditions after 10 years of injection, a,c,e,g,i) V_p, b,d,f,h,j) V_s. a,b) Pressure effects on fluid properties, c,d) pressure effects on the frame properties, e,f) total effect of pressure changes, g,h) effect of saturation, i,j) combined effect of pressure and saturation changes.

5.5.2 Zero-offset Reflectivity

To examine the ability to differentiate between pressure and saturation changes in the seismic response, the zero-offset reflectivity was predicted for two cases: first, a case with no pressure changes (Figure 5-11a&c) and second, allowing for both pressure and saturation changes (Figure 5-11b&d). Both the reflectivity after 10 years (Figure 5-11a&b) and the change in reflectivity from pre-injection conditions were plotted (Figure 5-11c&d).

CO_2 injection dramatically altered the top-reservoir reflection coefficient from a small positive value to a large negative one. At the base of the plume a positive reflection was generated between the structurally-trapped CO_2 and the brine-filled aquifer. When including the pressure increase, the change in top-reservoir reflectivity was even larger due to the greater overall decrease in V_p within the plume. The changes in reflectivity due to saturation changes were confined to the plume (Figure 5-11c), whereas pressure effects altered the top-reservoir and base-reservoir reflectivity away from the plume (Figure 5-11d). The increase in pressure altered the base-reservoir reflection coefficient from -0.001 to 0.02. Changing both the saturation and pressure conditions in the reservoir, increased the base-reservoir pushdown (Figure 5-12). The introduction of CO_2 produced a maximum base-reservoir reflection pushdown of 7 ms below the thickest portion of the plume, but no pushdown away from the plume. However pressure increases magnified the decrease in V_p and 12 ms pushdown was predicted below the plume. Away from the plume, the base-reservoir reflection was still pushed down by about 5 ms.

These results imply that pressure build-up could be inferred from changes in the reflection amplitude and pushdown away from the CO_2 plume, as well as anomalously high changes in the reflectivity. Determining whether the change in reflectivity is abnormally high would require knowledge of the reservoir properties, such as fluid properties, mineralogy and porosity.

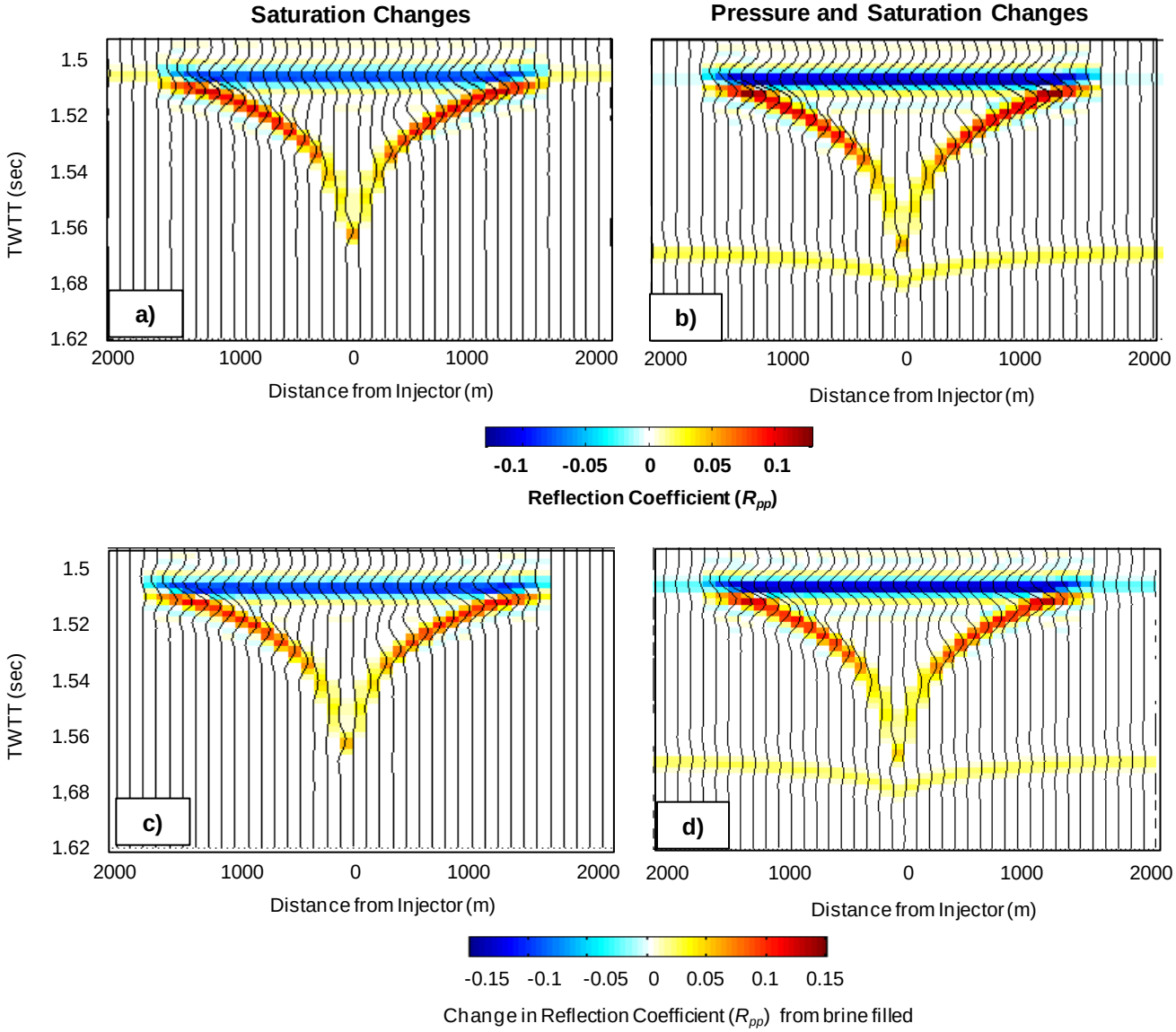


Figure 5-11 Zero-offset synthetic seismograms. a) After 10 years injection assuming constant pressure, b) after 10 years injection allowing pressure increase, c) change in the reflectivity (Figure 5-12a –baseline), from changes in saturation, d) change in reflectivity (Figure 5-12b-baseline), from changes in saturation and pressure.

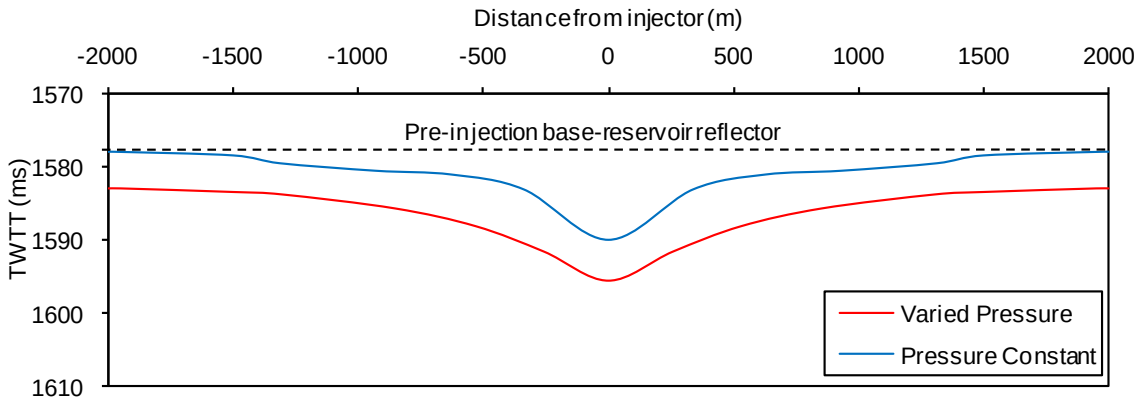


Figure 5-12 The base-reservoir pushdown assuming no change in pressure (blue) and allowing pressure to increase (red). Black dashed line represents the pre-injection base-reservoir reflection.

5.5.3 AVO Response

Figure 5-13 shows the changes in the seismic velocities, density and V_p/V_s ratio produced by changes in saturation and pore pressure. V_s appears to be the most useful seismic velocity to differentiate between pressure and saturation changes, but it is not normally directly available. However since pressure changes produced larger V_p changes, but lower V_p/V_s changes than saturation alone, the subsurface changes could be distinguished using AVO.

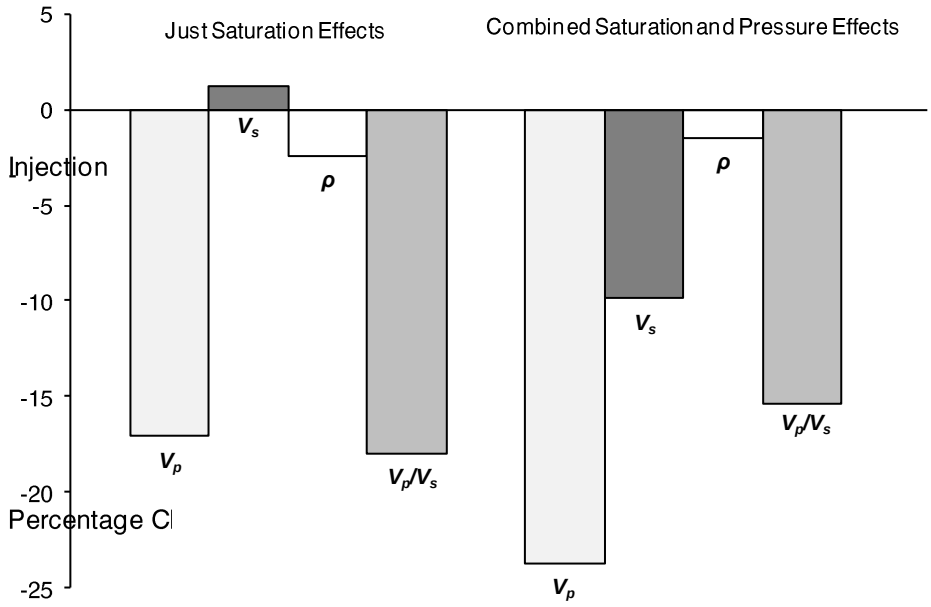


Figure 5-13 Percentage change in V_p, V_s, density (ρ) and V_p/V_s ratio from pre-injection conditions, resulting from saturation changes alone (55% CO_2) as well as a combination of saturation (55% CO_2) and pressure changes (8 MPa increase).

The reflectivity generated for the two scenarios and the difference between them at three angles of incidence are shown in Figure 5-14. Within the reservoir interval there are four reflections of interest, and the angle-dependent reflectivity was plotted for these four reflections (Figure 5-15):

- Top plume/ reservoir
- Base plume
- Top reservoir away from the plume
- Base reservoir

This reflectivity is discussed in terms of AVO intercept (*A*) otherwise known as the zero-offset reflectivity and the AVO gradient (*B*) which controls the magnitude at mid-far offsets.

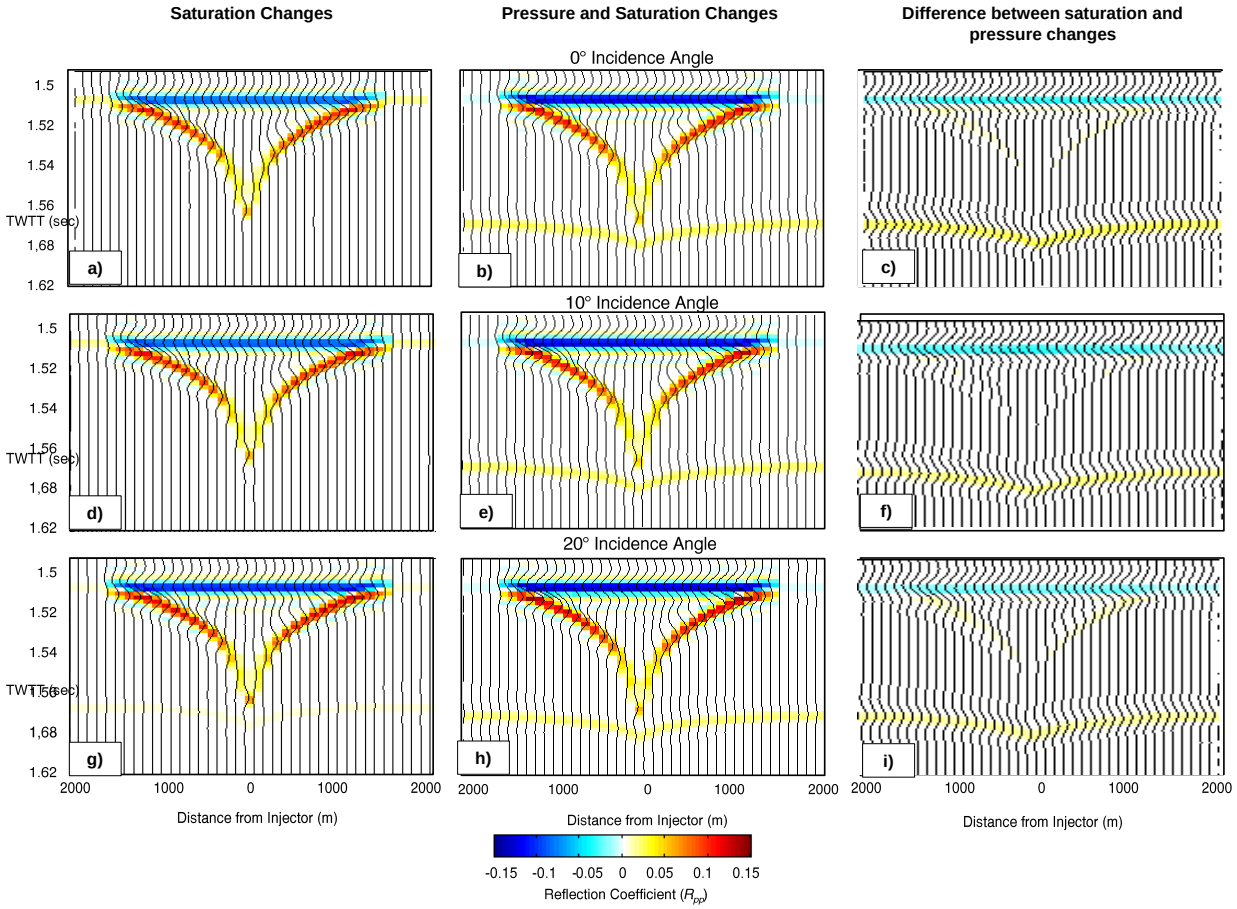


Figure 5-14 Synthetic seismograms produced taking into account changes in: a,d,g) saturation, b,e,h) both saturation and pressure, c,f,i) difference between pressure and saturation changes. Seismograms generated for different incidence angles to examine AVO: a,b,c) zero-incidence angle, c,d,e) 10° incidence angle, g,h,i) 20° incidence angle.

The reflections around the plume were affected by both pressure and saturation changes (Figure 5-15b&c). Having both a CO_2 plume and pore-pressure build-up resulted in a much larger changes in *A* than a plume alone would. The reflection coefficients for both the top and base plume, increased with offset. Saturation changes alone decreased *B* whereas pressure changes increased *B*, i.e. saturation changes resulted in greater brightening at mid/far offsets than combined pressure and saturation changes.

The reflectivity of both the top reservoir away from the plume and the base reservoir were only altered by increases in pressure (Figure 5-14c,f&i). The zero-offset top-reservoir reflectivity was initially positive, but the pressure increase resulted in a negative reflection. This polarity change and relatively large change in reflectivity from about 0.018 to -0.007 away from the plume could indicate pressure build-up. The base-reservoir reflectivity was also very sensitive to pressure build-up, which induced a change in polarity, from a small negative reflection to a positive one (0.024). *B* was very different for the two scenarios.

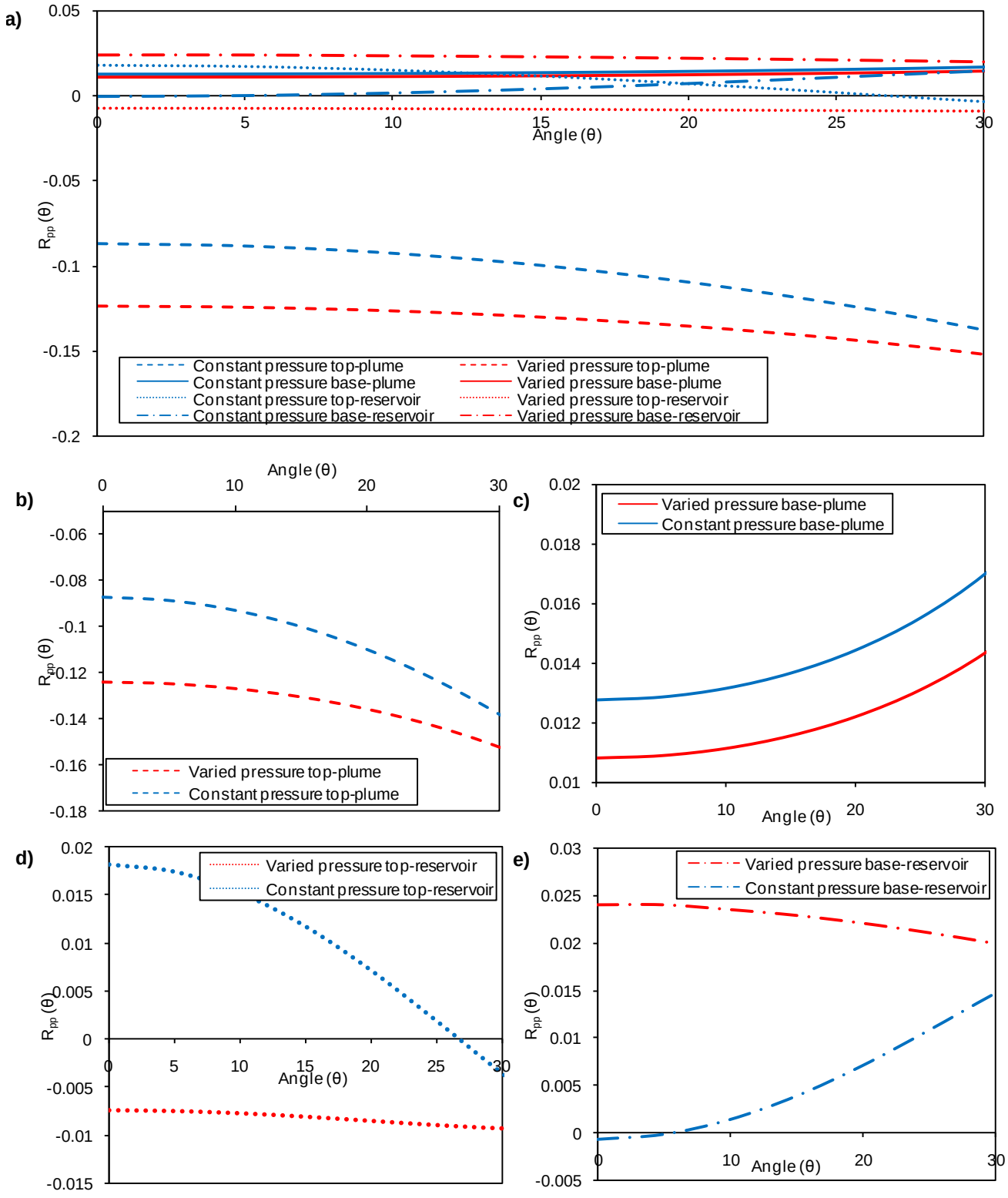


Figure 5-15 P-wave reflection coefficient (R_{pp}) plotted against incidence angle (in degrees), for two different scenarios: saturation changes (red), combination of pressure and saturation (blue.).a) All the reflections within the reservoir interval, b) top-plume reflection (i.e. at injector), c) base-plume reflection (i.e. generated off interface between brine and CO_2), d) top-reservoir reflection, (away from plume), b) base-reservoir reflection.

It was though that cross-plotting of *A* and *B* could simplify this analysis (Figure 5-17). The cross-plots were separated into reflections outside the plume (Figure 5-17a) and around the plume (Figure 5-17b). The top-reservoir reflectivity away from the plume showed that an increase in pore pressure decreased *A* and increased *B*, whereas within the plume CO_2 presence decreased both *B* and *A*. The inter-reservoir reflections were quite insensitive to pressure changes, so pressure changes would be best detected by analysing the top and base reservoir reflections. For the top-reservoir reflectivity in the region saturated by CO_2, a large change in *A* accompanied by a relatively small change in *B* would be indicative of a pore-pressure increase.

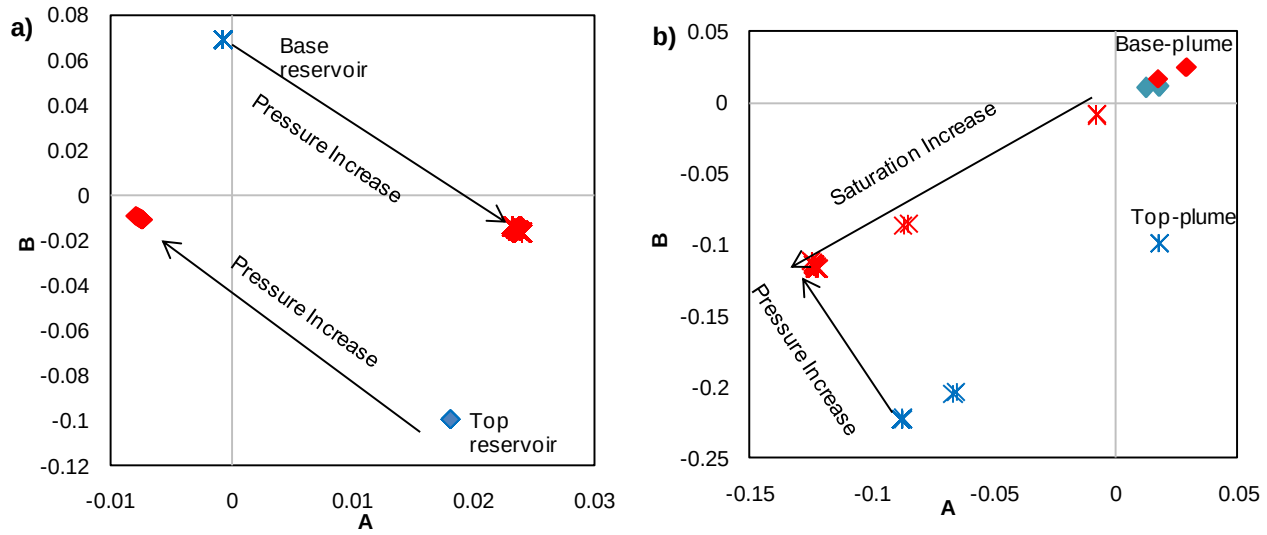


Figure 5-17 Cross-plot of the A and B attributes calculated for just saturation changes (blue), and for pressure and saturation changes (red), for certain reflectors: a) top reservoir (diamond) and base reservoir (cross), b) top plume (cross) and base plume (diamond

5.6 Summary

This Chapter demonstrated a workflow to combine outputs from ECLIPSE with the modelling approach used in Chapter 4. First, the sensitivity of seismic properties to typical changes in saturation and pressure, was established, then using fluid flow outputs the time-lapse seismic response was predicted.

CO_2 injection into a 10 km × 10 km × 100 m homogeneous clastic saline aquifer was simulated to predict the saturation and pressure changes during sequestration. Over ten years of injection 12.5 Mt of CO_2 was sequestered, producing a maximum well pressure of 22 MPa. The pressure increase spread throughout the reservoir, increasing the pore pressure from about 14.5 MPa to 22 MPa. Saturation maps show the plume growing laterally and upwards, causing CO_2 to pool below the caprock. Once injection ceased, the CO_2 continued to migrate upwards, and CO_2 at the trailing edge of the plume became residually trapped. As predicted in Section 3.8.2.1 ten years after injection ceased, the saturations in the reservoir were bimodal: 55% in the structurally-trapped plume, and 30% in the residually-trapped plume.

The sensitivity of the seismic response to pressure and saturation changes was assessed using the predicted maximum pressure and saturation changes. Altering the pore fluids from brine to a mix of 55% CO_2 and 45% brine increased V_s by ~1%, and decreased V_p by ~18%, and subsequently decreasing the V_p/V_s ratio. Pore-pressure changes altered the fluid properties, the grain framework properties and subsequently the relationship between V_p and S_{CO2}. Higher pore pressures increased the density and bulk modulus of both fluids, with CO_2 properties being more affected. Increasing the pore pressure decreased the effective pressure from 16MPa to 9MPa, which weakened the grain framework moduli. Reducing the effective pressure decreased both the seismic velocities: V_p by ~5% and V_s by ~6%, and the V_p/V_s ratio increased. The impact of pressure on the relationship between V_p and S_{CO2} was two-fold. First, CO_2 was stiffened, which increased the linearity of the relationship and second the decrease in the effective pressure weakened the rock making it more sensitive to fluid content. So at low CO_2 saturations the increase in pressure produced smaller changes in V_p than prior to injection, but at high saturations the pressure increase produced larger V_p changes. This was not something which was expected.

The seismic velocity in the reservoir was predicted using the saturation and pressure values for the tenth year. The overall changes in the velocities were calculated, then separated into their constituent parts: pressure effect on fluids, pressure effect on grain framework and saturation changes. Saturation changes only affected the plume, resulting in a large decrease in V_p (~18%) and a small increase in V_s (~1.5%). The effect of pressure changes on fluid properties appeared to only induce changes in the plume, this was explained by the higher sensitivity of CO_2 than brine to pressure. As the density of CO_2 increased V_s decreased. However the impact on V_p was more complicated. V_p decreased in the region of the plume containing high CO_2 saturation, but on the edge at low saturations V_p increased. Decreasing the effective pressure weakened the

grain framework and decreased both the seismic velocities throughout the reservoir. Combining these effects produced a V_p decrease of 25% in the plume and 5% in the surrounding reservoir, and a decrease in V_s in the plume of 11% and 10% away from the plume. CO_2 injection resulted in pressure increase, and the pressure and saturation changes magnified rather than masked each other.

Reflectivity was generated for two cases, first allowing saturation changes but keeping pressure constant and second allowing both saturation and pressure changes. CO_2 injection altered the top-reservoir reflection coefficient from a small positive to a large negative value, similar to the response in Chapter 4 to CO_2 injection. Combining pressure and saturation effects produced an even larger decrease in V_p and greater change in reflectivity and pushdown (from 7 ms to 12 ms) than saturation changes alone. Velocity changes due to saturation were limited to the CO_2-saturated region, whereas pressure build-up altered the response throughout the reservoir. If reservoir properties are well known, then a rock physics sensitivity study could determine whether the amplitude and pushdown changes are larger than could be attributed to saturation changes alone. As the seismic response to pressure changes persisted away from the plume they could indicate pressure build-up. Any well pressure measurements could be used to try and constrain the pressure values and relate them to the seismic response.

The sensitivity study indicated that substituting brine for CO_2 would decrease V_p/V_s, whereas pressure build-up would increase it. So AVO analysis could differentiate these effects. The AVO response from four different reflectors was considered: the top plume, base plume, top reservoir and base reservoir. The top reservoir and base reservoir reflection were only affected by pressure build-up and pressure increases decreased *A* and increased *B*. By contrast increasing CO_2 saturation decreased both *A* and *B*.

In conclusion, the integrated modelling approach was used to predict the time-lapse seismic response to changes in reservoir pressure and saturation during injection. Pore-pressure build-up magnified the changes in seismic response produced by saturation changes. Amplitude changes and pushdown resulting from pressure changes extended beyond the plume and could indicate pressure build-up. Although the pressure and saturation effects combined constructively for the zero-offset reflectivity, the opposite was true at mid-offset angles with pressure increasing the *B*, whilst increasing CO_2 saturation decreased it. Therefore at a clastic CO_2 sequestration site, pressure build-up could be distinguished from fluid-related changes to the time-lapse seismic response, by cross-plotting *A* and *B*. These results are summarised in Table 5-5

Table 5-5 Chapter 5 summary. Indicating the best data to be collected to achieve certain monitoring aims. Colours indicate the confidence with the approach.. Green: should succeed, orange: may succeed, red: unlikely to succeed.

Monitoring Aim	Zero- offset Amplitude	Near- offset Pushdown	Mid-offset Reflectivity
Detecting CO_2 migration	Established in Chapter 4, not altered by pressure.		
Distinguishing pressure and saturation			
Detecting pressure build-up			

6. Fluid Distribution and the Seismic Response

The fluid distribution model controls the relationship between the P-wave seismic velocity (V_p) and the fluid content. There is some debate as to which fluid-distribution model should be used when interpreting the time-lapse seismic response at sequestration sites and this uncertainty could introduce error into interpretation. This Chapter attempts to answer four fundamental questions surrounding this issue. First, how sensitive is the seismic response to the fluid distribution model? Second, could certain fluid distributions detrimentally impact on the ability to monitor CO_2 migration as established in Sections 4.3 and 4.4.? Third, can the fluid distribution within the reservoir be predicted using theoretical models and/or results from both laboratory and field studies? Fourth, can the fluid distribution in the reservoir be inferred from the measured seismic response?

A three-pronged modelling approach, which integrated rock physics and seismic modelling with reservoir simulation was used to examine these issues within a clastic saline aquifer. To predict a range of responses the end-member fluid distribution models were used: Gassmann-Reuss for the homogeneous lower bound and Hill for the patchy upper bound. The homogeneous response implies the length of fluid ganglia within the rock are below the critical length scale (50cm), whereas for a patchy response each fluid phase must be continuous over a length scale greater than 50cm. The critical length scale, which divides these behaviours, depends on the seismic frequency, which was explored using the White model.

The seismic response was greatly affected by the fluid distribution model used. In Section 4.4 it was found that when a homogeneous model was used the relationship between V_p and fluid content was controlled by the fizz-gas effect, whereas here it was shown that a patchy distribution produced a more linear relationship. The sensitivity of V_p to the fluid distribution depended on saturation, with a high sensitivity at low-intermediate saturations, but minimal sensitivity at high saturations. Thus when CO_2 is structurally trapped/migrating, the fluid distribution model used for analysis is inconsequential; whereas once residual trapping develops the choice of fluid distribution model is important.

The patchy relationship between V_p and S_{CO2} predicted using the Hill model impacted on the ability to monitor the migration of CO_2 as established in Section 4.4 when the Reuss model was used. The patchy model predicted a lower sensitivity to small quantities of CO_2, than the homogeneous model. However it was found that irrespective of the fluid distribution model the zero-offset reflectivity could be used to detect the entire plume, i.e. even the low CO_2 saturation residually-trapped region. Within the CO_2 plume a reflection was generated by the interface between structurally and residually trapped CO_2, unfortunately this was only significant when a patchy model was used. Using this reflection the amount of residual trapping in the reservoir could be estimated to validate storage security.

Accurate interpretation of the seismic response requires knowledge of which fluid distribution model to use. Two approaches were used to predict the appropriate model. First, a model was proposed based on the literature discussed in Section 2.5.5, and different fluid distribution models were used for capillary and structurally-trapped CO_2. The Hill average was used for high (>30%), mobile CO_2 saturations found during structural trapping whilst the Gassmann-Reuss average was used for low (≤30%), immobile CO_2 saturations resulting from residual trapping. The velocities generated using the proposed model were similar to those predicted by the homogeneous model due to the insensitivity of V_p to the fluid distribution model at high saturations, indicating that using a homogeneous model could be sufficient. Second, an upscaling study was performed to predict the appropriate model using outputs from fluid-flow modelling. These results tallied well with the proposed model and the portion of the reservoir containing residually-trapped CO_2 was best modelled using a homogeneous response, whereas the region saturated with structurally-trapped CO_2 was better predicted using an intermediate-patchy model (Brie, e=4). Relating the fluid distribution model to the trapping mechanisms implies that while trapping evolves through time and space, so will the appropriate fluid distribution model.

Knowledge of the appropriate fluid distribution model for a reservoir is required for both interpretation and potentially could be used to indicate whether the CO_2 is residually or structurally trapped. Different seismic parameters were examined to see whether they could be of use to extract the fluid distribution from the seismic response. Unfortunately due to the low density contrast between the brine and supercritical CO_2 the approaches examined, i.e. the use of AVO and converted shear wave reflectivity were unsuccessful. However in shallower reservoirs where CO_2 is gaseous, the density contrast between the fluids may be sufficiently large that these seismic properties could be used to distinguish the two end-member behaviours.

6.1 Introduction

Injecting CO_2 into a saline aquifer affects both the fluid content and the way in which the fluids are distributed in the pore space. This fluid distribution dictates the V_p-S_{CO2} relationship and was identified as an uncertainty at sequestration sites in Section 2.5.5. In this Chapter the effect of the fluid distribution in the reservoir on the ability to monitor sequestration is explored, along with an examination of whether the appropriate fluid distribution model can be either predicted or determined from the measured time-lapse seismic response. The seismic response was previously predicted using the lower end-member fluid distribution model in Section 4.3, where it was found that very small quantities of CO_2 could be detected with ease. Within this Chapter the examination is repeated using the upper end-member model. As the focus of this Chapter is to examine the effect of fluid distribution, the impact of pressure which was examined in Chapter 5 is neglected.

The reservoir used for this study was a clastic saline aquifer at 1500 m depth, whose properties are defined in Section 6.2. First, a rock physics study was conducted, to determine the sensitivity of the seismic response to the fluid distribution model (Section 6.3). The end-member models were used to predict the range of possible responses, and best seismic property for determining the distinguishing the models was examined (Section 6.3). Next the time varying response was examined (Section 6.4) using fluid-flow simulation results (Section 6.4). A proposed model which uses different end-member models for specified regions of the plume is outlined in Section 6.4.2.1. Using the fluid-flow simulation results the time-lapse seismic response was predicted in Section 6.4.2.2. The seismic response was then predicted using the proposed model (Section 6.4.2.3) and the ability to distinguish residually and structurally trapped CO_2 was examined (Section 6.4.3). Finally the fluid distribution in the reservoir during and after injection was predicted (Section 6.5). The predictions for different portions of the reservoir are given in Section 6.5.2. In Section 6.6 the results are discussed.

6.2 Reservoir Properties

With the exception of Section 6.5 the same reservoir properties were used here as in Section 4.4 and Chapter 5. The properties are given in Table 6-1. It was assumed that pressure was constant and that there was no interaction between the injected fluid and host rock and fluid during injection.

Table 6-1 Reservoir, fluid, mineral and frame properties for a homogeneous saline aquifer found at 1500 m depth.

Reservoir Properties			
Temperature		°C	50.5
Pressure	Lithostatic	MPa	31.7
	Hydrostatic	MPa	15.5
Porosity			0.31
Permeability	Horizontal	mD	570.0
	Vertical	mD	57.0
Fluid Properties			
CO_2	Density	kg/m^3	705
	Bulk Modulus	GPa	0.0993
	Viscosity	Pa.s	5.80E-05
Brine	Density	kg/m^3	1009
	Bulk Modulus	GPa	2.55
	Viscosity	Pa.s	6.10E-04
Mineral Properties			
Sandstone	Bulk Modulus	GPa	36.9
	Shear Modulus	GPa	44
	Density	kg/m^3	2650
Shale	Bulk Modulus	GPa	33.4
	Shear Modulus	GPa	22.25
	Density	kg/m^3	2741
Frame Properties			
Sandstone	Bulk Modulus	GPa	3.5
	Shear Modulus	GPa	4.3
Shale	Bulk Modulus	GPa	3.9
	Shear Modulus	GPa	3.9

The end-member fluid distribution models were used to combine the brine and CO_2 elastic properties and thus calculate the fluid bulk modulus. These models represent different responses of porous media containing different mixtures of CO_2 and brine to the propagation of the seismic wave, and their occurrence depends on the relationship between the size of the saturation heterogeneity and the critical length scale (L_c) (Equation 2-10). Here L_c was approximately 50 cm (assuming a frequency of 40 Hz), so fluids mixed finely below 50 cm would be considered homogeneous and would be modelled using the Gassmann-Reuss approach (Equations 3-28 to 3-30), whereas fluids separated over length scales greater than 50cm would be described as patchy and would be modelled using the Hill average (Equations 3-32 to 3-36). This Hill upper bound can be modified through the addition of constraints on the range of possibly saturations in the reservoir, such as the residual gas saturation (S_{gr}) and connate water saturation (S_{cw}) (Sengupta and Mavko 2003). These limits reduce the potential range of responses (MacBeth and Stephen 2008):

These constraints decrease the range of possible V_p values for a mixture of brine and CO_2 when the fluid distribution is not known (Figure 6-1). The key time for monitoring was deemed to be during and immediately following injection, when the water is being drained from the pores invaded by CO_2, therefore the Hill-drainage curve was used as the upper-bound during subsequent modelling.

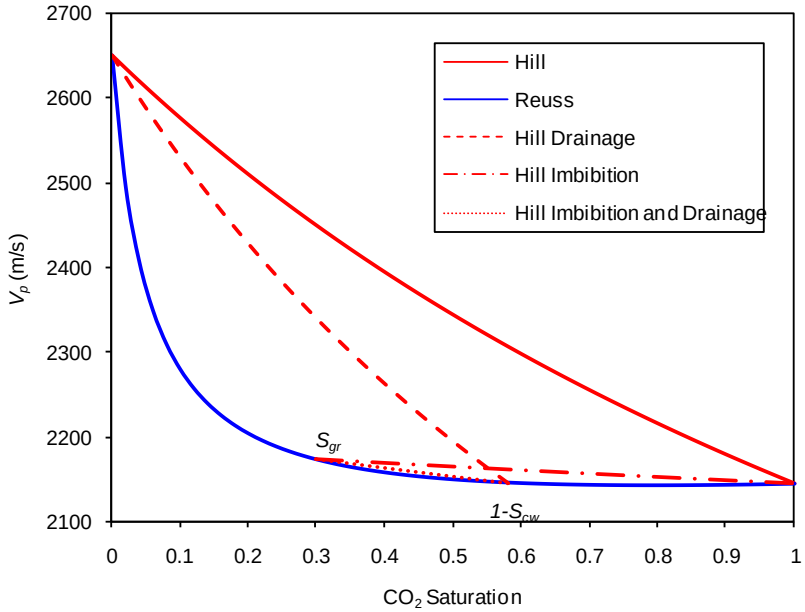


Figure 6-1 Relationship between V_p and S_{CO2} calculated using a Gassmann- Reuss model appropriate for a homogeneous response (Blue line) and a Hill model appropriate for a patchy distribution (Red lines), with additional constraints of Scw:42% and S_{rg}:30%, appropriate for the saturation conditions in the reservoir.

6.3 Sensitivity Study: End-member Fluid Distribution Models

6.3.1 Seismic Velocities and P-wave Impedance

Figure 6-2a&b shows the range of values of the seismic velocities as a function of fluid saturation. The shear-wave velocity (V_s) was independent of fluid distribution and quite insensitive to CO_2 saturation, whereas V_p was very sensitive to both fluid content and the fluid distribution model. The relationship between V_p and S_{CO2} in the homogeneous case was governed by the fizz-gas effect, however the patchy response produced a quasi-linear relationship. The greatest potential range of values lay in the low-intermediate saturations, with the predictions converging at very high saturations. At all saturations the Gassmann-Reuss model predicted a larger V_p decrease than the Hill model.

The dependence of the P-wave impedance and V_p/V_s ratio on the fluid distribution model indicates the effect which these models should have on the zero-offset reflectivity and AVO response (Figure 6-2c&d). The change in P-wave impedance, which determines the magnitude of the zero-offset reflectivity, had a very similar relationship with saturation as V_p. Using the detection criteria from Lumley (1997) the

smallest amount of CO_2 which produced a detectable change in the P-wave impedance was predicted (Figure 6-2d). In the homogeneous case, only 2% CO_2 was required to produce a detectable change, whereas it would require a saturation of 10% patchily-distributed CO_2 to produce a detectable change. So monitoring the migration of small quantities of CO_2 would be more challenging if the fluids were distributed in a patchy way. Also the patchy distribution would allow CO_2 saturation to be directly inferred from the zero-offset reflectivity, which is much simpler than the approaches applied in Section 4.4 to extract saturation when a homogeneous distribution was assumed. The V_p/V_s ratio which controls the P-wave reflectivity at mid-offsets, followed a quite similar trajectory to V_p, but it was slightly more sensitive to a greater range of saturations. Both the AVO intercept *(A)* and gradient *(B)* should depend on the fluid distribution model.

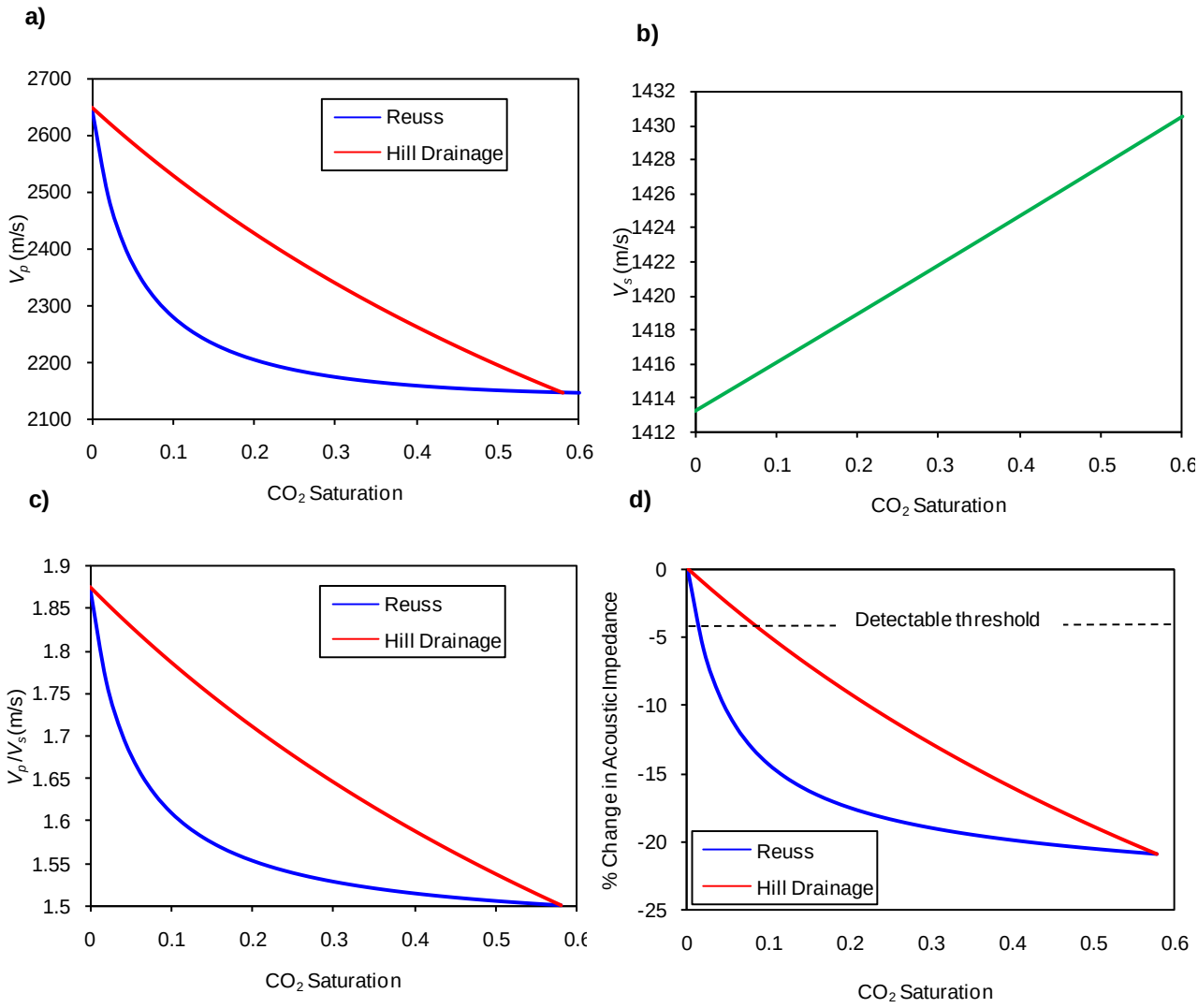


Figure 6-2 Variation in seismic properties with CO_2 saturation (S_{cw}=0.42) for two end-member fluid distribution models, Hill-drainage (red), Reuss (blue). a) V_p, b) V_s, which does not depend on fluid distribution, c) V_p/V_s ratio, d) Percentage change in P-wave impedance from the brine-filled case.

6.3.2 Zero-offset Reflectivity

The zero-offset reflectivity was predicted for a range of saturations using the velocities and densities of the reservoir and overburden (Figure 6-3). Introducing CO_2 into the pore space altered both the top-reservoir and base-reservoir reflectivity, and resulted in a pushdown of the base-reservoir reflection. The amount of amplitude changes and pushdown increased gradually with CO_2 saturation when a patchy model was used, whereas a homogeneous distribution resulted in the majority of the changes occurring for the first 15% CO_2. Consequently the response to a patchy distribution was much less sensitive to low CO_2 saturations, so monitoring plume migration would be easier if the fluids were homogeneously distributed. This result highlights an important problem for interpreting field seismic data when the appropriate fluid distribution model is unknown, as 16% homogeneously distributed CO_2 generated the same change in top-reservoir zero-offset reflectivity as 42% patchily-distributed CO_2. Therefore an accurate interpretation of the seismic response requires knowledge of the length scales at which the fluids are connected in the pore space.

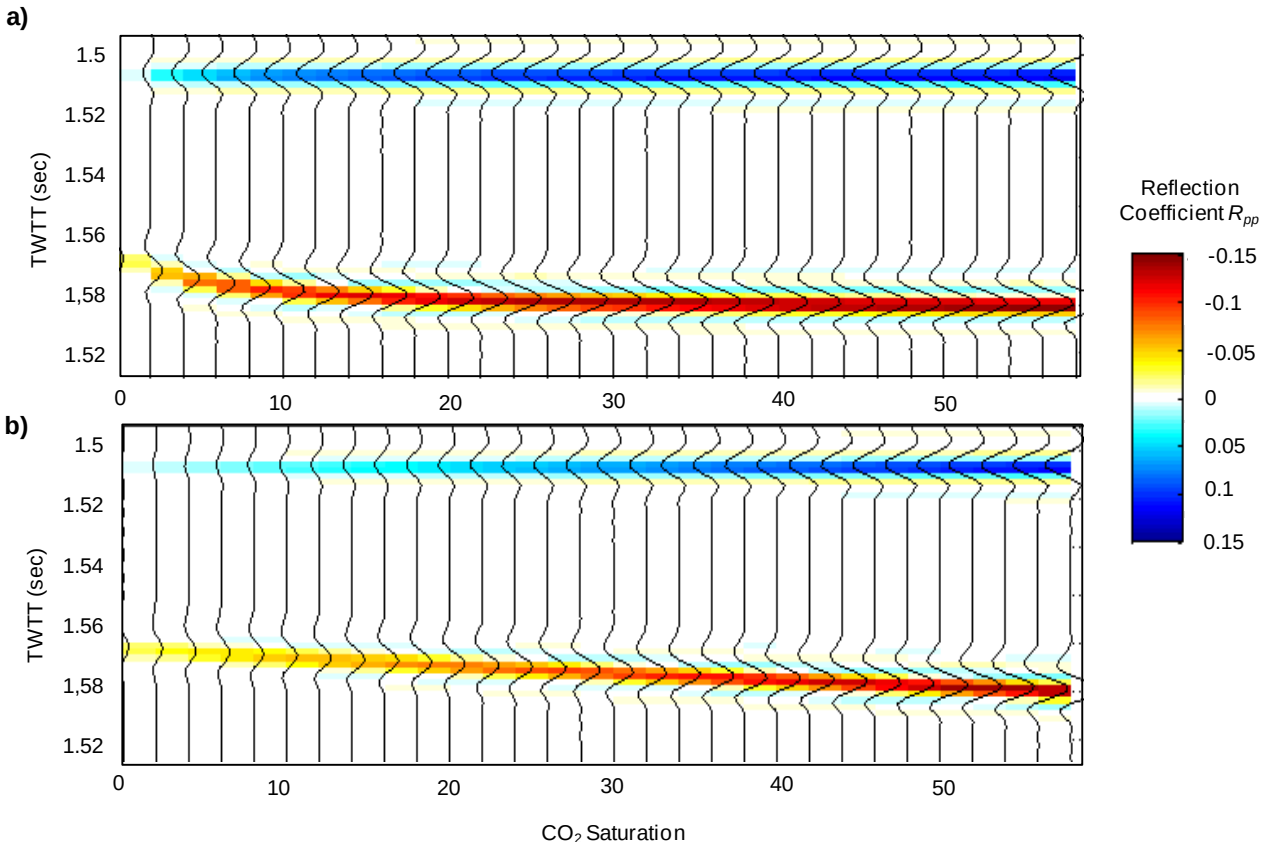


Figure 6-3 Zero-offset reflectivity generated using the CREWES package assuming a 40Hz Ricker wavelet, plotted for a 100 m thick sandstone containing varying amounts of CO_2 from brine-filled to 58% CO_2 in 2% increments: a) Reuss model, b) Hill model.

The time-lapse zero-offset reflectivity provides information about both the change in both the P-wave impedance (top-reservoir reflectivity) and the average reservoir V_p (base-reservoir pushdown). The P-wave impedance depends on both V_p and ρ, whereas the amount of pushdown only depends on V_p, so cross-plotting these changes may help distinguish the fluid distribution (Figure 6-4). For a given pushdown, the patchy response produced greater changes in P-wave impedance than the homogeneous response. This was because inducing 17.5 ms of pushdown required about a 500m/s decrease in $V_{p,}$ which could be produced either by 48% homogeneously-distributed CO_2 or 56% patchily-distributed CO_2. However the larger quantity of CO_2 in the patchy case decreased the density more than the homogeneous case, producing a larger change in P-wave impedance. Therefore it might be possible to determine the fluid distribution model from the zero-offset seismic response. This analysis may not however be appropriate at real sequestration sites, where the data are contaminated by noise and the reservoirs are thinner and saturated with varying amounts of CO_2.

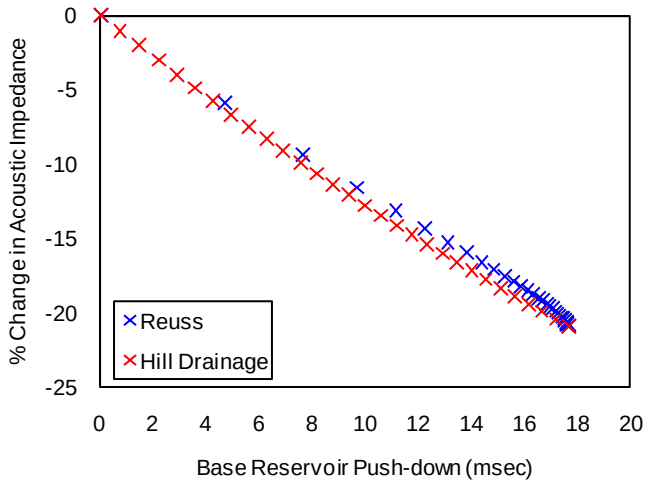


Figure 6-4 Base-reservoir pushdown plotted against percentage change in P-wave impedance for different CO_2 saturations (0-58% every 2%), calculated using the Reuss (blue) and Hill-drainage (red) models.

6.3.3 AVO Response

At non-zero offsets the magnitude of the P-wave reflection coefficient depends on V_p, V_s and ρ, and might therefore be used to differentiate different combinations of fluid content and fluid distribution, which produce the same zero-offset reflectivity. Also at these offsets an incident P-wave produces a converted reflected shear wave which could be used. Figure 6-5a shows the angle-dependent P-wave reflectivity for the pre-injection brine-filled conditions and two saturations which produce the same zero-offset reflectivity. The reflectivity was nearly identical for the two saturations for the whole angular range, indicating that AVO was not a useful attribute for distinguishing the different fluid distributions. The converted shear-wave reflectivity for these same saturations was plotted in Figure 6-5b. The homogeneous model predicted larger R_{ps} values at far offsets than the patchy model, indicating that a comparison of the P and P-S reflectivity could be used to differentiate the two saturation conditions, although the magnitude of the shear-wave reflectivity was very small and unlikely to be detectable.

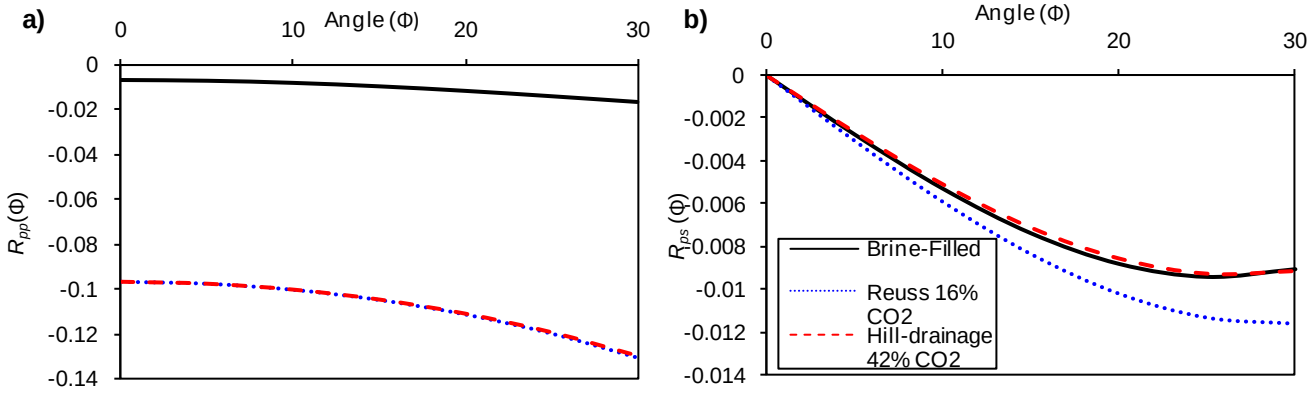


Figure 6-5 Angle-dependent reflectivity: a) R_{pp}, b) R_{ps}., plotted for three different saturations, brine-filled (black, solid), 16% homogenous CO_2 (blue dotted) and 42% patchy CO_2 (red dashed).

The AVO response was then examined further using a greater angular range, i.e. the curvature *C* was used (Figure 6-6a&b). In the patchy case, all the AVO attributes appeared to vary relatively linearly with CO_2 saturation, which was not the case for the homogeneous distribution. In the *A* and *B* cross-plot the different distributions plotted very closely, with the patchy response producing a slightly smaller change in *B* than the homogeneous model for a given change in *A*. The cross-plot of *A* and *C* (Figure 6-6b) was more successful at distinguishing the two responses, with a patchy distribution producing a smaller change in *C* for the same change in *A*. Unfortunately the difference was still small and the curvature is not normally measured. Therefore AVO cross-plotting for the conditions simulated here was not useful for differentiating patchy versus homogeneous fluid distributions. However in shallower reservoirs where the density contrast between brine and CO_2 is larger the approach may be more successful.

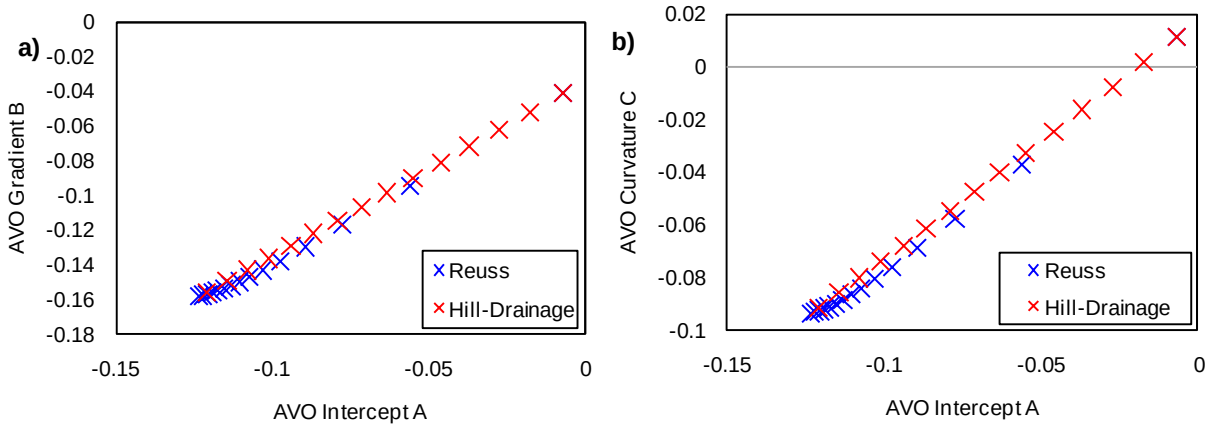


Figure 6-6 AVO cross plots for a range of saturations from 0-58% CO_2 in 4% increments, predicted using the Reuss model (blue) and the Hill-drainage model (red) a) AVO intercept versus gradient, b) AVO intercept versus curvature.

6.4 Time-lapse Response

The previous Section presented a study into the sensitivity of the seismic response to different combinations of saturations and fluid distribution model. In this Section the model was extended by including realistic time dependent saturation values generated by fluid-flow simulation (Section 6.4.1). These saturation maps were then combined with the two end-member fluid distribution models to predict the possible range of time-lapse seismic responses (Section 6.4.2).

6.4.1 CO_2 Injection

6.4.1.1 Injection Parameters

The aquifer had the same properties to that used in Chapter 5, although its layout differed. The aquifer was 10 km × 10 km × 100 m, and its layout is described in Figure 6-7 and Table 6-2. CO_2 was injected into the middle of the field at a rate of about 1 Mt/yr for 20 years, while brine was produced from eight production wells. Simulation continued for a further forty years to monitor the CO_2 migration after injection. Brine production was used to minimise pressure build-up (Bergmo et al. 2010).

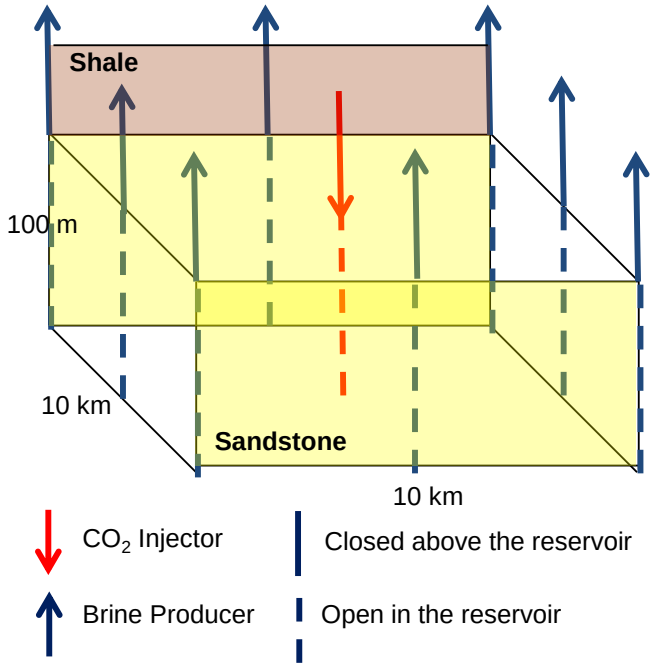


Figure 6-7 Simulation layout

Table 6-2 Inputs into ECLIPSE. Number refers to number of gridblocks, dimensions gives the gridblock dimension, wells, X and,Y, give well location, Z1 and Z2 give the interval over which the well is open in the reservoir, I/P represented injector/producer, tstep gives the timesteps for the calculation, R/P gives information on the controls on the well, either rate or pressure, and finally O/C states whether the well is open or closed for that time period.

Grid						**Wells**								
Number			Dimensions											
X	Y	Z	X	Y	Z	X	Y	Z1	Z2	I/P	TSTEP	R/P		O/C
100	100	50	100	100	2	50	50	1	50	INJ1	1*365	RESV	4500	OPEN
						1	1	1	50	PROD1	1*365	BHP	155	OPEN
						50	1	1	50	PROD2	1*365	BHP	155	OPEN
						100	1	1	50	PROD3	1*365	BHP	155	OPEN
						1	50	1	50	PROD4	1*365	BHP	155	OPEN
						100	50	1	50	PROD5	1*365	BHP	155	OPEN
						1	100	1	50	PROD6	1*365	BHP	155	OPEN
						50	100	1	50	PROD7	1*365	BHP	155	OPEN
						100	100	1	50	PROD8	1*365	BHP	155	OPEN
						50	50	1	50	INJ1	1*3650	RESV	4500	CLOSED
						1	1	1	50	PROD1	1*3650	BHP	155	CLOSED
						50	1	1	50	PROD2	1*3650	BHP	155	CLOSED
						100	1	1	50	PROD3	1*3650	BHP	155	CLOSED
						1	50	1	50	PROD4	1*3650	BHP	155	CLOSED
						100	50	1	50	PROD5	1*3650	BHP	155	CLOSED
						1	100	1	50	PROD6	1*3650	BHP	155	CLOSED
						50	100	1	50	PROD7	1*3650	BHP	155	CLOSED
						100	100	1	50	PROD8	1*3650	BHP	155	CLOSED

6.4.1.2 Dynamic Reservoir Properties

Within this synthetic case study 20 Mt of CO_2 was sequestered over the lifetime of the project (Figure 6-8a). The CO_2 spread throughout the reservoir over time (Figure 6-8b-d). The most important process controlling CO_2 movement during sequestration was gravitational segregation, which resulted in the injected CO_2 migrating to the top of the reservoir and becoming structurally trapped. It is important to note that in reality the CO_2 plume will only become trapped once it has found a structural or stratigraphic trap, until this point it will migrate updip. After injection ceased, CO_2 at the trailing end of the plume became residually trapped, whilst the higher-saturation mobile CO_2 continued to migrate upwards.

Uncertainties about the fluid distribution were highlighted here as the saturation, its distribution in the reservoir and the way the fluids are distributed in the pores at a given saturation varied in time and space (Figure 6-8b-g). The bimodal nature of the saturations predicted in the reservoir is demonstrated in Figure 6-8e-g with peaks residual and structural trapping respectively.

6.4.2 Time-lapse Seismic Response

6.4.2.1 Proposed New Modelling Approach

The fluid distribution/ saturation in the reservoir can be grouped into three classes or regions:

1. 100% water.
2. A continuous mobile CO_2 phase and connate (immobile) water.
3. A continuous mobile water phase and residual (immobile) CO_2.

Elastic properties must be calculated for each of these three types of distribution. The first case of 100% water is of course easy, but the elastic properties of the second and third cases are less easy to determine as the distribution consists of one continuous phase (connected over a length scale greater than the critical length scale) and an immobile phase. The elastic response will depend on whether the discontinuous ganglia in these cases exist in ganglia which are greater or less in size than the critical length scale. If the ganglia are greater in length then the response will be described by the patchy model, but if they are smaller it is not clear what model should be used.

Both experimental measurements (Cadoret et al. 1998; Domenico 1976; Knight and Nolen-Hoeksema 1990) and simulation studies (Kirstetter et al. 2006; Sengupta and Mavko 2003) suggest that different fluid-distribution models are appropriate for different behaviours in the reservoir. Fluid distributions resulting from imbibition seem to produce a homogeneous response, whereas fluid distributions from drainage produce a patchy response. During CO_2 sequestration in saline aquifers imbibition results in residually trapped CO_2, whereas drainage produces gas caps. Lebedev et al (2009) also found that patchy responses were found at higher saturations, due to greater connectivity over larger scales.

A physical justification for these different behaviours for different saturation processes could come from the pore-scale distribution of the fluids (as illustrated in Figure 3-15). It is usual to assume that the aquifer rock is water wet, so that the water phase will remain continuous even when its saturation has been reduced to connate water saturation. In this case the smaller pores in the rock remain filled with water, whilst a continuous film of water coats the walls of the larger pores. The CO_2 then fills the centre of these pore space throughout the network of larger pores. In this case it could be reasonable to assume that some of the connate water has a length scale greater than the critical length scale (although admittedly many of the water films are very thin) and so that fluid distribution can be considered as patchy. In contrast when water imbibes back into the pore space the CO_2 remains as small disconnected ganglia trapped by snap-off in the middle of larger pores (Roof 1970).

For this investigation it is proposed that the elastic properties of each of the three fluid distribution regions should be calculated using different models. The elastic response of the part of the aquifer that is filled with 100% water was calculated using the Gassmann equations (Equations 3-28 to 3-29). The elastic

response of the zone containing structurally-trapped CO_2 (>30%) was calculated using the Hill-drainage model (Equations 3-32 to 3-36) whilst the elastic response of the region containing capillary trapped CO_2 was calculated using the Gassmann-Reuss equations (Equations 3-28 to 3-30). This model does assume that the behaviour will change very rapidly between a homogeneous response below 30% CO_2 and a patchy response above, however in reality this transition would be more gradational.

6.4.2.2 End-member Models: Seismic Response

Figure 6-8k-m&q-s shows how the zero-offset reflectivity evolves as CO_2 is injected, with the plume growing and both the amplitude of the top-reservoir reflection and base-reservoir pushdown increasing with time. Structural trapping produced high CO_2 saturations (50-60%) in the central and upper portion of the plume, which in turn created large changes in the reflection coefficient (from -0.05 to -0.15) and about 10 ms of pushdown 20 years after injection ceased. At these high saturations the changes were almost independent of fluid distribution (Figure 6-1), and their large magnitude indicated that structural trapping could easily be detected for the range of responses. However residually-trapped CO_2 was typified by low-intermediate saturations at which V_p was most sensitive to the fluid distribution, and the predictions therefore diverged within this portion of the plume. The interface between residually-trapped CO_2 and brine produced a much larger reflection when a homogeneous distribution was assumed, although the refection magnitude was still high in the patchy case. Within the plume a reflection was generated from the transition between the residually-trapped and structurally-trapped regions (Figure 6-8l&r), with the patchy model predicting a much larger reflection than the homogenous model. This reflection could be used to quantify the amount of CO_2 trapped by each mechanism, but it was more difficult to detect as the plume thinned (Figure 6-8 m&s), due to tuning between the top-reservoir and base mobile CO_2 reflections. The magnitude of this reflection also depends on the relative permeabilities and in particular the values of the connate water and residual gas saturations. The range of possible responses shown here emphasises the importance of determining the fluid distribution prior to interpreting the seismic response.

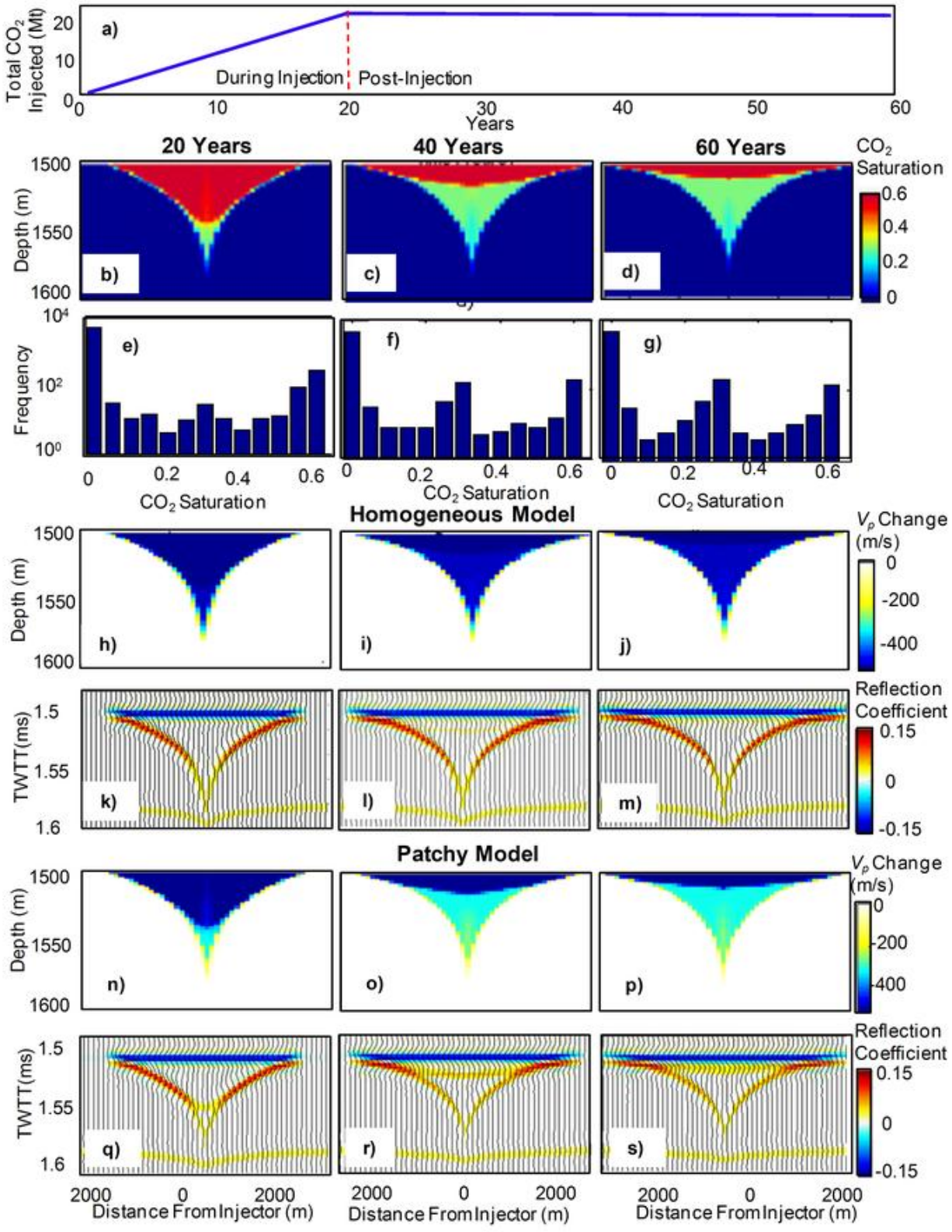


Figure 6-8 Amalgamation of results demonstrating the workflow from fluid-flow results to zero-offset seismic response. a) Graph showing the total amount of CO_2 injected against time. b-d) CO_2 saturation maps of a central portion of the reservoir over time. e-g) Saturation histogram showing frequency of saturations over time. h-j) V_p predicted using the Gassmann-Reuss (homogeneous) model. k-m) Zero-offset reflectivity generated using CREWES software with homogeneous velocities. n-p) V_p predicted using the Hill (patchy) model, k-m) Zero-offset reflectivity generated using CREWES with patchy velocities. Different time steps: b,e,h,k,n,q) after 20 years of injection, c,f,i,l,o,r) after 20 years injection and 20 years post injection, d,g,j,m,p,s) after 20 years of injection and 40 years post injection.

6.4.2.3 Proposed Model: Seismic Response

The previous approach utilised one end-member model for the entire aquifer, however the proposed model allows it to vary (Section 6.4.2.1). This modelling approach was used to predict the seismic response 20 years after injection ceased (Figure 6-8c), when both the structurally-trapped CO_2 plume and residually-trapped CO_2 plumes were well developed.

The V_p map, zero-offset reflectivity and reflectivity at 30° incidence angle are shown in Figure 6-9, where they can be directly compared to the end-member predictions. The values were very similar to those generated using the homogeneous model, because the patchy model was being used at high saturations where the two predictions coincide. The proposed model predicted a very small reflection off the interface between the two regions of the plume. The reflection coefficients increased at greater angles of incidence, indicating that far-offset data may be useful to monitor sequestration when the zero-offset response is not adequate.

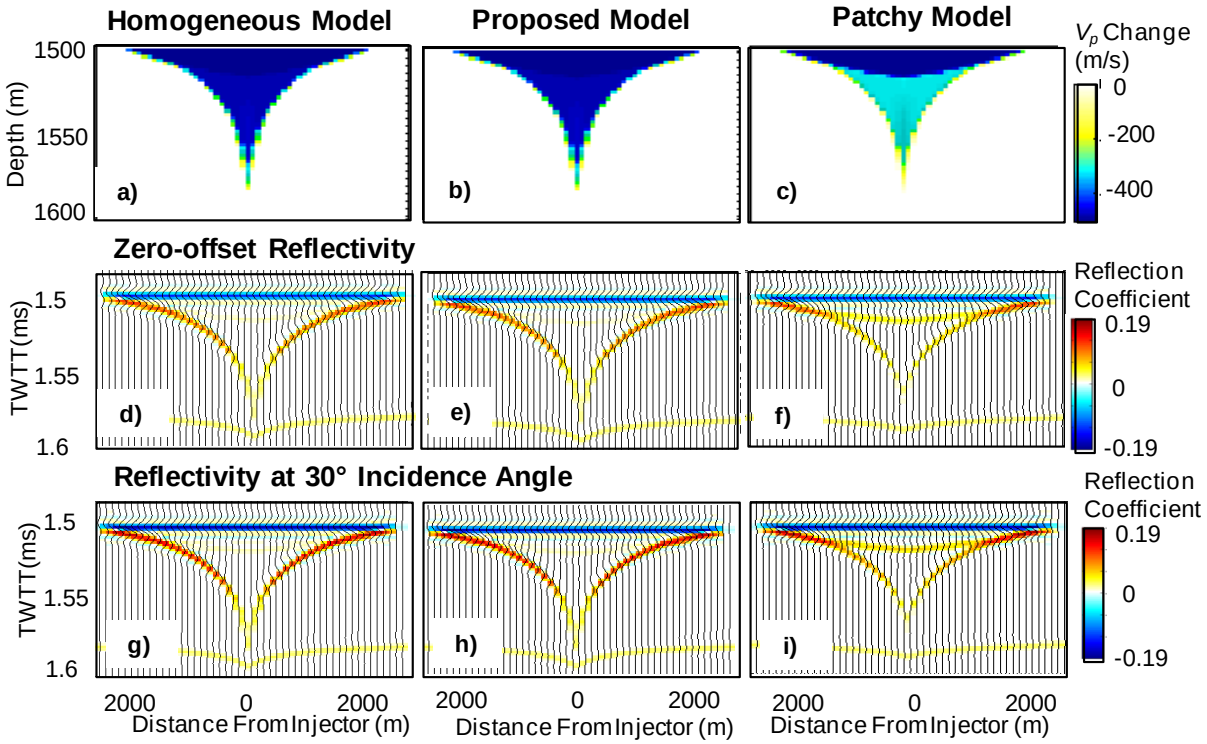


Figure 6-9 The seismic response after 20 years of injection and 20 years post-injection: a-c) V_p change from brine-filled, d-f) zero-offset reflectivity, g-i) reflectivity at 30° incidence angle. a,d,g) Homogeneous model. b,e,h) Proposed model model($S_{CO2}<S_{gr}$: Gassmann- Reuss, else:Hill. c,f,i) Modified Patchy model.

6.4.3 Determining the Trapping Phase

As the proposed model used different fluid-distribution models to represent residually- and structurally-trapped CO_2, the methods discussed in Section 6.3.1.3 to detect the fluid distribution model could be applied to determine the trapping phase. The saturations in the reservoir were bimodal (Figure 6-8e-f), so the different trapping mechanisms were assigned both a particular saturation and fluid distribution

(Figure 6-10). The AVO response was typical of a Class III sand. Residually-trapped CO_2 generated a smaller zero-offset reflectivity than structurally-trapped CO_2, but they had a similar gradient. This is shown in Figure 6-11a where structurally-trapped CO_2 generated higher *A* and *B* values than low saturations (~10%) at the plume edge. These saturation states plotted separately on the *A*-*B* cross-plot, which could help differentiate very high and low saturations, although the zero-offset reflectivity (*A*) alone may be sufficient.

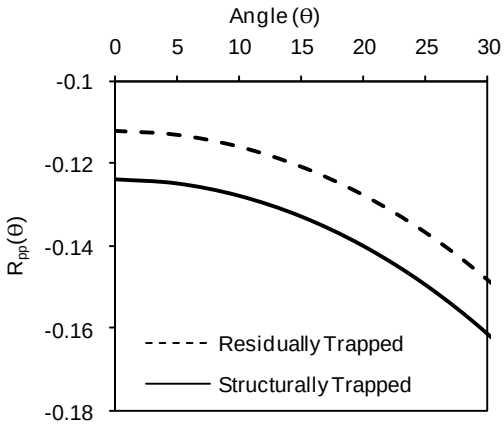


Figure 6-10 Top-reservoir reflectivity as a function of incidence angle to 30° for the two dominant saturations found in the reservoir 30% (residual) CO_2 assuming a homogeneous distribution and 60% (structural) CO_2 assuming a patchy distribution.

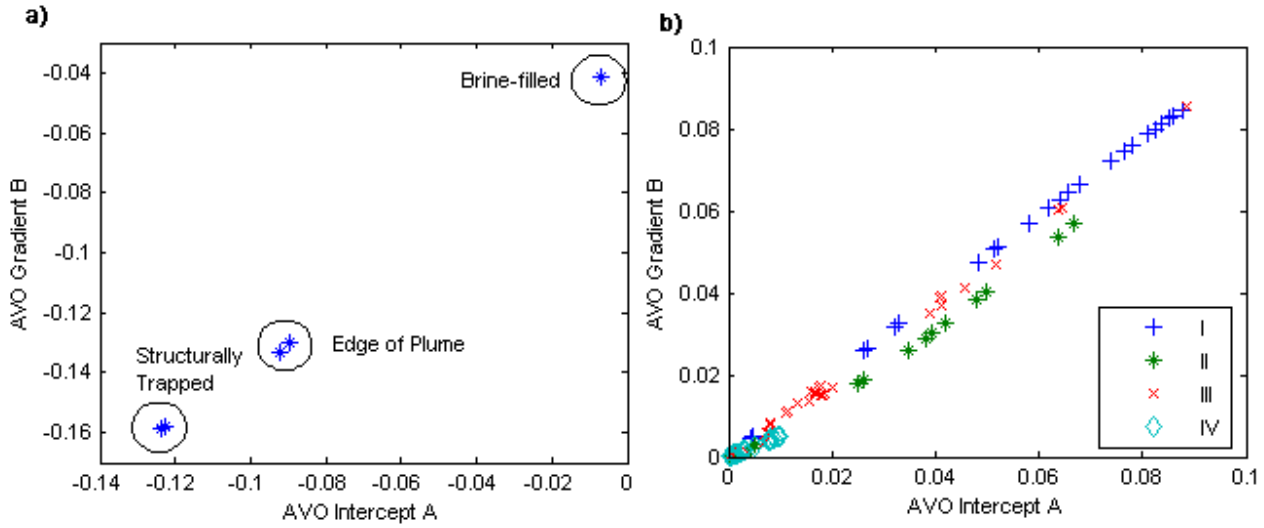


Figure 6-11 Plots of AVO attribute, A versus B after 20 years of injection and 20 years post injection. a) Reflections off the top of the reservoir, b) reflections within the reservoir interval, I: Edge of plume, II: interface between residual and structurally trapped CO_2, III: reflections within the residual CO_2 plume, IV: reflections within the structural CO_2 plume.

Reflections generated within the reservoir interval may also provide insight about the trapping phase. These reflections can be categorised into four types as illustrated in Figure 6-12a. These reflections were generated by the different saturation and velocity contrasts shown in Figure 6-12b. V_s and ρ changed linearly with saturation, whereas the relationship between V_p and saturation depended on the fluid distribution. The four reflection types were:

Type I: Plume interface with brine. There was a low saturation rim around the structurally-trapped plume, so this was an interface between a low/residual CO_2 saturations and brine. Across the interface there was a large V_p contrast, but saturation and subsequently V_s and ρ changes were low. This plotted with a high A and B value.

Type II: Interface between structurally-trapped and residually-trapped CO_2. Across the interface there was small change in V_p, but quite large saturation changes. This plotted with relatively high A and B values.

Type II: Within the residually-trapped plume. The Reuss model was used; therefore small saturation changes produced large V_p changes, but small V_s and ρ changes. This plotted with a range of A and B values.

Type IV: Within the structurally-trapped plume. The Hill model was used, so V_p, V_s and ρ all varied linearly with saturation, but they changes were smaller changes. This plotted with a low A and B value.

These results indicate that cross-plotting of the A and B may be used to determine the trapping phase within the reservoir and how it evolves through time. In particular the reflection off the interface between the structurally and residually trapped CO_2 will plot with a lower B value than reflections off the edge of the plume. As the difference in the A and the B values plotted in Figure 6-11b were small it may not be possible to distinguish the reflections in this case. At shallower sequestration sites, where there is a larger density contrast between brine and CO_2, distinguishing these different signatures may be easier.

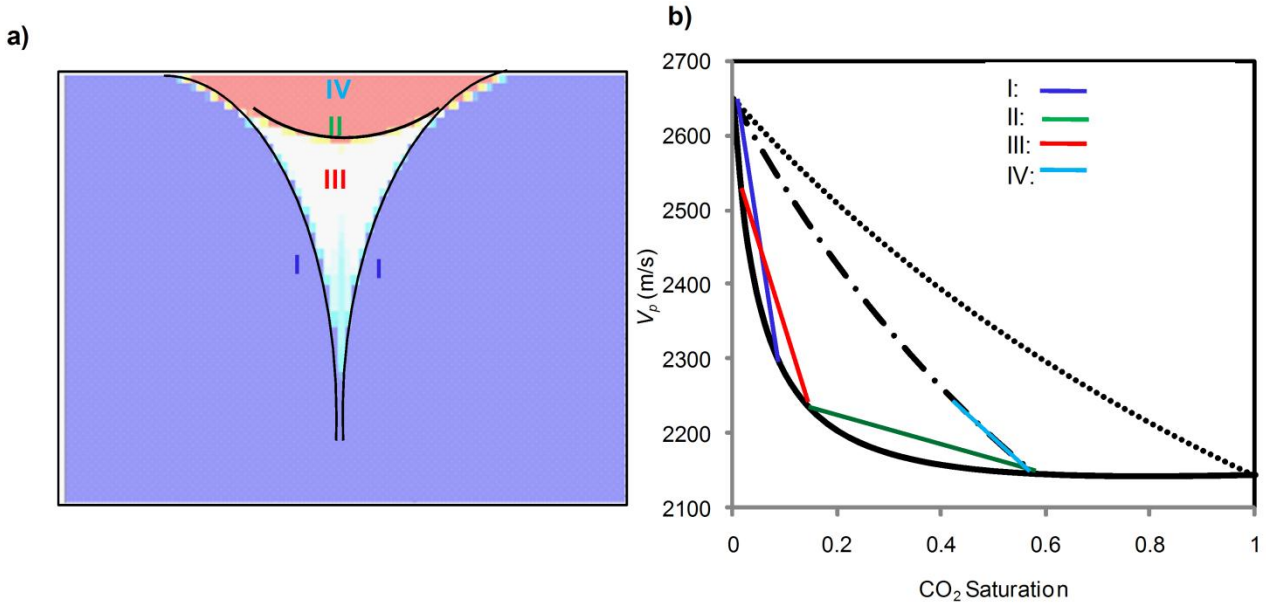


Figure 6-12 a) Schematic representation of CO_2 saturation within the reservoir, indicating where reflections are generated. b) V_p-saturation graph, showing the magnitude of the V_p changes expected across these interfaces.

6.5 Predicting the Fluid Distribution

The approach used in the previous Section exploited the fact that there appears to be a relationship between the fluid distribution model and trapping mechanism. To examine this further the fluid distribution during sequestration was predicted using an integrated methodology (Sengupta and Mavko 2003).

6.5.1 Modelling Approach

To predict the fluid distribution and its variation with time and space, an integrated methodology was used (Kirstetter et al. 2006; Sengupta and Mavko 2003). This methodology is shown in Figure 6-13. It uses the fact that pore-pressure variations induced in regions below the critical length scale can equilibrate during the seismic period and can be assumed to be homogeneously distributed. The approach is given here:

1. Fine-scale saturations were predicted by fluid-flow modeling, using gridblocks at the critical length scale (50 cm).
2. Fine-scale velocities were predicted from the saturations using a homogeneous model.
3. The fine-scale velocities were then upscaled to the seismic scale (50 m × 15 m), using the Hill (1963) averaging method, which is appropriate as there are no spatial variations in the shear modulus.
4. The coarse scale velocities were plotted against saturation, to indicate the V_p-S_{CO2} relationship.

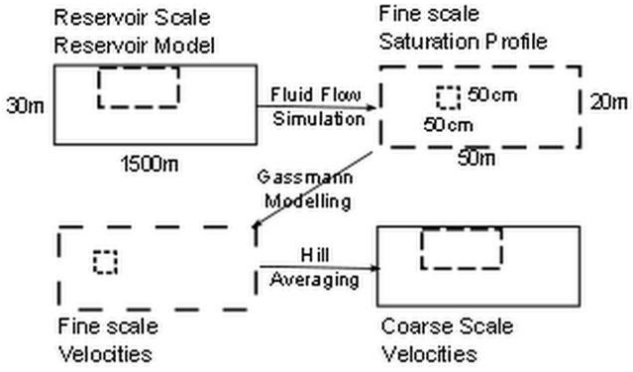


Figure 6-13 Schematic diagram of the methodology (modified from Sengupta and Mavko, 2003).

The fine-scale saturations were generated using 3000 × 1 × 80 50cm gridblocks, due to the fine resolution the reservoir size was limited to 1500 m by 40 m. CO_2 was injected into the middle of the field for one year at a rate of 3000 tonnes/year, while brine was produced from two production wells placed at the edge of the field. The simulation continued for eight years after injection.

There are a number of issues with this approach and the integration of information from reservoir simulation and rock physics modelling, which are discussed in Section 7.3.4.

6.5.2 Predictions

The behaviour of the injected CO_2 shown in Figure 6-14a-c was similar to that discussed in 6.4.1.2. As the vertical seismic resolution was 15m, the reservoir was separated into three regions: the top 15 m was referred to as "top-plume", the next 15m were called "base-plume", and finally the bottom 10 m contained very little CO_2, and was not examined. The saturation histograms of the top and base plume, demonstrates that the entire reservoir contained high saturations (>40%) during injection, however following injection there was a shift in the base of the plume towards lower saturations typical of residual trapping (Figure 6-14g-i).

The fine-scale elastic properties were calculated using these fine-scale saturations, and were then averaged using the Hill method to produce coarse-scale V_p values. These were then plotted against the average saturation within the gridblock (Figure 6-14j-l), for the top and base plume. Immediately following injection (Figure 6-14j), the V_p-saturation relationship for the entire reservoir appeared to be similar to the relationship predicted using the Brie empirical mixing model, with an *e* value of 4, which was referred to as intermediate-patchy. However post-injection (Figure 6-14k&l) residually-trapped CO_2 at the base plume was close to a homogeneous response. It was thought that the intermediate-patchy response resulted from gravity producing a sub-seismic resolution gas cap and the homogeneous response was due to capillary forces trapping CO_2 on the pore scale. Therefore a homogeneous model was appropriate for residually-trapped portions of the reservoir ($S_{CO2} \leq 30\%$), whereas the Brie model (e=4) was appropriate for portions of the reservoir containing structurally-trapped CO_2.

Eight years after the end of injection (Figure 6-14l), the Brie model was no longer appropriate at high saturations. This may be because residual trapping was occurring in the central upper portion of the reservoir, hence the coarse-scale gridblocks contained both high-saturation patchy behaviour and low-saturation homogeneous behaviour, which were then averaged. If there was no trap then CO_2 would continue to spread radially and if injection stopped eventually residual trapping would be dominant in the reservoir. In this case the homogeneous model would be appropriate for the entire reservoir.

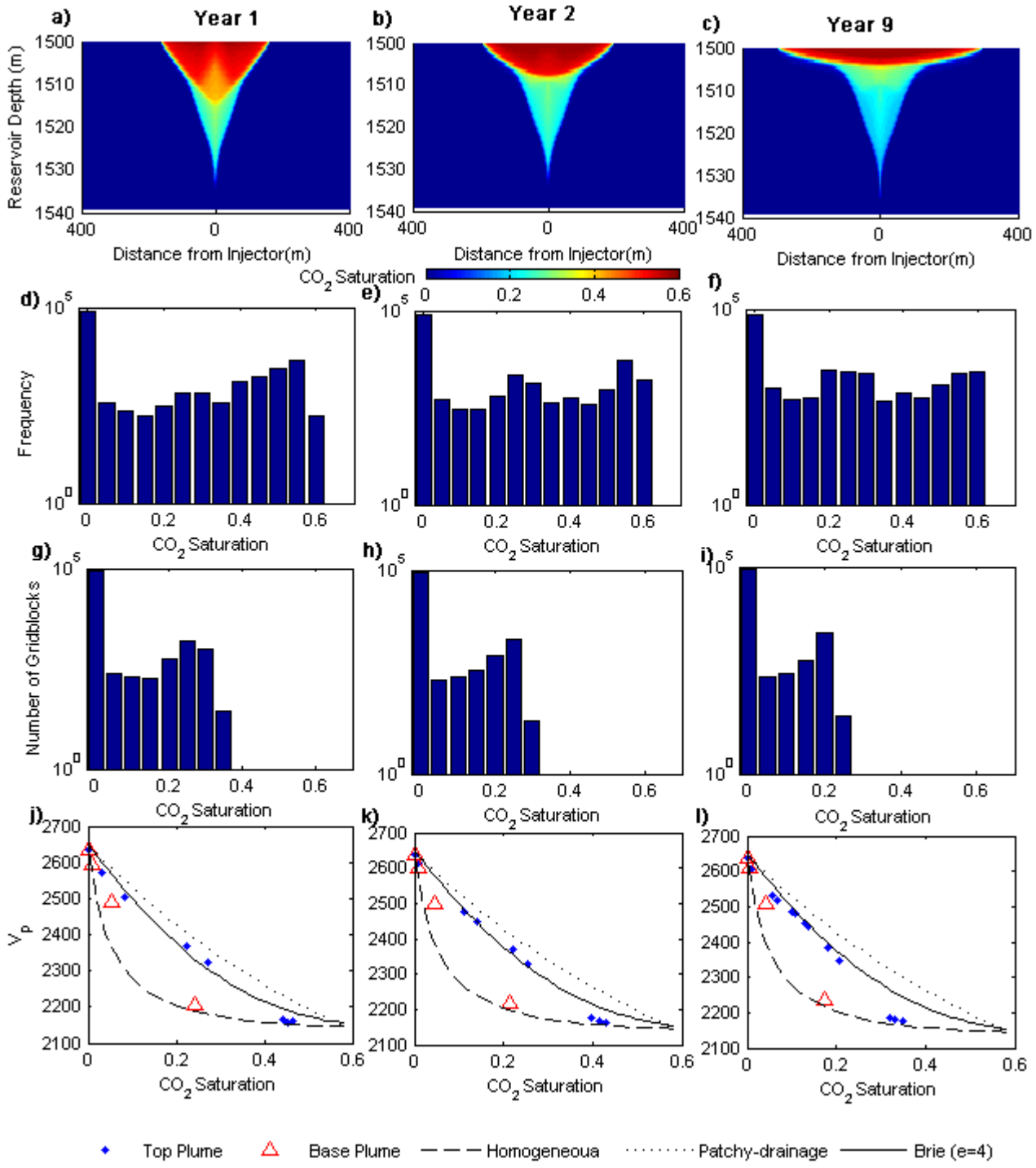


Figure 6-14 Diagram showing temporal and spatial variations in saturation and velocity during sequestration. a-c) CO_2 saturation maps of the reservoir. d-f) Saturation histograms for the top 15 m of reservoir, g-i) Saturation histograms for the base 15m of plume. j-l) V_p-CO_2 saturation relationships for the coarse scale velocities generated using Hill averaging, separated into top and base plume and compared with the homogeneous, patchy-drainage and brie (e=4) models. Different columns show certain years, a,d,g,j) After one year injection, b,e,h,k) after one year injection, one year post injection, and c,f,i,l) after one year injection and neight years post-injection.

6.6 Discussions

In this Chapter the issues introduced by uncertainty about the fluid distribution at a sequestration site were examined. This was done in three ways: first, through a rock physics sensitivity study, second, by integrating flow and rock physics modelling to predict the time-lapse seismic response and finally by combining fine-scale fluid-flow modelling and rock physics models to predict the appropriate fluid distribution model. Here these results are combined to answer four questions regarding the impact of fluid distribution on the seismic response:

- How sensitive is the seismic response to the fluid distribution?
- Could certain fluid distributions detrimentally impact on the ability to monitor CO_2 migration?
- Which fluid distribution model is appropriate during sequestration?
- Can the fluid distribution in the reservoir be detected using the seismic response?

The fluid-flow simulation results demonstrated that the CO_2 saturation and location in the reservoir will change during and after injection due to the interaction of gravitational, viscous and capillary forces. A unique part of this study is the incorporation of these simulation results which provides realistic saturation values over time and an idea of how the fluid is trapped within the pore space. This is then used to help answer the questions posed above.

How sensitive is the seismic response to the fluid distribution?

The dependence of V_p on the distribution of fluids in the pore space was modelled using end-member fluid distribution models, with the lower bound (homogeneous distribution) being predicted using the Gassmann-Reuss model, and the upper bound (patchy distribution) being found from the Hill average. The homogeneous fluid distribution produced a very non linear relationship between V_p-S_{CO2}, whereas the patchy distribution produced a quasi-linear relationship. These different relationships highlighted potential problems when attempting to monitor CO_2 migration and quantify the volume of CO_2 stored when the fluid distribution is unknown. If there is no knowledge of the reservoir properties to constrain the bounds, then there could be significant errors with interpretation. However this uncertainty was reduced by adding the connate water and residual gas saturations as limits on the range of saturations (Figure 6-1). This demonstrates the importance of having knowledge of the reservoir properties from core measurements when interpreting the seismic response.

Even with the connate water saturation as a constraint, the models still predicted quite different relationships between V_p and CO_2 content. The bounds indicated that the sensitivity of V_p to the fluid distribution varies with the amount of CO_2, with the greatest contrast between the predictions at low-intermediate saturations, whereas the predictions converge when approaching the upper saturation limit (1-

S_{cw}). Structurally-trapped CO_2 was present at high saturation of about 55%, which was close to this upper limit, so the velocities predicted within this portion of the plume were very similar for both models (Figure 6-9a&c). However the V_p predictions for residually-trapped CO_2 were very sensitive to the fluid distribution and the homogeneous model predicted larger decreases in V_p than the patchy model. Therefore during injection when CO_2 is found at high saturations it does not matter which model is used to analyse the seismic data, while knowledge of the fluid distribution is needed when interpreting reflections from regions of the reservoir containing residually-trapped CO_2. This dependence on fluid distribution was highlighted in Figure 6-8 k-m& q-s, with the reflection off the base residual-plume being weaker when predicted using a patchy model.

What impact does this have on the ability to detect CO_2 migration?

Detecting the extent of the CO_2 plume and its migration is a key aim for monitoring; however the ability to achieve this depends on the fluid distribution. The homogeneous model predicted a very high sensitivity to very small quantities of CO_2, but the patchy model was much less sensitive. For example using the zero-offset reflectivity alone 2% homogeneously-distributed CO_2 could be detected, but 10% patchily-distributed CO_2 was required for a detectable change. This emphasises the importance of determining the appropriate model for the reservoir before interpreting the time-lapse seismic response. However fluid-flow modelling results indicated that CO_2 was typically present at saturations above the 10% threshold, so it should always be detectable. In more challenging monitoring environments, for example a less porous cemented sandstone aquifer, the response may not be as sensitive. In this case the AVO response may be useful as the sensitivity increases at greater angles of incidence.

Distinguishing high and low saturations representative of different trapping mechanisms was shown to not be possible for a homogeneous distribution (Section 4.4), however the more linear change in V_p with saturation produced by a patchy distribution would allow this. The synthetic sections indicated that the regions of the reservoir saturated with structurally-trapped and residually-trapped CO_2 could be differentiated using the reflection generated by the interface between these two plume regions (Figure 6-8k-m&q-s). The magnitude of this reflection was much smaller than those for both the top-reservoir and the brine-CO_2 interface which represents the base of the plume, and its magnitude depended on which fluid distribution model was used. The patchy model predicted a much larger reflection than the homogeneous response. This indicates the potential for the zero-offset reflectivity to detect the transition within the plume between the residually-trapped and structurally-trapped CO_2. Again, increasing the angle of incidence increased the magnitude of this reflection, so AVO data could prove useful for detecting this intraplume reflection. This reflection may not be detectable in thinner accumulations due to tuning.

Which fluid distribution model is appropriate during sequestration?

The previous discussions assumed that the fluid distribution model was constant throughout the reservoir during sequestration. However the literature reviewed in Section 2.5.5 indicated that the distribution of the fluids in the pore space may depend on the saturation processes in the reservoir, with imbibition producing a homogeneous response and drainage resulting in a patchy response. A model was proposed which applied the end-member models to different regions as defined by their saturation. Structurally-trapped (>30%) CO_2 was modelled using Hill and residually-trapped (≤30%) CO_2 was modelled using Gassmann-Reuss.

This idea of using two different fluid-distribution models within the same reservoir was reinforced by the upscaling results (Figure 6-14). Residually-trapped regions of the plume follow the homogeneous trajectory, whereas structurally-trapped portions were best fitted using an intermediate-patchy response. Physically this implies fluids being present in patches but without the phases being completely separate at the critical length scale. Although there is a discrepancy regarding the exact model for structurally-trapped CO_2 the results do indicate that different models should be applied for different regions.

Figure 6-15 shows the proposed modelling approach and gives a justification for the assumption that on the mesoscale the connectivity of fluids will differ depending on whether the CO_2 is structurally or residually trapped. The saturation histograms show the response for a homogeneous reservoir, where the saturations separate quite evenly into 30 and 60%. However in reality within a heterogeneous reservoir a wider range of CO_2 saturations would be expected. This Figure illustrates the different scales at which the variations in fluid mixing can form. On the seismic scales there are differences defined by the plume which forms by gravitational forces, whereas on the mesoscale there are variations resulting from capillary forces. If the reservoir was heterogeneous, then these differences in fluid mixing could be generated over a full range of scales (as illustrated in Figure 2-21).

This analysis has demonstrated that as the dominant trapping mechanism varies through time, so will the appropriate fluid distribution model. Immediately following injection the reservoir should be modelled using a patchier model, whereas once residual trapping has developed the homogeneous model would be appropriate.

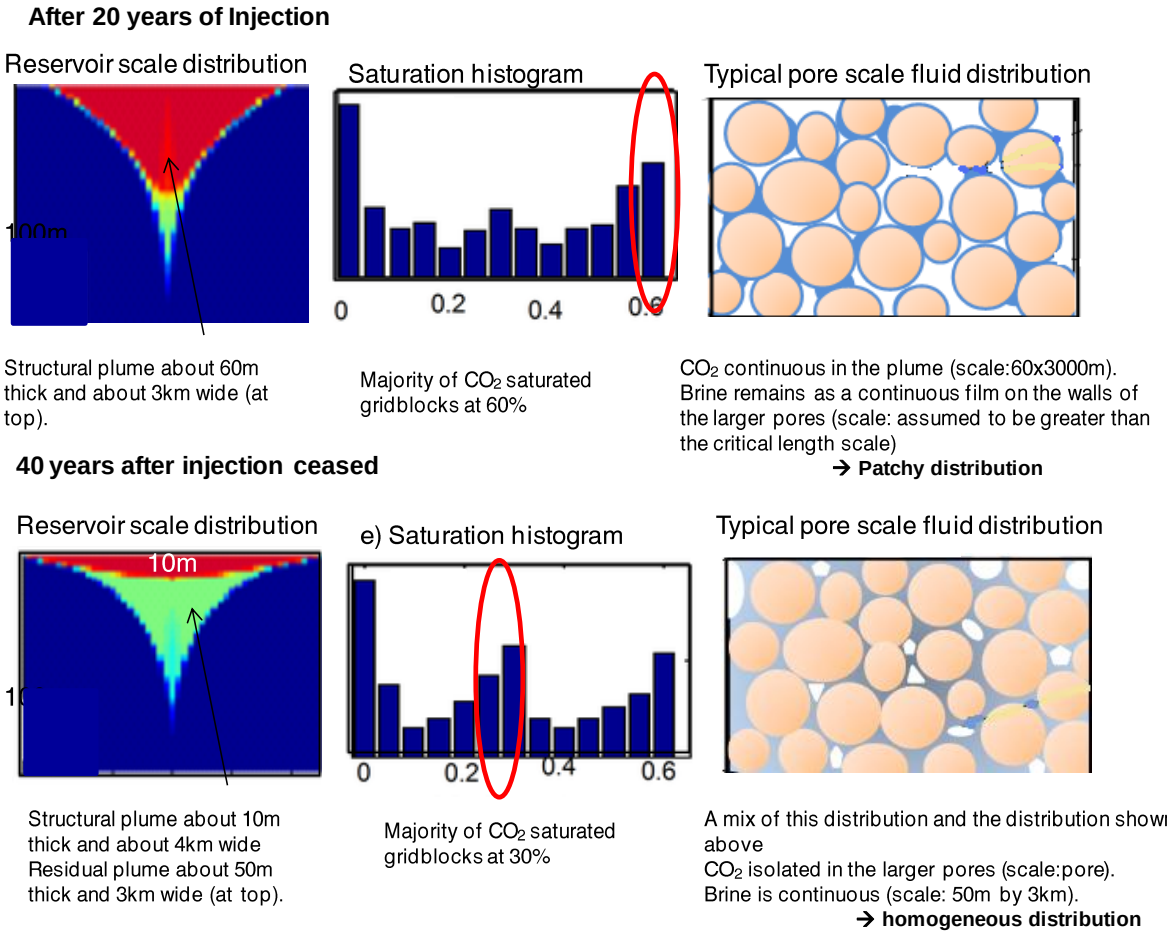


Figure 6-15 Cartoon illustrating the proposed model in terms of the results from this Chapter, and highlighting the scales over which fluid distribution variations can be seen in a homogeneous reservoir.

Can the fluid distribution in the reservoir be detected using the seismic response?

The approach proposed here used the fluid-distribution model as a proxy for the trapping mechanism, detection of either the fluid distribution or trapping type would greatly enhance the ability to interpret the seismic response. The sensitivity study indicated that converted shear-wave reflectivity might be able to distinguish fluid distribution models, although the magnitude of the difference was small. Using the proposed mixed fluid distribution model high and low saturations could be differentiated using the AVO response from the top-reservoir reflection, as structurally trapped CO_2 produced both higher gradient (B) and intercept (A) values than low CO_2 saturation saturations.

Again using the proposed model. The reflectivity in the plume highlighted the potential use of inter-reservoir reflections to determine the trapping phase. Cross-plotting of A and B may be able to differentiate the reflection generated by the interface between residual and structural CO_2 from the edge-plume reflection. Unfortunately the difference in the response was small and would require data with a high repeatability and a low noise level.

6.7 Conclusions

This study explored the issues posed by uncertainty about the fluid distribution at a sequestration site. One key thing demonstrated by this modelling process was how useful fluid-flow data and reservoir properties are for seismic interpretation. In particular including bounds on the saturation range limited the potential range of velocities and reduced the uncertainty. Three different modelling approaches were applied and a number of key conclusions can be made by integrating the results.

First, although it may be more challenging to monitor small amounts of CO_2 if the fluids are distributed in a patchy way, it is unlikely that CO_2 will be present at such low saturations that it will not be detectable. The zero-offset reflectivity clearly demonstrated this, with both the structural and residual portion of the plume being easy to monitor, irrespective of the fluid distribution. Although the residual CO_2-brine reflection was much smaller when a patchy distribution was used rather than a homogeneous distribution. The greatest sensitivity of V_p to the fluid distribution was at low-intermediate saturations typical of residually-trapped CO_2, whereas at high saturations representative of structurally-trapped CO_2 there was little or no difference between the model predictions. Therefore when CO_2 is present at high saturations during injection it does not matter which model is used to analyse the response, although it is important when CO_2 is present at low saturations.

Both the modelling results and literature review suggested that it is likely that different fluid-distribution models may be appropriate for different regions of the aquifer during sequestration. The model proposed here used the Gassmann-Reuss model for low saturation ($\leq$30%) residually-trapped CO_2 where the CO_2 is present as very small disconnected ganglia, and the Hill model for high saturations (>30%) where the CO_2 may be connected over scales greater than the critical length scale. This agreed relatively well with the Hill upscaling results, indicating that residually-trapped CO_2 should be modelled using the Gassmann-Reuss average. However it suggested that structurally trapped CO_2 should be predicted using an intermediate-patchy response (Brie, e=4). This idea of different fluid distribution models representing the different trapping mechanisms is important as it implies that because the dominance of these trapping mechanisms varies through time and space, so will the appropriate fluid distribution model. This may pose a problem for interpretation. However the velocity and reflectivity generated by the proposed and homogeneous model were very similar due to the convergence of the velocity predictions at high saturations, indicating that the homogeneous model could be sufficient in some cases.

The use of particular fluid distribution models to represent different trapping mechanisms implies that knowledge of the fluid distribution during sequestration would not only be required for interpretation, but could also provide information regarding the CO_2 trapping mechanisms. Cross-plotting of the top-reservoir A and B AVO attributes for the top reservoir could be used to differentiate structurally-trapped CO_2 and low-saturation CO_2. There is also the potential for converted shear-wave reflectivity to determine the

fluid distribution, however the magnitude of the difference between the models was small. Detecting the transition from structurally-trapped to residually-trapped CO_2 may be possible through the presence of a reflection within the plume, but the magnitude of this reflection depends on the fluid distribution. AVO cross-plots could indicate the trapping phase generating the intraplume reflections, although again the difference in the responses was small. Determining the fluid distribution using either the AVO or converted shear-wave reflectivity may be possible for shallower reservoirs, where there is a larger density contrast between brine and CO_2.

In conclusion, the ability of the zero-offset seismic response to track both structurally and residually-trapped CO_2 irrespective of the fluid distribution model used has been demonstrated, and the potential for detecting this transition from structurally-trapped to residually-trapped CO_2 was examined. It was suggested that different fluid distribution models may be appropriate for specified trapping mechanisms, with a homogeneous model being appropriate for residually-trapped CO_2 and a patchy/ intermediate-patchy model being appropriate for structurally-trapped CO_2. This is an important point as it implies that the appropriate fluid distribution model for interpretation may vary during sequestration and may differ for certain regions of the plume. Unfortunately attempts to extract the fluid distribution model and subsequently the trapping mechanism from the seismic response did not succeed due to the small density contrast between brine and supercritical CO_2. A summary of these results is presented in Table 6-3

Table 6-3 Chapter 6 summary. Indicating the best data to be collected to achieve certain monitoring aims. Colours indicate the confidence with the approach.. Green: should succeed, orange: may succeed, red: unlikely to succeed.

Monitoring Aim	Zero- offset Reflectivity		Mid-offset Reflectivity	Far-offset Reflectivity
	Amplitude	Pushdown	Amplitude	Amplitude
Detecting CO_2 migration	***More challenging when the patchy end-member model is used**			
Distinguishing residual and structural trapping				
Determining the fluid distribution				

7. Conclusions and Future Work

This final Chapter summarises the work performed and the results generated throughout this piece of research (Section 7.1). Using these results a seismic monitoring strategy was developed which is presented in Section 7.2. The results are also used to indicate topics which could warrant further research (Section 7.3).

7.1 Summary

7.1.1 Literature Review and Modelling Approach

Due to the potential environmental problems posed by the leakage of injected CO_2 from a storage aquifer into surrounding rocks or to the surface, extensive monitoring will be required at sequestration sites. Ideally this monitoring will be able to detect CO_2 migration, quantify the volume of fluid CO_2 stored (saturation), determine the CO_2 trapping phase and locate pore-pressure build-up.

Reviewing the literature on the use of time-lapse seismic surveys at sequestration sites (Chapter 2) highlighted five issues which could both impact on the ability of this technology to achieve the monitoring aims and could introduce uncertainty when interpreting the seismic response. These were:

1. The impact of reservoir properties on the sensitivity of the seismic response to CO_2 injection.
2. Difficulty in determining the CO_2 saturation due to the fizz-gas effect.
3. The fact the CO_2 phase may evolve through time.
4. The effect of pressure changes on the response.
5. Uncertainty about the appropriate fluid distribution model to use for seismic interpretation.

An integrated modelling approach was developed to investigate these issues at a generic sequestration site. Two approaches were used. The first predicted the sensitivity of the seismic response to subsurface changes by combining geological, rock physics and seismic modelling. The second approach additionally incorporated outputs from fluid-flow simulation, allowing for the prediction of the time-lapse seismic response. The first modelling approach was used to examine all the possible issues listed above, whereas the second approach was only used to examine pressure build-up and fluid distribution. With the exception of Section 4.3 (which investigated the impact of reservoir depth) the modelled injection reservoir was a clastic saline aquifer at 1500 m depth.

7.1.2 Key Findings

The thesis was divided into five chapters examining each of the issues highlighted by the literature review. These results are summarised below.

The effect of reservoir properties on the ability to monitor sequestration (assuming homogeneous fluid distribution):

- Depth was an important control on the sensitivity of the seismic response to fluid content. The magnitude of any change in the seismic response due to CO_2 decreased with increasing depth.
- V_p was more sensitive to the fluid content than V_s.
- Due to the non-linear V_p- S_{CO2} relationship, the zero-offset reflectivity was highly sensitive to small amounts (3% saturation) of CO_2 at all depths examined (<2500 m).
- The far-offset response had an even greater sensitivity to fluid content than the zero-offset reflectivity.

Difficulty in determining CO_2 the saturation due to the fizz-gas effect (assuming homogeneous fluid distribution):

- The zero-offset reflectivity could not be used to quantify CO_2 saturation and was not able to differentiate high (60%) and low (30%) saturations.
- Other seismic properties which are used to distinguish commercial and residual natural gas saturations were examined to see if they were applicable to supercritical CO_2.
    - Both the converted shear waves and AVO density parameter (*A*-*C*) were sensitive to fluid content, but the very small density contrast between brine and supercritical CO_2 caused the changes to be undetectable.
    - Attenuation was higher at low CO_2 saturations, particularly for gaseous CO_2. Unfortunately attenuation is not commonly recorded and at these low seismic frequencies the magnitude was low.
    - These approaches may be more applicable at shallow depths where CO_2 is gaseous.

The fact the CO_2 phase may evolve through time.

CO_2 can be gaseous, supercritical, dissolved in solution or precipitate as part of a solid phase. This work only investigated the first three of these changes. It was found that:

- Distinguishing gaseous and supercritical CO_2 possible through an AVO cross-plot of the *A* and *B* attributes, with gaseous CO_2 producing larger changes in *A* than supercritical CO_2, but a similar or smaller change in *B.*
- Distinguishing water saturated with CO_2 from pure water was not possible, as CO_2 dissolution had very little impact on the fluid's elastic properties. Although other studies indicated that although the effect of dissolution on the fluid properties may be small, it may produce a detectable increase in porosity due to the dissolution of susceptible minerals (McKenna et al. 2003).

The effect of pressure changes on the response:

- Increases in pore pressure altered both the fluid and frame properties.
    - The increase changed the relationship between CO_2 saturation and V_p.
    - The increase magnified the decrease in V_p caused by increasing CO_2 saturation.
    - The pressure build-up obliterated the small increase in V_s expected from increasing CO_2 saturation.
- Under some circumstances pressure changes may mask fluid content changes (Wulff et al. 2008), this was not seen here.
- The two seismic velocities had different sensitivities to pressure and saturation.
    - V_p was more sensitive to fluid content than V_s.
    - V_s was more sensitive to pressure changes than V_p.
- Detection of pressure build-up is required as it could results in failure of the reservoir or caprock.
    - Combined pressure and saturation changes resulted in a greater change in top-reservoir reflectivity and pushdown than saturation changes alone. Thus anomalously large changes in reflectivity could indicate pressure build-up.
    - The time-lapse seismic response produced by pressure build-up was not limited to the plume and changes away from the plume could indicate pressure changes.
    - Differentiating pressure and saturation changes was possible by cross-plotting *A* and *B*, as pressure build-up increased *B*, whereas saturation changes decreased *B.*

Uncertainty about the appropriate fluid distribution model to use for seismic interpretation.

The influence of different end-member fluid distribution models on seismic response was investigated:

- The end-member models predicted very different relationships between V_p and fluid content.
    - V_p was found to be most sensitive to the fluid distribution model at low to intermediate CO_2 saturations. The difference between the models was reduced by incorporating bounds on the possible range of saturations in the pore space defined by the connate water and residual gas saturation.
    - The homogeneous model predicted a greater sensitivity to small quantities of CO_2 than the patchy model
- Both structurally and residually trapped CO_2 were detectable using the zero-offset seismic response irrespective of which model was used via a reflection from the interface between structurally-trapped and residually-trapped CO_2:
    - The magnitude depended on the fluid distribution model used. The patchy model predicting a larger reflection than the homogenous model.
    - Could help quantify the amount of CO_2 trapped via different mechanisms.
- A model was proposed in which the fluid distribution model was related to the trapping mechanism, so the appropriate fluid distribution model may change with time and space.
    - Homogeneous model: residually-trapped portions of the plume
    - Patchy/ intermediate-patchy model: structurally-trapped CO_2.
- Due to the low density contrast between brine and supercritical CO_2 none of the approaches applied were able to differentiate the fluid distribution models. Indicating that seismic data could not be used to determine which fluid distribution model is most realistic.

Using these results conclusions can be made regarding the ability of time-lapse seismic surveys to accomplish the monitoring aims.

1. Zero-offset reflectivity can be used to detect the location of both the structurally-trapped and residually-trapped portions of the plume for a range of reservoir depths (500-2500 m). This ability to detect CO_2 migration using the zero-offset reflectivity was true irrespective of the fluid distribution model used.
2. Unfortunately none of approaches examined were able to provide CO_2 saturation to quantify the volume of CO_2 stored.

3. It was not possible to detect solubility trapping. However, a reflection was identified on the zero-offset reflectivity between the residually and structurally trapped portions of the plume, which could help quantify the amount of CO_2 retained by these trapping mechanisms. The AVO response may help to differentiate whether the CO_2 is gaseous or supercritical.
4. Detection of overpressure was possible using the zero-offset reflectivity, as a pressure increase produced anomalously large amplitude changes within the plume region and changes away from the plume. Distinguishing pressure and saturation changes required the use of AVO.

Overall this modelling approach highlighted the importance of conducting a monitoring sensitivity study and demonstrated the advantages of incorporating fluid-flow simulation results into a seismic sensitivity study.

7.2 Monitoring Approach

Currently there is public concern about the idea of injecting CO_2 and the possible dangers posed by leakage. Therefore for the moment the monitoring approach must consist of a technology with a proven track record for monitoring fluid movement and pressure changes in the subsurface, i.e. time-lapse seismic surveys. Once CO_2 sequestration is demonstrated to be safe, cheaper monitoring alternatives may be more appropriate, such as gravity and satellite surveying.

The approach to developing a monitoring strategy described here is focussed on time-lapse seismic surveys, however this approach could be modified to examine other geophysical techniques. The sensitivity study described in this thesis not only indicates how well injection can be monitored, but should be used as a guide to what data should be collected and how it should be analysed. Here the sensitivity study is first put in context of where it should fall in the site selection process (Section 7.2.1), and then using the results presented in Chapters 4, 5 and 6, suggestions are made regarding what data should be collected depending on the monitoring requirements for a site. A cartoon can be seen in Figure 7-1 which demonstrates this workflow.

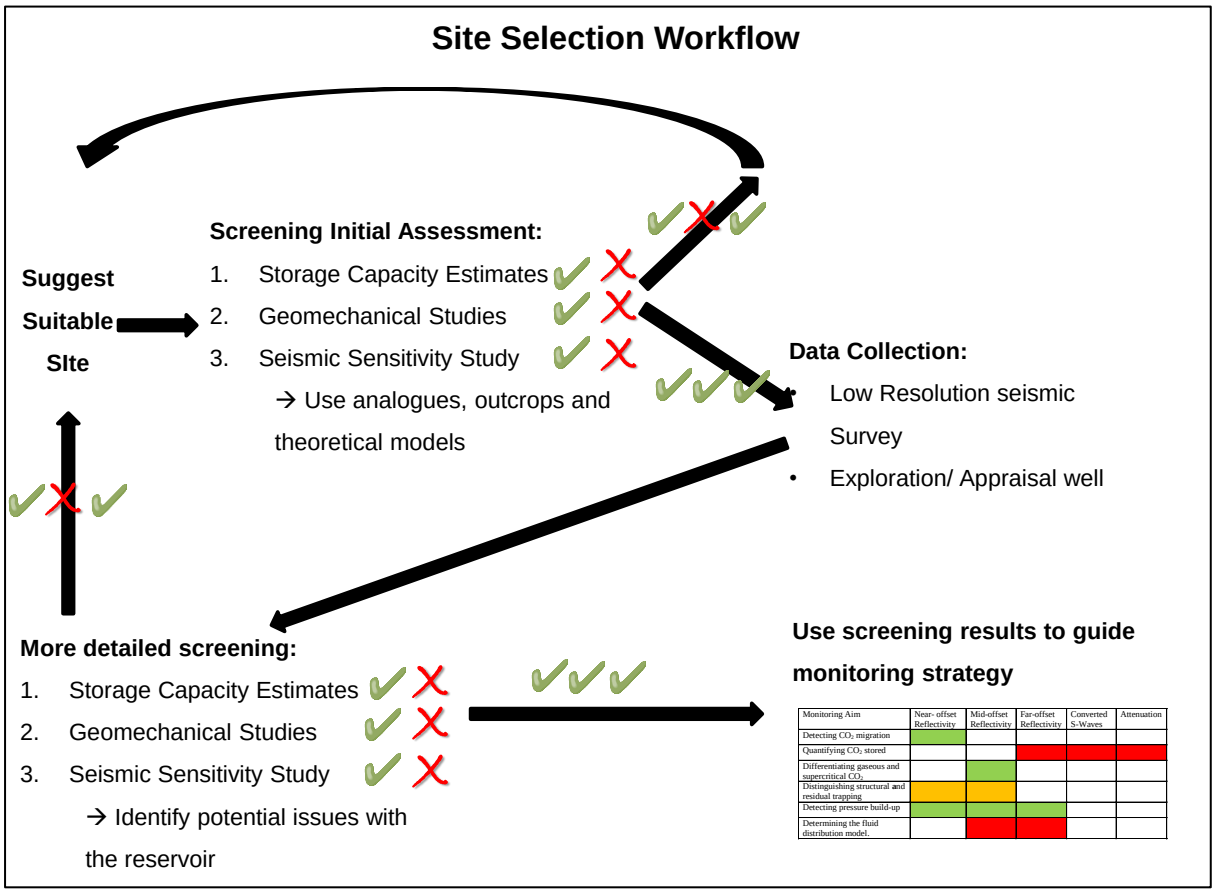


Figure 7-1 Cartoon illustrating the suggested site selection workflow. The ticks and crosses indicate the possible results from the screening and indicate the path which should be taken after the screening.

7.2.1 Site Selection

The ideas presented in this Section represent an idealised workflow for site selection based on the learnings from this research and do not necessarily represent the current, accepted approach. The selection of an aquifer for sequestration will be based on a number of well defined steps. Following the identification of a possible target formation there will be a site screening process, which will consist of storage capacity estimates to determine whether the site offers sufficient volume to make the project financially viable, geomechanical studies to determine safe injection pressures and a seismic sensitivity study to calculate if CO_2 injection into the formation could be monitored using time-lapse seismic surveys.

Within this idealised workflow this screening process will be conducted twice. First there will be an initial assessment, and then if the site fulfils all the requirements there will be a secondary assessment. The first phase will use information from analogues, outcrops and theoretical models, and the examination of seismic sensitivity will be similar to the rock physics sensitivity study conducted in Section 5.4. If the reservoir is found to have sufficient storage capacity, be geomechanically stable and have rock properties which are conducive for successful seismic monitoring, then this will warrant further data collection. Data collection will be in the form of a low resolution seismic survey to map reservoir architecture and better quantify the reservoir volume, and a well to measure reservoir properties. This additional data can be used to conduct more detailed storage capacity estimates, geomechanical studies and seismic sensitivity studies. At this stage a seismic sensitivity study similar to that in Section 5.5 will be conducted, i.e. fluid-flow simulation results should be included. This assessment stage will identify any potential issues with or unique properties of the reservoir, such as possible compartmentalisation or mineralogy highly conducive of mineral trapping. This knowledge will then be used to guide the monitoring strategy deployed at the site.

7.2.2 Monitoring Strategy

Prior to injection commencing, a monitoring strategy should be designed which will guide the scope of any surveys, i.e. what data will be collected and how often this should occur. These parameters will influence the cost of any monitoring. This Section will demonstrate how the outcomes from the seismic sensitivity study can be used to guide this process of survey design, and potentially how it can be used to reduce costs by clearly indicating which data is required. Using the results from the seismic sensitivity study the monitoring aims can be clearly stated, i.e. if there is possible issues with compartmentalisation, then a monitoring approach is needed which can detect pressure build-up. Presented here is the best data which should be collected to fulfil specific monitoring requirements.

- **Detecting CO_2 migration**, if there is concern about flow into surrounding formations.
    - **Zero-offset reflectivity.**
        - CO_2 invasion of the pore space will be indicated by a brightening of the reflectors and a pushdown of reflections below the plume.
        - The saturation front can be mapped using a near-offset stack.
    - **Mid to far offset reflectivity.**
        - Has a greater sensitivity to fluid content than the zero-offset response and would be collected if the sensitivity study indicated that the zero-offset reflectivity is inadequate**.**
- **Quantifying the amount of CO_2,** to verify containment.
    - No approach prove particularly successful, possible useful data:
        - Shallow aquifer: **converted shear-wave reflectivity** or **far-angle data.**
        - Deep aquifer: **attenuation** which would require **high frequency data** and spectral decomposition.
- **Determining CO_2 phase,** if there is uncertainty about the temperature and pressure conditions in the reservoir**:**
    - **Mid-offset data.**
        - Cross-plotting the AVO attributes *A* and *B*.
- Quantifying the amount of CO_2 retained via different **trapping mechanisms.**
    - **Dissolution:** no seismic property found to be sensitive.
    - **Differentiating structural and residual trapping:**
        - Shallow aquifer: potential for identified through **mid-offset reflectivity** (cross-plotting *A* and *B*).
        - Z**ero-offset reflectivity,** identify the interface between the plume regions.
- **Pressure build-up**, if identified as an issue during simulation studies.
    - **Zero-offset reflectivity,** identify pressure changes.
        - Pressure build-up should brighten the reflectivity and result in increased pushdown of the base-reservoir reflection.
        - Change in reflectivity away from the plume on the near-offset stacks indicative of pressure build-up.
    - **Mid-offset reflectivity**, differentiate pressure and saturation changes
        - Cross-plotting of the change in the *A* and *B* AVO attributes.
- Determining the appropriate **fluid distribution model.**
    - Shallow aquifers: possibly using **mid to far-offset reflectivity.**

- Deep aquifers: use **high frequency well-based techniques** for the interwell region, such as those used at Nagoaka.
- The model used may depend on the type of trapping in the reservoir:
  - **Structural trapping,** (immediately following injection) should be modeled using the patchy response.
  - **Residual trapping**, should be modeled as homogeneous.
  - Due to the relative insensitivity of V_p to fluid distribution at high saturations, it may be appropriate for the homogenous model alone to be used.

This information is summarised in Table 7-1.

Table 7-1 Indicating the best seismic data to be collected to achieve certain monitoring aims. It is assumed that if non-zero offset reflectivity is collected so is the zero-offset reflectivity. The colours indicate the confidence assigned to the approach.. Green: Should Succeed, orange: May succeed, red: Unlikely this approach will work.

Monitoring Aim	Zero- offset Reflectivity	Mid-offset Reflectivity	Far-offset Reflectivity	Converted S-Waves	Attenuation
Detecting CO_2 migration					
Quantifying CO_2 stored					
Differentiating gaseous and supercritical CO_2					
Distinguishing structural **a**nd residual trapping					
Detecting pressure build-up					
Determining the fluid distribution model.					

As the time-lapse method requires the subtraction of one survey from another, the acquisition parameters and processing sequence for the monitor surveys should be kept as similar as possible to that for the baseline survey (Lumley and Behrens 1998). This baseline survey should be conducted prior to injection. One method of assuring that acquisition is identical between surveys is the use of a permanent seismic array, such as that used successfully at the BP Valhall field in the Norwegian North Sea (van Gestel et al. 2008). These surveys should then be processed in an identical fashion, via parallel processing. van Gestel et al. (2008) presented a workflow for acquiring and processing time-lapse seismic surveys over a producing hydrocarbon field, this workflow could be modified and applied to monitoring sequestration. The study also discusses how seismic and well data can be used together to update both the static and dynamic reservoir models.

There are some practical limitations which may impact on this idealised monitoring approach. One is the issue of data quality and noise. For example at non-zero offsets the amount of noise will increase and the high frequencies will be attenuated, which may limit the angle range available for

interpretation. A second very important practical issue is that of cost. Time-lapse seismic surveys are commonly acquired over producing hydrocarbon fields, where the results influence decisions regarding wells and production strategy and therefore they can make a significant impact on profits. Whether this surveying method is financially viable at sequestration sites is another question. However the aims of monitoring at sequestration sites do differ from those at hydrocarbon fields, as during CO_2 injection the aim is to detect leakage and potential problems, whereas at producing oil and gas fields the time-lapse data will guide production decisions. Therefore the frequency of surveys required at sequestration sites is likely to be lower than that at hydrocarbon fields, thereby reducing the costs.

The frequency of surveys will be dictated by a mixture of cost concerned and the fluid-flow simulation results showing plume migration and pressure build-up. From the modelling results in Chapter 5 it was predicted that after 2 years of injection the pressure would increase about 2 MPa and the plume would grow to about 1000m wide. These changes would both be detectable on seismic surveys. At Sleipner about 6 identical seismic surveys have been conducted in 12 years, roughly one every 2 years (Arts et al. 2008). The first repeat survey was after 4 years of injection and showed a large plume, and the subsequent surveys have shown this plume grow. The frequency of surveys at Sleipner appears adequate to monitor the plume growth.

The cost of monitoring will vary significantly with certain factors, such as whether it is terrestrial or marine and whether a permanent acquisition array is used. Hendriks et al. (2004) estimated that the cost of repeat seismic surveys (conducted every 5 years) was 0.3 US$ per tonne of CO_2 stored. The overall cost of a sequestration site is highly variable (IPCC 2005), but estimates for onshore storage in Europe put the cost at about 2.8 US$ per tonne of CO_2 stored (Myer et al. 2002). Therefore the cost of time-lapse seismic surveys is small in comparison to the cost of the overall project, and potentially much cheaper than the costs which could be incurred by unidentified leakage. Due to the nature of sequestration and the tight financial constraints the monitoring should be carefully planned in advance to minimise on unnecessary acquisition and processing. This cost reduction can be guided by the results from the seismic sensitivity study as demonstrated in Table 7-1.

7.3 Modelling Challenges and Future Work

The results summarised in Sections 7.1 and 7.2 are from an initial phase of modelling the relationship between subsurface changes caused by CO_2 injection and the time-lapse seismic response. During this work a number of simplification and assumptions were made to allow specific variables to be examined. In future this modelling approach could be extended or modified to examine the impact of these simplifications and to explore other interesting issues to do with monitoring. While conducting this research a number of grey areas around the relationship between changes in the subsurface and its projection on the seismic response were highlighted. These uncertainties could warrant further examination. Here these modelling limitations and areas of uncertainty are discussed in detail, along with suggestions for future work and research.

7.3.1 Simplified Geological Modelling

The geological modelling used so far remained simple to allow the impact of specific changes in the reservoir on the seismic response to be isolated. The aquifer was a thick, high porosity, homogeneous sandstone, with a constant overburden. While this was appropriate for this initial modelling stage and provided clear understanding of the relationship between subsurface and seismic changes, it could have introduced some bias into the results. For example, the reservoir thickness (100 m) allowed for a clear distinction between the top-reservoir and base-reservoir reflections, however Section 4.3.2 demonstrated that this is not always the case. Also the lithology was quite ideal for monitoring and the seismic response to this particular lithology proved to be very sensitive to both pressure and saturation changes, which may over state the capabilities of time-lapse seismic monitoring. The focus of this thesis has been on injection into a saline aquifer, therefore it has been limited to two fluid phases, which would not be appropriate in depleted hydrocarbon fields. The presence of another fluid phase could complicate interpretation.

This existing modelling approach could be extended and modified to represent either a different or more complex geological setting. Varying the reservoir lithology, consolidation and cementation would allow for an examination of the seismic response in a "stiffer reservoir". Also as the vertical seismic resolution limits the ability to monitor thin accumulations, the reservoir thickness could be reduced to examine the impact of seismic tuning. Introducing heterogeneity into the reservoir would also be interesting. For example, placing baffles and barriers to flow would alter CO_2 migration, pressure build-up and fluid distribution. It would be interesting to explore how monitoring would be affected by this. Introduction of heterogeneities could also allow for an examination of saturation heterogeneities formed by geological variability. To examine the ability to monitor injection into a depleted hydrocarbon field, the model could be modified to introduce either oil and/or gas into the pore space.

The existing work focussed on detecting of changes within the target reservoir, but an interesting topic of further research could be looking at leakage into the caprock. This could be done in two ways: first, through a rock physics sensitivity study using caprock properties, and second, by using integrated and rock physics and fluid-flow simulation study, where the caprock has a low, but non-zero permeability. This would be a useful application, as leakage to the surface could be hazardous.

7.3.2 Seismic Modelling and Monitoring Approach

Up to this point the seismic modelling was performed using CREWES open-source software. This software allowed variables to be easily controlled and understood, but it imposed some limitations on the seismic modelling performed. For example an arbitrary value for seismic detectability was used instead of incorporating noise into the modelling. The examination of the AVO response also lacked statistical information about the detectability of the changes. These simplifications made it challenging to qualify which changes could be detected and interpreted. Also the current modelling approach solely considers field-scale time-lapse seismic surveys, whereas at existing sites this can be combined with results from gravity surveys and well measurements (Section 2.4.1).

The use of commercial seismic modelling software, such as Hampson-Russell (*CGGVeritas*) would allow realistic amounts of noise to be modelled and the statistical analysis of AVO attributes to be evaluated. This more robust qualification of the detectability of changes in the seismic response could help eliminate some of uncertainties with the results presented in Section 7.1, such as whether cross plotting *A* and *B* could help differentiate the different fluid distribution responses. Commercial software would also allow other techniques, such as spectral decomposition to be examined with relative ease. Spectral decomposition could be used to examine tuning and attenuation.

In addition to these seismic modelling modifications, the modelling approach could be extended to include other lower cost geophysical techniques identified in Section 2.4.1. It would be useful to fully compare the abilities and limitations of gravity and satellite surveys with those of the time-lapse seismic method. Also by incorporating these techniques into the modelling approach the use of joint inversion could be explored. Work performed at the Nagoaka site (Onishi et al. 2008) demonstrated the useful information which can be gained from well-based studies. Including this into the modelling would be interesting and could be particularly useful when examining the uncertainty of the fluid distribution and the challenges posed by the frequency dependence of the seismic response.

7.3.3 Application to a Specific Aquifer

To allow the results to be generalised with ease, the modelling was deliberately non-specific, however the approach could benefit from the use of some field data, such as well logs and seismic. The rock, fluid and reservoir properties were predicted using theoretical models, and the "idealised" aquifer lacked realistic dimensions and geometry. These properties dictate the sensitivity of the seismic response to fluid content, how the injected CO_2 migrates and any pressure changes.

Following the modifications and extensions suggested in Sections 7.3.1 and 7.3.2, the model could be applied to a specific field, preferably a site within the UK. A rock physics sensitivity study could be conducted to assess the ability to monitor CO_2 injection and the combined modelling approach could predict the time-lapse seismic response. The ultimate goal would be to perform this modelling approach for a field undergoing sequestration. Then the full monitoring strategy outlined in Section 7.2 could be applied and the time-lapse seismic response could be interpreted and analysed to test some ideas from Section 7.1. One result which could be tested is the differentiation of pressure and saturation changes by cross-plotting AVO attributes. Also the time-lapse data could be compared to the predictions from the integrated modelling approach, to update the reservoir model and better understand the behaviour of the injected CO_2 and the pressure changes within the aquifer.

7.3.4 Integration Issues

The increasing use of time-lapse seismic surveys as both a monitoring technique for sequestration and a tool to assess production from a hydrocarbon field requires greater integration of geological, rock physics and fluid-flow modelling. This work touched upon some of the issues associated with that integration, such as the problem of gridblock size and saturation and the way the relationship between V_p and S_{CO2} is affected by the connate water and residual gas saturation (Section 3.3.3.2.1). In general there is mismatch between the scales at which different disciplines "see" the reservoir. Geological information is available on the metre scale, the seismic resolution is on the order of decametres and fluid-flow simulation of CO_2 injection is commonly performed using gridblocks which are 100's of meters in size (Section 3.8.3). Furthermore the inclusion of fluid-flow information into the prediction of the seismic response, introduces an additional variable which impacts on the detectability of the CO_2 plume. This variable is the relative permeability, which dictates the typical CO_2 saturation in the plume.

A way in which this integrated approach could be improved would be through the use of a commercial simulation-to-seismic package, such as sim2seis (*Landmark*) which would allow for the reservoir simulation results to be taken straight into the seismic modelling package. This would allow for easier incorporation of reservoir heterogeneities and structure than the current approach. In addition the use of integrated software packages would alleviate the issues of scale highlighted in

Section 3.8.3. However this approach would remove some of the control gained by designing the rock physics modelling in C. There may be limitations such as which equation would be used to predict CO_2 properties. Plus the software would not allow for the development of the "proposed" model in Chapter 6, by which different fluid distribution models were applied to different reservoir regions.

An interesting application of the existing integrated modelling approach could be to examine the impact of relative permeability on the ability to monitor CO_2 injection. The relative permeability and subsequently the CO_2 saturation will control the magnitude of any changes in reflections within and around the plume Therefore this variable could place limitations on the ability to monitor plume migration in certain reservoirs.

The link between attenuation and residual gas saturation shown in Section 4.4.3 could indicate an area of future research, which combines fluid-flow and rock physics modelling. This link could be examined on the laboratory and well-scale to determine whether seismic attenuation could help quantify the amount of residually-trapped CO_2 within the pores. Another suggested topic for greater examination would be in understanding the way in which pore scale and mesoscale variations within the reservoir impact on the seismic response. This could help guide the way in which reservoir properties calculated by fluid-flow simulation are used to predict the seismic response.

7.3.5 Fluid Distribution

One important and potentially problematic issue highlighted here was that of fluid distribution. The fact that the majority of the modelling was performed using the end-member models may lead to an over simplification of the complex relationship between the pore fluids and rock matrix. Also the set-up of the proposed "mixed" fluid distribution modelling (Section 6.4.2.1) may have introduced artefacts into the results. The model uses one saturation value to transition from one model to another, whereas in reality this would be more gradual. This instantaneous change in behaviour may result in changes in the elastic and seismic properties of the reservoir which could predict a "fake" reflection. To understand this better would require knowledge of the scales over which the behaviours vary. In addition to these issues there are some problems trying to give physical justifications for some of the theoretical models used in Chapter 6.

The approach used in Section 6.5 to predict which fluid distribution model should be used to interpret the seismic response was somewhat awkward. The model assumed a link between gridblock size and fluid continuity, i.e. for gridblocks below the critical length scale the fluids can be calculated using the homogeneous model. In reality fluid continuity is actually determined by the rock structure and flow regime. The gridblocks merely discretise the flow equations, which assume continuity of the fluids across gridblocks unless two adjacent gridblocks have saturations of 1 and 0. In the same way providing a physical explanation for the "modified patchy" relationship discussed in Section 3.3.3.2.1

was challenging. A possible explanation was given in Section 6.4.2.1, but truly understanding these relationships would require a more extensive study.

Examining fluid continuity would require either pore scale modelling, which is not possible over length scales of more than a few mm due to computational limitations or laboratory experiments which would require an examination of both flow and seismic response in rocks of 1m or so (critical length scale) in size. These laboratory studies are commonly conducted at very high frequencies at which attenuation mechanisms other than mesoscopic patchy saturation dominate. This would make generalising laboratory results to the field-scale challenging. Well-based approaches, such as those conducted at Nagoaka (Sato et al. 2011) could bridge the gap between the pore and field scale.

Appendix

Appendix A

To calculate the AVO response the Zoeppritz equations were used (Zoeppritz 1919):

$$A_1 \cos\theta_1 - B_1 \sin\lambda_1 + A_2 \cos\theta_2 + B_2 \sin\lambda_2 = A_0 \cos\theta_1$$
$$A_1 \sin\theta_1 + B_1 \cos\lambda_1 - A_2 \sin\theta_2 + B_2 \cos\lambda_2 = -A_0 \sin\theta_1$$
$$A_1 Z_1 \cos 2\lambda_1 - B_2 W_1 \sin 2\lambda_1 - A_2 Z_2 \cos 2\lambda_2 - B_2 W_2 \sin 2\lambda_2 = -A_0 Z_1 \cos(2\lambda_1)$$
$$A_1 \gamma_1 W_1 \sin 2\theta_1 + B_1 W_1 \cos 2\lambda_1 + A_2 \gamma_2 W_2 \sin 2\theta_2 - B_2 W_2 \cos 2\lambda_2 = A_0 \gamma_1 W_1 \sin 2\theta_1$$

where Z_n: S impedance, W_n: P impedance and γ_n: V_s/V_p. Using these equations the reflection and transmission coefficients for the P, S and converted waves can be calculated, the code used to do this is shown in Appendix C.

The code was verified through visual comparisons with results from the CREWES Zoeppritz explorer (Margrave 2003), the parameters used to predict the reflectivity are shown in Table A1.

Table A-1 The seismic velocities and densities of the two layers, the interface between which generates a reflection. Subscript1 refers to the upper layer and subscript 2 refers to the lower layer.

	Case A Brine Filled	**Case B** 50% CO_2 Homogeneous	**Case C** 100% CO_2 Filled
V_{p1}	2646.9 m/s	2646.9 m/s	2646.9 m/s
V_{p2}	2627.6 m/s	2162.0 m/s	2161.7 m/s
ρ_1	2248.5 kg/m^3	2248.5 kg/m^3	2248.5 kg/m^3
ρ_2	2110.7 kg/m^3	2062.5 kg/m^3	2015.3 kg/m^3
V_{s1}	1316.2 m/s	1316.2 m/s	1316.2 m/s
V_{s2}	1421.7 m/s	1438.2 m/s	1455.0 m/s

The results are shown in Figure A-1, with the different cases being representative of different saturation conditions within the reservoir, as mentioned in Table A-1. The predictions appear identical therefore validating the code.

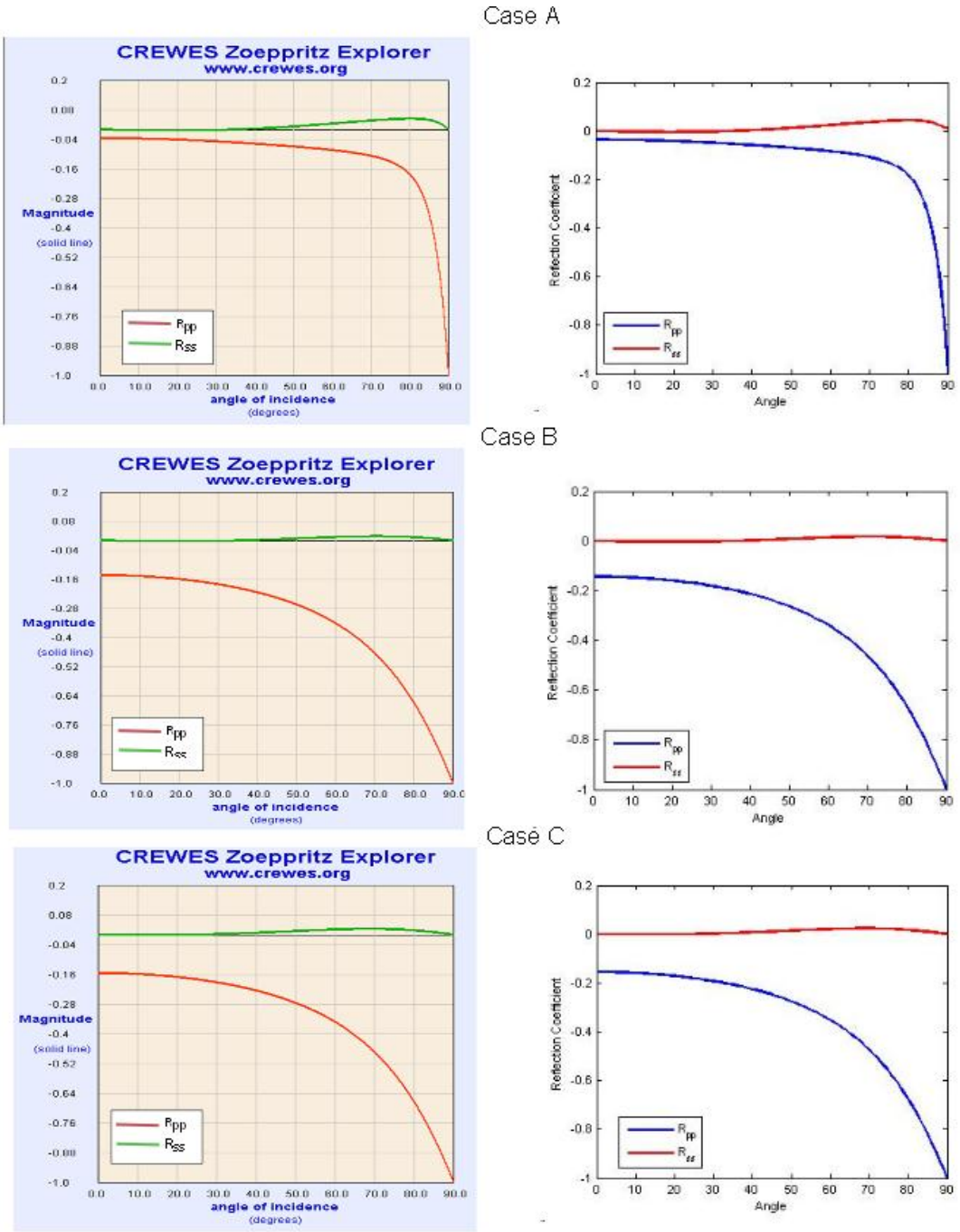


Figure A-1 Comparison of the results from CREWES Zoeppritz Explorer and the AVO response predicted using the code above, for three different saturation conditions.

Appendix B

The code for the White equations (Equations 3-48 to 3-49) was verified via a visual comparison with results published in Carcione et al, (2003), as shown in Figure B-1. It can be seen that visually the predictions appear identical.

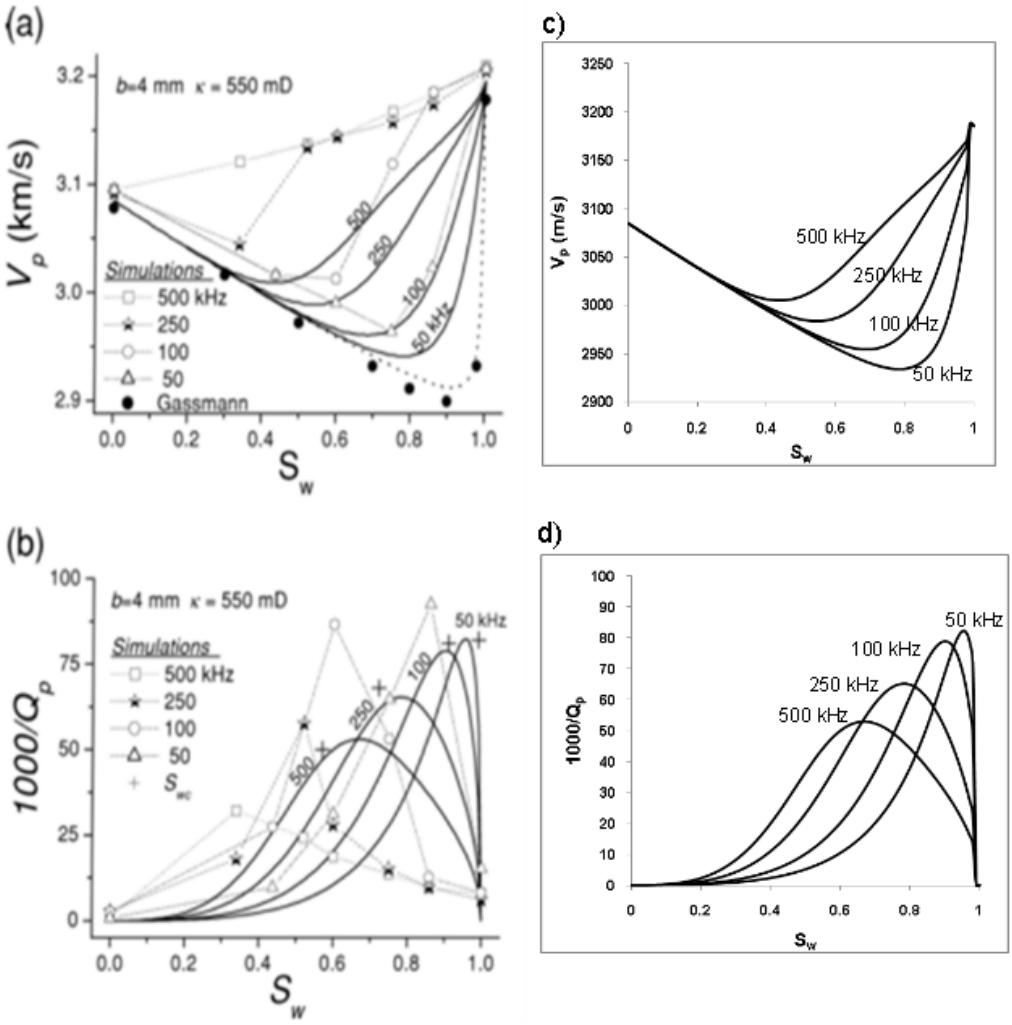


Figure B-1 Verification of the coding for the White (1975) equations. a&b) Results from Carcione et al (2003), c&d) Results generated by the code used in this thesis.

References

Aki, K., and P. G. Richards (1980), *Quantitative Seismology: Theory and Methods*, W.H. Freeman and Co.

Alvarez, E. and MacBeth, C. (2012) Constraining the Petro-elastic Model with a Flatlander's Interpretation of the 4D Signal. *74th EAGE Conference & Exhibition incorporating SPE EUROPEC.*

Arts, R., A. Chadwick, O. Eiken, S. Thibeau, and S. Nooner (2008), 10 years experience of monitoring CO_2 injection in the Utsira sand at Sleipner, offshore Norway, *First Break*, *26*, 65-72.

Arts, R., A. Chadwick, and O. Eiken (2004a), Recent time-lapse seismic data show no indication of leakage at the Sleipner CO_2-Injection site, in *7th International Conference on Greenhouse Gas Control Technologies*.

Arts, R., O. Eiken, A. Chadwick, P. Zweigel, B. van der Meer, and G. A. Kirby (2004b), Seismic monitoring at the Sleipner underground CO_2 storage site (North Sea), *Geological Society, London, Special Publications*, 233(1), 181-191.

Arts, R., O. Eiken, A. Chadwick, P. Zweigel, L. van der Meer, and B. Zinszner (2004c), Monitoring of CO_2 injected at Sleipner using time-lapse seismic data, *Energy*, *29*(9-10), 1383-1392,

Avseth, P., T. Mukerji, and G. Mavko (2005), *Quantitative Seismic Interpretation*, Cambridge University Press.

Azuma, H., C. Konishi, D. Nobuoka, Z. Xue, and J. Watanabe (2011), Quantitative CO_2 saturation estimation from time lapse sonic logs by consideration of uniform and patchy saturation, *Energy Procedia*, *4*, 3472-3477.

Bachu, S. (2003), Screening and ranking of sedimentary basins for sequestration of CO_2 in geological media in response to climate change, *Environmental Geology*, *44*(3), 277-289,

Bachu, S., W. D. Gunter, and E. H. Perkins (1994), Aquifer disposal of CO_2: hydrodynamic and mineral trapping, *Energy Conversion and Management*, *35*(4), 269–279.

Batzle, M., and Z. Wang (1992), Seismic properties of pore fluids, *Geophysics*, *57*(11), 1396-1408.

Bennion, B., and S. Bachu (2008), Drainage and Imbibition Relative Permeability Relationships for Supercritical CO_2/Brine and H_2S/Brine Systems in Intergranular Sandstone, Carbonate, Shale, and Anhydrite Rocks, *SPE Reservoir Evaluation & Engineering*, *11*(3), 487-496.

Bennion, D., and S. Bachu (2006), Dependence on Temperature, Pressure, and Salinity of the IFT and Relative Permeability Displacement Characteristics of CO_2 Injected in Deep Saline Aquifers, *Proceedings of SPE Annual Technical Conference and Exhibition*, 1-9.

Bergen, F. Van, H. J. M. Pagnier, L. G. H. van der Meer, F. J. G. van den Belt, P. L. A. Winthaegen, and R. S. Westerhoff (2002), Development of a field experiment of CO_2 storage in coal seams in the Upper Silesian Basin of Poland (RECOPOL), in *6th International Conference on Greenhouse Gas Control Technologies (GHGT-6)*.

Bergmo, P. E. S., A. Grimstad, and E. Lindeberg (2010), Simultaneous CO_2 injection and water production to optimise aquifer storage capacity, *International Journal of Greenhouse Gas Control*, 1-10.

Berryman, J. G. (1995), Mixture theories for rock properties, in *Rock Physics and Phase Relations: a Handbook of Physical Constants*, pp. 205-228, AGU, New York.

Biot, M. A. (1956), Theory of Propagation of Elastic Waves in a Fluid-Saturated Porous Solid. II. Higher Frequency Range, *The Journal of the Acoustical Society of America*, *28*(2), 179.

Bossie-Codréanu, D. (2008), The CO_2-EOR sequestration equation: recovery, dynamic monitoring, and co-optimization, *First Break*, *26*(January), 73-83.

Brie, A., Pampuri, F., Marsala, A.F. and Meazza, O., (1995) Shear Sonic Interpretation in Gas-Bearing Sands. Proceedings of SPE Annual Technical Conference and Exhibition. Society of Petroleum Engineers, 701-710

Brown, L. T., T. L. Davis, and M. Batzle (2002), Integration of rock physics, reservoir simulation, and time-lapse seismic data for reservoir characterization at Weyburn Field, Saskatchewan, 1708-1711.

Brown, S., G. Bussod, and P. Hagin (2007), AVO monitoring of CO_2 sequestration: A benchtop-modeling study, *The Leading Edge*, *26*(12), 1576-1583.

Bruce, B., and G. Bowers (2002), Pore pressure terminology, *The Leading Edge*, *21*(2), 170.

Buland, A., and H. Omre (2003), Bayesian linearized AVO inversion, *Geophysics*, *68*(1), 185.

Cadoret, T., G. Mavko, and B. Zinszner (1998), Fluid distribution effect on sonic attenuation in partially saturated limestones, *Geophysics*, *63*(1), 154-160.

Carcione, J. M., H. B. Helle, and N. H. Pham (2003), White's model for wave propagation in partially saturated rocks: Comparison with poroelastic numerical experiments, *Geophysics*, *68*(4), 1389-1398.

Carcione, J. M., S. Picotti, D. Gei, and G. Rossi (2006), Physics and Seismic Modelling for Monitoring CO_2 Storage, *Pure and Applied Geophysics*, *163*(1), 175-207.

Carroll, J. J., J. D. Slupsky, and A. E. Mather (1991), The Solubility of Carbon Dioxide in Water at Low Pressure, *Journal of Physical and Chemical Reference Data*, *20*(6), 1201.

Caspari, E., T. M. Müller, and B. Gurevich (2011), Time-lapse sonic logs reveal patchy CO_2 saturation in-situ, *Geophysical Research Letters*, *38*(13), 18-21,

Castagna, J. P., H. W. Swan, and D. J. Foster (1998), Framework for AVO gradient and intercept interpretation, *Geophysics*, *63*(3), 948-956.

Cavanagh, A. J., R. S. Haszeldine, and M. J. Blunt (2010), Open or closed? A discussion of the mistaken assumptions in the Economides pressure analysis of carbon sequestration, *Journal of Petroleum Science and Engineering*, *74*, 107-110.

Chadwick, A. et al. (2010), Quantitative analysis of time-lapse seismic monitoring data at the Sleipner CO_2 storage operation, *The Leading Edge*, *29*(2), 170-177.

Chadwick, R. A., R. Arts, O. Eiken, G. A. Kirby, E. Lindeberg, and P. Zweigel (2004a), 4D Seismic Imaging of an Injected $C0_2$ Plume at the Sleipner Field, Central North Sea, *Geological Society, London, Memoirs*, *29*(1), 311-320.

Chadwick, R. A., R. Arts, and O. Eiken (2005), 4D seismic quantification of a growing CO_2 plume at Sleipner , North Sea. In Dore, A.G. and B.A Vining (eds) Petroleum Geology: North-West Europe and Global Perspectives—Proceedings of the 6th Petroleum Geology Conference, 1385–1399.qPetroleum Geology Conferences Ltd. Published by the Geological Society, London.

Chadwick, R. A., P. Zweigel, U. Gregersen, G. A. Kirby, S. Holloway, and P. N. Johannessen (2004b), Geological reservoir characterization of a CO_2 storage site: The Utsira Sand, Sleipner, northern North Sea, *Energy*, *29*(9-10), 1371-1381.

Chopra, S., Z. Wang, M. Batzle, D. Han, and T. Mukerji (2004), Expert answers, *Recorder*, *18-24*.

Ciz, R., Toms, J., and Gurevich, B., (2005) Attenuation and dispersion of elastic waves in a poroelastic medium with spherical inclusions. Abousleiman Y.N., Cheng, A.H.D, Ulm, F.J. editors. *Proceedings of the 3rd Biot Conference on Poromechanics, University of Oklahoma*. pp 201-207

Davis, T. L., M. J. Terrell, R. D. Benson, R. Cardona, R. R. Kendall, and R. Winarsky (2003), Multicomponent seismic characterization and monitoring of the CO_2 flood at Weyburn Filed, Saskatchewan, *The Leading Edge*, *22*(7), 696-697.

Domenico, S. N. (1976), Effect of Brine-Gas Mixture on Velocity in an Unconsolidated Sand Reservoir, *Geophysics*, *41*(5), 882.

Dong, H. (2007), Micro-CT imaging and pore network extraction,

Doughty, C. (2007), Modelling geologic storage of carbon dioxide: Comparison of non-hysteretic and hysteretic characteristic curves, *Energy Conversion and Management*, *48*(6), 1768-1781.

Duan, Z., and R. Sun (2003), An improved model calculating CO_2 solubility in pure water and aqueous NaCl solutions from 273 to 533 K and from 0 to 2000 bar, *Chemical Geology*, *193*(3-4), 257-271.

Dutta, N. C., and H. Ode (1979), Attenuation and dispersion of compressional waves in fluid-filled porous rocks with partial gas saturation (White model) -Part I : Biot theory, *Geophysics*, *44*(11), 1777-1788.

Dvorkin, J., Nolen-Hoeksema, R., and Nur, A., (1994), The squirt-flow mechanism: macroscopic description. *Geophysics*. 59, 428-438.

Dvorkin, J. And Nur. A (1993) Dynamic poroelasticity: a unified model with squirt and the Biot mechanisms. *Geophysics* 58, 524-533.

Dvorkin, J. P., and A. Nur (1998), Acoustic signatures of patchy saturation, *International Journal of Solids Structures*, *35*(34-35), 4803-4810.

Dvorkin, J., and A. Nur (1996), Elasticity of high-porosity sandstones: Theory for two North Sea data sets, *Geophysics*, *61*(5), 1363-1370.

Ehlig-Economides, C., and M. J. Economides (2010), Sequestering carbon dioxide in a closed underground volume, *Journal of Petroleum Science and Engineering*, *70*(1-2), 123-130.

Eiken, O., I. Brevik, R. Arts, E. Lindeberg, and K. Fagervik (2000), Seismic monitoring of CO_2 injected into a marine aquifer, in *Expanded Abstracts*, vol. 70, pp. 1623–1626.

Eiken, O., P. Ringrose, C. Hermanrud, B. Nazarian, T. A. Torp, and L. Høier (2011), Lessons learned from 14 years of CCS operations: Sleipner, In Salah and Snøhvit, *Energy Procedia*, *4*, 5541-5548.

Ennis-King, J., and P. Lincoln (2002), Engineering Aspects of Geological Sequestration of Carbon Dioxide, *Proceedings of SPE Asia Pacific Oil and Gas Conference and Exhibition*.

Ennis-King, J., and L. Paterson (2005), Role of Convective Mixing in the Long-Term Storage of Carbon Dioxide in Deep Saline Formations, *SPE Journal*, *10*(3), 5-8.

Fayers, F. J., and A. H. Muggeridge (1990), Extensions to Dietz theory and behaviour of gravity tongues in slightly tilted reservoirs, *SPE Reservoir Engineering*, *5*, 487-494.

Flett, M., R. Gurton, and G. Weir (2007), Heterogeneous saline formations for carbon dioxide disposal: Impact of varying heterogeneity on containment and trapping, *Journal of Petroleum Science and Engineering*, *57*, 106-118.

Gasperikova, E., and G. M. Hoversten (2006), A feasibility study of nonseismic geophysical methods for monitoring geologic CO_2 sequestration, *The Leading Edge*, *25*(10), 1282-1288.

Gassmann, F. (1951), Elastic waves through a packing of spheres, *Geophysics*, *16*, 673-685.

Gestel, J.-P. van, J. H. Kommedal, O. I. Barkved, I. Mudal, R. Bakke, and K. D. Best (2008), Continuous seismic surveillance of Valhall Field, *The Leading Edge*, *27*(12), 1616-1621.

Ghaderi, A., and M. Landrø (2009), Estimation of thickness and velocity changes of injected carbon dioxide layers from prestack time-lapse seismic data, *Geophysics*, *74*(2), 17-28.

Girard, J.-F., N. Coppo, J. Rohmer, B. Bourgeois, V. Naudet, and C. Schmidt-Hattenberger (2011), Time-lapse CSEM monitoring of the Ketzin (Germany) CO_2 injection using 2×MAM configuration, *Energy Procedia*, *4*, 3322-3329.

Gist, G. A. (1994), Interpreting laboratory velocity measurements in partially gas-saturated rocks, *Geophysics*, *59*(7), 1100.

Global CCS Institute (2011), The global status of CCS: 2011, Canberra, Australia.

Gomez, C. T., and R. H. Tatham (2007), Sensitivity analysis of seismic reflectivity to partial gas saturation, *Geophysics*, *72*(3), 45-57.

González, E. F., T. Mukerji, G. Mavko, and R. J. Michelena (2003), Near and far offset P-to-S elastic impedance for discriminating fizz water from commercial gas, *The Leading Edge*, *22*(10), 1012-1015.

Gough, C. (2008), State of the art in carbon dioxide capture and storage in the UK: An experts' review, *International Journal of Greenhouse Gas Control*, *2*(1), 155-168.

Gunter, W. D., M. J. Mavor, and J. R. Robinson (2005), CO_2 storage and enhanced methane production: field testing at Fenn-Big Valley, Alberta, Canada, with application., in *7th International Conference on Greenhouse Gas Control Technologies (GHGT-7)*.

Han, D., M. Sun, and M. Batzle (2010), CO_2 velocity measurement and models for temperatures up to 200° C and pressures up to 100 MPa, *Geophysics*, *75*(3), 123-129.

Han, D., and M. Batzle (2002), Fizz water and low gas-saturated reservoirs, *The Leading Edge*, *21*(4), 395-398.

Hashin, Z., and S. Shtrikman (1963), A variational approach to the theory of the elastic behaviour of multiphase materials, *Journal of the Mechanics and Physics of Solids*, *11*(2), 127–140.

Haszeldine, R. S. (2009), Carbon capture and storage: how green can black be?, *Science*, *325*(5948), 1647-52.

Haszeldine, R. S., O. Quinn, G. England, M. Wilkinson, Z. K. Shipton, J. P. Evans, J. Heath, L. Crossey, C. J. Ballentine, and C. M. Graham (2005), Natural Geochemical Analogues for Carbon Dioxide Storage in Deep Geological Porous Reservoirs, a United Kingdom Perspective, *Oil & Gas Science and Technology*, *60*(1), 33-49.

Hauge, P. S. (1981), Measurements of attenuation from vertical seismic profiles, *Geophysics*, *46*(11), 1548,

Hebach, A., A. Oberhof, and N. Dahmen (2004), Density of Water + Carbon Dioxide at Elevated Pressures: Measurements and Correlation, *Journal of Chemical & Engineering Data*, *49*(4), 950-953.

Hendriks, C., Graus, W. and van Bergen, F., (2004) *Global carbon dioxide storage potential and costs*, Report Ecofys & The Netherland Institute of Applied Geoscience TNO, Ecofys Report EEP02002

Hill, R. (1963), Elastic properties of reinforced solids: some theoretical principles, *Journal of the Mechanics and Physics of Solids*, *11*(5), 357-372.

Holloway, S. (2009), Storage capacity and containment issues for carbon dioxide capture and geological storage on the UK continental shelf, *Proceedings of the Institution of Mechanical Engineers, Part A: Journal of Power and Energy*, *223*(3), 239-248.

Hunt, J. R., N. Sitar, and K. . Udell (1988), Nonaqueous phase liquid transport and cleanup: 1. Analysis of mechanisms, *Water Resources Research*, *24*(8), 1247-1258.

IPCC (2005), Special Report on Carbon Dioxide Capture and Storage,

Ide, S. T., K. Jessen, and F. Orr Jr (2007), Storage of CO_2 in saline aquifers: Effects of gravity, viscous, and capillary forces on amount and timing of trapping, *International Journal of Greenhouse Gas Control*, *1*(4), 481-491.

Jaeger, J. C., N. G. Cook, and R. Zimmerman (2007), *Fundamentals of Rock Mechanics*.

Johnson, D. L. (2001), Theory of frequency dependent acoustics in patchy-saturated porous media, *The Journal of the Acoustical Society of America*, *110*(2), 682-694.

Johnson, J. W., J. J. Nitao, and K. G. Knauss (2004), Reactive transport modelling of CO_2 storage in saline aquifers to elucidate fundamental processes, trapping mechanisms and sequestration partitioning, *Geological Society, London, Special Publications*, *233*(1), 107-128.

Juanes, R., C. W. MacMinn, and M. L. Szulczewski (2009), The Footprint of the CO_2 Plume during Carbon Dioxide Storage in Saline Aquifers: Storage Efficiency for Capillary Trapping at the Basin Scale, *Transport in Porous Media*, *82*(1), 19-30.

Juanes, R., E. J. Spiteri, F. M. Orr, and M. J. Blunt (2006), Impact of relative permeability hysteresis on geological CO 2 storage, *Water Resources Research*, *42*(12), 1-13.

Juhlin, C., R. Giese, K. Zinck-jørgensen, C. Cosma, H. Kazemeini, N. Juhojuntti, S. Lüth, B. Norden, and A. Förster (2007), Case History 3D baseline seismics at Ketzin , Germany: The CO_2 SINK project, *Geophysics*, *72*(5), 121-132.

Kabir, N., B. Lavaud, and G. Chavent (2000), Estimation of the density contrast by AVO inversion beyond the linear approximation: An indication of gas saturation, in *Society of Exploration geophysics 70th annual meeting, expanded abstracts*.

Kazemeini, S. H. (2009), Seismic investigations at the Ketzin CO_2 injection site, Germany: applications to subsurface feature mapping and CO_2 seismic response modelling. Unpublished PhD Thesis.

Kazemeini, S. H., C. Juhlin, and S. Fomel (2010), Monitoring CO_2 response on surface seismic data; a rock physics and seismic modeling feasibility study at the CO_2 sequestration site, Ketzin, Germany, *Journal of Applied Geophysics*, *71*(4), 109-124.

Kendall, R. R., R. Winarsky, T. L. Davis, and R. D. Benson (2003), *9C, 4D seismic processing for the Weyburn CO_2 flood, Saskatchewan, Canada*.

Kirstetter, O., P. Corbett, J. Somerville, and C. MacBeth (2006), Elasticity/saturation relationships using flow simulation from an outcrop analogue for 4D seismic modelling, *Petroleum Geoscience*, *12*(3), 205-219.

Knight, R., and R. Nolen-Hoeksema (1990), A laboratory study of the dependence of elastic wave velocities on pore scale fluid distribution, *Geophysical Research Letters*, *17*(10), 1529-1532.

Korbøl, R., and A. Kaddour (1995), Sleipner vest CO_2 disposal-injection of removed CO_2 into the Utsira formation, *Energy Conversion and Management*, *36*(6-9), 509–512.

Kumar, A., A. Datta-Gupta, R. Shekhar, and R. L. Gibson (2008), Modelling Time Lapse Seismic Monitoring of CO2 Sequestration in Hydrocarbon Reservoirs Including Compositional and Geochemical Effects, *Petroleum Science and Technology*, *26*(7), 887-911.

Kumar, A., M. Noh, R. C. Ozah, G. A. Pope, S. Bryant, K. Sepehrnoori, and L. W. Lake (2005), Reservoir Simulation of CO2 Storage in Deep Saline Aquifers, *SPE Journal*, *10*(3), 336-348.

Lackner, K. S. (2003), A Guide to CO2 Sequestration, *Science*, *300*(5626), 1677-1678.

Landrø, M. (2001), Discrimination between pressure and fluid saturation changes from time-lapse seismic data, *Geophysics*, *66*(3), 836-844.

Landrø, M., O. A. Solheim, E. Hilde, B. O. Ekren, and L. K. Stronen (1999), The Gullfaks 4D seismic study, *Petroleum Geoscience*, *5*(3), 213-226.

Landrø, M., H. H. Veire, K. Duffaut, and N. Najjar (2003), Discrimination between pressure and fluid saturation changes from marine multicomponent time-lapse seismic data, *Geophysics*, *68*(5), 1592-1599.

Lebedev, M., J. Toms-Stewart, B. Clennell, M. Pervukhina, V. Shulakova, L. Paterson, T. Muller, B. Gurevich, and F. Wenzlau (2009), Direct laboratory observation of patchy saturation and its effect on ultrasonic velocities, *The Leading Edge*, *28*(1), 24-27.

Lei, X., and Z. Xue (2009), Ultrasonic velocity and attenuation during CO_2 injection into water-saturated porous sandstone: Measurements using difference seismic tomography, *Physics of the Earth and Planetary Interiors*, *176*(3-4), 224-234.

Lindeberg, E., and D. Wessel-Berg (1997), Vertical convection in an aquifer column under a gas cap of CO_2, *Energy Conversion and management*, *38*, S229–S234.

Liu, Y. (1998), Acoustic properties of reservoir fluids. Unpublished PhD Thesis

Lumley, D. (2010), 4D seismic monitoring of CO_2 sequestration, *The Leading Edge*, *29*(2), 150-155.

Lumley, D. E., R. A. Behrens, and Z. Wang (1997), Assessing the technical risk of a 4-D seismic project, *The Leading Edge*, *16*(9), 1287.

Lumley, D. E., and R. A. Behrens (1998), Practical Issues of 4D Seismic Reservoir Monitoring: What an Engineer Needs to Know, *SPE Reservoir Evaluation & Engineering*, *1*(6).

Lumley, D., D. Adams, R. Wright, D. Markus, and S. Cole (2008), Seismic monitoring of CO_2 geo-sequestration: realistic capabilities and limitations, in *SEG Las Vegas 2008 Annual Meeting*, pp. 2841-2845.

Ma, J., and I. Morozov (2010), AVO modelling of pressure-saturation effects in Weyburn CO_2 sequestration, *The Leading Edge*, *29*(2), 178-183.

MacBeth, C., and K. Stephen (2008), Seismic scale saturation relations in turbidite reservoirs undergoing waterflood, *Geophysical Prospecting*, *56*(5), 693-714.

Macbeth, C., M. Floricich, and J. Soldo (2006), Going quantitative with 4D seismic analysis, *Geophysical Prospecting*, 54, 303-317.

Margrave, G. F. (2003), Numerical Methods of Exploration Seismology with algorithms in MATLAB.,

Mathieson, A., J. Midgley, K. Dodds, I. Wright, P. Ringrose, and N. Saoul (2010), CO_2 sequestration monitoring and verification technologies applied at Krechba, Algeria, *The Leading Edge*, *29*(2), 216-222.

Mavko, G., T. Mukerji, and J. Dvorkin (1998), *The Rock Physics Handbook*, Cambridge University Press.

Mavko, G., and T. Mukerji (1998), Bounds on low-frequency seismic velocities in partially saturated rocks, *Geophysics*, *63*(3), 918-924.

Mavko, G., and Jizba, D. (1991) Estimating grain-scale fluid effects on velocity dispersion in rocks. *Geophysics*.

McKenna, J. J., B. Gurevich, M. Urosevic, and B. J. Evans (2003), Rock Physics- Application to geological storage of CO_2, *APPEA*.

Meadows, M. (2008) Time-lapse seismic modelling and inversion of CO_2 saturation for storage and enhanced oil recovery. *The Leading Edge*, 27, 506-516..

Morris, J. P., R. L. Detwiler, S. J. Friedmann, O. Y. Vorobiev, and Y. Hao (2011), The large-scale geomechanical and hydrogeological effects of multiple CO_2 injection sites on formation stability, *International Journal of Greenhouse Gas Control*, *5*(1), 69-74.

Murphy, W. F. (1982), Effects of partial water saturation on attenuation in Massilon sandstone and Vycor porous glass, *The Journal of the Acoustical Society of America*, *71*(6), 1458.

Murphy, W. F. (1984), Acoustic measures of partial gas saturation in tight sandstones, *Journal of Geophysical Research*, *89*(B13), 11549–11559.

Müller, T. M., and B. Gurevich (2005), Wave-induced fluid flow in random porous media: Attenuation and dispersion of elastic waves, *The Journal of the Acoustical Society of America*, *117*(5), 2732.

Myer, L. R., G. M. Hoversten, and E. Gasperikova (2002), Sensitivity and cost of monitoring geologic sequestration using geophysics, in *Proceedings of the 6th international conference on Greenhouse Gas Control Technologies (GHGT-6)*, pp. 377-382.

NIST (2011), National Institute of Standards in Technology (NIST) Standard Reference Database Number 69,

Nghiem, L., P. Sammon, J. Grabenstetter, and H. Ohkuma (2004), Modelling CO_2 Storage in Aquifers with a Fully-Coupled Geochemical EOS Compositional Simulator, in *Proceedings of SPE/DOE Symposium on Improved Oil Recovery*, Society of Petroleum Engineers.

Nooner, S., O. Eiken, C. Hermanrud, G. Sasagawa, T. Stenvold, and M. Zumberge (2007), Constraints on the in situ density of CO_2 within the Utsira formation from time-lapse seafloor gravity measurements, *International Journal of Greenhouse Gas Control*, *1*(2), 198-214.

Obi, E.-O. I., and M. J. Blunt (2006), Streamline-based simulation of carbon dioxide storage in a North Sea aquifer, *Water Resources Research*, *42*(3), 1-13.

Onishi, K., T. Ueyama, T. Matsuoka, D. Nobuoka, H. Saito, H. Azuma, and Z. Xue (2008), Application of crosswell seismic tomography using difference analysis with data normalization to monitor CO_2 flooding in an aquifer, *International Journal of Greenhouse gas Control*, 1-11.

Onuma, T., and S. Ohkawa (2009), Detection of surface deformation related with CO2 injection by DInSAR at In Salah, Algeria, *Energy Procedia*, *1*(1), 2177-2184.

Osif, T. (1988), The effects of salt, gas, temperature, and pressure on the compressibility of water, *SPE13174*, *3*(1), 175–181.

Partyka, G., J. Gridley, and J. Lopez (1999), Interpretational applications of spectral decomposition in reservoir characterization, *The Leading Edge*, *18*(3), 353.

Pawar, J. R., N. R. Warpinski, J. C. Lorenz, R. D. Benson, R. B. Grigg, B. A. Stubbs, P. H. Stauffer, J. L. Krumhansl, S. P. Cooper, and R. K. Svec (2006), Overview of a CO2 sequestration field test in the West Pearl Queen reservoir, New Mexico, *Environmental Geoscience*, *13*(3), 163-180.

Peng, D.-T., and D. B. Robinson (1976), A new Two-Constant Equation of State, *Industrial and Engineering Chemistry: Fundamentals*, *15*, 59-64.

Pentland, C. H., R. El-Maghraby, S. Iglauer, and M. J. Blunt (2011), Measurements of the capillary trapping of super-critical carbon dioxide in Berea sandstone, *Geophysical Research Letters*, *38*(6), 2007-2010.

Plug, W., and J. Bruining (2007), Capillary pressure for the sand–CO_2–water system under various pressure conditions. Application to CO_2 sequestration, *Advances in Water Resources*, *30*(11), 2339-2353.

Preisig, M., and J. H. Prévost (2011), Coupled multi-phase thermo-poromechanical effects. Case study: CO_2 injection at In Salah, Algeria, *International Journal of Greenhouse Gas Control*.

Pride S.R., Berryman J.G. and Harris J.M., (2004) Seismic attenuation due to wave-induced flow. *Journal of Geophysical Research.*

Pruess, K., T. Xu, J. Apps, and J. Garcia (2003), Numerical Modeling of Aquifer Disposal of CO_2, *SPE Journal*, (October 2002), 26-28.

Qi, R., T. C. LaForce, and M. J. Blunt (2008), Design of carbon dioxide storage in aquifers, *International Journal of Greenhouse gas Control*, 1-11.

Quan, Y., and J. M. Harris (1997), Seismic attenuation tomography using the frequency shift method, *Geophysics*, *62*(3), 895.

Ravazzoli, C. L., and J. L. Gómez (2011), AVA seismic reflectivity analysis in carbon dioxide accumulations: Sensitivity to CO2 phase and saturation, *Journal of Applied Geophysics*, *73*(2), 93-100.

Ribeiro, C., and C. MacBeth (2006), Time-lapse seismic inversion for pressure and saturation in Foinaven field, west of Shetland, *first break*, *24*.

Roberts, G. (2000), Wide-angle AVO, *70th Ann. Internat. Mtg: Soc. of Expl.*, 134-137.

Roof, J. G. (1970), Snap-Off of Oil Droplets in Water-Wet Pores, *Society of Petroleum Engineers Journal*, *10*(1).

Rossi, G., D. Gei, S. Picotti, and J. M. Carcione (2008), CO_2 storage at the Aztbach-Schwanenstadt gas field: a seismic monitoring feasibility study, *first break*, *26*, 45-51.

Rutqvist, J., J. Birkholzer, F. Cappa, and C.-F. Tsang (2007), Estimating maximum sustainable injection pressure during geological sequestration of CO_2 using coupled fluid flow and geomechanical fault-slip analysis, *Energy Conversion and Management*, *48*, 1798-1807.

Rutqvist, J., and C. Tsang (2002), A study of caprock hydromechanical changes associated with CO_2-injection into a brine formation, *Environmental Geology*, *42*, 296-305.

Saito, H., D. Nobuoka, H. Azuma, Z. Xue, and D. Tanase (2006), Time-lapse crosswell seismic tomography for monitoring injected CO_2 in an onshore aquifer, Nagaoka, Japan, *Exploration Geophysics*, *37*(1), 30-36.

Sato, K., S. Mito, T. Horie, H. Ohkuma, H. Saito, J. Watanabe, and T. Yoshimura (2011), Monitoring and simulation studies for assessing macro- and meso-scale migration of CO2 sequestered in an onshore aquifer: Experiences from the Nagaoka pilot site, Japan, *International Journal of Greenhouse Gas Control*, *5*(1), 125-137.

Schlumberger (1991), *Log Interpretation Principles/Application*, Houston, TX: Sclumberger Wireline & Testing.

Schlumberger (2009), ECLIPSE reference manual,

Sclater, J. G., and P. A. F. Christie (1980), Continental stretching: an explanation of the post-mid-Cretaceous subsidence of the central North Sea basin, *Journal of Geophysical Research*, *85*(B7), 3711–3739.

Sengupta, M., and G. Mavko (2003), Impact of flow-simulation parameters on saturation scales and seismic velocity, *Geophysics*, *68*(4), 1267-1280,

Sheriff, R. E., and L. P. Geldhart (1995), *Exploration Seismology, 2nd Edition*, Cambridge University Press.

Shi, J.-Q., Z. Zue, and S. Durucan (2007), Seismic monitoring and modelling of supercritical CO_2 injection into a water-saturated sandstone: Interpretation of P-wave velocity data, *International Journal of Greenhouse gas Control 1*, 473-480.

Shuey, R. T. (1985), A simplification of the Zoeppritz equations, *Geophysics*, *50*(4), 609-614.

Siggins, A. F., and D. Dewhurst (2003), Saturation, pore pressure and effective stress from sandstone acoustic properties, *Geophysical Research Letters*, *30*(2), 10-13.

Sodagar, T. M., and D. C. Lawton (2011), Seismic modelling of CO_2 fluid substitution for the Heartland Area Redwater CO2 Storage Project (HARP), Alberta, Canada, *Energy Procedia*, *4*, 3338-3345.

Span, R., and W. Wagner (1996), A New Equation of State for Carbon Dioxide Covering the Fluid Region from the Triple-Point Temperature to 1100 K at Pressures up to 800 MPa, *Journal of physical and chemical reference data*, *25*(6), 1513-1558.

Spycher, N., K. Pruess, and J. Ennis-King (2003), CO_2-H_2O mixtures in the geological sequestration of CO_2. I. Assessment and calculation of mutual solubilities from 12 to 100°C and up to 600 bar, *Geochimica et Cosmochimica Acta*, *67*(16), 3015-3031.

Stevens, S. H., J. A. Kuuskraa, and R. A. Schraufnagel (1996), Technology spurs growth of U.S. coalbed methane, *Oil and Gas Journal*, *94*(1), 56-63.

Stewart, R. R., J. E. Gaiser, R. J. Brown, and D. C. Lawton (2002), Converted-wave seismic exploration: Methods, *Geophysics*, *67*(5), 1348.

Sun, M., and D. Han (2009), Velocity Properties of CO_2-saturated Water and Methane-saturated Water at Temperatures up to 200°C and Pressures up to 138 MPa, in *SEG Houston 2009 International Exposition and Annual Meeting*, pp. 2095-2099.

Tatham, R.H., and M.D. McCormack (1991) Multicomponent Seismology in Petroleum Geoscience. Society of Exploration Geophysicists

Toms, J., T. M. Müller, and B. Gurevich (2007), Seismic attenuation in porous rocks with random patchy saturation, *Geophysical Prospecting*, *55*(5), 671-678.

Torp, T., and J. Gale (2004), Demonstrating storage of CO_2 in geological reservoirs: The Sleipner and SACS projects, *Energy*, *29*(9-10), 1361-1369.

Trani, M., R. Arts, O. Leeuwenburgh, and J. Brouwer (2011), Estimation of changes in saturation and pressure from 4D seismic AVO and time-shift analysis, *Geophysics*, *76*(2).

Tura, A., and D. E. Lumley (2000), Estimating Pressure and Saturation Changes From Time-Lapse AVO Data, in *Proceedings of Offshore Technology Conference*, pp. 0-3, The Offshore Technology Conference.

Vandeweijer, V. et al. (2009), CO_2 storage in saline aquifers: In the Southern North Sea and Northern Germany, *Energy Procedia*, *1*(1), 3079-3086.

Vanorio, T., G. Mavko, and S. Vialle (2010), The rock physics basis for 4D seismic monitoring of CO_2 fate: Are we there yet?, *The Leading Edge*, *29*(2), 156-162.

Vasquez, G., J. Justen, M. S. D. Santos, M. Morschbacher, R. Sansonowski, M. De Carvelho, E. Vargas, and J.-L. Formento (2010), Stress history of producing reservoirs and 4D seismic studies: Some often-forgotten aspects, *The Leading Edge*.

Verdon, J. P., J. Kendall, D. J. White, D. A. Angus, Q. J. Fisher, and T. Urbancic (2010), Passive seismic monitoring of carbon dioxide storage at Weyburn, *The Leading Edge*, *29*(2), 200-206.

Walton, K. (1987), The effective elastic moduli of a random packing of spheres, *Journal of the Mechanics and Physics of Solids*, *35*, 213-226.

Wang, Z. Z. (2001), Y2K Tutorial Fundamentals of seismic rock physics, *Geophysics*, *66*(2), 398 - 412.

Wang, Z., and A. Nur (1989), Effects of CO_2 flooding on wave velocities in rocks with hydrocarbons, *SPE Reservoir Engineering*, *4*(4), 429–436.

Watts, G. F. T., D. Jizba, D. E. Gawith, and P. Gutteridge (1996), Reservoir monitoring of the Magnus Field through 4D time-lapse seismic analysis, *Petroleum Geoscience*, *2*(4), 361.

White, D. (2009), Monitoring CO_2 storage during EOR at the Weyburn-Midale Field, *The Leading Edge*, *28*(7), 838-842.

White, D. J., G. Burrowes, T. L. Davis, Z. Hajnal, K. Hirsche, I. Hutcheon, E. Majer, B. Rostron, and S. Whittaker (2004), Greenhouse gas sequestration in abandoned oil reservoirs: The International Energy Agency Weyburn pilot project, *GSA today*, *14*(7), 4–10.

White, D. J., and J. W. Johnson (2009), Integrated geophysical and geochemical research programs of the IEA GHG Weyburn-Midale CO_2 monitoring and storage project, *Energy Procedia*, *1*(1), 2349-2356.

White, J. E. (1975), Computed seismic speeds and attenuation in rocks with partial gas saturation, *Geophysics*, *40*(2), 224-232.

Widess, M. B. (1973), How thin is a thin bed?, *Geophysics*, *38*.

Wulff, A., A. Gerhardt, T. Ridsdill-Smith, and M. Smith (2008), The role of rock physics for the Enfield 4D seismic monitoring project, *Exploration Geophysics*, (November 2007), 108-114.

Wyllie, M. R. J., and A. R. Gregory (1956), Elastic wave velocities in heterogeneous and porous media, *Geophysics*, *XXI*(1).

Xu, H. (2006), Calculation of CO_2 acoustic properties using Batzle-Wang equations, *Geophysics*, *71*(2), 21-23.

Yamamoto, H., and C. Doughty (2011), Investigation of gridding effects for numerical simulations of CO_2 geologic sequestration, *International Journal of Greenhouse Gas Control*.

Yuh, S. H. (2003), Time-lapse Seismic Monitoring of Subsurface Flow. Unpublished PhD Thesis.

Zoeppritz, K. (1919), Uber reflexion und durchgang seismischer Wellen durch Unstetigkerlsflaschen., *Uber Erdbebenwellen VII B. Nachrichten der Koniglichen Gesellschaft der Wissenschaften zu Gottingen Math. Phys.*, *K1*, 57-84.